Ultra Selective and Sensitive Electrochemical Detection of Anti-Cancer and Anti-Viral Drugs by Optimized Nano-Bio-Sensors

THÈSE N^{O} 7402 (2017)

PRÉSENTÉE LE 23 JUIN 2017

À LA FACULTÉ INFORMATIQUE ET COMMUNICATIONS
LABORATOIRE DES SYSTÈMES INTÉGRÉS (IC/STI)
PROGRAMME DOCTORAL EN MICROSYSTÈMES ET MICROÉLECTRONIQUE

ÉCOLE POLYTECHNIQUE FÉDÉRALE DE LAUSANNE

POUR L'OBTENTION DU GRADE DE DOCTEUR ÈS SCIENCES

PAR

Nima ALIAKBARINODEHI

acceptée sur proposition du jury:

Prof. C. Dehollain, présidente du jury
Dr S. Carrara, Prof. G. De Micheli, directeurs de thèse
Dr P. Estrela, rapporteur
Prof. S. Ingebrandt, rapporteur
Prof. M. GIJS, rapporteur

ÉCOLE POLYTECHNIQUE
FÉDÉRALE DE LAUSANNE
Suisse
2017

Acknowledgements

Firstly, I would like to express my sincere gratitude to my supervisors, Dr. MER Sandro Carrara and Prof. Giovanni De Micheli, for the trust they put in me from the beginning, including the preparation of my Masters thesis, and also for providing me with the opportunity of working on a challenging, multi-disciplinary and innovative project. I thank them for their constant and encouraging support during the preparation of my thesis, and for their efforts in creating a wonderful and relaxed atmosphere at the work place.

For the same reasons I would like to thank Dr. Pedro Estrela, who managed PROSENSE so well that he made it one of the most fruitful periods of my life in scientific, social and cultural aspects. I am also grateful to him for patiently supervising me during my secondment in the University of Bath, where I was introduced to the innovative world of biosensing.

I would like to thank the Marie Curie Initial Training Network-PROSENSE for the funding, and all its members for their sustained guidance, patience, and encouragement throughout my research.

I would like to give special thanks to Prof. Sven Ingebrandt, Dr. Jan Tkac, Dr. Jaroslav Katrlik, Dr. Virginia Chu, Prof. Joao Pedro Conde, Dr. Chris Allender, Dr. Bowen, Prof. O'Kennedy, Dr. Guido Drago from the PROSENSE network for all the time and efforts they put on our intensive trainings during PROSENSE workshops in their respective institutes.

Thanks to Christina Govoni, Marie Halm and Lucie Auberson for their help and patience with the EPFL administration, and their willingness to manage unintentional difficulties.

I want to thank the members of my thesis jury: Prof. Catherine Dehollain - the president, Dr. Pedro Estrela, Prof. Dr. Sven Ingebrandt and Prof. Martinus Gijs for accepting my invitation to evaluate my thesis, and for the time and effort they put into reading it and providing useful feedback.

I would like to thank all my colleagues in PROSENSE and the LSI laboratory, and to show special gratitude to the close friends who helped me face so many difficulties in completing my PhD. I would like to thank my colleague and close friend Ioulia Tzouvadaki, with whom I have shared the joy and the pain of PhD research during all these years, as well as her enthusiastic collaboration: proofreading of the thesis, devoted discussions and unforgettable moments. I would like to acknowledge her, especially, for her collaboration and intensive work on memristive biosensors for drug monitoring. Thanks to Irene, for all the useful advice on the most complicated matters of electrochemistry. Thanks to Dr. Hassan Ghasemzadeh for all the discussions and information, and for always being ready to help. I would like also to thank Dr. Pawan Jolly and Dr. Nikhil Bhalla for all their help and friendship, and acknowledge them for their collaboration on field-effect biosen-

sors. I would also like to acknowledge Dr. Anna Miodek for her collaboration on the same project. Special thanks go to other close friends in the University of Bath, Nello Formisano and Pavel Zhurauski, and to my great roommate Dr. Federico Angiolini for his intellectual discussions.

The years of my PhD have been the best of my life so far: fun, full of new experiences and trips around the world in the company of great people: my friends and colleagues.

Special thanks to the Iranian community in Lausanne for all the fun, new experiences, outdoor adventures, and for organizing great ceremonies.

My deep gratitude to my beloved wife Sahar Aliakbar, for all the experiences we are sharing together, her energy and enthusiasm, her flawless organization of everything, and for all the support in my life. The same gratitude goes to my parents for their unconditional support and love.

8th February, 2017

Abstract

Reliable, low cost, and accessible drug monitoring systems for individualized healthcare, especially chemotherapy for malignant diseases like prostate cancer and AIDS, are highly desirable. This is even more critical for drugs like abiraterone and TFV, with very narrow and low (submicro-molar) therapeutic windows.

Point-of-care biosensors for drug monitoring offer a solution for this kind of therapy: bringing treatments to the patient's bedside and eliminating interfering factors in medical treatments like interindividual differences (genetic profile, age, race, gender, etc.), environmental agents and the influences of other drugs (drug-drug interactions, adverse effects, etc.). Moreover, point-of-care biosensors provide access to reliable, fast and cheap cutting-edge technology for a large population. In particular, such a novel chemical therapy will suppress the morbidity rate and treatment time, as well as providing better screening of patients, and tighter monitoring of treatment. Consequently, this would lead to an improvement in patients' medical treatments and overall quality of life. In other words, improved treatment efficacy and less side effects for patients.

The objective of this thesis is to investigate biosensors for the monitoring of drugs for chemotherapeutic treatment for prostate cancer and AIDS. The first part of this work is devoted to the development of biosensors to target three main groups of drugs : electroactive drugs, drugs that involve an enzyme in their metabolic pathway and drugs that are neither electroactive nor interact with enzymes in the body. The second part is devoted to offering a reliable solution for selective and sensitive point-of-care biosensing for anti-prostate cancer drugs and anti-AIDS drugs.

Screen-printed based biosensors with nanofunctionalization are offered for electroactive drug detection as a solution for prostate-cancer personalized medicine. Several steps of optimization have been performed to boost their electrochemical performance towards detection of Etoposide (a prostate cancer drug) in its therapeutic range, and also preparing the biosensor for the development of an enzymatic biosensor. Furthermore, they have been used to observe the quantum blockage in gold nanoparticles, and to investigate its impact on the biosensing performance.

Secondly, an enzymatic biosensor for monitoring drugs, which involve cytochrome P450 enzymes in their metabolic pathway in the body, is presented as a second solution for prostate-cancer personalized medicine. This kind of sensor is produced by immobilizing the cytochrome P450 enzyme over the already-mentioned optimized biosensor. The biosensor is utilized for investigating abiraterone electrochemistry, and subsequently the detection of abiraterone in buffer and human serum are reported for the first time.

Finally, affinity-based biosensors are proposed to address the detection of drugs that are neither electroactive nor interact with enzymes in body. Tenofovir, an anti-HIV drug, is targeted in this case to help find also a solution for HIV personalized medicine.

To this aim, an aptamer-based sensing surface is obtained and optimized after intensive optimization, and the experimental testing of different possible surfaces. This surface is formed on the active part of a field-effect transistor transducer, and also a memristive nanowire transducer as a recognition element to develop the affinity based biosensors. At this stage, these two biosensors were experimented successfully for Tenofovir monitoring.

In spite of the promising response of aptamer-based field-effect biosensors, the therapeutic range of Tenofovir was still not within the limits of detection obtained, so a more sensitive biosensor became necessary. To address this issue, and also to demonstrate a novel detection methodology, a second biosensor was developed to push the performance of the biosensor to the very limits, and to obtain the best-reported performance for drug monitoring. To this aim, a recently offered memristive transducer was employed in drug monitoring for the first time. This also helped to achieve a holistic detection approach with the possible applications over a wide range of drugs with only small modifications. This is even more critical for therapeutic compounds with very low concentrations in the circulatory system.

The discoveries in this thesis are of great importance of point-of-care therapeutic drug monitoring and personalized medicine for prostate cancer and AIDS, with the possibility of extending the proposed applications to a wide range of drugs.

Keywords

Biosensors, point-of-care, therapeutic drug monitoring, carbon nanotubes, cytochrome P450, prostate cancer personalized medicine, AIDS personalized medicine, abiraterone, tenofovir, etoposide, specific surface area, electroactive surface area, Coulomb blockade, field-effect transducer, memristive silicon nanowire, aptamer.

Résumé

Il est important d'avoir des systèmes TDM fiables, économiques et accessibles pour des soins de santé individualisés, et particulièrement, pour la chimiothérapie des maladies malignes comme le PCa et le SIDA. Ceci est encore plus critique pour des médicaments comme l'abiraterone et le TFV qui requièrent une fenêtre thérapeutique très étroite et faible (submicro-molaire).

Les biocapteurs « point-of-care » utilisés pour la surveillance des médicaments offrent une solution pour les thérapies qui apportent des traitements près du patient et éliminent les facteurs interférents dans les traitements médicaux tels que les différences inter-individus (profil génétique, âge, race, sexe etc.), les agents environnementaux et d'autres drogues influences (interactions médicamenteuses, effets indésirables, etc.).

De plus, les biocapteurs « Point-of-care » permettent d'accéder à une technologie de pointe fiable, rapide et économique pour un grand nombre de personnes. En particulier, une telle thérapie chimique supprimerai le taux de mortalité et la durée du traitement tout en fournissant un meilleur dépistage des patients et une surveillance accrue du traitement. Ce qui, par conséquent, conduirai à des améliorations dans les traitements médicaux et la qualité de vie des patients. En conséquence, une meilleure efficacité du traitement et des effets secondaires moins élevés pour les patients.

L'objectif de cette thèse est d'étudier les biocapteurs pour la surveillance des médicaments pour les chimiothérapies du cancer de la prostate et du SIDA. Ce travail est divisé en deux parties principales. D'une part le nous présentons développement de biocapteurs pour surveiller trois groupes de médicaments principaux : les médicaments électro-actifs, les médicaments qui impliquent une enzyme dans leur métabolisme et les médicaments qui ne sont ni électro-actifs ni interagissent avec les enzymes dans le corps, et d'autre part nous proposons une solution fiable plus sélective et sensible des biocapteurs « point-of-care » pour les médicaments contre le cancer de la prostate et pour les médicaments contre le SIDA.

Trois types de biocapteurs sont présentés dans la première partie. Premièrement les biocapteurs à sérigraphie avec nano-fonctionnalisation sont proposés pour la détection électro-active de drogues comme une solution pour la médecine personnalisée contre le cancer de la prostate. Plusieurs étapes d'optimisation ont été réalisées pour amplifier leurs performances électrochimiques en vue de la détection de l'étoposide (médicament contre le cancer de la prostate) dans la gamme thérapeutique et aussi préparer le biocapteur pour le développement d'un biocapteur enzymatique. De plus, nous avons pu les utiliser pour observer le blocage quantique des nanoparticules d'or et étudier son impact sur la performance des biocapteurs.

Deuxièmement, un biocapteur enzymatique pour surveiller les médicaments, qui impliquent l'enzyme du cytochrome P450 dans leur métabolisme sur le corps, est présenté comme autre solution pour la médecine personnalisée du cancer de la prostate. Ils sont produits par l'immobilisation de l'enzyme cytochrome P450 par rapport au biocapteur optimisé déjà mentionné. Ensuite, nous utilisons un biocapteur pour étudier l'électrochimie de l'abiraterone, puis la détection de l'abiraterone dans le tampon et le sérum humain, démontré ici pour la première fois.

Enfin, des biocapteurs basés sur l'affinité sont proposés pour traiter la détection de médicaments qui ne sont ni électro-actifs ni interagissent avec des enzymes dans le corps. Tenofovir, un médicament anti-VIH, est ciblée dans ce cas pour aider à trouver aussi une solution pour la médecine personnalisée de VIH.

A cet effet, une surface de détection à base d'aptamère est obtenue et optimisée après des étapes d'optimisation intensive et des essais expérimentaux de différentes surfaces possibles. Cette surface est formée sur la partie active d'un transducteur à transistor à effet de champ et également un transducteur à nano-fils memristif comme élément de reconnaissance pour développer les biocapteurs basés sur l'affinité. A ce stade, ces deux biocapteurs ont été expérimentés avec succès pour le suivi du ténofovir.

Dans un cas où le premier biocapteur à effet de champ avait une réponse prometteuse, le deuxième biocapteur visait à pousser les performances du biocapteur à des extrêmes, à obtenir la meilleure performance rapportée pour la surveillance des médicaments et d'employer pour la première fois un transducteur memristif dans le domaine de la surveillance des médicaments. Puisqu'il y a toujours le besoin de biocapteurs plus précis et plus sensible, spécialement quand une méthodologie proposée a la possibilité d'être utilisée sur un large éventail de médicaments juste avec de petites modifications, ceci est encore plus critique quand l'on considère que la gamme thérapeutique des médicaments dans le corps humain est différente les uns des autres en fonction de leur pharmacocinétique et pharmacodynamique et peut atteindre des valeurs très faibles.

Les résultats de cette thèse sont d'une grande importance dans le suivi médicamenteux thérapeutique point of care et la médecine personnalisée du cancer de la prostate et du VIH, avec la possibilité d'étendre les applications proposées à un large éventail de médicaments.

Mots-clés

Biocapteurs, point-of care, surveillance de medicaments, nanotubes de carbone, cytochrome P450, cancer de la prostate, médecine personnalisée, VIH, abiraterone, tenofovir, etoposide, surface spécifique, blocage quantique, transducteur a effet de champs, memristor à nanofil de silicium, aptamer.

Contents

List of Figures

List of Tables

Chapter 1 Introduction

According to the President's Council of Advisors on Science and Technology,[1] "personalized medicine refers to the tailoring of medical treatment to the individual characteristics of each patient; to classify individuals into subpopulations that differ in their susceptibility to a particular disease or their response to a specific treatment so that preventive or therapeutic interventions can then be concentrated on those who will benefit, sparing expense and side effects for those who will not."[2] Therefore, personalized medicine is the science of distinguishing the interindividual differences in every population in terms of their susceptibility to a particular disease or their response to a specific treatment, and It does not necessarily require the creation of new medical treatments for a patient. In other words, the final aim of personalized medicine is to provide a specific and optimized medical treatment for every individual by delivering the proper treatment at the right time. Highly advanced personalized medicine incorporates personal genetics, protein profiles or metabolomics (pharmacogenomics, transcriptomics, proteomics and pharmacometabonomics) to strengthen healthcare at a more personalized level, particularly aiming at the classification of patients into subgroups, trying to predict their therapeutic response to chemical treatments (chemotherapy). Despite their important role in shaping our insight into personalized therapy, serious limitations have hampered their progress towards mass application in this field: an inability to provide absolute certainty as a stand-alone approach, the need of invasive sample preparation, a lack of sufficient knowledge about the correlation of protein profiles and drug response and, finally, too much complexity. [3–9] On the contrary, personalized medicine needs an accurate empirical technique with a corrective approach based on the quantitative monitoring of drug response at any point in time after the administration.

1.1 Pharmacology and personalized medicine

The interindividual differences expressed by different genetic profiles of people alter the relations between the drug concentrations in a patients' body with therapeutic effects and the drug metabolism pathways in the body. This means a deviation of the estimated drug concentration over time, and a different therapeutic response from what was expected. [10, 11] The behaviour of drugs in the human body and the effect of the body on an administered drug needs to be understood to explain the reason behind the significance of interindividual variability in chemical treatment, and to highlight the significance of drugs concentration monitoring. Types of variability can be classified as Pharmacodynamics and pharmacokinetics. These are important concepts in phar-

[1] On April 27, 2009, President Obama announced the President's Council of Advisors on Science and Technology (PCAST). PCAST is an advisory group of the nation's leading scientists and engineers who directly advise the President of USA and the Executive Office of the President. PCAST-makes policy recommendations in the many areas where understanding of science, technology, and innovation is key to strengthening our economy and forming policy that works for the American people.[1]

macology, explaining the relations between drug concentration and effect, as well as the parameters that modulate drug concentration over time. Not considering their variability causes a lack of efficacy and even unexpected harmful effects. [12]

1.1.1 Pharmacodynamics

Pharmacodynamics describes the effect of a specific drug and the magnitude of this effect on the human body, the efficacy and potency of the drug. Efficacy describes the capability of drug to produce a response and is expressed as the median effective concentration, while potency is the required amount of drug concentration to produce a reponse of specific intensity. Pharmacodynamics is also used to evaluate the safety of drugs by monitoring the concentration of drugs in people and relating the dose of the drug to the percentage of people who show the required response or side effect. The therapeutic index, or the difference between median effective concentration and median toxic concentration, is a factor that determines the safety of that drug. Figure 1 on the left presents an example of the relation between the dose and the produced response of three generic drugs, the so-called dose-response curve, and on the right it shows a relation between the drug concentration and its effect on the examined population. The left graph is a comparison between the 3 generic-drugs in terms of efficacy and potency, and shows that for a specific response intensity, for instance 60% of maximum, a higher concentration of drug 3 and then drug 2 is required. Therefore drug 1 is more potent than drug 2 and and drug 2 is more potent than drug 3. In addition, drug 3 has not properly produced the required response, meaning that it has less efficacy than the others.

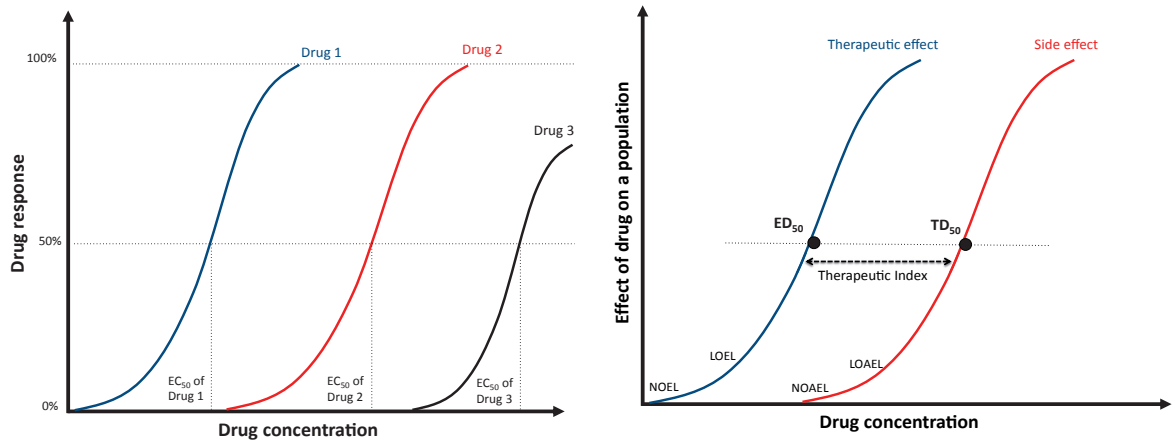

Figure 1. Examples of dose-response relationships. Left figure: compares the efficacy and potency of 3 drugs. Drug 1 is more potent than drug 2 and drug 2 more potent than drug 3, while drug 3 has less efficacy compared to the other two drugs. Right figure: relation between the concentration of the administered drug and the percentage of population showing a specific response. The difference between median effective dose (ED50) and the median toxic dose (TD50) is the therapeutic index of the drug. NOEL/NOAEL and LOEL/LOAEL stand for No Observable Effect/Adverse Effect Level, Lowest Observable Effect/Adverse Effect Level..

Pharmaceutical companies estimate therapeutic drug index by experimenting a limited set of people to obtain the drug concentration and effect on population curve. However these results are not applicable on a word wide scale with a huge variability in terms of genetic profile, race, environment, and food and nutrition habits.

1.1.2 Pharmacokinetics

The second pharmacological factor that affects the drug monitoring is called “Pharmacokinetics”, and explains the actions of the body on a drug that influences the speed of drug action (onset time), intensity of effect and the clearance time (the time interval that drug is active). Pharmacokinetics consists of four main phases: Adsorption, Distribution, Metabolism, and Excretion, abbreviated to ADME.

Absorption: the process by which a drug moves from the site of administration to the blood or site of action, it explains how quickly and in what quantity a drug reaches its intended target (site) of action.

Distribution: process of drug movement from the blood to and from the tissues. It is affected by lipophilicity and the affinity of the drug to bind to plasma proteins.

Metabolism: bio-alteration of the drug in the human body that causes a biotransformation to an inactive form of compound that is easier to be excreted from the body. Beside inactive forms, there are some drugs that, after metabolic transformation, are equally active (e.g. 25luoxetine), more active (e.g. iosartan), toxic (e.g. acetaminophen), or are transformed to a prodrug (e.g. codeine). Metabolism is carried out in two phases. Phase 1 involves oxidation, and hydrolysis reactions on the external compound (xenobiotics) by means of enzymes such as cytochrome p450 (CYP450) monoxygenase system, NADPH-cytochrome reductase, esterases, and amidases etc. Phase 2 is the conjugation of the drug to a water-soluble adduct using the polar handle from Phase I. Phase 2 reactions include glucuronidation, sulfation, glutathione conjugation, amino acid conjugation, acylation and methylation. One of the most abundant enzymes in the human body (2.5% of total hepatic microsomal proteins) are CYP450 that are responsible for ~ 75% of the metabolism of drugs. The metabolism is highly affected by age, sex, pathology, food and nutrition status, environment, tobacco and alcohol use, drug-drug interaction, pharmacogenetics and chromopharmacology[2].

Excretion: the process of removing the xenobiotics from body. Urine (kidneys; for hydrophobic substances), Bile, faeces, lung (volatile substances), sweat, tears, reproductive fluids, milk etc. are some examples of excretion pathways.

To have a successful chemical treatment it is important to maintain the concentration of drugs in the circulatory system of the human body in the right range, called the therapeutic window: the beneficial range of drug concentration without causing significant adverse effects. A typical plasma concentration to time profile, after an oral drug administration of the drug, is shown in Figure 2. [13] This identifies some important characteristics related to the behaviour of drugs in the body. C_{max} indicates the maximum concentration of drugs that is absorbed, and reaching body fluids. Rate of absorption, t_{max}, is the time required to achieve maximum concentration. AUC, or area under the curve, represents the overall systemic exposure to the drug, and is used to measure the

[2] It is the study of how the effects of drugs vary with biological timing and endogenous periodicities.

[3] A second medication to suppress side effects of main drug.

[4] Prostate cancer is a malignant tumour of the prostate gland, a walnut-sized organ located in front of a man's rectum and below the bladder. The

bioavailability of an administered drug. Bioavailability is the portion of the drug administered orally that reaches the circulatory system after passing several physiological barriers. A relative term that compares the total amount of parent drug that is delivered to the central compartment by oral, mucosal, parental, inhalation or percutaneous routes versus intravenous (*i.v.*) injection ($Bioavailability = \frac{AUC}{AUC_{i.v.}}$). Bioavailability for *i.v.* administration is = 1 (100% bioavailable), while for other routes it is less because of Incomplete absorption and first-pass metabolism. It is estimated by comparing the AUC for a single i.v. dose and other routes of dosage. Clearance of the drug can be observed with gradual diminishing of concentration after reaching the C_{max} caused mainly by distribution, metabolism, and excretion. One of the most important parameters for medical treatment is the therapeutic window (or range), defined as the optimum range of drug concentration, where the probability of successful chemical treatment with low side effects is highest. On the figure, it is described as the difference between the minimum effective concentration and the minimum toxic concentration. The last presented parameter is the duration of action, or the time that the plasma drug level is within the therapeutic window, and is the time interval during which the drug has the maximum therapeutic effect.

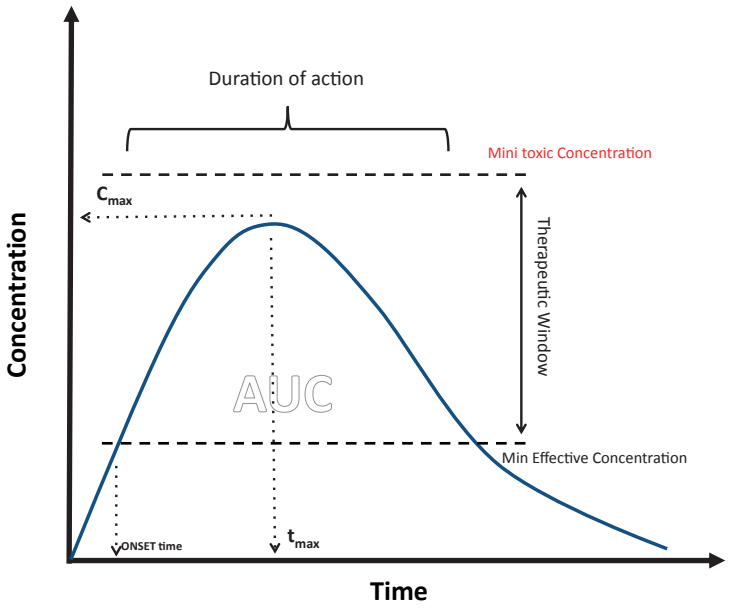

Figure 2. A typical concentration versus time curve for a generic drug administered orally by the patient. Important factors such as time of activation (onset time), maximum concentration (Cmax), and therapeutic window are identified on the graph.

The usefulness of pharmacokinetics lies in deciding the optimum dosage regimen for the administration of a given drug to achieve its therapeutic objective, for example, maintaining the concentration within the therapeutic range. The dosage regimen defines the concentration and time interval of drug intake to produce the required clinical response. Pharmacokinetics of a drug is obtained by measuring its concentration in body fluids over time and following the path of the drug along the ADME phases. However, expanding the results obtained for a small number of experimented patients in clinical trials to a worldwide population does not necessarily result in the best treatment for all.

1.2 Therapeutic drug monitoring

Traditionally, drugs are administered in time intervals prescribed by clinicians based on the pharmacokinetics and pharmacodynamics (PK) data of drugs obtained by pharmaceutical companies, for a limited population of people.

The four basic PK parameters determining a dosage regimen are bioavailability, clearance, half-life and volume of distribution. [13] Clearance is the volume of blood or plasma that is completely cleared from the drug per unit of time, and it is a measure of the efficiency of drug elimination; half-life ($t_{1/2}$) characterizes the monoexponential decline in drug concentration after administration, and is the time required for the plasma concentration to decrease by one-half; volume of distribution is a hypothetical concept that is a proportionality factor to relate the amount of drug in the body to the concentration measured in plasma.

Therefore using these data on patients worldwide may reduce the efficacy and even the safety of chemotherapy from expectations due to the interindividual differences (age, race, gender, genetics, diseases) or other interfering factors like drug-drug interaction, diet, smoking, drinking habits, etc. [10] Even traditional medicine prescription relies on the trial-and-error model. This means making a diagnosis, prescribing a drug, evaluating patient response, and changing the medication or dosage if the outcome is not effective. The overall performance of traditional dosing regimes using data obtained from pharmaceutical companies and trial-and-error prescriptions by doctors is very low and the consequences have a huge impact.

Adverse effects account for 4.2-30% of hospital admissions in the USA and Canada, 5.7-18.8% of admissions in Australia, and 2.5-10.6% of admissions in Europe. [14] The Institute of Medicine (IOM), in the United States, reports 98,000 deaths per year caused by preventable adverse events that occur in the hospital setting, with annual costs (lost income, disability, and health care costs) between U.S.$17 billion and U.S.$29 billion. [15] Another study ranks adverse drug effect as one of the top 10 causes of death and illness in the developed world, claiming 100 000 to 218 000 lives in the United States annually with direct medical costs from US$30 to $130 billion annually in the US. These values are in the same order or even more costly than some of the high-cost diseases such as diabetes ($45 billion), obesity ($70 billion), and cardiovascular diseases ($199 billion). [16] A record-based study on about 57 000 hospitalizations between 2006 and 2007 in Germany reported average treatment costs of approximately €2250 for a single adverse effect reaction and a total cost of €434 million per year. [17] The traditional approach in Therapeutic Drug Monitoring (TDM) costs the health-care system millions of unnecessary dollars in wasted therapies to cure the side effects and extended lengths of stay in hospital, and still it is not efficient enough to cure the patients. In addition, an estimated 2.2 million adverse drug reactions occur each year in the U.S. accounting for 6-7% of all hospitalization, and this includes more than 100,000 deaths, [18] costing the health care system billions of dollars. Another study demonstrated that adverse drug events caused by inappropriate therapy result in more than 770,000 cases of injury and deaths each year in the U.S., and an average increase of length of stay in hospitals of 3.1 days. [19]

To explain the importance of interindividual variations further, it is beneficial to consider cytochrome P450 enzyme expression in people, as the main metabolizer of xenobiotics in the human body.

1.2.1 Cytochrome P450 expression

Cytochrome P450 enzymes (abbreviated as CYP450s or CYPs) are a large group of enzymes involved in the metabolism of over 1'000'000 different xenobiotic and endogenous compounds. [20] Depending on the organism, they contribute to vital processes including carbon source assimilation, biosynthesis of hormones and or structural component of cells, and also carcinogenesis and degradation of xenobiotics. [21] More importantly, CYPs are the major enzymes involved in human drug metabolism and bioactivation, accounting for about 75% of the total number of different metabolic reactions. In humans, only 5 isoforms of P450 are responsible for the metabolisms of 95% of all known pharmacological compounds. [22, 23] CYP450s belong to the hemoproteins superfamily. The letter P in P450 represents the word pigment, while the number 450 reflects the wavelength of maximum adsorption in spectroscopy. More specifically, concentrated quantities of protein appear red at sight due to the iron atom present in their active site. Cytochrome enzymes have been identified in all domains of life. At present, more than 11500 distinct proteins are known, but only 57 of them are present in humans. [22] Cytochromes P450 are classified in families, subfamilies, isoforms and polymorphisms according to their amino acid sequence homology. The nomenclature of the P450 enzyme indicates this information and includes the acronym CYP, a number showing the family, a letter for the subfamily, a second number for the isoform, an asterisk sign (*) and finally a number for the polymorphism (e.g. CYP2B6*4). Cytochrome polymorphism is one of the major causes in the differences of drug metabolism among individuals. It has been estimated that 20 to 25% of all drug therapies lead to different therapeutic outcomes because of genetic differences. [24] According to the differences in P450 expression, a population can be classified in 4 major phenotypes, as ultrarapid metabolizers, extensive metabolisers, intermediate metabolizers and poor metabolizers. Ultrarapid metabolizers present 3 or more genes encoding a specific P450, and therefore show an increased enzymatic activity, extensive metabolizers carry 2 functional genes and present standard enzymatic activity, intermediate metabolizers are deficient in one allele and, thus, show reduced activity, while poor metabolizers lack the functional enzyme due to a defective genetic profile, and they have a very low or no metabolism of the specific compound.

Different rates of metabolism in people, based on their difference in CYP450 expression, are good examples to demonstrate the significance of interindividual differences. Figure 3 illustrates a graphic view of a population of patients with different genetic profiles subjected to a similar dosage regime for a standard medical treatment, as advised by a pharmaceutical company. Considering different metabolizing rates, a standard drug prescription for a population may cause the following responses: extensive metabolizers would respond as expected with most efficacy and a minimum of side effects. Intermediate metabolizers would still show reasonable therapeutic effects. However, ultrarapid metabolizers would clear the drug from their circulatory system much faster than expected and advised by pharmaceutical companies. Therefore, the following admin-

istration of drug does not help to maintain an average steady-state concentration in the therapeutic window of the drug, as expected. This means the medical treatment will not cure the patient. Above all, the prescribed dosing regime for poor metabolizers will cause an accumulation of drug concentration in the circulatory system that is more than the estimations of the pharmaceutical companies. This means that the concentration will surpass the minimum toxic concentration and can even reach lethal concentrations (refer to 1.1.1 and 1.1.2 subsections).

Figure 3. Qualitative illustration of the effect of interindividual differences on the outcomes of medical treatments. One population of people with different CYP450 phenotypes subjected to one dosing regime for medical treatment shows normal therapeutic effects (white), no effect (blue) or even severe adverse effect (red). Adopted with permission from www.dreamstime.com.

1.2.2 Therapeutic drug monitoring for personalized medicine

TDM is the “clinical practice of measuring specific drugs at designated intervals to maintain a constant concentration in a patient's bloodstream, thereby optimizing individual dosage regimens”. [25] It is unnecessary or too costly to employ TDM in many medical therapies. However, it is used for monitoring drugs with narrow therapeutic ranges, drugs with marked pharmacokinetic variability, medications for which target concentrations are difficult to monitor, and drugs known to cause therapeutic and adverse effects. These include antifungal, antiretroviral, anticancer drugs, anticonvulsant and immunosuppressant drugs, theophylline, aminoglycosides, and psychotropic drugs. [26] The process of TDM is established based on the assumption that there is a definable relationship between blood concentrations and clinical effects (therapeutic, adverse or toxic effects). [25, 27] TDM is the basis of personalized medicine, since it has transformed the traditional weight-based dosing regimes (or fixed dosing regimes) to a drug therapy based on individualization by providing the ability to characterize sources of variability in drug disposition and response. TDM formed the basis for personalized medicine, and has evolved to include pharmacogenomics and other biomarker-driven strategies for patient segmentation. [28] The currently preferred analytical method for monitoring the concentrations of targeted drugs in plasma are chromatographic and immunochemistry methods. Combination of liquid chromatography with mass spectrometry

(LC-MS) has resulted in a new potential tool for TDM applications that offers higher speed and even selectivity with respect to the single MS detection method. [29] This selectivity has made it easier to develop methods for new compounds and to use generic sample preparation procedures. LC-MS/MS also offers the potential to use multi-component approaches for routine methods. One such example is the development and successful application of LC-MS/MS for the simultaneous analysis of several immunosuppressive drugs. [30] These methodological achievements pave the way for the possibility of providing a broader service than in the past. TDM is requested whenever patients present not-sufficient response to medical treatment, or they are suffering from sever side effects that are beyond expectations (based on the PK data). Other applications of TDM are for the assessment of patients' compliance with the prescribed treatment regime, when a new dosing regime is applied, in case of change in co-medication[3], and at the times that the clinical status of the patient is changed [27]. The clinical status of patients change due to age, pregnancies, other illnesses, infections, emotional and physical stresses, accidents, surgeries, or other illnesses. This is even more relevant for chronic diseases and medications that are taken over a long period.

TDM follows this procedure: After the request is assessed, sampling, analysis and interpretation of results should be ideally reported within a single working day in order to ensure a quick and safe regimen optimization. Samples are collected at a prescribed time after the drug administration to capture the peak (or steady state) concentration, and the trough level. The blood sample timing depends on the drug type, the route of administration and adsorption. Data is evaluated by a team who are eligible to take the final decision on the modification of the medical therapy, taking into account patient-related and drug-related variables, including the timing of sampling, dosage, patient demographic information (i.e. sex, age, concomitant disease, ethnicity, etc.), comedications and the therapeutic range of the administered drug. The final decision might suggest a change in the dosage, a change in the medication or the continuation of the therapy. [27]

As has been previously demonstrated in this study, TDM plays an important role in personalized medical treatment and has brought many undeniable advantages to the field of medical treatment. However, several limitations have hampered its progress and the expansion, inhibiting any possible implementation for individual medical treatment. TDM is very complex and demanding in terms of cost and time, so that it is not considered an efficient determinative solution for personalized medicine. For instance, currently used analytical techniques, like LC-MS, are costly and need bulky and complicated instruments that require highly trained personnel. Therefore, TDM is centralized in a few laboratories or specific centers in a way that greatly decreases the accessibility of this technique, and increases overall costs and time consumption. Moreover, human error in blood sampling, potentially complex interpretation of the data and lack of knowledge about PK data related to the specific drug decrease the accuracy and reliability of TDM. The other limiting factors are the sampling of potentially significant amounts of blood, pre-analytical precautions, thorough clinical data recording, shipment to a distant laboratory and delivery of results after a significant delay. A study on the accuracy of TDM results for antidepressant drugs reveals that be-

[3] A second medication to suppress side effects of main drug.

tween 25% and 40% of requests for TDM were inappropriate and that the interpretation of the results led to roughly 20% of therapeutic adjustments being incorrect. [31] The success of personalized medicine and TDM depends on having accurate, fast, automated, cheap and miniaturized diagnostic tests with high accessibility for a worldwide population. In the following sections the significance of better therapies for specific diseases will be investigated, and biosensors will be introduced as an innovative solution to overcome the limitations of TDM.

1.3 Relevance of TDM for malignant diseases

Although drug monitoring is not an option for every medical treatment, it can provide critical benefit for the highly invasive chemical treatment (chemotherapy) of malignant diseases such as cancer, HIV and Hepatitis B, which are mainly toxics. In these diseases the therapeutic windows of the medications are very narrow, and as a consequence there is a high likelihood that the chemical treatments show insufficient response or even cause adverse effects. In addition, the drugs used in these therapies are very toxic and the side effects are severe, so maintaining the steady-state concentration in the therapeutic window is critical for the quality of life of patients.

1.3.1 Prostate cancer and chemotherapy

Prostate cancer (PCa)[4], with a predicted rate of 10.6/100,000 men death in 2016 (Table 1), has the third cancer related morbidity among men in EU with correspondence of almost 10% of total cancer death. [32] In the United States, it is the most commonly diagnosed cancer in men, with 180,000 new cases and about 31,000 deaths occurring annually. [33] PCa has a very slow progress without any observable symptoms during the first stages of the disease. This leads to late diagnosis of the tumour, and a higher probability of metastasis.

Table 1. Indication of most important cancer related mortality. [32]

EU*		Observed no death 2011	Predicted no of death 2016	Lower prediction limit	Upper prediction limit
sex	**cancer**				
Men	Lung	185 707	183 800	181 553	186 115
	Colorectum	90 412	95 600	94 432	96 707
	Prostate	72 330	75 800	74 672	76 999
	pancreas	39 056	42 600	41 974	43 250
Women	Breast	91 291	92 300	91 060	93 544
	Lung	79 474	89 700	88 177	91 144
	Colorectum	77 478	77 800	76 641	78 953

***European Union**

PCa can be incurable and even lethal even if only diagnosed in the later stages. Diagnosis currently relies on a histological analysis performed by collecting sample tissues through a biopsy. Different types of treatment are available for patients with prostate cancer. Some treatments are standard

[4] Prostate cancer is a malignant tumour of the prostate gland, a walnut-sized organ located in front of a man's rectum and below the bladder. The prostate is a gland in the male reproductive system.

(the currently used treatment), and some are being tested in clinical trials. There are seven types of standard treatment for PCa: active surveillance (watchful waiting), surgery (castration), radiotherapy and radiopharmaceutical therapy, hormone therapy, chemotherapy, biological therapy and biophosphonate therapy. Hormone therapy through drugs and chemotherapy are more relevant to drug monitoring:

Hormone therapy

The survival and growth of prostate cells and, more importantly, prostate tumour cells are directly related to testosterone, and this is the reason that hormone therapy, with the aim of decreasing the level of testosterone in the body, is one of the first and oldest active therapies against PCa. The biological pathway that leads to the survival of PCa tumours is explained properly by [33] as follows:

« In the hypothalamus, androgens bind to the androgen receptor (AR) to stimulate the production of luteinizing hormone (LH)-releasing hormone (LHRH). LHRH travels to the pituitary where it interacts with LHRH receptors (LHRH-Rs).

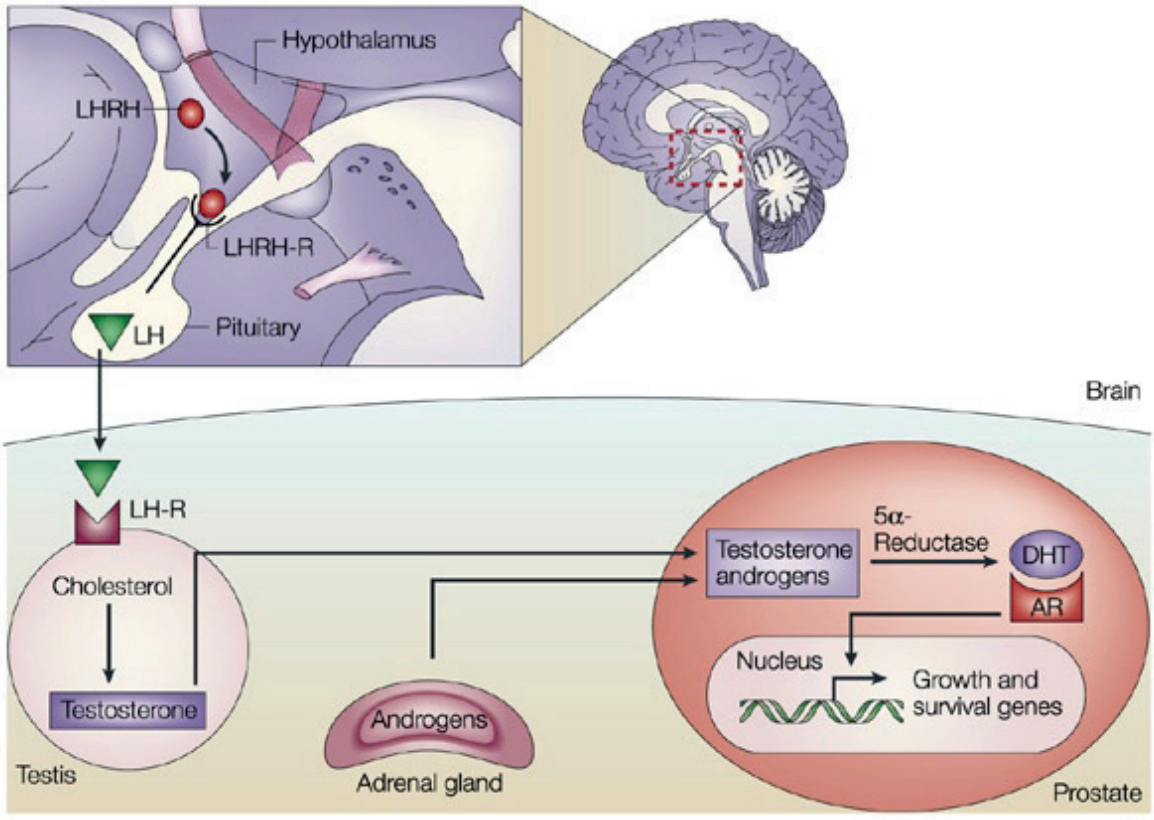

Figure 4, Androgen production and action. Reprinted with permission from [33].

This interaction stimulates the release of LH. LH that is released by the pituitary binds to LH receptors (LH-R) in the testes, inducing production of testosterone, which is synthesized from cholesterol. Testosterone enters prostate cells, where it is converted to dihydrotestosterone (DHT) by the enzyme 5alpha-reductase. DHT binds tightly to AR, enters the cytoplasm, and the complex

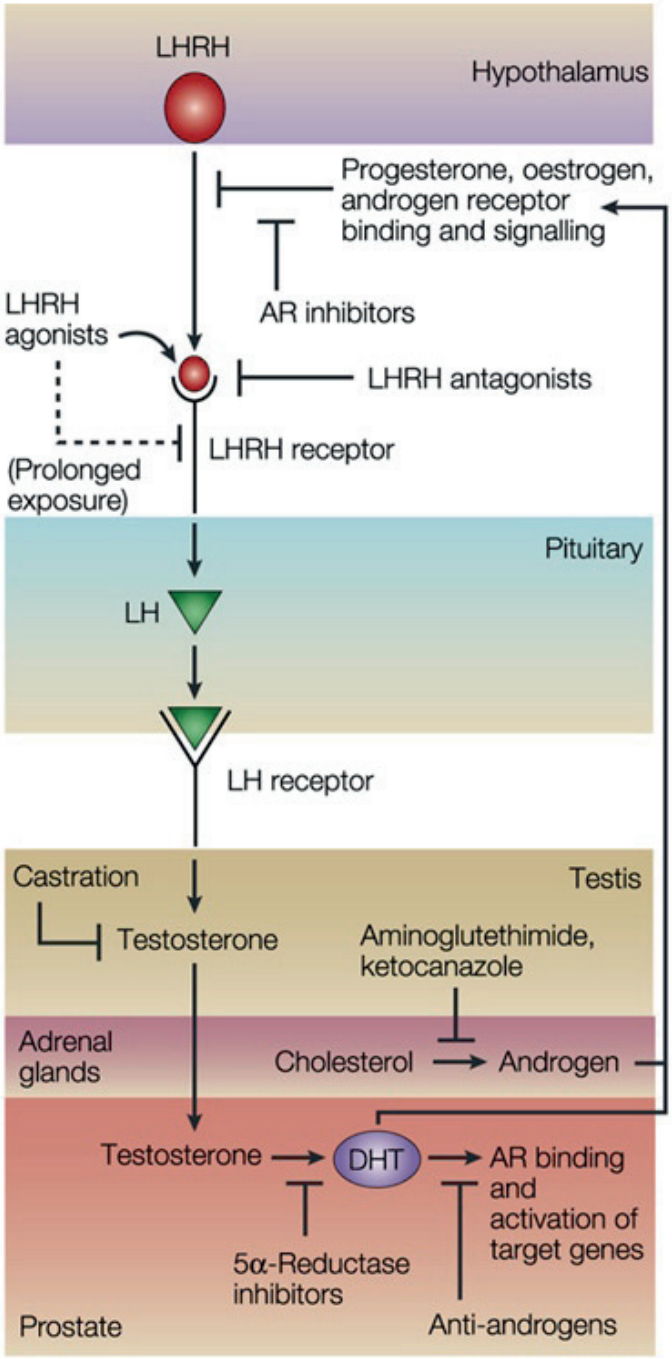

translocates to the nucleus where it activates the transcription of genes that regulate cell growth and survival. Increased testosterone levels can also decrease LHRH and LH production through negative-feedback-loops, thereby maintaining serum testosterone at physiological levels. The adrenal gland can also produce androgens.» The graphical explanation is illustrated in Figure 4.

Hormone therapy tries to stops cancer cells from growing by interfering in the survival pathway of tumour cells.[5] For instance, AR inhibitors block the negative feedback of androgens and LHRH agonists elevate the release of LHRH and LH. This eventually increases the testosterone level (the 'testosterone flare'). Prolonged exposure to LHRH agonists, however, downregulates the LHRH receptor, decreasing LH release and inhibiting testosterone production. LHRH antagonists, on the other hand, directly inhibit the LHRH receptor, leading to decreased production of LH and testosterone. Some inhibitors target adrenal androgen production. 5-α reductase inhibitors block the conversion of testosterone to DHT. AR inhibitors are also direct inhibitors of DHT in addition to their blockage effect on the feedback loop.

Figure 5. Multiple ways to regulate androgen production. Reprinted with permission from [33].

Testosterone is not the cause of prostate cancer, but is considered an essential factor for the growth of tumours. Although, over 90% of androgenic activity in the circulation is due to testosterone, there are other pathways parallel to the one mentioned at Figure 5, and there are many other circulating androgenic compounds as a result, including androstenedione, dehydroepi-

[5] Surgical castration also decreases testosterone levels by removing the source of production (testes).

androsterone (DHEA) and dehydroepiandrosterone sulphate (DHEA-S). Many of these compounds are adrenal products that can be converted to the metabolically active DHT. This is the main reason behind PCa resistance to different types of hormone therapy. [34]

Abiraterone chemotherapy is a type of hormone therapy for patients suffering from metastasized castration-resistant prostate cancer. Administration of this agent causes testosterone suppression, thus shrinking the number of testosterone-sensitive tumour cells all over the body. The mechanism of action is based on the inhibition of the steroidogenic enzyme "17α-hydroxylase/C17, 20 lyase (CYP17A1)" that catalyzes the 17alpha-hydroxylation of pregnenolone and progesterone, and the subsequent formation of dehydroepiandrosterone and androstenedione, as precursors of testosterone. [35]

Abiraterone acetate, a prodrug[6] of abiraterone, was developed to overcome poor bioavailability. Abiraterone acetate is converted in the body to its active form abiraterone. It was approved by the Food and Drug Administration (FDA) in United States on April 28, 2011, [36] and later in Europe [37] and Canada [38] for the treatment of male subjects with metastatic castration-resistant prostate cancer, who have received prior chemotherapy containing docetaxel, or chemotherapy-naive patients.

The therapeutic range of abiraterone in circulatory system is up to 1 µM for a typical dose of 1000 mg injected per day. [39] In many cases, such a dose is the right one to maintain the concentration of abiraterone in this range and, therefore, to achieve a successful chemotherapy, since lower concentration cannot provide a medical benefit and higher concentrations will cause severe side-effects due to overdosing.

1.3.2 AIDS and chemotherapy

AIDS stands for acquired immunodeficiency syndrome. AIDS is the final stage of human immunodeficiency virus, or HIV, infection. HIV attacks the body's immune system, specifically the CD4 cells (T cells), which help the immune system fight off infections. If left untreated, HIV reduces the number of CD4 cells (T cells) in the body, making the person more vulnerable to infections or infection-related cancers. Over time, HIV can destroy so many of these cells that the body cannot control infections any more. The opportunistic infections or cancers take advantage of a very weak immune system and signal that the person has AIDS, the last state of HIV infection.

According to the recent AIDS epidemic update of « The Joint United Nations Programme on HIV and AIDS (UNAIDS) », there are around 33.4 million people living with AIDS all over the word, among whom are 47% women and even 6% children. In 2008, 2.7 million new cases of AIDS, and 2 million AIDS-related deaths were reported; 850 000 cases of adults and children in 2008 living with AIDS. In Western and Central Europe alone there are 30 000 new infections and 13 000 cases of mortality. [40] Despite the success in HIV prevention and a decline in the numbers of new infections and annual reported death, AIDS is still a major global health priority. The number of people

[6] A biologically inactive compound that can be metabolized in the body to produce a drug.

living with AIDS is increasing and AIDS-related ilnesses remain one of the leading causes of death between adults and children globally. HIV/AIDS is the fourth leading cause of death world-wide (2.9 million deaths) and the leading cause of death in Africa. What is more, projections to 2030 indicate that major vascular diseases, including HIV/AIDS, will remain the leading source of the burden of global disease. [41]

HIV is a lentivirus that is a subgroup and complex form of retroviruses. The virion structure of a retrovirus is illustrated in Figure 6. Simple and complex retroviruses both contain two copies of linear, nonsegmented, single-stranded RNA. They encode gag, env and pol genes. Gag is responsible for matrix, capside and nucleocapside proteins encoding (MA, CA and NC, respectively), env encodes surface envelope (SU) and transmembrane envelope proteins ™, and pol is involved in the encoding of enzymatic proteins as reverse transcriptase (RT), protease (PR) and integrase (IN). [42]

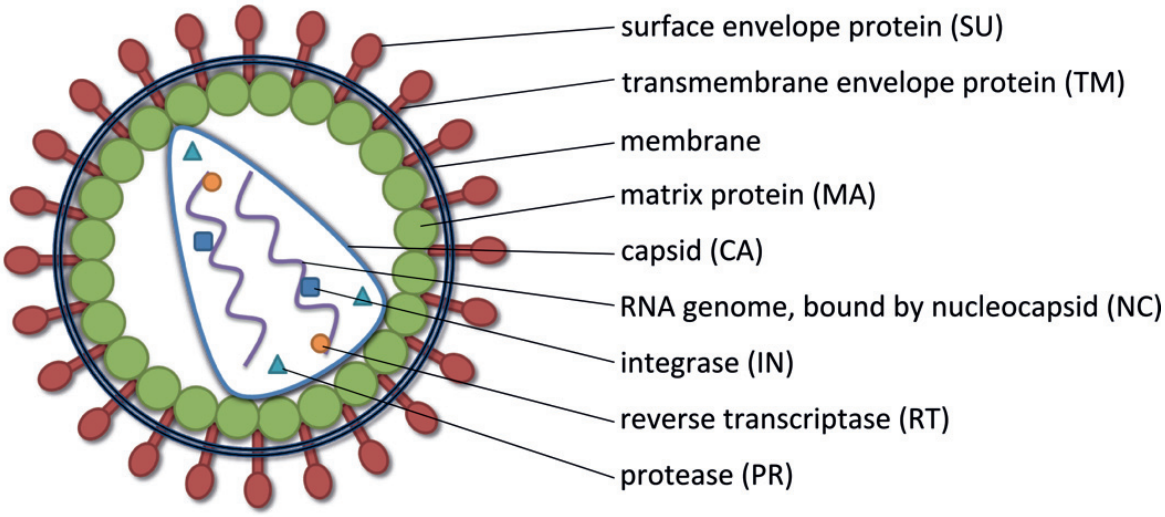

Figure 6. Basic structure and main components of retrovirus virion. Reprinted with permission from Labome [42].

Retroviruses are defined by their ability to reverse the normal flow of genetic information from genomic DNA to mRNA. Figure 7 demonstrates a typical retroviral replication cycle that is the reason behind the dangerous infectious nature of a virus, and a key for its survival. Retroviral replication is initiated by the intracytoplasmic penetration of the virion core, a process mediated by the specific interaction of the viral envelope glycoprotein with a host cell surface receptor. Subsequently, the virion-associated reverse transcriptase transcribes the single-stranded viral RNA genome into a double-stranded linear DNA proviral intermediate. This proviral intermediate then migrates to the nucleus where the viral integrase enzyme acts to covalently link the retroviral genome to the host chromosomal DNA, thereby forming the retroviral provirus[7]. After the integration, significant viral mRNA are synthesized in nucleus that after reaching the cytoplasm encode the HIV regulatory proteins, « Tat and Rev » (Figure 7).

[7] The host cell chromosome Integrated with viral genome (by IN enzyme) is referred to as a provirus.

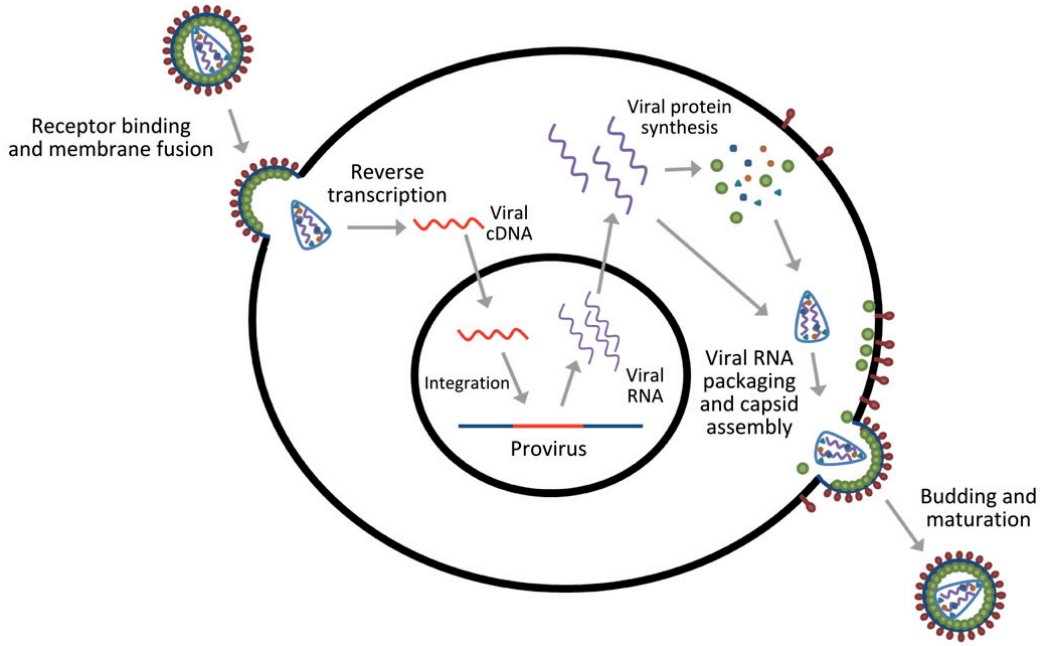

Figure 7. Retroviral Replication cycle. A virus interacts with the cellular receptor and enters the cell. The viral cDNA is produced through reverse transcribing the RNA genome by RT. Viral DNA then enters the nucleus and is integrated into the host genome by IN enzyme to form the provirus. Next, viral proteins and viral genomic RNAs start to be synthesized, encapsulated and bud from the cell to acquire a cellularly derived membrane. Finally, the particle matures when the Gag and Gag-Pol polyproteins are cleaved by the viral protease. Reprinted with permission from Labome [42].

Tat establishes a positive feedback loop in production of the Rev protein that results in the accumulation of critical levels of Rev. This then stops the loop and encodes the viral structural proteins. This process can then be divided into two steps of regulatory and structural phases. In the cytoplasm, two viral genomic RNAs associate with replication enzymes and the core proteins assemble around them, forming the virus capsid. As it migrates towards the cell surface, the Gag and Gag-Pol polyproteins are cleaved by the viral protease, resulting in a mature, infectious particle. The mature particle then buds from the cellular membrane, thus acquiring its envelope. [42, 43]

Tenofovir (TFV) is an antiretroviral agent approved by FDA on 26 October 2001 for the treatment of HIV-1 infection in adults and paediatric patients. [44] TFV is classified as a nucleotide analogue reverse transcriptase inhibitor (NRTI). Reverse transcriptase, as explained above, is a crucial viral enzyme in retroviruses such as HIV and hepatitis-B virus infections. Tenofovir acts as chain terminator, following intracellular phosphorylation to the triphosphate form (in one or two steps), and, after removal of the diphosphate group, incorporation at the 3'-end of the viral DNA chain, and prevents, as a result, the elongation of DNA and the multiplication of HIV. It is administered orally at a once-daily dose of 300 mg in the form of Tenofovir Disoproxil (prodrug of Tenofovir) to increase the bioavailability. [44, 45] Based on the pharmacokinetics data after oral administration of TFV the circulatory plasma concentration is in the range of some nano-molar up to 860 nM. Tenofovir does not involve any CYP450 enzyme in its metabolic pathway, and is metabolized by mitochondrial adenylate kinases. [44, 46, 47]

1.4 Biosensors and healthcare

Reliable, low cost and accessible TDM systems for individualized healthcare, especially for chemotherapy of malignant diseases like PCa and AIDS are highly desirable. Such a therapy can improve the morbidity rate and time of treatment by increasing the treatment's efficacy, as well as providing a higher quality of life for patients under treatment, thanks to its suppression of side effects. Improvements to the TDM in terms of the costs (economical and time-related criteria) of the process in reducing the mortality and morbidity of the diseases are widely discussed. [48] Several attempts are mentioned in the literature monitoring systems to support communication between the TDM team members for optimum interpretation of the results to assure the reliability of the whole system. [27, 49, 50] These aspects are even more critical for drugs like abiraterone and TFV with very narrow and low (submicro-molar) therapeutic windows. Biosensors, as a solution for such TDM system, are the combination of the following elements: Analyte, recognition element and transducer (Figure 8).

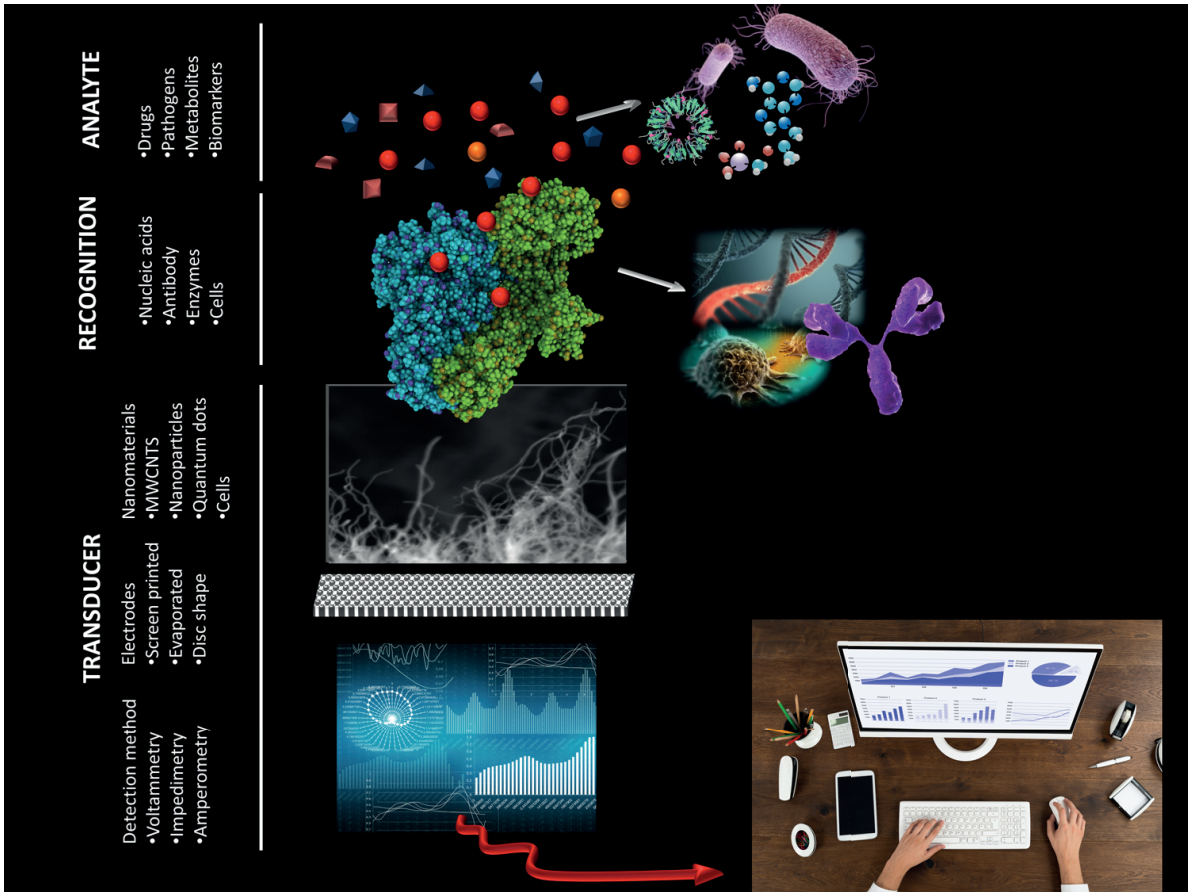

Figure 8. Main elements of biosensor. Adopted with permission from www.dreamstime.com.

Analyte: the target molecule for sensing. It can be a pathogen (bacteria, viruses etc.), metabolite (lactate, glucose, ascorbic acid, etc.), biomarker (DNA, RNA, mRNA, toxins, proteins, etc.), chemical compound (drugs and other xenobiotics).

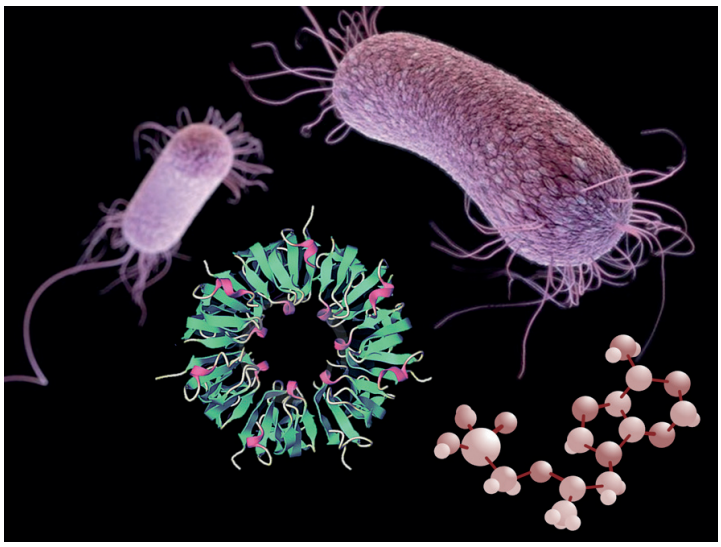

Figure 9. Examples of analytes under experiment. Top: pathogens (bacteria). Below left: protein. Below right: drug. Adopted with permission from www.dreamstime.com.

Recognition element[8]**:** it is the recognition element that enables the target to be sensed by the transducer, and is the place that the interaction/reaction between analyte and the sensing surface happens. It is normally a biomolecule that, based on the target molecule and application, can be a DNA, aptamer, RNA, enzyme etc.

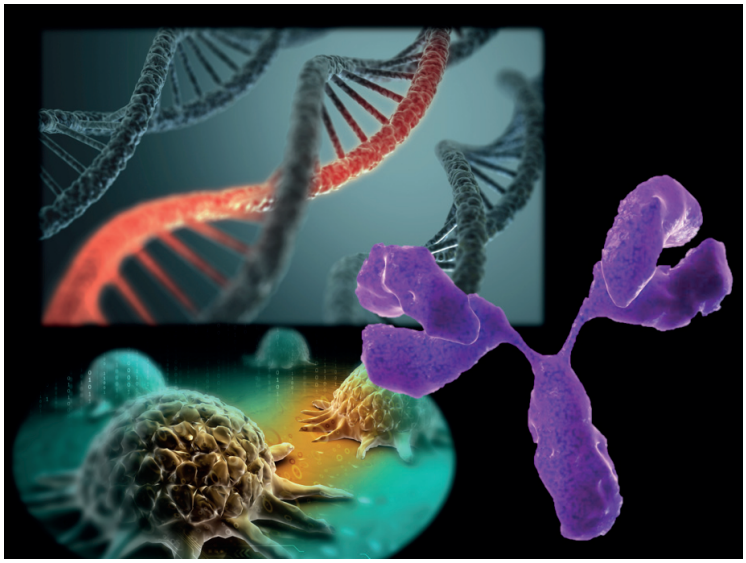

Figure 10. Examples of biomolecules used as recognition element. From top and left: DNA, Cell, and Antibody. Adopted with permission from www.dreamstime.com.

[8] There are also biosensors for recognizing electroactive species that do not need any biomolecule on the sensing surface.

Transducer: is a part of biosensor that senses and transfers the bioevent happening at recognition element to an electrical signal that is measurable and can be analyzed and controlled by the user. Typical transducers are voltammetric, amperometric, impedimetric, field effect etc.

Biosensors can be classified according to the type of recognition element, as immunobiosensors, enzymatic biosensors, DNA-based biosensor, cell-based biosensors; and according to the transduction element, as optical, piezoelectric, electrochemical, thermometric, field effect and memristive biosensors. The electrochemical biosensors are successfully commercialized, more prevalent and more numerous. [51] These are further subdivided into amperometric, potentiometric and impedimetric biosensors. The history of biosensors began with the fabrication of enzyme electrodes by Leland C. Clark in 1962. After that researchers from numerous fields of science have come together to develop more sophisticated, reliable biosensors for medical practices specifically to detect targets that have a relationship with diseases. They must do this effectively and quickly, this is paramount for diagnoses of diseases by biomarker detection, drug discovery, and for developing various research assays. In addition, therapeutic compounds may be considered to provide more innovative, adapted technology for the improvement of TDM.

1.4.1 Bench to bedside

Among different biosensor technologies, point-of-care (POC) is one of the most promising in daily hospital practice.

POC biosensors provide access to reliable, fast and cheap cutting-edge technology for a large population of people. In particular, the development of POC biosensors for cancer and AIDS therapy will decrease the mortality and increase the quality of life of patients by providing better screening of patients, and tighter monitoring of treatment. The main advantages of POC biosensors (e.g. electrochemical based biosensors) over traditional optical techniques for TDM are their availability, cost effectiveness, simplicity and portability. Drug biosensors are key to bringing treatments to the patient's bedside, and the complete renewal of the traditional dosing regimen as a mechanism that administers the drug based on the patients' characteristics (genetic profile, age, race, gender, environmental agents, etc.), and drug influences, including pharmacodynamics, pharmacokinetics, drug-drug interactions, adverse effects, etc. [10, 52–54] In other words, patients take advantage of point-of-care biosensors to control the circulating drug concentration over time themselves, and to administer the necessary drugs.

The lack of proper POC devices has decreased the efficacy of the chemical treatment as reported in [55]. Response rates of patients to medications from different therapeutic classes ranged from 25% for oncology to 62% for depression, as shown in Figure 11.

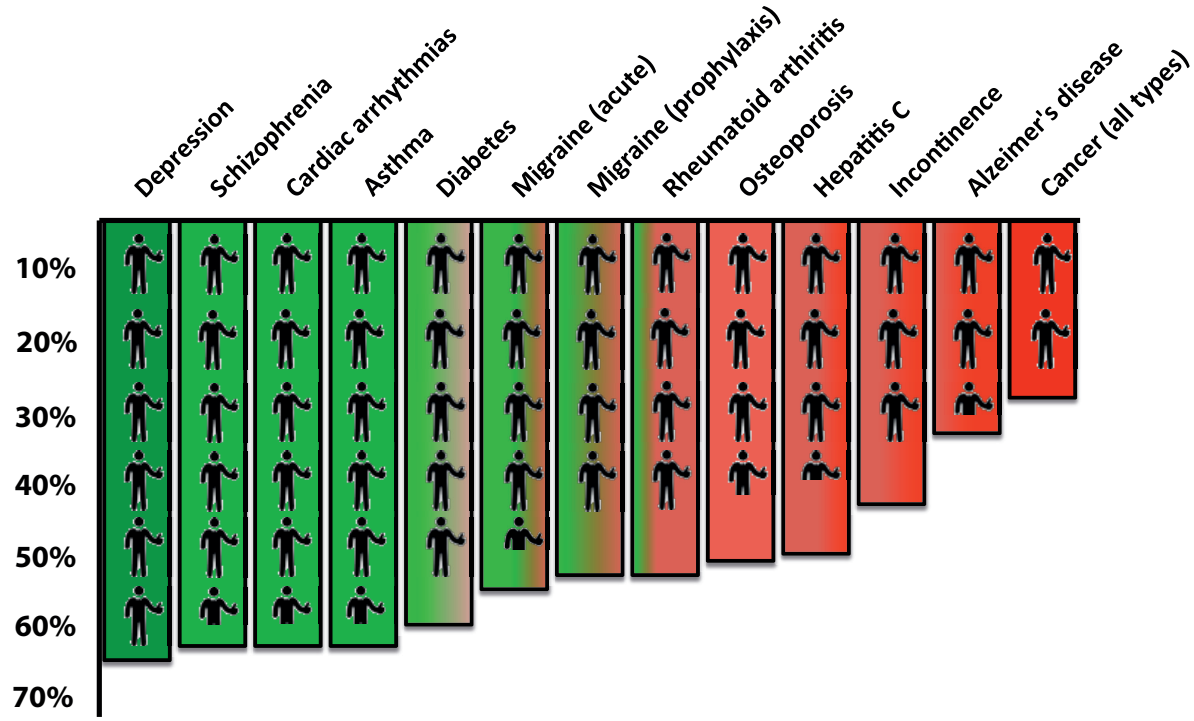

Figure 11. Rate of drug treatment efficacy.

The adoption of biosensor technology and its emergence in health care applications, as demonstrated by the increasing interest of the market towards the development of point-of-care biosensors, is a direct response to the need of patients and national health care systems for better TDM. The development of a POC, disposable or implantable, biosensor for drug monitoring would improve the patients' compliance and the TDM practice. The diffusion of cheap POC TDM procedures can also improve the quality of drug production by providing accurate data about PK of drugs. Furthermore, the automatic data collection can help discover unknown drug interactions; pharmacokinetics and pharmacodynamics data obtained from TDM can be classified and used to predict therapeutic outcomes in new patients with similar clinical history, or in the design of new compounds. Finally, the introduction of implantable biosensors may be useful in preclinical research on animals. Constant monitoring of pharmacokinetics during toxicology and efficacy investigations could provide better information during the preclinical development of a drug.

1.4.2 Market study

Considering the drug monitoring biosensors that is more related to the scope of this work, the only available biosensors in the market are screening tests for drug abuse without quantifying the concentration, which can analyze both blood and urine samples. Drug tests such as Signify®ER drug screen test, Triage®Drug of abuse Panel, Alere™ Toxicology drug screening system, QuickScreen™ Pro- Multi Drug Screening Tests and Rapid Drug Screen™, are some examples. [56, 57] For instance, the Alere™ Toxicology system can measure up to 11 drugs with one device, such as acetaminophen, amphetamines, barbiturates, benzodiazepines, methamphetamines, tricyclic antidepressants, as well as narcotic substances (e.g. cocaine, marijuana, etc.). [58] In addition, Omni-

ca co. have developed « PaperSpray Ambient Ionization system™ » a prototype POC drug detection system that can analyze complex samples (whole blood, urine, saliva, and fresh tissue samples) in 3 to 5 minutes with no sample preparation. Their system uses disposable paper-spray cassettes and includes an Ion source instrument connected to a miniaturized mass spectroscopy. However, their system has not solved the issues of traditional TDM as it is still bulky and complex. It needs trained personnel and is just suitable for clinics and not for the patients' bedside. [59] Another example is The Medimte MiniLab produced by Medimate Minilab company specific for detection of Lithium ions, a drug for the people suffering from Bipolar Disorder, in urine or blood samples. Although this device has most of the requirement mentioned for POC drug monitoring, it is specific to just ions due to the capillary-conductivity detection methodology of biosensor. [60–62] Therefore, it cannot be considered as an effective methodology for POC drug monitoring.

1.5 Summary

While new, biosensors can be designed to be small, inexpensive, and easy to use. Moreover electrochemical biosensors provide an immediate reading of the substance of interest. Cost reduction and simplicity of employment may allow the diffusion of TDM test from a small number of specialized laboratories to a bigger number of medical centers or even the patient's houses. Home testing can simplify the life of patients and reduce the cost of hospitalization. The development of automatic sampling procedures and remote data transmission can reduce the human error during analysis and data manipulation. An electronic device can automatically collect relevant information regarding patient status, testing procedure and analyses results, and send this data directly to a specialized center for clinical interpretation. Ideally a patient can self-test at home and receive new therapeutic indications online.

At the moment, the market does not offer many options for drug detection, despite the fact that the demand for such POC biosensors for TDM, and personalized medicine is increasing in the market. The lack of suitable device on the market can be mainly due to the challenges in developing reliable and enough sensitive drug biosensors with suitable cost and low complexity. While, finding one methodology to be applied on all the drugs is difficult, it is affordable to classify the drugs into subgroups based on their specific and common electrochemical properties and provide a proper solution for their detection. It will help to pave the path for novel biosensors emerging by suppressing the effort, time, and cost needed to target so many drug molecules.

This thesis will present a number of reliable highly sensitive and selective biosensors, which are able to target a wide range of drugs according to their electrochemical properties. These biosensors will be characterized and put to the test in the following chapters.

1.6 Objectives of thesis

The objective of this thesis is to investigate biosensors for the monitoring of drugs for chemotherapy for prostate cancer and AIDS. This work is divided into two main parts:

A) Developing biosensors to target three main groups of drugs: electroactive drugs (EAD), drugs that involve an enzyme in their metabolic pathway and drugs that are neither electroactive nor interact with enzymes in the body.

B) Investigate reliable solutions for selective and sensitive POC biosensing of anti-prostate cancer drugs and anti-AIDS drugs.

To this purpose, one electroactive drug specific to prostate cancer treatment, one drug with enzyme interaction that is part of PCa chemotherapy, and a drug specific to AIDS treatment, without any electroactivity or enzyme interaction, were chosen as model targets. Targeted drugs were: etoposide, abiraterone and TFV, respectively. The direct electrochemical drug biosensor is produced based on well-established screen-printed technology. Screen-printed-electrodes (SPEs) were purchased commercially to avoid complexity on a well-studied topic.

A crucial task at the start of this study was the optimization of these direct electrochemical biosensors for drug detection. The sensing surface of electrodes were nanostructured to enhance the performance of the biosensor in terms of sensitivity and detection limits, to resolve one of the main challenges in sensing the drugs specific to malignant diseases: to cover the entire therapeutic window. The circulatory concentration of these drugs is normally very low, so it is a challenge to make sure that electroactive and enzymatic biosensors capture those low signals.

The performance of drug detection can be greatly improved by the innovative use of nanomaterials, characterized by nanostructuring and an increased applied potential scan rate:

1. This study started with calculating theoretically the gain of multiwalled carbon nanotubes (MWCNTs), bismuth oxide semiconductor nanoparticles (Bi_2O_3 NPs) and gold nanoparticles (GNPs) in terms of additional electroactive surface area on bare electrode (EASA). EASA was considered as a common factor to all the biosensors, each with different nanostructures. When looking at the impact of the physical and electrical nature of nanostructures on the performance of biosensors, this led to a much more reliable comparison.

2. The role of nanoparticle dimensions and quantum physics on performance was observed and investigated.

3. The next step was to optimize the gain in terms of EASA by means of the nanomaterials. The recorded signal would increase with more EASA, but it maximized at some point and then decreased.

4. The same optimization was performed on the scan rate of applied potential in cyclic voltammetry. Scan rate plays an important role in the amplitude of the Faradaic signal of interest, and the amplitude of the capacitive signal of no interest (which will be explained in de-

tail later). Scan rate also shows a compromising behavior, as it maximizes at some point and then decreases.

Then the optimized biosensors, by means of two leading nanostructures, were tested for their ability to detect Tenofovir, in a final comparison for EAD detection. The final results proved the capability of the biosensors for etoposide detection with a superior performance than has been seen in the literature.

When the optimization of the biosensor was performed and characterized, the optimized biosensors were biofunctionalized with CYP450 enzyme to have a proper recognition element for enzymatic drug detection. Enzymatic biosensors were just nanostructured with MWCNTs thanks to their physical properties, which are suitable for enzyme immobilization without attenuating their catalytic activity. These properties can be classified as: first, their large available surface area for enzyme immobilization; second, the large 3D form, full of features and voids on a surface that is highly suitable for the immobilization of biomolecules; third, the hydrophobic surfaces that attract hydrophobic sites on the surface of the enzyme. The enzymatic biosensors with optimized configuration were experimented on abiraterone detection. The electrochemistry of abiraterone was observed for the first time, and the leading performance of this enzymatic biosensor in buffer and human serum demonstrated the quality of the enzymatic biosensor thus produced, for abiraterone detection and prostate cancer TDM as well as any other drug with enzyme interaction in their metabolic pathway - with some modifications, of course.

The last part of this study involves the biosensing of compounds with no electroactivity and without any enzyme in their metabolism, based on their pharmacokinetics data. The other object of this part of the thesis is to enhance the selectivity and sensitivity of biosensing for drug detection, and to reach new levels and standards in these areas for the first time:

1. An aptamer-based biosensor was developed, to take advantage of the sensitivity of MOSFETs as signal transducers, and of their selectivity of DNA. An aptamer based field effect biosensor was successfully tested, detecting TFV in buffer and human serum with the very high sensitivity and selectivity that were required for TFV detection. It was also tested for real-time monitoring with positive results.

2. A memristor aptamer based biosensor was also characterized and tested to detect TFV for the first time with the aim of boosting the biosensing performance to extreme degrees. Extending the application of a methodology to a class of small molecules, containing a vast number of drugs, sometimes needs very low detection-limit, as the therapeutic range of drugs in circulatory systems can reach very low values. In addition, it was beneficial to demonstrate the application of this newly available detection method on drug monitoring for the first time. In the end, regeneration of the recognition surface as well as the applications of the proposed memristive biosensor for in-serum detection was successfully demonstrated, and the results proved the suitability of such methods for the detection of TFV and many other drugs.

The proposed biosensor exploited the optimized recognition surface of field effect biosensors, while the transducer was an array of miniaturized silicon nanowires. This increased the sensitivity, as the transducer was itself a nanostructure at the same scale of biomolecules. Using an array of nanowires for detection provided more reliable statistical data. The performance of the memristor biosensor was superior, in terms of the limits of detection, to all drug biosensors that have been reported, to the best of our knowledge.

1.7 Thesis organization and outline

Following on from the first chapter, which was an introduction to personalized medicine and biosensing, the thesis is organized as follows:

Chapter 2 introduces biosensors for electroactive drug detection. It starts with an overview on the theories behind electroactive drug detection and state-of-the-art concerning the use of nanostructuring for biosensing applications. Theories about calculation of specific surface areas, and electroactive surface areas added to the interface of biosensors are discussed with the aim of equalizing it between differently-nanostructured biosensors under experiment. Different nanomaterials are studied with this technique to find out their catalytic properties and the physical phenomena behind them (e.g. quantum blockage) and, consequently, their impact on enhancing the performance of the proposed biosensors. This chapter goes on to describe a biosensor based on screen printing technology, using nanostructuring with gold nanoparticles and multi-walled carbon nanotubes for the TDM of prostate cancer. To this aim, several optimizations are reported on biosensors with the aim of monitoring etoposide (prostate cancer drug) in its therapeutic range, and also preparing it for the development of the enzymatic biosensor that is the subject of the next chapter.

Chapter 3 presents an enzymatic biosensor for monitoring the drugs that include the cytochrome P450 enzyme in their metabolic pathway through the body. In this case, abiraterone is considered as the target, another anti-prostate cancer drug. The biosensor is here obtained by immobilizing a layer of the enzyme as a recognition surface over the already-developed and optimized substrate. In this chapter, an overview of the state-of-the-art in the development of enzymatic biosensors is presented. Considering that the target has been detected electrochemically for the first time, biosensors of other targets are discussed and compared. Then the description and results related to utilizing the biosensor for investigating abiraterone electrochemistry. Subsequently, abiraterone detection in buffer and human serum is reported for the first time.

Chapter 4 proposes a new class of biosensors, so-called affinity-based biosensors, to address the detection of drugs that are neither electroactive, nor can be detected by cytochrome P450. In this section the targeted drug is Tenofovir, and two biosensors are proposed and tested in order to detect it as a solution for the TDM of HIV. This is done to, first of all, push the limit of detection to the extremes and obtain the best-reported performance for drug monitoring and, secondly, to employ a recently offered transducer called memristor in drug monitoring, for the first time.

This chapter includes a section about the background on aptamers as the biomolecule use as the recognition probe in this part of thesis, and continues with introducing field effect and memristive transducer, as well as, state-of-the-art on the biosensing approaches mentioned. The examples explained in this section of chapter 4 are mostly about affinity-based biosensors targeting many different molecules, since just a few works are published on Tenofovir detection. Then, the aptamer-based field-effect biosensor is proposed and its sensitivity and selectivity for Tenofovir detection in buffer is reported and compared with the literature. Its application for in-plasma and real-time monitoring is also investigated, as a proof of concept. Above all, an ultra-sensitive affinity-based biosensor is proposed and successfully demonstrated detecting Tenofovir in plasma and human serum with high regeneration properties. It has been developed utilizing memristive silicon nanowires as a novel transducer in drug monitoring.

Chapter 5 provides and overview on all the important achievements in this thesis, and indicates the further efforts that need to be put into several aspects of this thesis in order to continue and finalize what has been started.

Chapter 2 Detection of electroactive drugs

Electrochemical voltammetric/amperometric biosensors are of great interest to point-of-care electroactive drug detection, and also for the development of enzymatic biosensors. This is achieved thanks to their low-cost of fabrication, simplicity, and their miniaturization possibilities. Miniaturization and integration of the technology in a small device is essential for the development of portable and non-expensive devices, and it can be achieved by microelectronic compatible technologies.

In order to maximize the performance of a biosensor it is very important to characterize and optimize the recognition and transducer element. One of the techniques to optimize the performance is to increase the electron transfer rate and the conductivity of the sensing surface by taking advantage of the high electro-active surface area (EASA) of nanostructures. In this section a nanostructured direct-electrochemical biosensor for detection of electroactive drugs will be proposed, characterized and successfully tested, in order to detect H_2O_2 (a simple electroactive compound), and etoposide, an electroactive compound and a common cancer drug, as a model of any electroactive therapeutic compound. This section of thesis has two main aims:

Firstly, to bring a deeper insight into the properties of nanostructures in improving the electrochemical performance of biosensors, and investigating the possible reasons behind them. To this aim, the interface of the nano-biosensor is nanostructured with different nanomaterials, in order to keep the added EASA. The performance of differently-nanostructured biosensors were tested for a response to H_2O_2 detection, and compared to obtain an insight into the impact of the nanomaterials in electron transfer (current amplitude).

Secondly, the nano-biosensors with better performance were optimized towards having maximum electron transfer with the target molecule. Optimization was started with the best scan rate of applied potential with cyclic voltammetry (CV) as the detection method, and followed by finding the optimum additional-EASA on the electrodes obtained by means of nanostructuring.

The final aim of optimization was to create optimum enzymatic biosensors, so the electroactive biosensors were not pushed to their ultimate electrochemical performances at this stage. Nevertheless, the response of electroactive biosensors resides well inside the therapeutic range of etoposide (section 2.2), showing the suitability of the proposed biosensor for electroactive drug monitoring.

Electrochemical bioelectrodes have shown to be a promising system to replicate the time-consuming and costly laboratory experiments and analysis that are currently used for TDM,. Therefore, they can be the connection between TDM and site testing, emergency room screening,

bedside monitoring and home self-testing. [63, 64] Electrochemical bioelectrodes provide an interface between the redox site of the target metabolite and the electronic part of the biosensors. Most bioelectrodes act as transducers to convert biological events into electric current by applying a fixed potential over the electrode and target (amperometry), or sweeping the applied potential in a range (voltammetry) and measuring the current. Amperometry experiments are beneficial because of their high sensitivity and large linear range, whilst voltammetry experiments provide the option of multi-target detection. [65] Many different non-enzymatic [66–68] bioelectrodes have been proposed in literature that can be useful to this purpose. The role of nanostructuring in enhancing the electrochemical performance of bioelectrodes is widely studied and reported, [69–71] but to the best of our best knowledge there is not enough work done on the optimization of nanostructured biosensors to facilitate the electron transfer with targeted drugs.

2.1 Development and optimization of direct-electrochemical biosensors

2.1.1 Background and state of the art

Redox reactions

Redox reactions are a family of reactions that are concerned with the transfer of electrons between species. Oxidation refers to the loss of electrons, while reduction refers to the gain of electrons. Each reaction by itself is called a "half-reaction".

$$O + e^- \xrightarrow{K_{red}} R \quad (1)$$

$$R \xrightarrow{K_{ox}} O + e^- \quad (2)$$

Combination of half reactions is a complete redox reaction. An example of a redox reaction:

$$Cu(s) + 2Ag^+(aq) \rightarrow Cu^{2+}(aq) + 2Ag(s) \quad (3)$$

The chemical that causes other ones to lose electrons (that have been oxidized) is an oxidizing agent named oxidant, and the compound that gives electrons to other molecules (have been reduced) is a reducing agent, or reductant. In the equation above, Ag+ is the oxidizing agent and Cu(s) is the reductant. The reductive and oxidative currents related to Equations 1 and 2 are:

$$i_O = FAK_{ox}C_R \quad (4)$$

$$i_R = -FAK_{red}C_O \quad (5)$$

Where F = 96,500 C/mol is Faraday's constant, A is the area that current passes through and C_R and C_O are the concentration of reactants at the surface. [72, 73]

Screen-printed three-electrode redox cells for electrochemical detection

Since reactions are generally detected only in close proximity to the electrode surface, the electrodes themselves play a crucial role in the performance of electrochemical biosensors. Based on the functionality of a specific electrode, its detection quality is influenced by the electrode material, its surface modification and its dimension. Electrochemical sensing usually requires a reference electrode (R.E.), a counter or auxiliary electrode (C.E.) and a working electrode (W.E.), also known as the sensing or redox electrode. The R.E. is kept at a distance from the reaction site in order to maintain a known and stable potential. The W.E. serves as the transduction element in the biochemical reaction, while the C.E. establishes a connection to the electrolytic solution so that a current can be applied to the working electrode (block diagram in Figure 12). These electrodes should be both conductive and chemically stable. Commonly used materials are platinum, gold, carbon (e.g. graphite, glassy carbon), silicon or even carbon nanotubes (CNTs) ; the inks depend on the analyte and application. They are ideal for low cost, disposable devices specially designed to work with microvolumes of sample.

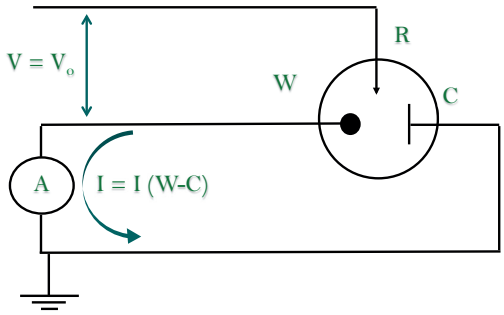

Figure 12. Block diagram of the driving/reading configuration of a three-electrode redox cell

The W.E. is the main substrate, which the electrochemical devices measure the current to obtain the chemical activities within the analyte. This is also the place to deposit the nanostructures or immobilize the enzymes to improve the electron transfer rate between the electrode and the target. In order to force the current to flow between the target and the carbon substrate we need to apply a voltage over them, so the R.E. has been put in direct contact with the analyte and the device sustains a potential between R.E. and W.E. Nevertheless, due to the impedance existing in the path of the electrons, there is a potential drop, which counters the stability of the potential. This impedance is mainly due to the double layer at the interface between the sensing layer and the background solution and then the resistivity of the solution. To solve the potential drop, the current between the R.E. and W.E. should be zero, thus it must be collected by another electrode that is C.E. [72, 73] A very recent work published by Trouillon *et al.* [74] used a needle sensor consisting of a three-electrodes redox cell for the time-resolved electrochemical detection of dopamine in a hybrid microfluidic/electrochemical. Taking advantage of electrochemical detection they have successfully demonstrated the very first real-time and quantitative chemical investigation of dynamic mechanisms at artificial cells-on-paper samples, with sufficient sensitivity down to nM concentrations. [74]

Conventional laboratory-based stripping measurements had relied on Hg-based electrodes. The substitution of these electrodes for new disposable test strips is an alternative that presents many advantages for these determinations. [75] Such strips are produced by printing planar films of gold, silver, carbon etc. on an inexpensive plastic or ceramic support. The strip is considered as a disposable electrochemical cell, onto which the sample droplet is placed. Since the 1990s screen-printing technology, adapted from the microelectronics industry, has offered high-volume production of extremely inexpensive, yet highly reproducible and reliable single-use sensors. [76] This technique holds great promise for on-site monitoring, and the use of screen-printing technology in the serial production of disposable low-cost electrodes for the electrochemical determination of a wide range of substances. Screen-printed electrodes (SPEs) are devices that are produced by printing different inks on various types of plastic or ceramic substrates. The pattern and number of single electrodes can be designed according to their applications, and large compositions of materials are available as inks for printing. Therefore, a wide variety of devices of this type are commercially available. The schematic of a three-electrode electrochemical cell and an SPE version are depicted in Figure 13.

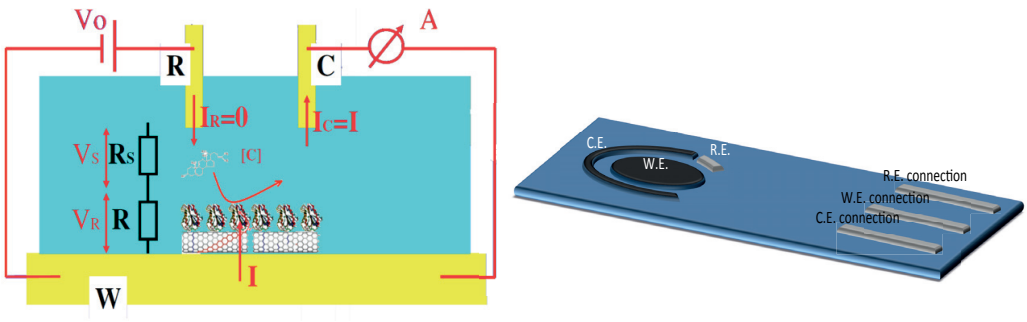

Figure 13. Left: Schematic of three-electrode electrochemical cell (reprinted with permission from [73]). Right: a typical SPE used as an electrochemical cell.

The great versatility allowed by the SPEs lies in the wide range of ways in which the electrodes may be modified. The printed W.E. may be enhanced by depositing very different substances such as nanostructures, enzymes, polymers, complexing agents, nucleic acids, etc. [77]

Nanostructuring

Functionalizing the surface of a working electrode with nanomaterials is an attractive approach to facilitate the electron transfer between the electrode and reactant, thanks to their ability to modulate the energy bands at the interface (Figure 14). The coupling between W.E. of the biosensor and the analyte is limited by a tunnelling barrier. [73] For instance, in the reduction of an electroactive species the electron jumps from the fermi level of metal (electrode) to the lowest unoccupied molecular orbital (LUMO) of the molecules. The LUMO is the first available orbital that accepts electrons. On the other hand, in oxidation reaction the electron from highest occupied molecular orbital (HOMO) of the molecules jumps to the Fermi level of the metal. HOMO is the last occupied orbital releasing electrons. In CV experiments the electrons jump to/from molecular orbitals from/to the electrodes through a tunnelling barrier that suppresses the electron transfer rate described by the following equation:

$$k_{ET} = \frac{2\pi}{\hbar} V_T^2 FC \quad (6)$$

Where FC is the Franc-Condon-weighted density of states[9], V_T^2 is the electronic coupling between the molecules and the electrode[10] and ħ is Planck's constant. Nanostructuring, as illustrated in Figure 14, decreases this barrier and enhances the electron transfer rate by increasing the electronic coupling between the electrode and the analyte. [73]

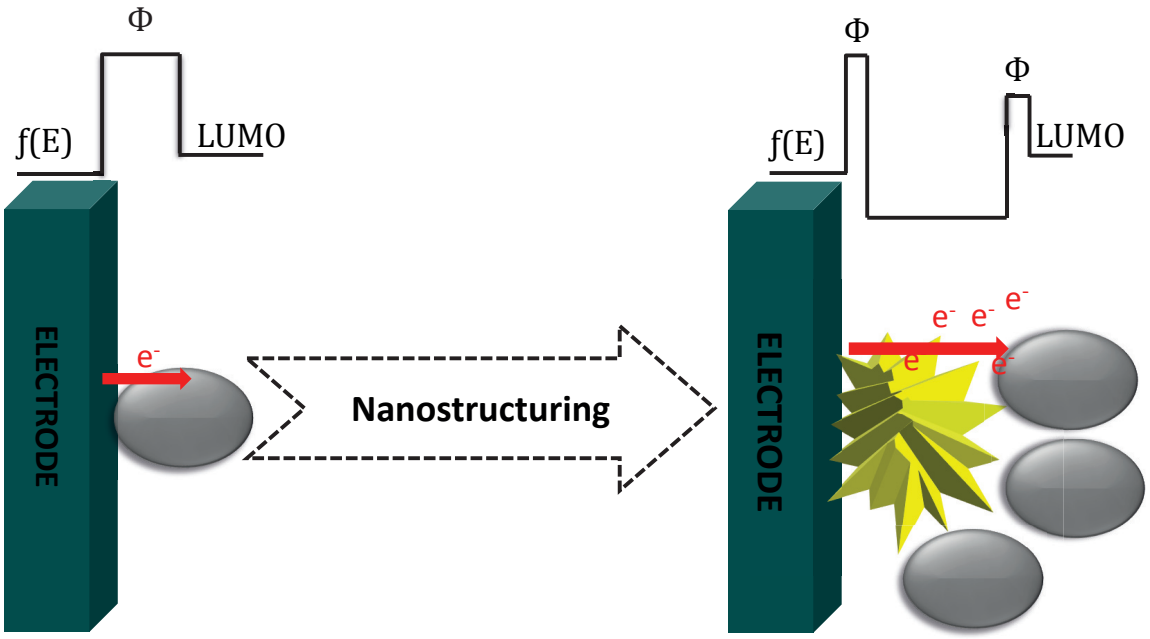

Figure 14. Impact of nanostructuring on electron transfer. Higher surface to volume ratio means higher active sites for reaction and facilitated electron transfer leads to higher affinity for reaction.

Moreover, abundance of defects and sharp edges on the surface of nanomaterials provide affinity sites for electron transfer with electroactive agents, as well as a proper immobilization site for recognition probes. [78] There are specific properties related to nanomaterials that brings them with extra advantages over their bulk stabs that makes them very interesting for biodetection approaches: [78, 79]

1. **Small size:** Nanoparticles often possess unexpected chemical, physical, optical and electrical properties as they are small enough to confine their electrons and produce quantum effects. [80] For example, gold is an inert element, meaning it does not react with many

---

[9] Weighted density of states is the integrated overlap of the wave functions at equal energies of molecules and electrode atoms, and is computed from Marcus classical form of overlapping harmonic oscillators:

$FC = \frac{1}{\sqrt{4\pi\lambda kT}} e^{-(\lambda kT\sqrt{-\Delta G^0 - \lambda})}$

λ is the energy arising from increased polarity of redox center, ΔG^0 is the Gibbs free energy between two electron states, and k is the Boltzmann constant.

[10] Electronic coupling is related to the tunneling distance:

$V_T^2 = V_0^2 e^{-\beta(\phi)d}$

V_0 is the maximum electronic coupling at null distance, $\beta(\phi) = \sqrt{\frac{2m}{\hbar}(\beta(\phi) - eV)}$ is exponential decay of the electronic coupling that depends on potential applied across barrier V and electron mass m, ϕ is tunneling barrier.

chemicals, whereas at the nanoscale, gold nanoparticles become extremely reactive and can be used as catalysts to speed up reactions. Nanostructures melt at much lower temperatures. [81] For example, GNPs melt at ~300 °C for 2.5 nm-sized nanoparticles that is much lower than gold slabs melting at 1064 °C. Absorption of solar radiation in photovoltaic cells is much higher in materials composed of nanoparticles than it is in thin films of continuous sheets of material. In other words, the smaller the particles, the greater the solar absorption. The most important small-size property of nanostructures in this work is their enhanced electrical properties or their higher electron transfer rate with respect to their macromaterial, or even compared to the nanoparticles of the bigger size. The quantized electron energy levels in gold nanoparticles is observed and reported for some nanomolar size nanoparticles as being similar [82] to the ones widely reported for semiconductor nanoparticles such as cadmium selenide (CdSe NPs) [83, 84]. The bandgap between the conduction and valence band of nanometer-sized nanoparticles with quantized energy levels increases as the size decreases, and this pushes the electrons in the conduction band toward higher energies that makes them more and more excited. This means a higher driving force and, as a result, a higher electrons transfer between nanoparticle and target molecule. The small energy difference attained by decreasing the particle size is sufficient to increase the electron transfer rate by nearly 3 orders of magnitude with decreasing particle size from 7.5 nm to 2.5 nm. [83]

2. **Large surface to volume ratio:** The surface of materials is the place that reactions take place, so the greater the surface of a e volume, the greater the reactivity. Surface to volume ratio of particles increases drastically as their size decreases. When a given volume is divided into small pieces, and the surface area of the particles increases, a greater portion of atoms is located at the surface compared to the interior of the particles. For instance, a particle of 30 nm has 5% of the atoms on the surface. This number increases to 20% for 10 nm particles and 50% for 3 nm particles. A particle with a high surface area has a greater number of reaction sites than a particle with low surface area, and thus, results in higher chemical reactivity. [78] For instance, nanometer and micrometer sized magnetic beds have attracted lots of attention as their large effective surface area offers efficient capture of proteins. [85] Magnetic beads have many applications in POC biosensing, especially in affinity-based biosensors, as they can be used in microfluidics and lab-on-a-chip applications, where they are manipulated and separated effectively using magnetic fields. [85, 86]

   The level of activity of a nanostructure can be inferred from its specific surface area (SSA). It is a property of solids equal to their total outer surface area per unit of mass, solid or bulk volume, or cross-sectional area. [87–89] It is defined either by surface area divided by mass (with units of m^2/g), or surface area divided by the volume (units of m^2/m^3 or m^{-1}). It has a particular importance for adsorption, heterogeneous catalysis, and reactions on surfaces. Several empirical approaches are utilized to measure the SSA of different materials, including methylene blue (MB) absorption stain test, ethylene glycol monoethyl ether (EGME) method, Brenauer-Emmett-Teller (BET) gas adsorption method and Protein Retention (PR) method. [87, 90, 91] The SSA can also be calculated theoretically, by dividing the mathematical formula of the surface area by the mass, making some assumption about the

particle shape. The drawback of this technique is that it does not take into account the surface area associated with the texture of the particles' surface. However, the simplicity of this technique is very interesting for the application in this thesis. As SSA is the area over mass, and the surface/volume increases as the size of the material decreases, then SSA is inversely proportional to the size. Indeed, there is a double effect of the particle size on the specific surface: as the particle size decreases, the SSA increases not only due to the inverse relationship between the specific surface and the size, but also because the shape of the small particles tends towards platy and rod-like geometries. [89]

3. **Tailorable properties:** Tailorable physical properties are directly relate to size, composition and shape, and are a very important aspect of nanomaterials. These properties have been used widely in biology, such as in bioconjugation and cellular labelling, for the past four decades. [92] Moreover, new synthesis, fabrication, and characterization methods for delicate modulation of the nanomaterials size, shape, and composition allows exquisite control of their properties. The ability to tailor the physical and electrical properties of nanomaterials carefully is essential for their application in biodetection. Specifically, varied sizes, shapes, and compositions of metal nanoparticles and quantum dots can now be achieved that helps to produce materials with specific electrical, emissive, absorptive, and light-scattering properties, [93, 94] which make these materials ideal for multiplexed metabolism detection. Bandgap tunability and the resulting shifts in absorption/emission energies have been extensively researched in nanoparticles [95] and in homogeneous nanorods made of materials with reasonably large exciton Bohr radii, such as CdSe. [96] Some recent advances in tailoring the nanostructures properties for biosensing applications include a composition of platinum nanopetals: platinum nanospheres are developed on bare platinum electrodes, and used to electroactively screen glucose concentrations without involving any enzyme thanks to highly increased EASA and, thus, electron transfer with the glucose molecules. [97] Forming a combination of various shapes of nanostructures, called nanocomposites, can be very useful for bioelectrochemical applications. [98, 99] A ternary nanocomposite material based on rGO is a good example that was developed by the decoration of AuNPs and polypyrrole (PPy) as a cross-linker for glucose detection. [100] Another good example for the relevance of nanomaterial tailorable properties in biodetection are the size-dependent electronic and photonic properties of some-nanometer particles, or quantum dots (QDs), that are considered as one of the most attractive features of nanomaterials for attaining a band gap gradient in quantum dot solar cells, [101–103] enzymatic fluorometric biosensors, [104] QDs-based resonance energy transfer biosensor for food monitoring, [105] drug monitoring [106] etc. For instance, a photoluminescence biosensor was fabricated on the basis of multilayer shells CdSe/ZnSe/ZnS QDs for rapidly detecting the residues of trichlofon pesticide with concentrations of 0.01 ppm to 5 ppm. [107] In other work, metal oxide nanowires are developed by physical vapor deposition for chemical warfare agents and some selected toxic industrial compounds detection. [108]

Widely used nanostructures

Many novel nanostructures are developed and exploited to enhance the electron transfer rate between electrodes and targets, thus increasing the performance of the devices.

Semiconductor nanoparticles' electrochemical and optical properties are tunable with their size. Blue shift in the absorption edge of nanoparticles (NPs), while decreasing their size, is a well-known example of this. [109] This and many other size dependent properties are the result of a high amount of surface atoms and quantum effects. [110] Many applications in electronics, [111, 112] catalysis and sensing, [113, 114] solar-energy conversion, [115, 116] and optoelectronics [117, 118] take advantage of these tunable behaviors. Bi_2O_3 NPs [119, 120] present enhanced catalytic and electrochemical activity given its bulky material. [121] These are induced by high surface/volume ratio, high defect concentration on surfaces (porous morphology), and unique electronic properties. [122, 123] These properties as well as nontoxic nature and biocompatibility make them a suitable choice for biosensing applications. [124]

Conductivity and nanoscale dimensions of metal NPs (mostly gold NPs) is utilized in many enzymatic [125, 126] and non-enzymatic [127] bio sensing applications. To this aim, they are deposited on a wide range of substrates by electro-deposition, [127] self-assembly [128, 129] and precipitation [125, 130] techniques. Strong adsorption band of metal NPs is another quantum scale effect, which is absent in their either individual atoms or bulk materials. This and many other optical properties of metal NPs are originated from surface plasmon resonance phenomenon. [131] Gold NPs with negative net charge adsorb biomolecules without attenuating their bioactivity; [132] thus offering many potential applications as bio-labels, [133] or enzymes' immobilizing platform. [126] Their size and surface chemistry, and consequently their optical and electrochemical properties, are easy to modify. This feature has made gold nanoparticles one of the most widely used nano materials in point-of-care medical devices and industrial products. [80, 125] The increment in sensitivity with the decreasing dimensions of GNPs has also been reported. [134] The authors proved an enhancement of the amperometric response (I_{max}) in a glucose detection system by decreasing the size of GNPs from 13 nm to 6 nm and then to 3.5 nm (66.2 μA, 73.8 μA, and 76.2 μA, respectively).

CNTs are one of the building blocks of nanotechnology. They are cylinders of one (SWCNTs) or more layers (MWCNTs) of graphene with open or closed ends. As mentioned before they have a hundred times the tensile strength of steel, and the best thermal conductivity after pure diamonds. [79] Perfect CNTs have all carbons bonded in a hexagonal lattice except at their ends. Diameters of SWNTs and MWNTs are typically 0.8 nm up to 2 nm and 5 nm up to 100 nm (typically 10 – 20 nm), respectively. CNT lengths range from less than 100 nm to several centimeters, thereby bridging molecular and macroscopic scales. On-going interest in CNTs as components of biosensors and medical devices is motivated by the dimensional and chemical compatibility of CNTs with biomolecules, such as DNA and proteins. Adsorption of target molecules on the surface of the CNTs directly or through bioprobes alters the electrical (for instance impedance or current-voltage characteristics) and optical response of the tubes. [135] Therefore, CNT-equipped biosensors with promising performance can be developed with the functionalization of the CNTs surface used as

recognition probes such as coatings, functional groups, proteins and nucleic acids, [136] and appropriate sensor design (e.g., field effects, capacitance, Raman spectral shifts, and photoluminescence). [137, 138] MWCNTs, considering the applied synthesis method and surface treatment, can display metallic, semi-metallic, or super-metallic conductivity. They provide hollow cores, useable for immobilizing platforms, and 1D electron confinement with a very high mean free path. Consequently, MWCNTs play an important role in biomedical diagnostics by improving the electron-transfer kinetics towards the redox center of enzymes or biomolecules. [139–141] MWCNTs are grown on a vast variety of substrates by means of chemical vapor deposition, [142, 143] electrophoretic deposition, [144] arc discharge, [145] laser ablation (evaporation), [146] as well as some new techniques including solar energy evaporation, plasma torch, underwater AC electric arc, and microgravity environment. [147] All in all, MWCNTs with high surface to volume ratio, good mechanical properties, and great electrical conductivity provide improvements in terms of sensitivity, selectivity and limits of detection (LOD). [141]

Crystal layers on the surface of materials have a great capacity to relieve stress, much more readily than the same crystal material in bulk. The Hellmann-Feyman theorem in quantum mechanics explains that surface layers form an oscillatory-type relaxation behavior inwardly oriented toward the regions of higher charge density, and this phenomenon is intensified in large surface to volume ratio materials such as nanostructures. [148] For instance, CNTs are probably the strongest fibers available. Several recent papers have shown that MWNTs are extremely rigid rods of very low density with unique mechanical properties. [149] These properties depend critically on the arrangement of the graphitic planes, which confirms that MWCNTs, as long as the graphitic planes are aligned with the tube axis, maximize the effect of the very high in-plane elastic constant of graphite. The tensile strength, and Young's modulus, have been estimated to be 45 GPa and 1.2 TPa, respectively, for SWNTs and 150 GPa and 900 GPa, respectively, for MWCNTs. [150–152]

2.1.2 Characterization of the nanomaterials properties in use

The gain in terms of Surface Area is one of the key advantages of nanomaterials. However, it is not the only gain that biosensors can get from the use of nanomaterials. This section demonstrates that different nanostructuring can offer different gains in terms of sensitivity, detection limit, and redox potential, albeit providing the same gain in terms of increased surface area. Calculating and equalizing the additional EASA coming from nanostructuring will help to have a more reliable comparison between nanostructures of different nature, size and shape. To this aim, biosensors based on MWCNTs, GNPs and Bi_2O_3 NPs with similar EASA on W.E. are produced and put to the test with cyclic voltammetry and chronoamperometry to detect hydrogen peroxide (H_2O_2).

Materials and methods

SPEs with carbon electrodes (model DRP-C110) and MWCNTs powder were purchased from DROPSENS. The electrodes consist of a 0.12 cm^2 carbon W.E., a carbon R.E. and a Ag C.E. Dispersion of dodecanethiol functionalized gold nanoparticles, with an average particle size of 4 nm and

concentration of 2% (w/v) in toluene, was provided by SIGMA-ALDRICH (Spain), and diluted by toluene to obtain density of 1 mg ml^{-1}. H_2O_2 (weight 30%) was supplied by Reactolab SA (Switzerland) and was diluted with a phosphate buffer solution (PBS-0.1M, pH7.4) to get a 25mM solution. Powder of multi-walled carbon nanotubes (diameter 10 nm, length 1-2µm, 90% purity, 5% COOH functionalization) was purchased from DropSens, and was dissolved in chloroform to the concentration of 1 mg ml^{-1}. The dispersion was subjected to sonication for 1 hour to achieve a homogeneous solution. Bi_2O_3 NPs, developed in Politecnico di Torino (Figure 15-Center), were dissolved in acetone to the density of 2 mg ml^{-1} and sonicated to obtain a homogeneous solution. To functionalize the sensing surface of biosensors, W.E. of electrochemical cells were nanostructured by covering the working electrode with 100 µg (50 µl) of Bi_2O_3 NPs, 4.8 µg (4.8 µl) of MWCNTs and 13.5 µg (13.5 µl) of GNPs in steps of 5 µl, 0.8 µl and 3 µl (four steps of 3 µl and one step of 1.5 µl), respectively. The electrodes were allowed to dry after each step, and at the end were stored at room temperature. [125]

Bi_2O_3 NPs were synthesized starting from a bismuth salt following the Metal Organic Chemical Vapor Deposition (MOCVD) process. MOCVD was selected due to the possibility of optimizing various parameters with the scale up from a few milligrams to kilograms. The metal organic precursor was evaporated in inert atmosphere with regulated temperature, so as to form metal nanoparticles. By varying the MOCVD experimental conditions, it was possible to tailor the properties of the crystals at the atomic scale. Bismuth(III) nitrate pentahydrate ($Bi(NO_3)_3{\cdot}5H_2O$; Aldrich, 98% purity) was used as a bismuth and oxide atomic source for synthesizing Bi_2O_3 NPs. The first step of the process was to get rid of the residual air using pure argon gas flow. Then the furnace was brought to a thermal equilibrium at the required deposition temperature (600°C). In the furnace, the high temperature leads to the pyrolysis of the starting material, $Bi(NO_3)_3 \cdot 5H_2O$, into a gas mixture, which ultimately leads to the nanoparticle growth inside the glass vial. When the growth process ended, the furnace was allowed to cool down to ambient temperature, while maintaining the inert gas flow.

Electrochemical measurements (CA and CV) under aerobic conditions were carried out using AutoLab Potensiostat/Galvanostat and functionalized electrodes as sensing elements. In voltammetry experiments the surface of the active element of the sensor was covered by 100 µl of 25 mM H_2O_2 solution and the device was configured to sweep the voltage in the range of -1 to +1 (vs. Ag) with the scan rate of 100 mV s^{-1}. The peak positions of voltammograms (Table 2) were assessed by curve fitting, using the IGOR Pro software (Wavemetrics, Lake Oswego, OR, USA). The best fit for the voltammogram shapes was obtained when constant baseline and Gaussians were used. [153]

To perform the chronoamperometry the electrodes were immersed inside 10 ml of PBS (0.1M, PH-7.4) in which H_2O_2 was injected in steps of 100 µM to a total amount of 500 µM. The applied potential was set slightly above the oxidation peak obtained from the voltammogram analysis. To achieve a better evaluation, statistically, four SPEs were functionalized with one type of nanostructure and tested using CA. Then the calibration curves were evaluated after removing the blank measurements from the data obtained. In the next step, the slope of the calibration curve

was divided by surface area of the working electrode to identify the normalized sensitivity. Standard deviations were calculated using Excel.

The LOD of linear calibration curves was calculated based on International Union of Pure and Applied Chemistry-IUPAC standards, using Equation 7, [154] where ΔD is the standard deviation of blank measurements, S is the sensitivity (the slope of linear curve), and K=3 is a parameter accounting for the confidence level (K = 1, 2, or 3 corresponding to 68.2 %, 95.4 %, or 99.6 % of statistical confidence, respectively). to calculate the LOD of dose-response curves fitted by nonlinear functions, the method of Armbruster et al. [155] has been employed - as will be explained in detail, in section 3.4.1.

$$LOD = \frac{K\Delta D}{S} \tag{7}$$

At this point in the study, responses of biosensors obtained from the four SPEs were averaged and represented on an I-V curve to obtain the calibration curve, and then the linear range of the curve was analyzed to obtain the sensitivity, and the LOD corresponding to the nanostructure. This procedure was repeated for every nanostructure and the results are summarized in Table 2.

A MERLIN scanning electron microscope (Carl Zeiss, Germany) was used to perform Scanning Electron Microscopy (SEM) of the nanostructures. SEM images of MWCNTs with a diameter of 10 nm and length of 1 – 2 µm, Bi_2O_3 NPs of the size 64 nm and GNPs of the size 4 nm are presented in Figure 15. SEM was used to confirm that the nanostructures had roughly the shape and size expected, and that the surfaces of working electrodes were completely coated. ImageJ software was used to analyze the SEM images of Bi_2O_3 NPs (Figure 15) to measure the average diameter, as this was a homemade sample. [156]

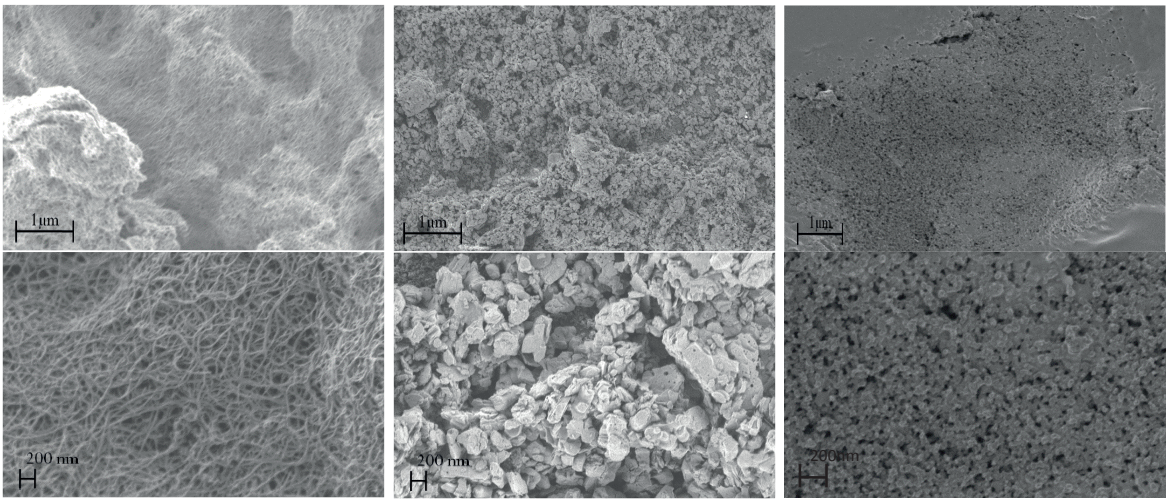

Figure 15. SEM images of the surface of working electrodes functionalized as follows - left column: MWCNTs, center column: Bi_2O_3 NPs, right column: Au NPs.

Specific surface area calculation

SSA of Bi_2O_3 NPs: SEM images (Figure 15-Center) present a roughly spherical morphology of Bi_2O_3 NPs with an average diameter of 64 nm. The density of bismuth oxide is equal to 8.9 g cm^{-3}. The SSA can be calculated as follows:

$$\begin{cases} SSA = \dfrac{A}{V \times \rho} = \dfrac{3}{r \times \rho} \\ A = 4 \cdot \pi \cdot r^2 \\ V = \dfrac{4}{3} \cdot \pi \cdot r^3 \end{cases} , \begin{matrix} r = 32nm \\ \rho = 8.9 \left(g/cm^3 \right) \end{matrix} \Rightarrow SSA(Bi_2O_3) = 10.5 \left(m^2/g \right) \quad (8)$$

SSA of GNPs: GNPs can be also considered roughly as spheres, based on the SEM images (Figure 15-Right). Provider data sheets have an average diameter of 4 nm, and a density of 19.3 g cm^{-3}. Thus, its SSA is equal to:

$$\begin{cases} SSA = \dfrac{A}{V \times \rho} = \dfrac{3}{r \times \rho} \\ A = 4 \cdot \pi \cdot r^2 \\ V = \dfrac{4}{3} \cdot \pi \cdot r^3 \end{cases} , \begin{matrix} r = 2nm \\ \rho = 19.3 \left(g/cm^3 \right) \end{matrix} \Rightarrow SSA(GNPs) = 77.7 \left(m^2/g \right) \quad (9)$$

SSA of MWCNTs: The SSA of MWCNTs is calculated following the work of A. Peigney, et al. [157] CNTs are closed cylindrical geometries, so for calculation of the SSA it is enough to take the outer surface into account. Also the high aspect ratio (>1000) gives us the possibility to neglect the small surface area at both tips. MWCNTs consist of several concentric shells inside with an inter-shell distance of merely $d_{s\text{-}s} \approx 0.3400$nm (Figure 16). In addition, the length of the C-C bonds in a curved graphene sheet is equal to the planar sheets ($d_{c\text{-}c}$=0.1421nm). As a result the SSA of CNTs is equal to the SSA of one side of a graphene sheet (GS) :

$$\begin{cases} SSA(CNT) = SSA(GS) = \dfrac{s_h}{w_h} \\ \mathrm{S_h} = 3d_{c-c}^2 \dfrac{\sqrt{3}}{2} = 5.246 \times 10^{-20} m^2 \\ w_h = 2 M_c / \mathrm{N} = 3.988 \times 10^{-23} g \end{cases} \Rightarrow SSA(CNT) = 1315 \, m^2/g \quad (10)$$

S_h is the surface of one hexagon, which corresponds to two carbon atoms, and w_h is its atomic weight (M_c=12.01$\frac{g}{mol}$, Avogadro number N=6.023×$10^{23}$$mol^{-1}$).

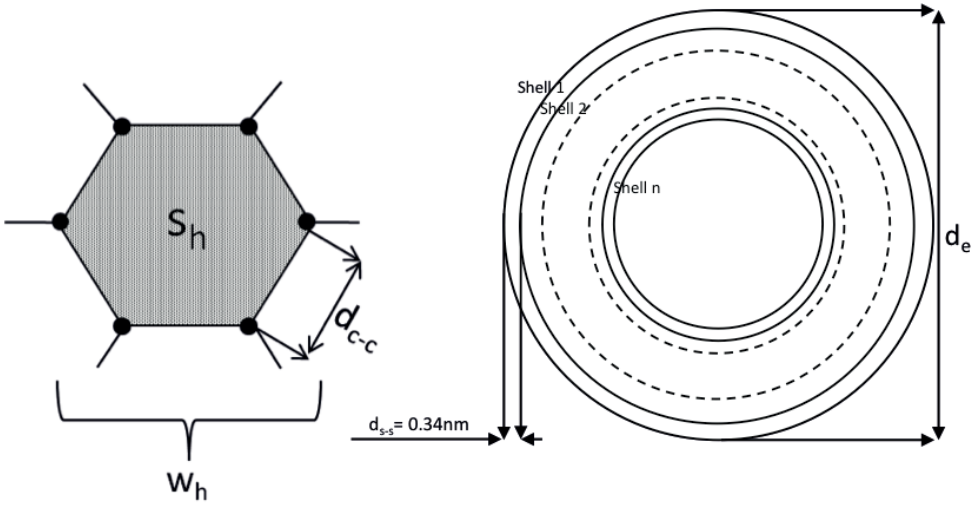

Figure 16. Left: schematic illustration of the arrangement of carbon atoms in a graphene sheet. Right: concentric graphene shells of MWCNTs. Adapted from [157].

A MWCNT with an external diameter d_e, length L and n shell has an external surface of $s_{MW} = \pi L d_e$. The weight of this external surface w_{MW} can be calculated as the multiplication of the surface of one side of all graphene sheets (s_{GS}) and its surface weight (w_{GS}). To find s_{GS}, we need to calculate the s_{MW} of all the shells and add them:

$$s_{GS} = s_{MW1} + s_{MW2} + s_{MW3} + \cdots + s_{MWn} \quad (11)$$

The surface of all the graphene sheets which compose the MWNT is:

$$s_{GS} = \pi \cdot L \cdot d_e + \pi \cdot L(d_e - 2d_{s-s}) + \pi \cdot L(d_e - 4d_{s-s}) + \cdots + \pi \cdot L(d_e - (n-1)d_{s-s}) \quad (12)$$

The different terms successively represent the surface of the external shell (number 1), of the first internal shell (number 2) and so on up to the innermost shell (n). This expression can be simplified:

$$s_{GS} = \pi \cdot L[nd_e - 2d_{s-s} \sum_{i=1}^{n-1} i], for\ n\ shells \quad (13)$$

Number of shells (n) is calculated accordingly to the work of S. Haruehanroengra and W. Wang. [158]

$$N_{shells} = 1 + \frac{D_{out} - D_{in}}{2 \times \delta}, \frac{D_{in}}{D_{out}} = \frac{1}{2} D$$

$$=> N_{shells} = 1 + \frac{D}{4 \times \delta} = 8 \quad (14)$$

Where $D = 10nm$ is diameter of the MWCNT, and $\delta = 0.34nm$ is the van der Waals distance. This result is in agreement with SEM results (Figure 15-Left), the current literature and DropSens company sources. By knowing the number of shells (n = 8), the diameter (d_e = 10nm), s_{MW} and w_{MW}, we can finally calculate the SSA of MWCNTs:

$$SSA(MWCNT) = \frac{s_{MW}}{w_{MW}} = \frac{SSA(GS)\cdot d_e}{nd_e - 2d_{s-s}\left[\sum_{i=1}^{n-1} i\right]}\ ,\begin{cases} n = 8 \\ d_e = 10nm \end{cases}$$

$$=> SSA(MWCNT) = \frac{1315\cdot d_e}{nd_e - 0.68\left[\sum_{i=1}^{n-1} i\right]} = 215.7\,\frac{m^2}{g} \quad (15)$$

Equal EASA

The SSA of nanomaterials is their outer surface area per unit of mass, while EASA is the total amount of surface area that can be achieved by a specific amount of nanostructuring (in terms of mass). In other words, the EASA is equal to the multiplication of deposited mass by characteristic SSA that a nanomaterial offers.

$$EASA_{MWCNT} = X_{MWCNT} \times SSA_{MWCNT} \quad (16)$$

Therefore, the calculated SSA (Equations 8, 9 and 15) was used to calculate the mass of nanostructures that needed to be deposited over the electrodes to have an equal EASA by means of each nanomaterial, theoretically. To do so, additional-EASA over electrodes nanostructured with 100 µg of Bi_2O_3 NPs was considered as the reference (Equation 17), and the amounts of MWCNTs and GNPs to achieve almost the same additional-EASA were calculated., as follows.

$$100\times10^{-6}\times SSA_{Bi_2O_3} = 100\times10^{-6}g\times10.5\,\frac{m^2}{g} = 1050\,mm^2 \quad (17)$$

The amount of MWCNTs and GNPs for the deposition was calculated according to Equation 18 and 19, respectively.

$$1050\,mm^2 = X_{MWCNT}\times SSA_{MWCNT} => 1050\,mm^2 = X_{MWCNT}\times215.7\,\frac{m^2}{g} =>$$

$$X_{MWCNT} = 4.8\,\mu g \quad (18)$$

$$1050\,mm^2 = X_{GNP}\times SSA_{GNP} => 1050\,mm^2 = X_{GNP}\times77.7\,\frac{m^2}{g} =>$$

$$X_{GNP} = 13.5\,\mu g \quad (19)$$

SPEs were coated with an amount of nanostructures based on the above-mentioned values. They are referred to hereafter as Bi_2O_3–100, Au–13.5, and MWCNTs–4.8.

Experimental evaluation of theoretically calculated EASA

As a proof of concept, the additional EASA by nanostructuring was also obtained experimentally, following the work of Fotouhi *et al.* [159] by depositing 20 µg of MWCNTs over W.E. of biosensors and using them for the detection of a Ferro/Ferricyanide 1mM solution. This means that 4314 mm^2 of EASA was deposited, based on the theory descripted above (Equation 16; Table 3). The recorded voltammograms are demonstrated in Figure 17.

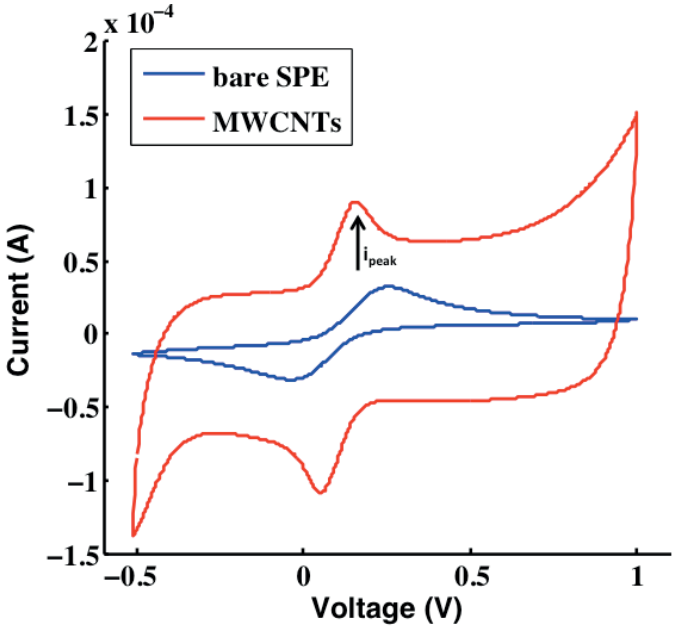

Figure 17. Recorded voltammogram of a MWCNTs-based biosensor for Ferro/Ferricyanide 1 mM detection (red curve) in comparison with the response of the bare biosensor (blue curve).

The measured oxidation peaks were analyzed with Nova software to obtain the peak amplitudes by removing the capacitive current from main Faradaic signal. Then using Randles-Sevcik equation (Equation 20) [73] the EASA available on the surface (A in formula) is measured.

$$i_{peak}(0,t) \propto nFA\left(\frac{nFDv}{RT}\right)^{1/2} C(0,t) \qquad (20)$$

Where n = number of electrons transferred in oxidation/reduction reaction, F = Faraday constant in C mol^{-1}, A = surface area in cm^2, D = diffusion coefficient in cm^2 s^{-1}, t = time, T = temperature in K, R = Gas constant in J K^{-1} mol^{-1}, C = concentration in mol cm^{-3} and finally v = scan rate in V s^{-1}.

The scan rate for this experiment was set to 100 mV s^{-1} and the potential window was between -0.45 and 1 V. The voltammetry was carried out until a stable and reliable signal was obtained (5 cycles). The diffusion coefficient of a redox couple is well known, and is equal to 6.20×10^{-6} cm^2 s^{-1}. [159] Therefore, a measured EASA of 4385 mm^2 is obtained from the equation that is in full agreement with the concept, and can be offered as a reliable proof of the proposed theory.

Electrochemical enhancement by means of MWCNTs, Bi_2O_3 NPs and GNPs

Cottrell and Randles-Sevcik equations verify the direct relationship between the electrochemical Faradaic current and the surface area of electrodes. Furthermore, it has been proven by Carrara et al. [160] that the sensitivity (S) calculated from the Faradaic current versus concentration is directly related to the additional electroactive surface area. Equation 21 describes the relation between the sensitivity of an electrochemical sensor, driven with fixed potential, and EASA.

$$S = \frac{nF(A_g + A_{nanostructure})\sqrt{D}}{A_g\sqrt{\pi t}} \quad (21)$$

where n = number of electrons, F = Faraday constant, D = diffusion coefficient, t = time and A_g = surface area of W.E. of SPE. In addition, there is a factor, $A_{nanostructure}$, representing the contribution of additional-EASA due to nanostructuring of the substrate.

Redox-peak positions by CV - Nanostructured electrodes were tested using CV under the same experimental conditions as those applied to detect H_2O_2–25 mM. The acquired voltammograms are shown in Figure 18. A clearly detectable oxidation peak can be observed for Au–13.5 at 386 mV, which is lower than 589 mV and 790 mV found with MWCNTs–4.8 and for Bi_2O_3–100, respectively. Oxidation peak positions in Table 2 show a negative shift of 302 mV and 99 mV for GNPs, and MWCNTs, in respect to SPE, while a positive shift of 102 mV for Bi_2O_3 NPs can be observed. The peak positions for fully-irreversible systems in thin layer models were proposed by Hubbard. [161] Later, Streeter et al. [162] described that in the case of nanostructuring, semi-infinite planar diffusion is not applicable, and the peak positions should be described by a thin layer model. The following equation (where E_f is the formal electrode potential or Nernst potential and l is the thickness of the thin layer) defines the peak positions of such a system in CV:

$$E_p = E_f + \frac{RT}{\alpha F}\ln\left(\frac{\alpha F \upsilon}{RTlk_0}\right) \quad (22)$$

As l decreases, the amount of electroactive species trapped inside the thin layer is reduced, and thus, the layer depletion is faster. This means that redox peaks shift toward lower values. Carrara et al. [160] reported CV responses of some MWCNT-based electrodes not obeying this thin layer model (layering effect). For example, ferricyanide, and etoposide did not show any layering effect, and ifosfamide[11] opposed it when metabolized by CYP450-3A4. In this work it is demonstrated that Au–13.5 and MWCNTs–4.8 conform to the layering effect with an almost 300 mV and 100 mV negative shift of the oxidation peak, while Bi_2O_3–100 opposes it with a 100 mV positive shift. The same behavior was reported in the current literature. For instance, Yin et al. [163] and Yang et al. [164] reported an approximately 100 mV and 50 mV negative shift of the redox peak in H_2O_2 detection after applying GNPs. Moreover, Hu et al. [165] demonstrated that Au nanostructuring decreases the ascorbic acid (AA) redox peak (345 mV) while the peak of uric acid (UA) was not affected at all. Considering MWCNTs, a 100 mV negative shift of the H_2O_2 redox peak was observed in the work by Woo et al. [166] Also, Habibi and Pournaghi-Azar [167] reported 348 mV, 374 mV, and 450 mV negative shifts regarding the DA, AA, and UA redox peaks, respectively. To the best of our knowledge, less work has been done on the electrochemical behavior of Bi_2O_3 NPs than has been done on H_2O_2. Nevertheless, an approximately 100 mV positive shift was observed by Taufik et al. [168] when using Bi_2O_3 NPs in a DNA biosensor.

[11] Ifosfamide is a chemotherapeutic agent chemically related to the nitrogen mustards and a synthetic analogue of cyclophosphamide. It is active as an alkylating agent and an immunosuppressive agent.

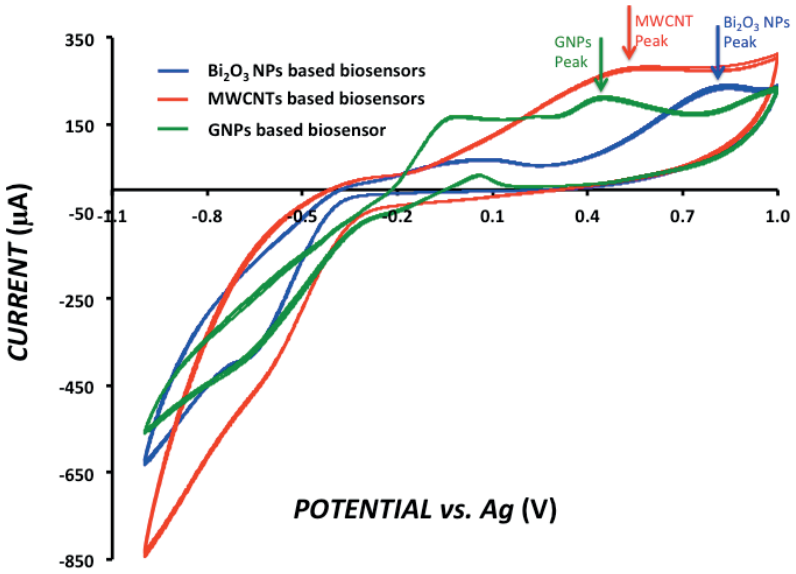

Figure 18. CV response of nanostructures for the detection of H_2O_2–25 mM: Bi_2O_3–100 (blue curve), MWCNTs–4.8 (red curve), Au–13.5 (green curve). Potential sweep: –1 and +1 V (versus Ag), scan rate: 100 mV s^{-1}.

Various shifts reported in the literature for a specific nanostructure are caused by the difference in the electrode preparation techniques (different working electrodes, size of nanoparticles, additional electroactive surface area, etc.). For example, a 500 mV negative shift of the H_2O_2 redox peak with MWCNTs nanostructuring was reported; [160] this value is five times higher than that reported here (100 mV). This is due to the difference in the amount of deposited nanostructures, since almost six times as many (30 µg) MWCNTs were used than in this study (4.8 µg).

The present study and the above mentioned examples prove that CV responses of sensors are influenced not only by the additional electroactive surface. In order fully to analyze and predict their electrochemical behavior a combination of elements, including bare electrodes, nanostructures, immobilized enzymes, and target molecules should be considered.

Electrochemical performance comparison by CA - Amperometric detection of electroactive targets was carried out to compare the various nanostructuring impacts on the electrochemical performance of biosensors. To this purpose, the above-mentioned biosensors Bi_2O_3–100, Au–13.5, and MWCNTs–4.8 were put to use to detect several concentrations of H_2O_2 (as explained in materials and method) with the applied potential fixed to 850 mV, 450 mV, and 620 mV, respectively. In addition, a bare SPE was examined with an applied potential of 750 mV, as a reference. H_2O_2 was injected in PBS (pH 7.4) by 100 µM steps in the range of 0–500 µM. The system gave a clear step response after each injection, with the amplitude directly related to the concentration of H_2O_2 (Figure 19).

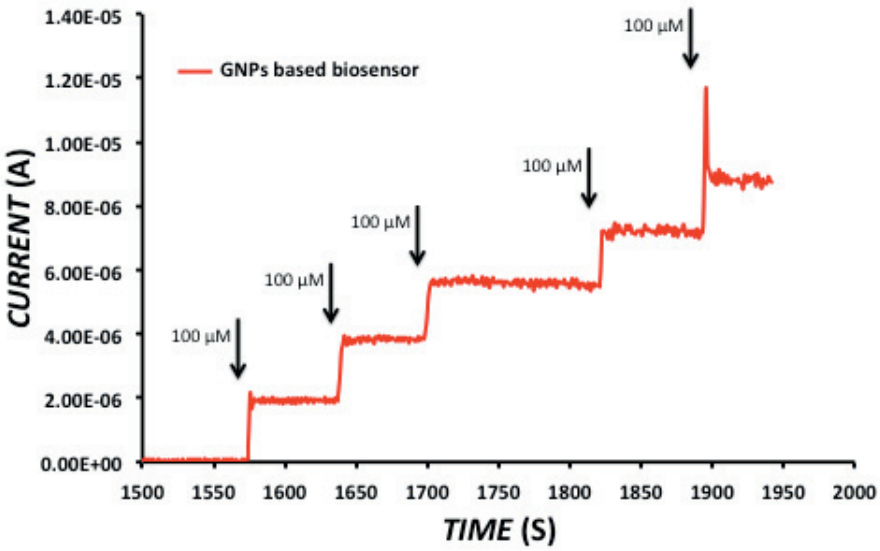

Figure 19. Typical CA response of Au-13.5 biosensors. Injections are performed some moments before the steps.

Steps related to each injection were averaged and converted to points in the calibration curve shown in Figure 20. Standard deviations were calculated for each step and they are presented in the figure as error bars. Blank measurements and system noise were averaged and removed from the data for higher precision. [154] The calibration curve of GNPs represented on Figure 20 shows a steeper slope than the other curves, as GNPs enhanced the sensitivity compared to the referential bare SPE, while Bi_2O_3 NPs and MWCNTs show lower improvement. Quantitative values of sensitivity and the LOD in Table 2 present more than a three-fold sensitivity improvement by nanostructured GNPs compared to the bare electrode. This is better than what is obtained by Bi_2O_3 NPs and nanostructured MWCNTs: an improvement of ~60%. This demonstrates the high impact of GNPs in facilitating the electron transfer with an electroactive target. As a result, GNPs were chosen as a candidate for the nanostructuring of biosensors for drug monitoring purposes. Although the enhancement achieved by using GNPs is already reported, there is little work on the impact of GNPs on H_2O_2 detection in comparison with two other known nanomaterials. For instance, Li et al. [169] have reported an increment in sensitivity by comparing calibration curves of their electrodes for H_2O_2 detection with and without GNPs.

The other two nanostructures show an electrochemical performance of the more or less same level. However, the EASA related to Bi_2O_3 NPs nanostructuring (1050 mm^2) were almost the maximum achievable with the drop-coating technique used in this study, but still much more EASA could be gained through depositing more MWCNTs on the surface (refer to 2.1.4 for more detail). Therefore, MWCNTs were chosen as the second type of nanostructures for drug monitoring, the final aim of this section being intended to provide a proper tool for enzymatic biosensors in terms of maximum electrochemical performance and good biomolecule immobilization.

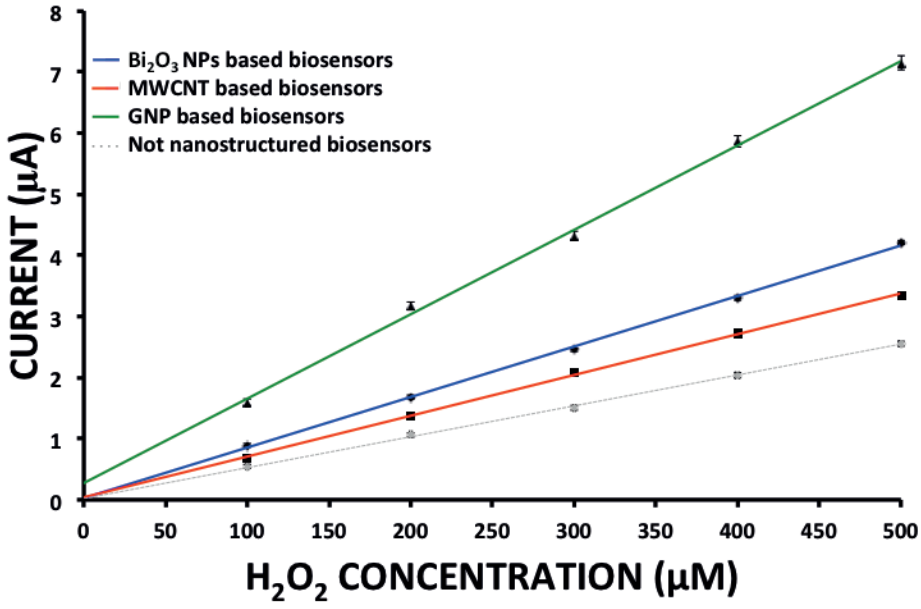

Figure 20. Calibration curves obtained by analyzing the CA response of the nanostructured electrodes and bare SPE. The slope of the lines identifies the sensitivity related to each nanostructure.

Electroactive compound detection by potentiometric/amperometric Bi_2O_3 NPs, GNPs, and MWCNT-based biosensors demonstrated different sensitivity, LODs and peak positions despite the fact that the electroactive area on their recognition interface was the same. These findings prove that there are also some other factors contributing to the electrochemical behavior of nanostructures. Physical properties of the surface (such as the level of porosity and defects), the layering effect, and size dependent properties such as quantum effects are some of these factors. The latter factor is more interesting since the electrodes functionalized with GNPs, with dimensions under the limit of 10 nm (quantum dots), exhibit the best performance. This demonstrates the qualitative effect of dimensions on the electrochemical performance. Further details will be presented in section 2.1.5.

Table 2. Electrochemical performance of nanostructured biosensors, with bare biosensor for purposes of comparison

	Bare SPE*	**MWCNT-4.8**	**Bi_2O_3-100**	**Au-13.5**
Sensitivity (nA µM^{-1} cm^{-2})	40 ± 5	54 ± 2	74 ± 12	129 ± 15
LOD (µM)	19.4 ± 6.8	8.4 ± 0.3	17.3 ± 7.2	19.7 ± 5.3
Peak positions (mV)	668 ± 7.9	457 ± 0.4	790 ± 1.4	386 ± 0.6
Additional EASA (mm^2)	0	1050	1050	1050

*W.E. surface area : 0.12 cm^2

The optimization of the chosen nano-biosensors (MWCNT and GNPs-based), in terms of scan rate and additional-EASA, are explained in detail in ensuing sections (2.1.3 and 2.1.4, respectively). The aim of these two sections is to improve the sensitivity and the limit of detection of GNP and MWCNT-based nano-biosensors to find out the best choice for quantifying the concentration of

etoposide, and to prepare the biosensor for the biomolecule immobilization that will be explained in Chapter 3.

2.1.3 Optimization of detection method for electroactive drugs

As a first optimization, CV as the detection method was optimized in terms of the scan rate of the applied-potential. Increasing the applied-potential scan rate in CV increases the measured current amplitude at an interface that is explained by the Randles-Sevcik equation (Equation 20). [73] It represents direct proportion between the current peak amplitude and the scan rate. Nevertheless, it does not continue forever, and at some point the current cannot keep up with the scan rate increments, therefore it reaches saturation (Figure 21).

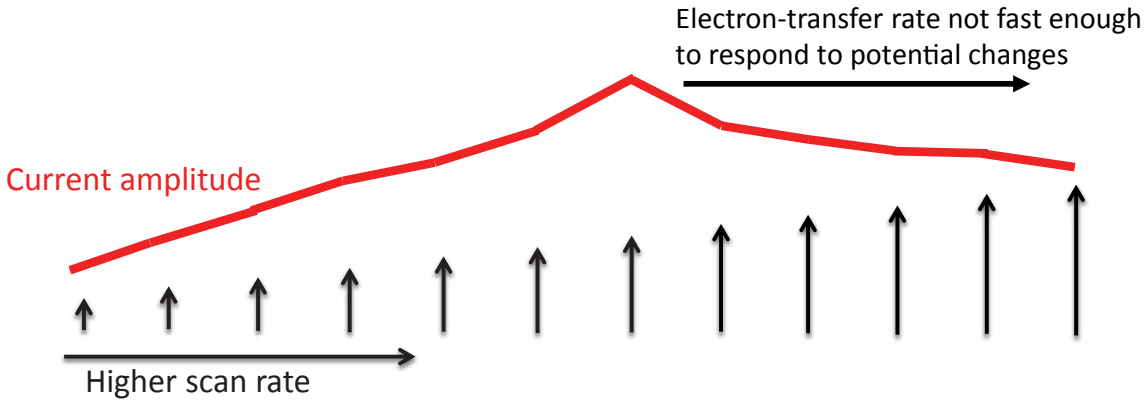

Figure 21. Qualitative relations between the scan rate of applied-potential and the current amplitude

This can be explained by the double-layer effect at the interface of liquid and the electrode. The ions in the solution create a double-layer phenomenon right in the vicinity of the interface. These layers need to be charged/discharged before any electron transfer similar to a capacitance in electrical circuits and, in fact, have been indicated in the equivalent circuits of the system electrical behaviour. Therefore, at some point charging and discharging of the double-layer capacitance at the interface cannot follow the potential scan rate. It looks like that rate of reaction is slow, compared to the scan rate. Therefore, the current is no more a function of the scan rate, and it reaches saturation.

Material and method

Biosensors were fabricated using commercial SPEs manufactured by Metrohm (DRP−110) as described in previous sections. Powder of MWCNTs (diameter: 10 nm; length: 1 to 2 µm; 90% purity), functionalized with COOH was purchased from DropSens (Spain), which was dispersed in chloroform at a concentration of 1 mg mL^{-1}, and was sonicated for 1 hour to achieve a homogeneous solution. Dispersion of hydrophilic GNPs (OD-1; 0.06 mg mL^{-1}), stabilized with Tannic acid, was purchased from Sigma-Aldrich.

SEM images of the surface nanostructured with MWCNTs (Figure 22-top) showed the quality of the sample used, as well as its surface coverage. Transmission electron microscopy (TEM) was

used to characterize the physical properties of the purchased sample. An selection of the TEM images of the sample is presented at the bottom of Figure 22, alongside the SEM image of the MWCNT sample after deposition (Figure 22-top). The TEM image clearly showed the spherical shape of the nanoparticles used with an average diameter of 5.22 ± 0.01 nm (Figure 22-bottom). The presented TEM image was analyzed by ImageJ software to find the average size.

PBS (100mM; pH-7.4) was procured from Sigma-Aldrich, dissolved in distilled water and stirred to obtain the homogeneous solution. It was used as a supporting electrolyte in experiments. Etoposide powder was purchased from Sigma-Aldrich and was dissolved in dimethyl sulfoxide (DMSO) at a concentration of 10 mM. TEM and SEM images presented in Figure 22 were taken using a Tecnai Osiris device and a MERLIN device, respectively. All image analyses have been performed utilizing ImageJ software. [156] Autolab potentiostat/galvanostat (PGSTAT128N) was used for CV under aerobic conditions.

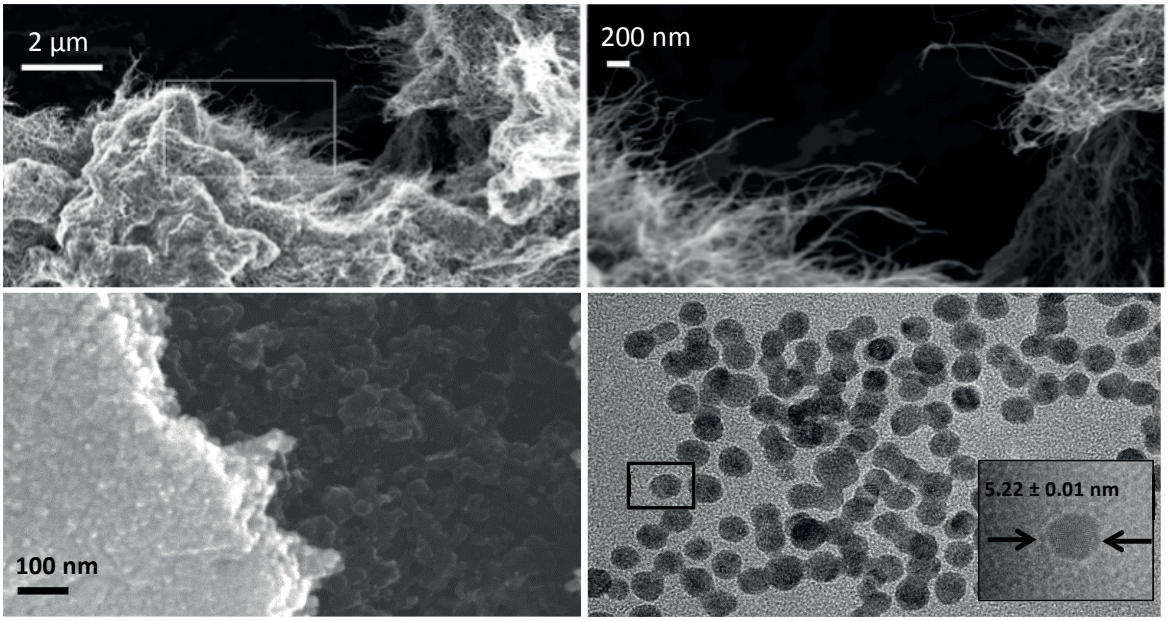

Figure 22. SEM image of MWCNTs deposited on W.E. of SPE. Top left: the surface of a working electrode, which is covered by MWCNTs. Top right: magnification of the area specified on the left figure showing MWCNTs with an average diameter of 10 nm. Down left: SEM image of GNPS deposited on W.E. of SPE. Down right: TEM image of hydrophilic sample of GNPs with average diameter of 5.22 ± 0.01 nm. Inset: one spherical GNP is pointed out.

The functionalization of the SPEs with nanostructures was carried out using a drop-casting technique for ease of action, while also minimizing the interferences. For instance, to prepare SPEs equipped with hydrophilic GNPs (GNP-SPEs), 290 µl of 0.06 mg mL^{-1} stock dispersion was dropped over the W.E. in steps of 10 µl to obtain an overall mass of 17.4 µg of GNPs. EASA have been calculated using SSA of each material, with the mass of deposited nanomaterials as explained in subsection “electro active surface area calculation” in section 2.1.2. As described before, EASA (in mm^2) has been used as the unit rather than mass (in µg) to provide reasonable comparison between electrodes equipped with different types of nanomaterials.

In order to perform the scan rate optimization, biosensors were nanostructured with constant and similar additional-EASA and were directed to detect a 70 µM solution of etoposide with various

potential scan rates (vs. Ag) in the range of 10 mV s^{-1} and 120 mV s^{-1}. At this step having the same EASA was not necessary, as the detection responses were not compared. Thus, nanostructured biosensors were functionalized with 30 µg of MWCNTs (6471 mm^2 of EASA) to produce MWCNTs-based biosensors (named MWCNT-SPE-6471), with 69.6 µg of GNPs (4314 mm^2 of EASA) to produce GNP-based biosensors (named GNP-SPE-4314). The schematic of the biosensor produced is illustrated in Figure 23.

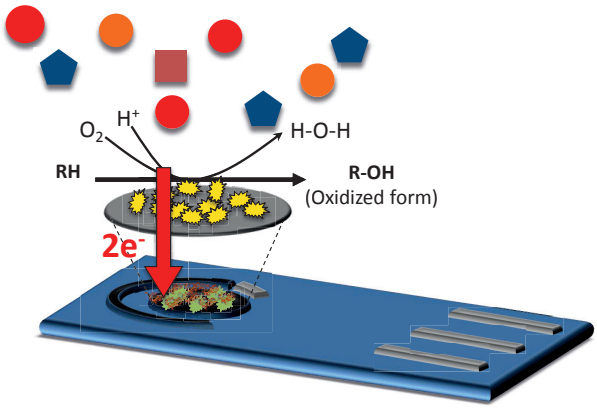

Figure 23. Schematic of a nanostructured SPE-based biosensor used in optimization experiments and for electroactive drug detection.

To obtain the voltammograms, the first 100 µl of etoposide 70 µM solution in PBS covered the active part of the cell. The biosensor was configured to swap the voltage between -1 and +1 for 10 cycles to achieve a stable result. Typical voltammograms recorded during the detection of a 70 µM etoposide solution by the MWCNT-based biosensor is presented in Figure 24. The right side of the figure demonstrates the polynomial baseline that is used in analysis of the data, the peak amplitude (with respect to the baseline) and the position, in both scan rate and EASA optimization experiments.

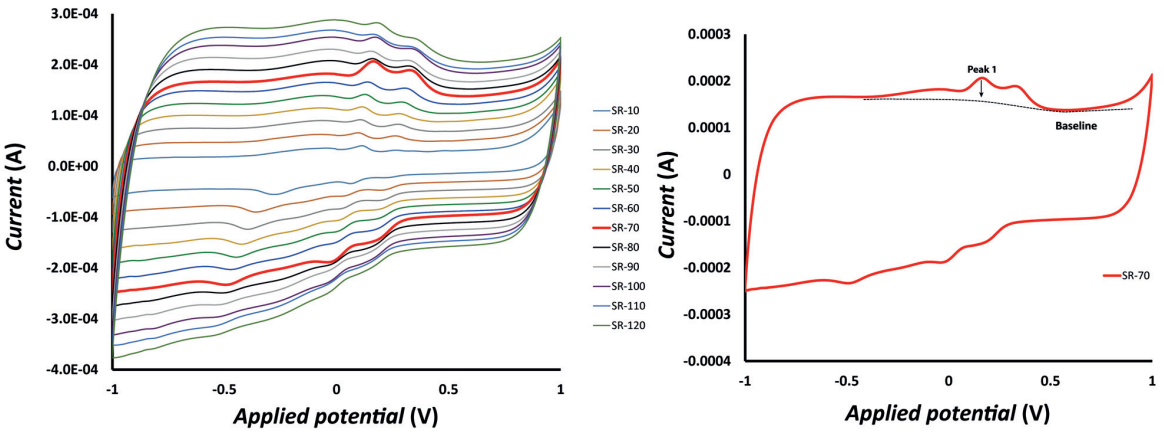

Figure 24. Left: recorded voltammograms of MWCNTs-based biosensor for different scan rates. 70 mV s^{-1} exhibits highest peak amplitude. Right: baseline type and the etoposide oxidation peak that were considered in scan rate and EASA optimizations.

Recorded voltammograms were analyzed by Nova software to find and measure etoposide oxidation peaks. The capacitive current of the voltammograms were removed and the baseline of oxida-

tion peaks were corrected to obtain only the Faradaic current peaks related to the oxidation of etoposide. These peak amplitudes were averaged out, and are presented in Figure 25. Error bars in the figure indicate the standard error related to triplicate measurement for each scan rate by three separated biosensors.

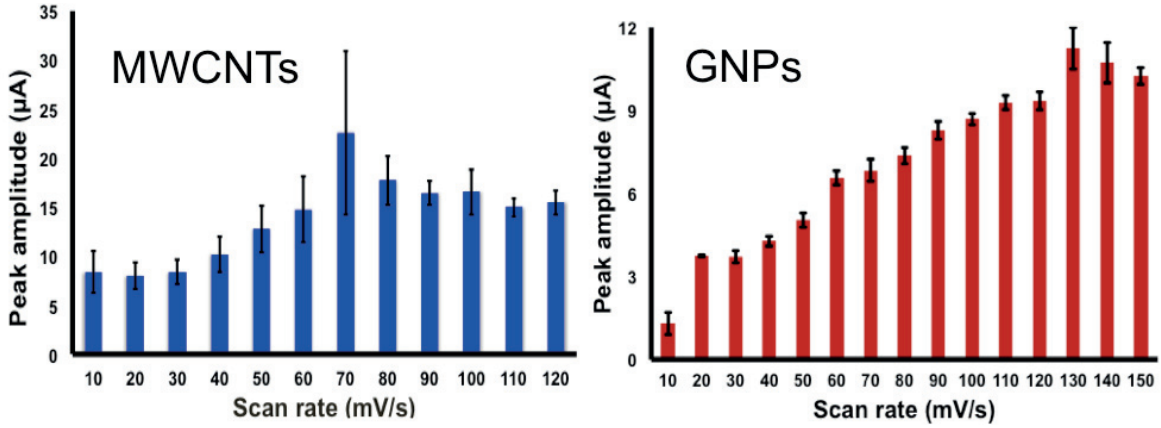

Figure 25. Left: optimum potential scan rate (vs. Ag) for MWCNTs-based nano-biosensors equal to 70 mV s^{-1}. Right: optimum potential scan rate (vs. Ag) for GNPs-based nano-biosensors equal to 130 mV s^{-1}.

Recorded responses represent the optimum scan rate for voltammetric experiments equal to 70 mV s^{-1} and 130 mV s^{-1} respectively for MWCNT- and GNP-based biosensors. In the detection of their electroactive target.

2.1.4 Optimization of nanostructuring in terms of added EASA on electrodes

The second optimization is in terms of additional-EASA by means of nanostructuring. Increasing the amount of nanostructures and, as a result, the added EASA on W.E. has been explained in detail in the section on Nanostructuring in 2.1.1. More EASA means a higher reaction rate and higher affinity for reaction at the interface, as well as a higher recorded current amplitude in an electrochemical detection. On the other hand, at some point the physical contact of analyte with lower layers of nanostructures is interrupted. This means that the current will not increase any more with more nanostructuring after that (Figure 26).

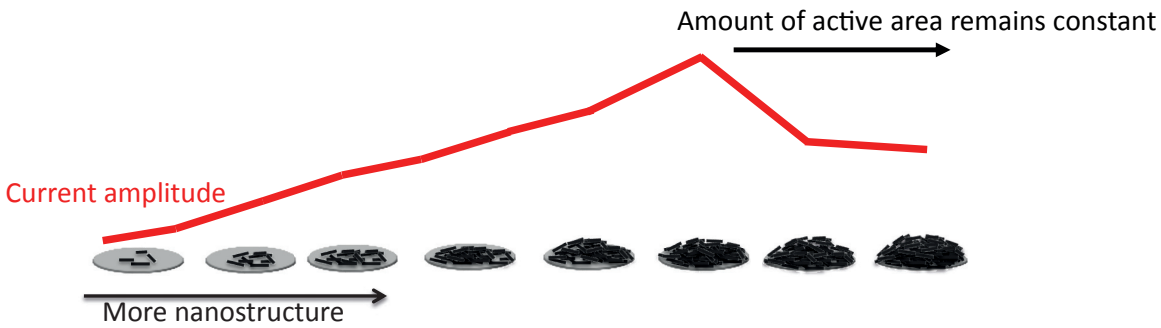

Figure 26. Qualitative relation between adding EASA over W.E. by nanostructuring and measured current amplitude

Nanostructuring optimization started with MWCNT based electrodes production. To do so, electrodes were functionalized with MWCNTs ranging from 0 to 40 µg with a step of 5 µg (bare SPE, MWCNT-SPE-1078, MWCNT-SPE-2157, …, MWCNT-SPE-8628). Next, the additional EASA for each electrode were calculated (2.1.2) and the opposite calculation was performed to find the mass of GNPs that was needed for deposition in order to acquire same additional-EASA. This procedure is summarized in Table 3. The GNP based biosensors were named as follows: bare SPE, GNP-SPE-1078, …, GNP-SPE-8628. For instance, 17.4 µg of GNPs were deposited over W.E. of an electrode to produce GNP-SPE-1078.

Table 3. Data obtained for amount of MWCNTs and GNPs in micro-grams to have the same EASA in mm^2

EASA	1078.5	2157	3235.5	4314	5392.5	6471	7549.5	8628
Amount of	5	10	15	20	25	30	35	40
Amount of GNPs	17.4	34.8	52.2	69.6	87.0	104.4	121.8	139.2

Nano-biosensors were then characterized with a voltammetric detection of 70 µM etoposide solution, with a scan rate fixed to 70 mV s^{-1} and 130 mV s^{-1} for MWCNTs and GNPs (refer to 2.1.3 or more detail), respectively. According to graphs presented in Figure 27, the maximum electrochemical performance for electroactive drug detection can be achieved utilizing MWCNT-based biosensors with 4314 mm^2 of EASA and a potential scan rate of 70 mV s^{-1}, and GNP based biosensors equipped with 6471 mm^2 of EASA and a scan rate of 130 mV s^{-1}.

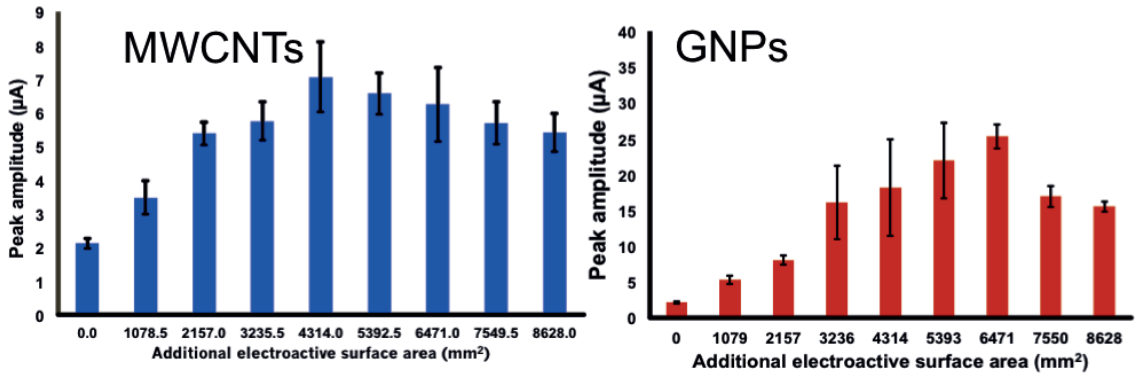

Figure 27. Etoposide averaged-oxidation peak amplitudes for nano-biosensors functionalized with different amounts of nanomaterials. Left: the maximum response observed for biosensors equipped with 20 µg of MWCNTs (4314 mm^2 of EASA). Right: the maximum response observed for biosensors equipped with 104 µg of GNPs (6471 mm^2 of EASA).

The next section deals with the relation between the NPs dimension and quantum phenomena and their impact on enhancing the electrochemical performance of nano-biosensors. It has already been reported that GNPs with decreasing diameter can provide electrochemical enhancements. For instance, in [24] it is explained that by decreasing the size of GNPs from 13 nm to 6 nm and then to 3.5 nm, the maximum current is increased to 66.2 µA, 73.8 µA, and 76.2 µA, respectively. However, this is the first time that this phenomenon has been observed and characterized experimentally on electroactive drug detection, to the best of our knowledge.

2.1.5 Impact of GNP size and rising quantum blockage

Advances in nanotechnology have helped emerging new materials and devices that have widely improved performances in electrochemical sensing. Electron transfer at the sensing surface has been largely improved by using gold nanoparticles. [170] Moreover, the nano-size scale of such electrochemical devices offers new phenomena, e.g., the non-enzymatic detection of glucose [97] or the memristor effect for ultrasensitive aptamers-based sensing of cancer markers. [171]

However, the Coulomb blockade has been never exploited for electrochemical sensing, although it promises an improved electron transfer due to the possibility of quantum confinement in a limited region of space, if quantum particles of sufficiently small size are integrated in the electrochemical sensing surface. The quantum phenomenon of the coulomb blockade, predicted by Likharev and Averin in 1986, [172] had initially been observed only at very low temperature (very low on the Kelvin scale) in point-contact junctions [173] and in metallic granules, [174] while it has been discovered at room temperature, first in metallic particles, [175] and then in semi-metallic ones, [176, 177] only in the 1990s - thanks to the nano-scale sizes of the structures used (a very few nm).

The aim of this section is to present electrochemical sensing enhancement based on Coulomb Blockade. The quantum device was fabricated by using SPE-based electrochemical sensors functionalized with gold nanoparticles of enough small lateral size [82] in order to allow for the quantum blockade phenomenon at room temperature. The device was realized in several versions by changing the size of particles and demonstrating that only the right sizes for single-electron trapping, as predicted by the theory of coulomb blockade, returned an improved device performance. The electrochemical performance of the quantum device is compared to the response of a MWCNT-based biosensor to demonstrate the superior performance of this new quantum-based electrochemical detection.

The proposed quantum device is tested with the detection of an anti-cancer electroactive drug, etoposide, to show its advantage as an electroactive-drug screening tool. Such a new kind of electrochemical quantum-device paves the way towards novel and improved diagnostics in personalized medicine, including but not limited to cancer therapy.

Material and method

Powder of MWCNTs with diameter of 10 nm; length of 1 to 2 μm; 90% purity, functionalized with COOH was purchased from DropSens (Spain), which was dispersed in chloroform to the concentration of 1 mg mL^{-1}, and was sonicated for 1 hour to achieve a homogeneous solution. Samples of GNPs coated with dodecanethiol, were provided by NanoPartz™ (USA) in 20 mg mL^{-1} solutions, as 9 separated dispersions of GNPs with diameters of 1.8 nm, 3 nm, 5 nm, 10 nm, 15 nm, 30 nm, 50 nm, 100 nm. Electrochemical sensing quantum devices were fabricated based on the same commercial SPEs as in the previous section, manufactured by Metrohm (DRP−110).

The functionalization of SPEs with nanostructures was carried out with a drop-casting technique, following a well-known protocol. [125] Electrodes were stored at ambient temperature after each

deposition for drying and for storage. EASA have been calculated using the specific surface area (SSA) of each material and the amount of mass used for electrode preparation following the sub-section "electro active surface area calculation" in section 2.1.2. As described before, EASA has been used as the unit, rather than mass, to provide a reasonable comparison between electrodes equipped with different types of nanomaterials. 6471 mm^2 of EASA was added over the working electrode by GNP nanostructuring according to the results obtained for the etoposide-detection optimization (please see 2.1.4 for more details).

GNPs with smaller sizes bring higher gain in terms of EASA, so to achieve the same amount of EASA (6471 mm^2) a small amount of them (in terms of mass) is sufficient. For instance, a SSA of 172.71 $m^2\ g^{-1}$ was calculated for 1.8 nm-GNPs, following the discussion in SSA calculation in sub-section 2.1.2, so 1.87 µl of its 20 mg mL^{-1} GNP dispersion was drop-cast on the surface to add the optimum EASA, equal to 6471 mm^2. The values related to other GNP samples are mentioned in Table 4.

Table 4. Data related to GNP nanostructuring to add 6471 mm^2 of EASA

GNPs size (nm)	SSA	Mass of deposition (µg)	Volume of deposition
1.8	172.71	34.47	1.87
3	103.63	62.44	3.12
5	62.18	104.07	5.2
10	31.09	208.14	10.41
15	20.72	312.31	15.61
30	10.36	624.61	31.23
50	6.22	1040.35	52.02
100	3.12	2074.04	103.70

A typical sample of GNPs with a diameter of 5 nm was analyzed to estimate the quality of the commercially provided sample. To this aim, SEM and TEM were used to characterize the sample and the acquired images, as represented in Figure 28-a (TEM image) and Figure 28-c (SEM image), were analyzed by ImageJ software.

This SEM image verified the complete surface coverage of the W.E. by the GNPs after nanostructuring. The analysis of TEM image by ImageJ software gave an average diameter of 4.5 ± 0.7 nm that proved the quality of the purchased samples. The size distribution of the GNP sample is shown in Figure 28-b. These particles present a coating that stabilise the particles and assure a precise size of the particle core. That coating is not visible under the SEM imaging due to the alkyl groups in the coating chain and, therefore, microscopy only returned the image of the metallic core of the particle. In addition, SEM images acquired on the different sizes of the used GNPs have confirmed the average size declared by the seller, as shown in Figure 28 for the case of the 5 nm particles.

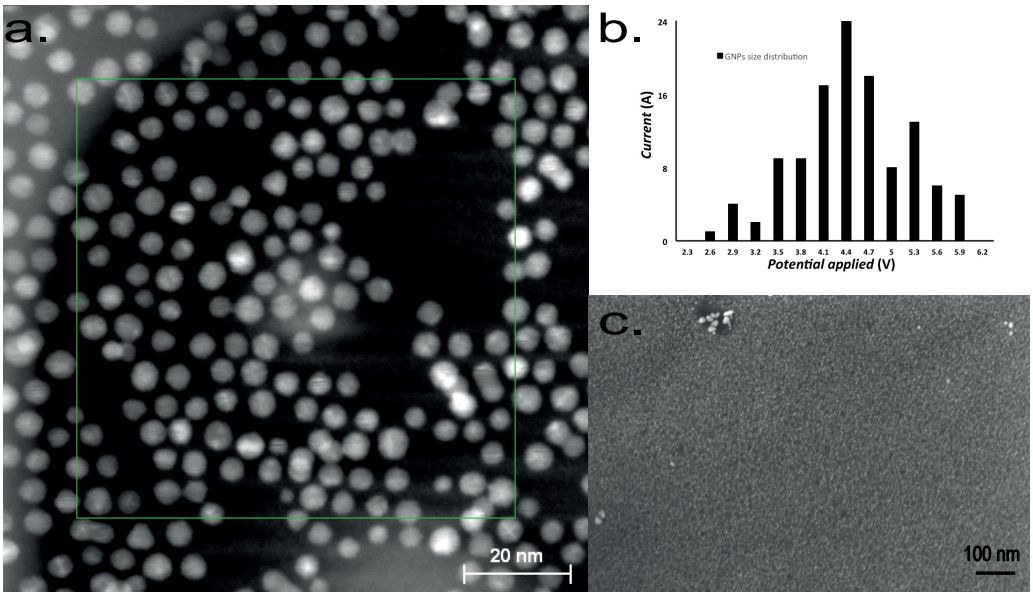

Figure 28. a) STEM image of the used nanoparticles. b) Size distribution of GNPs inside the green rectangle in the STEM image. c) STEM image of the nanostructured surface. An average diameter of 4.5 ± 0.7 nm was evaluated by ImageJ software analysis on STEM images of 5nm GNP samples.

If the metallic core of the particle is small enough to provide coulomb trapping at room temperature, then the particle core behaves as a quantum dot during the transfer of electrons from the chemical specimen to the electrode surface of the sensing device during the redox processes that allow the compound detection (Figure 29).

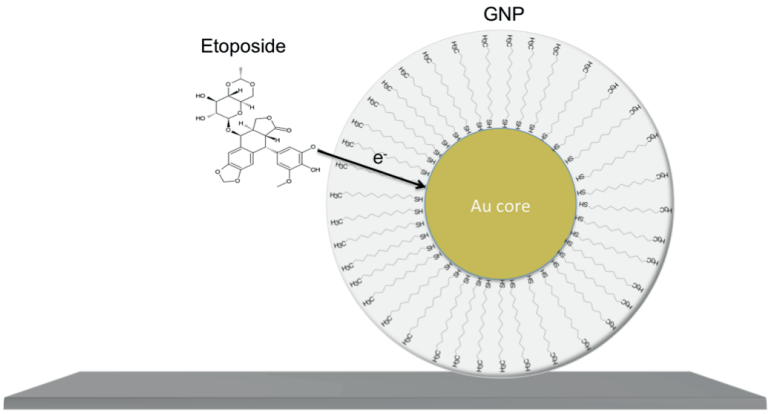

Figure 29. The gold nanoparticles stabilized by an organic coating behave as quantum dots when the Au core of the particles is small enough to allow Coulomb Blockade to occur at room temperature, and also the alkyl-tail behaves as a quantum barrier. In this case, the electron-transfer from the drug (etoposide) to the core of the particle happens through a hopping conductivity along the alkyl chains, while the particle metallic core provides the quantum hole that traps electrons.

In this case, the quantum dot behaviour of the particle provides a kind of “electrons reservoir” to the redox reactions and, therefore, it enhances the electron transfer from the detected drugs to the electrode surface. In other words, the electrochemical-sensing interface now presents now a series of quantum dots that support drugs detection by supplying a more efficient way to transfer

electrons from the drug compound to the working electrode of the sensor. To verify this, a detailed study on typical cyclic voltammograms has been performed.

An Autolab potentiostat/galvanostat (PGSTAT128N) was used to acquire Square Wave Voltammetry (SWV) measurements under aerobic conditions. To acquire the voltammograms, 100 µl of etoposide solution with concentration of 200 µM (PBS as background electrolyte) had covered the active part of the electrode, and voltage was swept between - 500 mV and 800 mV. Autolab device was configured to perform 2 cycles for SWV to achieve a stable result. The step potential, stair amplitude and frequency of SWV were set to 5 mV, 20 mV, and 10 Hz, respectively. Autolab NOVA software (Metrohm) was utilized to correct the baseline of the voltammograms to provide a better comparison between peak amplitudes. To this end, baselines were fitted with appropriate lines and subtracted from the data. [178] One example of the acquired voltammograms is shown in Figure 30, and two important peaks of etoposide, as well as the baseline used for subtracting the background signal, are pointed out in the figure.

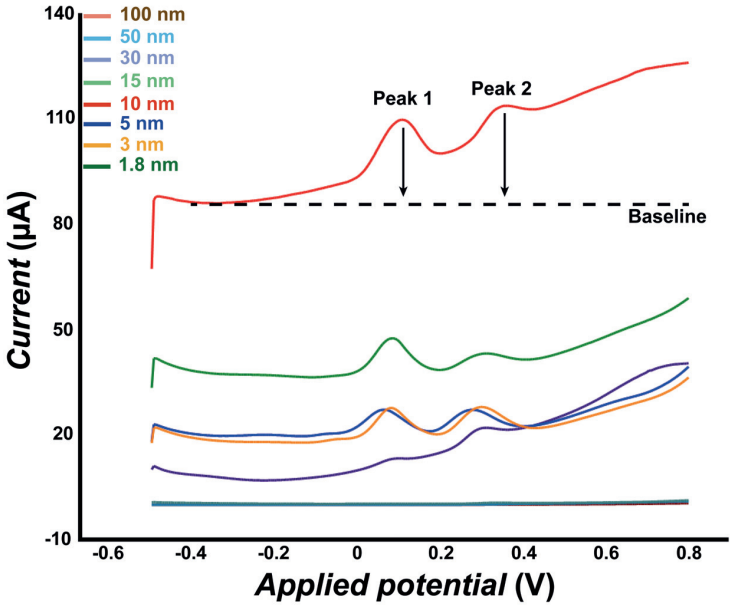

Figure 30. SWV responses of etoposide oxidized in contact with GNPs of various sizes. Two oxidation peaks of etoposide, and the baseline are pointed out on the response of 10 nm sample.

Square wave voltammograms (SW-voltammograms) acquired in the voltage region from -0.4 up to 0.8 volts , are represented for comparison in Figure 31. These were achieved by using quantum devices fabricated utilizing GNPs of different sizes after baseline correction. They clearly show two oxidation peaks of the etoposide as observed and published in the literature by a range of authors (Figure 30 and Figure 31). [179] As expected, the first oxidative peak (Peak 1) is observed at around +80 mV while a second peak (Peak2) is located at around +300 mV. The different amplitudes and relative positions of the peaks registered already show the different quantum efficiency provided by the different quantum dots, despite the fact that the voltammogram looks very similar for all the particles used. The SW-voltammograms in Figure 31 clearly show a different layering Effect (see Equation 22 in section 2.1.2) on the two oxidation-peaks of the Etoposide on our quantum sensing devices. In fact, the shift in potential of Peak 1 caused by using, for example, GNPs

with the size of 10 nm instead of 1.8 nm, is about 30 mV, while the same change of device results in a larger shift, about 50 mV, on Peak 2. Therefore, with the same nanostructured surface, the same redox species (but a different redox reaction) shows a slightly, but not negligible, difference in the layering effect. Even more interesting is the fact that the electron transfer efficiency is changing in a different manner for the two registered peaks, by changing the size of the nanoparticles. For example, Peak 1 and Peak 2 have a very similar amplitude in devices realized with particles of 3 or 5 nm (in between 6 and 8 μA), while they present very different Faradaic currents when registered with those devices fabricated with particles of 10 or 30 nm in size (Figure 31 and Figure 32).

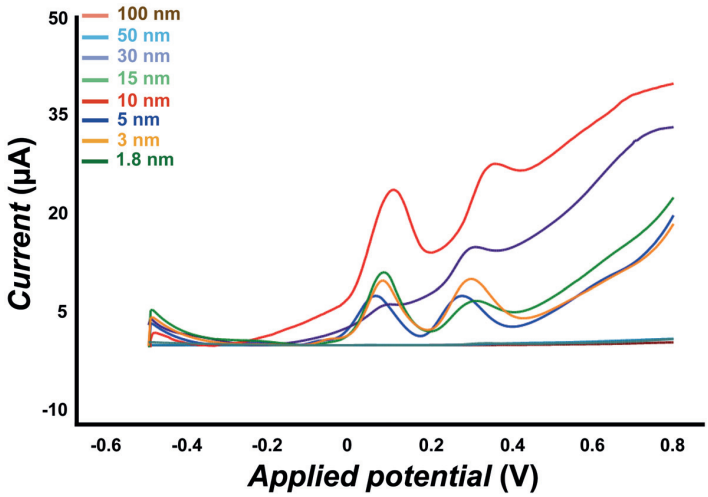

Figure 31. SWV responses recorded during the detection of etoposide by quantum devices, fabricated by using GNPs of different sizes indicated in the key.

Furthermore, it was stated in 2.1.2 that the current amplitude and sensitivity are directly proportional to the electroactive area of the recognition element of the biosensor available to the analyte. However, all the quantum devices in this experiment are created by adding a certain amount of nanomaterials in order to assure the very same EASA. Despite this effort, not only is the quantum efficiency in the electron transfer during the redox reactions different on the different quantum devices (e.g., different heights for the same peak in Figure 31), but the quantum efficiency in the electron transfer during the different redox reactions is different even on the same device (e.g., different Peak 1 and Peak 2 amplitudes related to one size of GNPs in Figure 31). Interestingly, a quite evident peak current, in the range of tens of μA, is registered on those devices fabricated with an average diameter below 15 nm, while the current due to redox reaction related to etoposide oxidation goes down for larger particles until it vanishes completely for a size larger than 50 nm (Figure 32). This happened in opposition to the predictions of equation 18 that exactly the same peak current would be observed, because the efficiency in the electron-transfer of the surface is be only related to the increase of the EASA. This phenomenon is clearly unrelated to sensitivity-surface area equations (Equation 21), and comes as a result of a different quantum efficiency occurring for the two redox reactions.

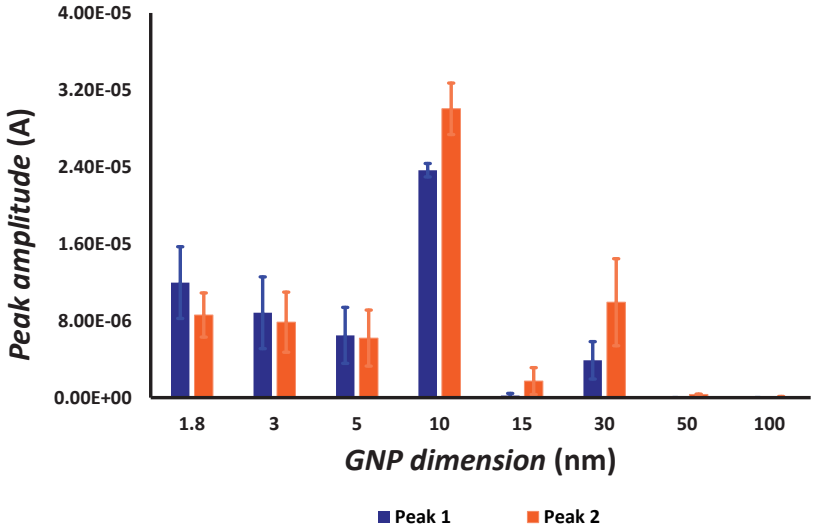

Figure 32. First (blue) and second (red) oxidation peaks of etoposide as measured with different quantum sensors obtained with nanoparticles of different sizes. Error bars indicate here the typical measurement of standard errors obtained in measurements series performed with several sensors fabricated with the same particle sizes.

Quantum efficiency is, indeed, related to coulomb blockade occurring in the particle core. In fact, the theory of quantum blockade explains that the electron trapping that occurs inside a quantum dot only when the trapping energy overcomes the thermal excitation (Equation 23) that usually brings the electrons out of the dot. [172] This happens alongside the quantization of energy levels inside the quantum dot., which means that electrons are trapped in these discrete levels of energy, waiting for a very small disturbance to move out, and this turns the quantum dot into a reservoir of electrons, waiting for the electroactive analyte.

$$\frac{e^2}{2C} > KT \tag{23}$$

This equation imposes values at around 10^{-18} F to the equivalent capacitance C of the system, in order to observe Coulomb Blockade phenomena at room temperature. Moreover, if Equation 23 is satisfied, then a clear appearance of steps should be observed along the Current/Voltage curves in specific conditions, as an echo of the electron-electron interaction inside the particle with respect to the current flux passing through the dot. This phenomenon has been observed and reported, under the name of Coulomb Staircase. It has been observed in Current/Voltage curves showing steps like a stair both at a few kelvin [173, 174] and at room temperature. [175, 176] Observations of the Coulomb Staircase have been registered, in 1997, in electrochemical experiments done with a pair of electrodes with a size of 2.5 and 3.2 nm, immersed in an electrochemical solution. [180] Very similar phenomena were observed in the current-voltage characteristics (voltammograms) of quantum devices in a few experiments (Figure 33) in this thesis. Observations of a Coulomb blockade need extremely controlled conditions, and the possibility of other factors in forming these observed stairs cannot be excluded. However, they can be considered as a signature of a Coulomb blockade when put alongside the electrochemical efficiency observed, taking into account that they happened for nanoparticles of just below 15 nm at similar conditions.

The theory of the Coulomb Blockade says these steps are equally distributed in voltage by following an equation that relates this voltage stepping to the equivalent capacitance of the quantum system: [172]

$$V_{step} = \frac{e}{C} \tag{24}$$

Considering the typical sizes of metallic cores of the proposed quantum dots and the typical length of the alkyl chains in their stabilizing coatings, their equivalent capacitance can be computed at the electrochemical interface as: [181]

$$C = A_{particle}\frac{\varepsilon\varepsilon_0}{r}\frac{r+d}{r} = 4\pi\varepsilon\varepsilon_0\frac{r}{d}(r+d) \tag{25}$$

(ε0 = 8.85×10-12 F m-1; ε = permittivity of dodecanethiol = η_{dt}^2 = 2.13, from η_{dt} = refractive index = 1.46 @ 20°C; r = radius of the Au core; d = length of the capped molecule), and we can conclude that the particles embedded in this electrochemical interface behave as quantum dots with an equivalent capacitance ranging from 0.3 up to 340 aF, which correspond to a voltage step from 500 mV down to 0.5 mV for the GNPs with sizes from 1.8 to 100 nm. The values of the equivalent capacitance correspond quite well with the possibility of observing the Coulomb Staircase at room temperature, [172] as well the step voltage-spacing observed in the experiments presented here (around 50 mV in Figure 33).

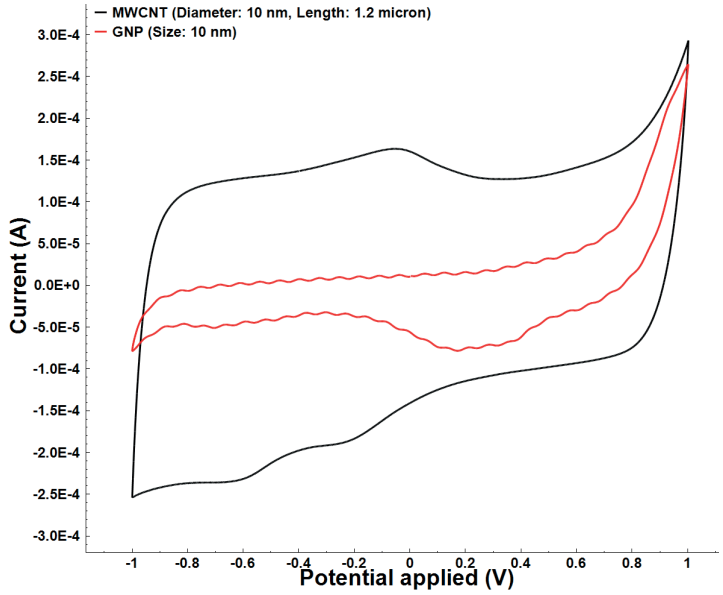

Figure 33. Coulomb Staircase observed in Cyclic Voltammograms. Particular cyclic voltammograms acquired on the quantum device and showing typical staircase due to coulomb trapping occurring in the nanoparticles when behaving as quantum dots (red curve). In contrast, cyclic voltammograms of a normal nanomaterial (MWCNTs) with no quantum blockage effect (black curve).

It has already been demonstrated that the appearance in the current/voltage curves of equally spaced-in-voltage oscillations, instead of steps, is also related to the Coulomb Blockade. [176, 177] Therefore, the current steps clearly observable in Figure 33 for potentials larger than 550 mV and

the oscillations registered at lower potentials are both related to the Coulomb Blockade. The Coulomb Blockade effect is clearly affecting the electrochemical detection in the proposed devices in this thesis, as well. In fact, Figure 32 clearly shows quite an efficient electron-transfer in redox reactions involving the detection of the etoposide for quantum devices built with particle sizes well below 15 nm, the efficiency is highly reduced in between 10 and 50 nm, and completely lost for particles larger than 50 nm. This is a strong signature that by moving towards 10 nm particles, the Coulomb Blockade affects the electron transfer with the target, and as a result, boosts the electrochemical performance of biosensors.

2.2 Drug detection using an optimized biosensor

Optimized MWCNT-based and GNP-based biosensors in terms of applied-potential scan rate (subsection 2.1.3), nanostructuring (subsection 2.1.4) and NPs size (subsection 2.1.5) are used to detect etoposide in order to compare their performance in terms of sensitivity and LOD. Three electrodes were produced for each nanomaterial using optimum additional EASA and tested by CV using optimum scan rate configuration. A concentration of target solution, etoposide (PBS as background solution), was increased from 0 (blank measurement) to 60 µM in steps of 10 µM, corresponding to the therapeutic range of etoposide. [182] Acquired voltammograms were analysed, as in the procedure for SW-voltammograms mentioned above (Figure 30) to measure the Faradaic peak amplitude related to oxidation of etoposide. The peak amplitude obtained for each concentration of etoposide was placed on a graph to form the calibration curve of the biosensor (Figure 34). LODs were calculated using Equation 7. Quantitative data of sensitivity and LODs, as well as the optimization configuration specific to each nano-biosensor, are indicated in Figure 34.

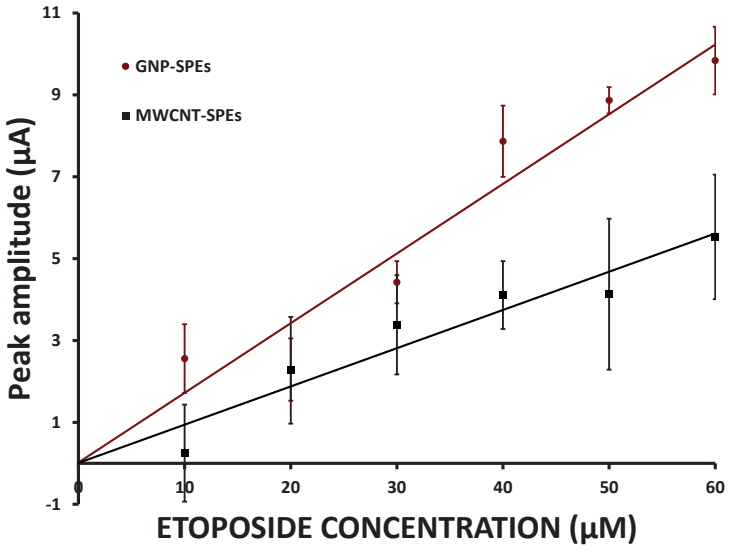

Figure 34. Calibration curves related to MWCNT-based biosensors and GNP-based biosensors. Nano-biosensors were prepared using 6471 and 4314 mm^2 of additional-EASA, respectively, and were tested with CV to detect etoposide with concentration varying in a range of 0 to 60 µM as is shown on the horizontal axis. Scan rates were set to 130 and 70 mV s^{-1}, respectively. Data points are shifted, to provide more clarity on sensitivity differences, by 2.95 µA and 1.2 µA for MWCNT and GNP curves, respectively.

Nano- Biosensors showed a sensitivity of 0.98 ± 0.41 μA μM^{-1} cm^{-2} and 1.43 ± 0.26 μA μM^{-1} cm^{-2}, and an LOD of 1.52 ± 0.89 μM and 1.29 ± 0.48 μM for MWCNT and GNP based electrodes (Table 5). Presented data shows better etoposide detection performance for GNP-based biosensors with a size of 10 nm (quantum devices) compared to MWCNT-based devices in terms of either sensitivity or LOD. Moreover, comparing the limit of detection achieved in this work with the therapeutic range of etoposide (from 10s of μM to 100 μM) [66, 182, 183] verifies that both nano-biosensors are qualified enough for etoposide detection. Low enough LOD, high sensitivity (even at very low concentrations) and simple functionalization make the proposed GNPs a suitable option for the detection of electroactive drugs such as etoposide. The enhanced electrochemical performance of GNP-based biosensors (10 nm in diameter) over MWCNT verions in the detection of etoposide cannot be explained without taking into account that both nanostructured biosensors were experimented at their optimum configurations. In fact, it can be inferred that the size of nanoparticles (that is under the 10 nm) and the proven quantum effect (refer to subsection 2.1.5) have taken a significant role in improving the electron transfer and, as a result, a better biosensing performance. Therefore, we have a direct proof of the key role of the Coulomb Blockade in the working principle of our sensing devices. Their efficiency in the electron transfer in redox reactions involving a drug is therefore demonstrated. This definitely opens the way for the realization of improved electrochemical quantum devices for applications in diagnostics for personalized medicine.

Table 5. Electrochemical performance related to each nano-biosensor and their specific optimization information

Biosensor type	**Optimized scan rate**	**Optimized nanostructuring mass**	**Sensitivity (μA μM^{-1} cm^{-2})**	**LOD (μM)**
MWCNTs-based nano-	70	20	0.98 ± 0.41	1.52 ± 0.89
GNPs-based nano-biosensors	130	104	1.43 ± 0.26	1.29 ± 0.48

In next section, a CYP450 enzyme will be immobilized on the platform as a recognition probe, to create an optimum enzymatic nano-biosensor for personalized prostate cancer chemotherapy.

2.3 Direct electroactivity of abiraterone

As mentioned above (section 1.3.1) abiraterone is a recent and widely used anti-PCa drug. The therapeutic range of Abiraterone in the circulatory system is up to 1 μM for a typical dose of 1000 mg injected per day. [39] Such a dose is the right one to maintain the concentration of abiraterone in this range and, therefore, to achieve a successful chemotherapy, since lower concentration cannot provide a medical benefit, while higher concentrations will cause severe side effects due to overdosing. Therefore, it is of high significance to monitor the concentration of abiraterone in the patient's body. However, it is not possible to provide a proper solution for such monitoring without having enough information about the electrochemistry of the target. The electrochemistry of abiraterone has not been explored, so in this thesis the direct interaction of abiraterone with an direct electrochemical biosensor functionalized with MWCNTs was investigated for the first time.

The electrochemical interaction of abiraterone with MWCNT without the involvement of any enzyme caused an increment of MWCNT peaks, as is demonstrated in Figure 35. This proved the direct electron transfer between the drug and the MWCNT. In these experiments, the response of MWCNTs-based direct electrochemical biosensors in a blank buffer and 30 µM abiraterone solution was recorded.

High drug concentration was used in this experiment to accelerate the fouling effect and make it more observable. Electrodes were then washed with distilled water, and remeasured in a blank buffer. This procedure was repeated several times. Results (Figure 35) showed a 15 µA increment of MWCNT peak after interaction with abiraterone compared to with the blank buffer. The recorded peak was reduced for only 5 µA compared to the peak obtained for a drug-spiked sample in the buffer after the washing, while the original blank measure was 20 µA smaller. This demonstrates that the drug remained attached to the surface of the MWCNTs after the electron exchange. Furthermore, a stable response of ~32 µA was observed at the second cycle of experiment. This shows that the surface was covered with drug residues that prevented the signal to be increased to the previous detected amount for drug detection, and even prevented the signal to be reduced after washing to the previous recorded amplitude in the blank buffer.

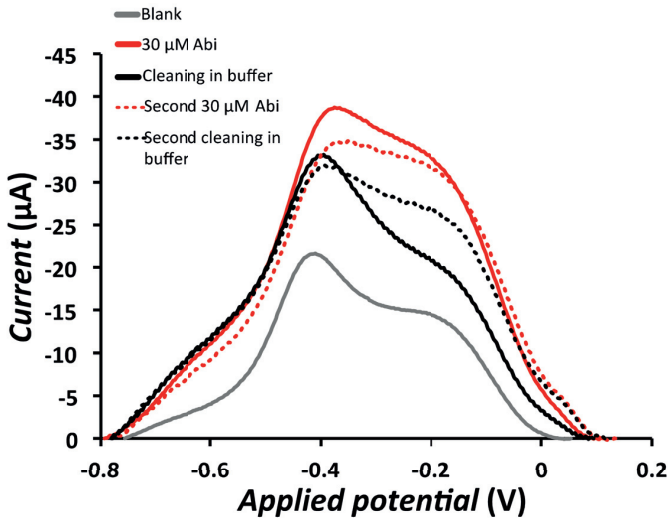

Figure 35. Direct electrochemical response of abiraterone and MWCNTs, with the electrode-fouling effect caused by attachment of drug molecules on the surface. Reprinted with permission from [184]

Electrochemical responses of nonenzymatic biosensors clearly demonstrated the direct electroactivity of abiraterone when reacting with MWCNT, as well as an electrode-fouling effect. The electroactivity of abiraterone provides the possibility for the direct detection of this compound using an EAD-biosensing approach; nevertheless the observed uptake of drug molecules over MWCNTs and the fouling effect caused is a significant interference for this application. In the next chapter, an enzymatic biosensor will be introduced that solves this issue and offers a proper solution for abiraterone monitoring in human serum.

2.4 Original contribution

As mentioned earlier in the chapter many works have been carried out and documented in the literature on characterizing the importance of nanostructuring in analyte detection. For instance, etoposide detection has already been demonstrated with a lower LOD than this study. [66, 185]

However, this part of thesis aimed to optimize the nano-biosensors for enzymatic drug detection, showing that the quality at this level of nano-biosensors for etoposide detection was satisfactory in terms of LOD.

Above all, the following results are reported for the first time, to the best of our knowledge, in this thesis:

First: The proper characterization of nanomaterial properties and their impact on electrochemical performance. This is the first work that compares the electrochemical enhancement obtained by means of nanostructuring while keeping an equal gain in terms of EASA.

To this purpose, similar EASA were added to active electrodes of commercial SPEs using MWCNTs, Bi2O3 NPs and GNPs, and they were set to sense H_2O_2 in a PBS buffer. The amount of nanomaterials was calculated, taking into account the SSA with the aim of equalizing the additional electro-active surface area. Chrono-amperometric investigations on MWCNTs and Bi_2O_3 NPs-based SPEs show closer behavior in terms of sensitivity, but better results for MWCNTs in redox potential and LOD. Electrodes nano-structured with GNPs show better sensing performance and less redox potential (oxidative peak position).

Second: Demonstrating the high performance of GNPs-based nano-biosensors for H_2O_2 detection compared to two other nanostructures. In this work, the sensitivity of electrodes to H_2O_2 increased more than three-fold compared to a bare carbon electrode. Interestingly, the size of the tested GNPs are 4 nm, under the limit of ~10 nm where the quantum effects are dominant.

Third: Optimization of nanostructured biosensors in terms of amount of deposited nanomaterial (or additional-EASA achieved by that) and potential scan rate was performed, followed by a comparison of the electroactive drug detection response of optimized nano-biosensors.

Optimized MWCNT and GNP based nano-biosensors were compared using etoposide as a target. GNP based electrodes exhibit better electrochemical improvements in terms of both sensitivity and limit of detection.

Fourth: The impact of GNP size on electron transfer was demonstrated, as was its relation to quantum phenomena such as the Coulomb Blockade, and its effect on drug detection.

A third step of optimization was performed on GNP based nano-biosensors in terms of NPs size. A series of SPE based biosensors was developed with various sizes of GNP, and the results clearly showed a change of performance according to the size of the GNPs, considering that the deposited EASA was always the same. An analysis of the data demonstrated the quantum blockage (coulomb staircase) and its effect on boosting the electron transfer performance of the electrodes.

Fifth: Direct electron transfer between abiraterone molecules and MWCNTs was recorded for the first time, and represented in Figure 35. An electrode-fouling phenomenon was also observed in this direct interaction of the drug and MWCNTs, mainly due to the adsorption of drug molecules on the surface. Therefore, abiraterone is classified as electroactive drug molecules with electrode-fouling characteristics.

A comparison of the performance of optimized electrodes for etoposide monitoring in buffer showed higher electrochemical performance of GNP based nano-biosensors for electroactive drug detection. It should be pointed out that one of the aims of this part of thesis was to optimize the performance of nano-biosensors, to make them ready for etoposide detection, so no effort has been made to push the performance of optimized nano-biosensors to their extreme at this level. Nevertheless, the LOD and sensitivity of both nanostructured biosensors fell sufficiently within the therapeutic range of etoposide, proving the suitability of detection methodology for electroactive drug detection.

Chapter 3 Enzymatic biosensors

A biosensor, as explained earlier (section 1.4), is a device to sense a bioevent and convert it to a signal that can be analyzed and observed. They consist of three main elements: Analyte, recognition element, and transducer. The analyte is the molecule under experiment, the recognition element is the biosensing surface that includes a bioprobe that is needed for the specific detection of an analyte, and can be a cell, a DNA, or an enzyme. Enzymes are catalysts of many biochemical reactions. CYP450 enzymes are a big and multigene family of proteins (Figure 36), which metabolizes over 1'000'000 different xenobiotic and endobiotic lipophilic substances. They are also involved in the regulation of a wide range of metabolic activities that are essential to homeostasis. Most of CYP450, as with other metabolizing enzymes, resides in the hepatocytes in the liver. The main activity of CYP450 enzymes is to transform lipophilic molecules into hydrophilic molecules for easy excretion through kidneys and urine. [186] CYP450 enzymes metabolize ~75% of all known pharmacological compounds. Over 7'700 individual CYP450 species have been identified, in which 57 have been identified in human hepatocytes, and only 15 metabolize drugs and other chemicals in human body. Among these 15, five are involved in ~95% of biotransformation reactions of drugs specifically. [23] Moreover, three CYP450 families of CYP450 1, 2 and 3 are mainly responsible for the biotransformation of drugs and toxins in the human body. [11]

This ability of CYP450 enzyme to detect a specific class of drugs brings a great advantage to the enzymatic biosensors proposed here. This makes it possible to detect multiple drugs simultaneously by using just one enzymatic biosensor. Therefore, they can be used for the monitoring of the cocktails of drugs that are normally administered for chemotherapy of malignant diseases like cancer. It is a significant property of enzymatic biosensors that they need to be employed with extreme caution, choosing a proper CYP450 enzyme specific to all the drugs in the cocktail, and proper strategies need to in place to identify different drug interactions. Multiple drug detection by enzymatic biosensors has been reported in the current literature. [50, 66] They have used the difference between the Faradaic peaks position, obtained due to the different interaction of targeted drugs with the same CYP450, to distinguish different drug peaks.

As mentioned briefly before (subsection 1.2.1), CYP450 has a specific nomenclature that represents the name of enzyme (cytochrome), a number to indicate its gene family (CYP450 1, CYP450 2, CYP450 3, etc.), a letter indicating the subfamily (i.e. P450 1A, P450 2A, P450 2B, P450 2C, etc.) and a number for the gene that identifies the isoforms. Isoforms are different proteins coded by an individual gene within the subfamily. Different isoforms of a family, such as CYP450 3A1 and CYP450 3A4, have 97% of their general sequence in common, to keep the same functionality and exhibit high conservation of the protein structure. [187]

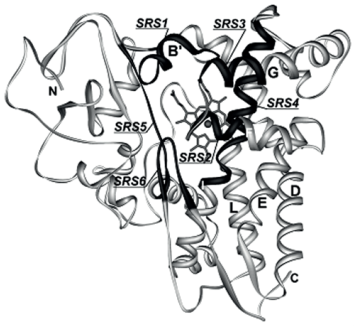

Figure 36. Ribbon representation (distal face) of cytochrome P450s fold. Substrate recognition sites (SRS), and α-Helixes are shown and labelled. Reprinted with permission from [188].

Figure 36 shows P450 enzymes common 3D-topology: A) a core is formed by a four α-helix bundle composed of three parallel helices labelled *D*, *L*, and *I* and one anti-parallel helix *E*. [188] B) *α* helices hold in place the heme-iron group that is the active site of the enzyme. C) The heme moiety, ferriprotoporphyrin-9, supports an iron atom, which is the core of the enzyme and is responsible for the substrate oxidation. [186, 189] This core, in most CYP450s, is a relatively rigid part of the protein structure, and because of the iron atom located in it the CYP450s are classified as metallo proteins. D) The active site of enzyme is a very flexible region of structure that facilitates the conformational changes needed for accommodating substrates of different sizes. [186] E) Several binding areas, or substrate recognition sites (SRS), inside their active site. [188] This multiple binding of sites, and as a result, the competitive binding of substrates cause some isoforms, including 3A4, 1A2, 2E1, 2D6, and 2C9, to exhibit atypical kinetics behavior due to conformational or chemical changes after binding a first substrate. [190, 191]

A substrate's oxidation and reduction reactions are catalyzed by CYP450 thanks to the capability of the metal atom in the heme group of CYP450 to receive or lose electrons easily. This is done according to the *NADPH* (nicotinamide adenine dinucleotidephosphate) or *NADH* (nicotinamide adenine dinucleotide) mono-oxygenation reaction, described by the equation:

$$RH + O_2 + NAD(P)H + H^+ \rightarrow ROH + H_2O + NAD(P)^+ \quad (26)$$

Where *RH* is a substrate that is hydroxylated through the insertion of one oxygen atom to form *ROH*, while the second atom of oxygen is reduced to water. The substrate is, thus, transformed in a hydrosoluble compound, easier to be excreted in urine. In summary, the electrocatalytic transformation of a substrate is coupled to the electrocatalytic reduction of oxygen. [192]

All CYP450s have associated redox partners, such as cytochrome *b5* and CYP450 oxidoreductase (POR), to supply them with electrons for their catalytic activities (Figure 37). POR is a flavoprotein complex with two flavins that act as electron carriers, *FAD* (flavin adenine dinucleotide) and *FMN* (flavin mononucleotide). *FAD* moiety in POR takes electrons from *NADPH* to facilitate its cellular transformation to $NADP^+$, and, thus, is reduced to $FADH_2$. Then $FADH_2$ reduces *FMN* to $FMNH_2$, which in turn passes its two electrons to the heme group of CYP450. [193] Cytochrome *b5* is an electron transport heme-protein the same as CYP450. This protein converts *NADH* to NAD^+ to make proton gradients that, finally, stimulate the flow of electrons. [186] The reaction indicated

by Equation 26, is a complex catalytic cycle, reported in Figure 37. In this cycle, *RH* is the CYP450 substrate, while *ROH* is its oxidized form. The first step is to bind the substrate (*RH*) to the CYP450 active site (no 2 in figure) followed by the first electron transfer, that causes the reduction of the ferric heme Fe^{3+} to Fe^{2+}, (no 3 in figure). The introduction of oxygen activates the heme group and induces the creation of an intermediate, the *oxy-CYP450* complex, (no 4 in figure). The second electron transfer, the rate limiting step of the cycle, generates a *peroxo-ferric* intermediate (no 5a in figure), and then its protonated form *hydroperoxo-ferric* intermediate (no 5b in figure). It follows the heterolysis of the *O–O* bond that causes the release of a water molecule and the creation of a highly active *Iron(IV)-oxo ferryl* intermediate (no. 6 in figure). This reactive intermediate drives the transformation of an oxygen atom into the substrate, leading to the formation and release of the *ROH* product (no 7 in figure), and, finally, the regeneration of the initial state of the heme group (no 1 in figure). [188] Three instable intermediates or abortive reactions are illustrated on the figure. Shunts lead to substrate dissociation and the production of intermediary products with the regeneration of the active site to the initial condition (no. 1 in figure).

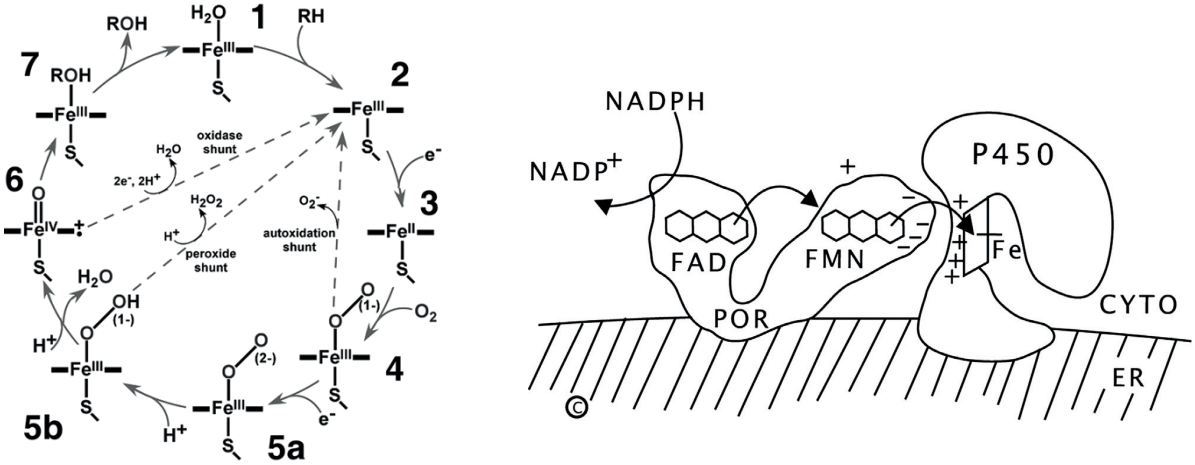

Figure 37. Left: CYP450 catalytic cycle, and shunt reactions in dash-lines. Right: msCYP450-POR system in endoplasmic reticulum. Adapted with permission from [188, 193].

In enzymatic SPE-based biosensors presented in this thesis, CYP450 enzymes are immobilized on the surface of the W.E. electrode as the recognition element, where two electrons needed for the completion of the monoxygenation reaction are supplied by the electrode. CV is used as a detection technique to activate/inactivate the redox center artificially, since it brings out the ability to scan the desired voltage-interval, when looking for specific Faradaic peaks of CYP450 oxidation/reduction.

In the absence of a substrate the immobilized enzyme gives peak-like signals resulting from the reversible transformation of its redox center. This current flow will continue until all the immobilized enzymes will have their redox center reduced, i.e. they are active. Therefore, a peak-shape Faradaic current is generated. Ideally, a potential sweep in the opposite direction will regenerate the active site, producing a symmetrical peak. In the presence of a CYP450 substrate, a catalysis reaction occurs, and the electrons from the active site are further transferred to the substrate, allowing the heme to accept new electrons from the electrode and producing a Faradaic contribution known as catalytic current. The recorded Faradaic current is associated only to the electron

transfer between the enzyme and the electrode - the analyte is not involved in it, since it is not an electroactive species. On the other side, oxygen that exists in the sample solution is also a substrate of the CYP450 enzyme, so the signal will increase in presence of CYP450 substrate, including drugs, even oxygen. [125] In aerobic CV (oxygen present in solution) experiments the current peak related to oxidation of CYP450 disappears. Adding the analyte to the sample increases the reduction peak while, in anaerobic conditions, oxidation and reduction peaks are both observable, but the reduction peak is smaller than in the aerobic condition. [125] The potential for the heme group at the core of the enzyme to go under oxidation/reduction reaction (peak positions) changes according to the detection system configuration. This includes the type of electrode's material, nanostructuring, enzyme immobilization and type of enzyme, since all these factors can significantly alter the electron transfer rate and affinity. [194, 195] Therefore, it is very important to make a careful study, and identify the redox peaks related to CYP450 catalytic activity in interaction with every specific sensing surface, as well as every specific drug that might be the enzyme's substrate.

In humans, only 5 CYP450 isoforms are responsible for the metabolisms of 95% of all known pharmacological compounds. [22, 23] This makes the CYPs promising candidates for the construction of biosensors for TDM. In principle, a sensor bearing the 5 cytochromes altogether can be used to follow the drug response of individuals in almost every kind of pharmacological treatment.

CYP-based biosensors have already been developed for a vast range of drugs [196] and they can also be employed to measure drug metabolism reactions that are extremely valuable for the identification of drug-drug interactions in drug development. Recent review papers [196, 197] report CYP450 biosensors based on many different techniques of protein immobilization, but also on several enzyme preparations: purified CYP450, recombinant CYP450 or microsome systems.

3.1 Background of CYP450 and enzymatic biosensors in drug detection

Bacterial CYP450 has been used for biosensing applications in a solution or on bare electrodes since the mid-1990s, including CYP450-based biosensors for the detection of drugs. [194] The very first attempts at developing these enzymatic biosensors as a reliable and more portable system were to employ amperometry techniques alongside electroactive mediators to eliminate the need of *NADH* and *NADPH* cofactors and their necessary regeneration steps. *Cobalt (III)* sepulchrate trichloride was used as a mediator for the electrocatalytical reduction of proteins containing different CYP450s and *NADPH-CYP450* reductase to catalyze the hydroxylation of steroids and the N-demethylation of drugs. [198] Further, mediators such as flavin mononucleotide, flavin-adenine dinucleotide or riblofavins [199, 200] were covalently bound to cytochrome CYP450 2B4 and 1A2 cross-linked onto a screen-printed rhodium graphite electrode for the direct amperometric measurement of cholesterol or aminopyrine. However, these redox mediators, used in conjunction with redox enzymes, raised other problems like complexity, and low specificity due to stimulating less interesting interfering reactions alongside the main reaction between the enzyme and the electrode.

More advanced enzymatic biosensors offered mediatorless electron transfer from electrode directly to the active site of the enzyme. These biosensors usually showed better selectivity, because they are able to operate in a potential range closer to the redox potential of the enzyme, becoming less exposed to reactions with interfering species coexisting in samples. In this approach, the electrode is used as electron source for the CYP450 cathodic reduction that is coupled with the analyte transformation. The generation of cathodic current and its measurement is therefore the direct indicator of CYP450-dependent analyte transformation. This means that in this mediatorless approach, without the existence of electron donors like *NADPH* or *NADH*, it is very important to enhance the electron transfer to very high extents in order to facilitate the redox reaction at the heme group, considering that the heme group is deeply ensconced in the heart of the CYP450 structure. Moreover, immobilization of the enzyme on the sensing interface must maintain the natural form of the enzyme and, as a result, its catalytic activity. To this purpose, the orientation of immobilized enzymes on the surface needs to be considered in order to have proper electron movement and active sites available for drug binding.

Recently published reviews [196, 197] describe the progress made in the last 20 years on the strategies for P450 immobilization on electrode surfaces, for their successful biotechnological applications and commercial exploitation. The main progress has been made possible through a combination of both enzyme and electrode engineering methods.

Recognition element: Many efforts have been made to improve the immobilization of enzymes on the sensing surface as recognition probes, and to prepare microsomal or recombinant enzymes with optimized configurations. As has been explained in detail in recent reviews [194, 196, 197, 201] the most common Immobilization techniques include using biomembranes or vesicles, encapsulating in polymers (using polypyrrole polymer, agarose, chitosan and sol-gels), Layer-by-Layer (LBL) or Langmuir-Blodgett (LB) films[12], Covalent bonding on self-assembled monolayers (SAMs), nanostructuring (electrostatic attractions, hydrophobic attractions). A recent work has proven that a hydrophobic surface can improve the immobilization of microsomal CYP450s (msCYP450s) thanks to the abundance of hydrophobic regions on the surface of CYP450, and the lipids that compose the microsome. [66, 202]

An alternative approach is to work on the enzyme structure itself to improve its functionalities. An interesting approach, described as Molecular Lego [197], is based on the construction of recombinant enzymes using domains taken from different proteins that own improved functionalities. Examples of domains are special amino acids anchoring the protein to the plasmatic membrane, amino acids responsible for the interaction with other proteins, and more efficient reductase domains. [203] This protein-engineering method promotes not only a correct covalent-oriented immobilization, but also the modulation of the catalytic performance of CYP450s. Alternatively, it is possible to include the natural redox partners with the P450 in vesicular systems, called microsomes or microsomal systems (msCYP450) containing CYP450 and POR. A microsome is obtained from the fragmentation of the endoplasmic reticulum of the proteins (P450, POR, cytochrome b5),

[12] Multiple layers of oppositely charged polyelectrolytes were adsorbed as a multi-layer film via electrostatic attraction.

and its reconstruction in vesicles that can be isolated by centrifugation. These protein/membrane systems are used by pharmaceutical companies in assays for drug research due to their low production costs with respect to recombinant CYP450s. Microsomes provide a natural environment for both CYP450s and their natural redox partners. As presented recently in a study, [204] immobilized msCYP450s on a polycation-coated electrode facilitated the direct electron transfer according to the natural electron transfer path from electrode to POR and then the to active site of CYP450. As indicated above, the improvement in immobilization of msCYP450s by hydrophobic forces is demonstrated, and the catalysis of a substrate was successfully detected, [66, 202] proving that microsomes offer a better environment for the enzyme, as the presence of POR improves the efficiency of the enzyme.

Baj-Rossi, C., et al. have conducted a deep study on immobilization of msCYP450 on MWCNTs using LBL technique, [66] where they demonstrated the hydrophobic residues on the surface of enzymes formed by N-terminal residues, [205] and also by the C-terminal end of an F-G loop. [206] They have proven theoretically and experimentally the success of immobilization of one protein layer on the surface of CNTs with an average size of 3 to 6 nm that corresponds to the thickness of the CYP450 enzyme. Later, in other work [207] they have identified the reduction peaks related to the interaction of their immobilized enzyme and the surface. Furthermore, they have employed the system to detect a range of drugs such as cyclophosphamide[13], ftorafur[14], ifosfamide and naproxen[15] using proper CYP450 isoform (Table 6). They have also studied the stability of microsomal CYP450 1A2 enzyme in continuous monitoring. [208] To do so, an enzyme was immobilized on MWCNTs by drop-coating, and was incubated in 100 mM PBS (pH 7.4) for 36 h. Cyclic voltammograms were continuously acquired every 90 min, to reduce the scans applied to CYP and saving its catalytic activity. Cyclic voltammograms were recorded in aerobic conditions and in the absence of any substrate. The peak showed good stability for the first 16 h, and then started to decrease gradually. It reached about 70% of its initial amplitude after 22 h, and about 20% after 36 h.

The storage stability of the CYP450 enzymatic biosensors has been extended up to 3 weeks without attenuation of catalytic activity using aqueous silicate (Ludox solution) [209] and agarose gel. [210]

Nanointerface: The impact of nanostructuring to the enhancement of electron transfer and, thus, its vital role in developing nano-biosensors was explained in detail in Chapter 2. The advances and efforts made on preparing the Nanointerface between the electrode and the target (drug or stabilized probe) were also pointed out. In addition to that, nanostructuring offers other advantages in enzymatic biosensing. They prevent the formation of an insulating layer of proteins on the surface

[13] Used in chemotherapy of lymphoma and leukaemia as the precursor of an alkylating nitrogen mustard antineoplastic and immunosuppressive agent that must be activated in the liver to form the active aldophosphamide.

[14] It is a chemotherapeutic fluorouracil prodrug used in the treatment of cancers, normally administered in combination with other drugs: tegafur/uracil and tegafur/gimeracil/oteracil. When metabolised, it becomes 5-fluorouracil.

[15] An anti-inflammatory agent with analgesic and antipyretic properties. Both the acid and its sodium salt are used in the treatment of rheumatoid arthritis and other rheumatic or musculoskeletal disorders, dysmenorrhea, and acute gout.

that suppresses the electron transfer, due to the adsorptive denaturation of proteins onto bare metal electrodes. [211] Electrochemical measurements have also been carried out with CYP450s immobilized on bare electrodes, showing poor electron transfer with the target in the system. [194, 212]

Improving the stabilization of enzymes without loss of their initial catalytic activity is of primary importance for the development of enzymatic biosensors. Targeting the binding properties of nanomaterials for the immobilization of enzymes provide the means for the development of a more reliable analytical biosensor in terms of the accuracy of measurements, the sensor-to-sensor reproducibility and the shelf and operational lifetimes. The stabilization of enzymes using certain additives such as electrolytes, polyelectrolytes, polyols has proven to be a very efficient method in the preparation of stable biosensors. At the same time, the immobilization of enzymes by either entrapment into inorganic, organic or polymeric matrices, or by covalent bonding on solid supports, has also been very effective. The primary purpose of all these immobilization methods is to decrease the tendency of the enzyme to unfold, by increasing its rigidity. For instance, porous carbon is an activated carbon that consists of mesopores and has been proven to be an excellent immobilization matrix for the stabilization of enzymes. [213] Recently, glassy carbon electrodes were nanostructured with graphene, gold nanorod and polythionine, on which DNA, specific for the human papillomavirus, was immobilized as a recognition probe. [214] An amperometric acrylamide biosensor with remarkable sensitivity and selectivity was fabricated by immobilization of Hb onto a nanocomposite of cMWCNT and Fe_2O_4 nanoparticles (NPs), electrodeposited onto gold electrode through a polymer chitosan film. [215] The sensor presented a quick response, wider linear range, lower limit of detection (0.02 nM), good reproducibility, and long stability. Recently, an immunosensor was reported for cancer detection utilizing poly (diallyldimethylammonium chloride) (PDDA)-functionalized CNTs for the assembly of HRP and concanavalin A (ConA) on the gold electrode. Utilizing the biospecific interaction between HRP and ConA, PDDA modified CNTs form a complex of CNTs/PDDA/HRP/ConA which, later on, combined with Ab labelled HRP and form a sandwich. The immunosensor exhibits a good linear range from 0.05–5 ng/mL to 5–200 ng/mL and a detection limit of 0.018 ng/mL. [216] A fresh glucose biosensor was fabricated using free CNTs and an enzymatic electrode immobilizing glucose oxidase (GOx), GOx coating and GOx precipitate coating. This sensor showed a remarkable improvement in sensing, stability and electron transfer. [217]

3.2 Enzymatic biosensor development

In this section, an enzymatic biosensor will be proposed and characterized that was developed and successfully used for abiraterone detection in a buffer and in human serum. The biosensor was produced based on electrochemical screen-printed electrodes (SPE) functionalized with CYP450 enzyme. CYP450 enzymatic biosensors have been very attractive for developing POC drug monitoring systems, thanks to their simplicity, low cost and feasibility for miniaturization. However, despite the body of related research available, there is no commercially available device based on this system, to the best of our knowledge; mainly because of the difficulties to reach the sub-micromolar limit of detection needed for the drug monitoring of malignant diseases, such as

cancer. In this work, an optimized enzymatic SPE based biosensor is then presented and successfully tested to detect abiraterone in human samples below the micro-molar level.

The enzymatic biosensors developed for this thesis are produced based on commercially available SPEs (Metrohm; DRP-110) functionalized with MWCNTs (DropSens; diameter: 10 nm; length: 1 to 2 µm; 5% COOH activation) to enhance the recorded signal, and biofunctionalized with cytochrome P450 3A4 enzyme (Sigma-Aldrich; Microsomal; stored at -80˚C; CYP3A4) as recognition part (cSPE/MWCNTs/CYP3A4 biosensor). The SPEs include a carbon working electrode (W.E.; area: 0.12 cm2), a carbon counter electrode and a silver reference electrode. MWCNTs were dispersed in chloroform to the concentration of 1 mg mL^{-1}, and were sonicated for 1 hour to achieve a stable homogeneous solution.

Optimization of this kind of biosensor for drug detection in terms of scan rate and additional-EASA has been already mentioned at subsections 2.1.3 and 2.1.4, respectively. Nanofunctionalization of SPEs with MWCNTs was carried out by a drop-casting technique to enhance the electroactive surface area by 4314 mm^2 following subsection 2.1.4. In the drop-casting procedure 20 µL of MWCNT dispersion (in steps of 4 µL) were dropped over the working electrode by pipette and allowed to dry after each step. Nanostructured SPEs were then stored at ambient temperature. The final electrode was stable and robust, as MWCNTs were attached over the W.E. by Van der Waals attachment and hydrophobic interactions. To form the biosensing surface, nanostructure electrodes were coated by 9 µl of CYP3A4 enzymes and incubated at +4˚C overnight to immobilize the enzyme molecules on the surface through physical adsorption and hydrophobic attractions. Finally, electrodes were washed with distilled water to remove any loosely bound proteins, and stored at +4˚C for further use. Optimized nanostructuring enhances the performance of the biosensor in terms of sensitivity and the limit of detection. MWCNTs immobilize CYP3A4 molecules by physical adsorption due to attraction between the hydrophobic domains. MWCNTs also help to stabilize enzyme molecules and maintain their shape and catalytic activity by forming a 3D porous structure over the surface and a large effective surface area for CYP450 adsorption.

Electrochemical detection was performed on spiked human serum (Sigma-Aldrich; used as received) and spiked PBS samples to record the biosensor response to a varied range of drug concentration. To do so, abiraterone powder (Medchemtronica, Stockholm, Sweden) was dissolved in dimethyl sulfoxide, initially at a concentration of 10 mM, to be used as a stock solution.

To acquire the biosensor CV responses to abiraterone in PBS buffer solutions, bioelectrodes were immersed in a beaker containing 10 ml of buffer, and gently stirred. This stirring will help to maintain the redox environment, and assures that the observed response is due to a drug-enzyme reaction. For different concentrations of drugs, an adequate amount of abiraterone stock solution (10 mM in DMSO buffer) was added to the beaker solution. In case of in-serum abiraterone detection, abiraterone was added adequately to the samples of human serum to the final concentrations of 250 nM to 3 µM, and the W.E. of bioelectrodes were covered with 100 µL of spiked serum. An Autolab potentiostats/galvanostats (PGSTAT128N, Metrohm, Netherlands) was used for CV experiments under aerobic conditions. Optimization of CV in terms of the best scan rate versus Ag and to achieve the highest sensitivity for drug detection is explained in detail in subchapter 2.1. To follow

that, the scan rate was fixed to 70 mV s^{-1} (versus Ag) and the potential was scanned between -0.8 V and +0.6 V. In order to obtain a stable response for all the tested electrodes, the process was repeated 10 times. Acquired voltammograms were analyzed with the Nova Software (Metrohm) for baseline correction and to remove the faradaic current from the capacitive background. Reduction peaks were considered for investigation, having performed the acquisitions in the presence of oxygen. For data interpretation, a suitable baseline was set for the faradaic current of the reduction peaks. A sample voltammogram obtained in this work, with the corrected baseline, is illustrated in Figure 38.

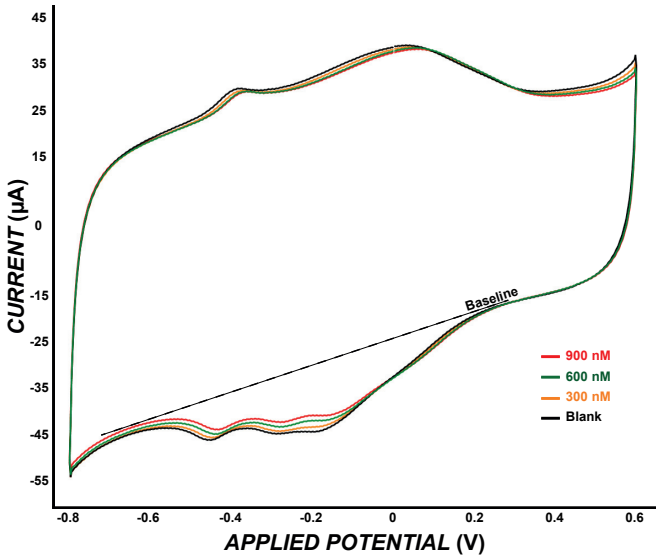

Figure 38. A typical voltammogram obtained for the enzymatic monitoring of abiraterone. Inset shows the acquired faradaic peaks after baseline correction and the capacitive current removal. Reprint with permission from [184].

3.3 Abiraterone electrochemistry

The unexplored electrochemical behaviour of abiraterone in interaction with the cytochrome P450 3A4 (CYP3A4) enzyme is investigated in this section. The direct electroactive reduction of abiraterone in interaction with MWCNTs was explained in section 2.3, where an electrode fouling effect related to abiraterone was registered as well. Taking advantage of an immobilized enzyme over the optimized biosensors of the previous section not only provides a solution that can be used for drugs that need an enzyme, but also solves the problem of electrode fouling for abiraterone detection, as it prevents the direct interaction of abiraterone and nanomaterials on the surface.

The immobilization of the CYP450 enzyme over MWCNTs, using the same protocol of this thesis, has been already investigated by Baj-Rossi et al. [66] They have used Monte Carlo simulation, and also SEM to propose and prove their concept that this protocol covers all the available surface of MWCNTs with one layer of protein (10 ± 4 nm).

Electrochemical analysis started with the identification of different peaks detected on the voltammograms. Several different biosensors were fabricated by changing the nanostructuring and enzyme in the biofunctionalization of SPEs, including: carbon electrode biofunctionalized with

msCYP3A4 (Carbon/msCYP3A4), MWCNT nanostructured electrodes biofunctionalized with msCYP3A4 (Carbon/MWCNT/msCYP3A4), MWCNT nanostructured electrodes biofunctionalized with pure CYP3A4 (Carbon/MWCNT/pureCYP3A4) and not biofunctionalized MWCNT nanostructured electrodes (Carbon/MWCNT). Then, it continued with investigating the abiraterone impact on catalytic response of CYP3A4 utilizing Carbon/MWCNT/msCYP3A4 electrodes and CV as detection method (Figure 39). At last, the direct electroactivity of abiraterone in interaction with MWCNTs-nanostructured sensing surface of Carbon/MWCNT nanosensors is studied without involving any enzyme.

The results reported in this work are significant for personalized medicine and point-of-care chemical treatment, especially to improve the life expectancy and quality of life of patients with prostate-cancer.

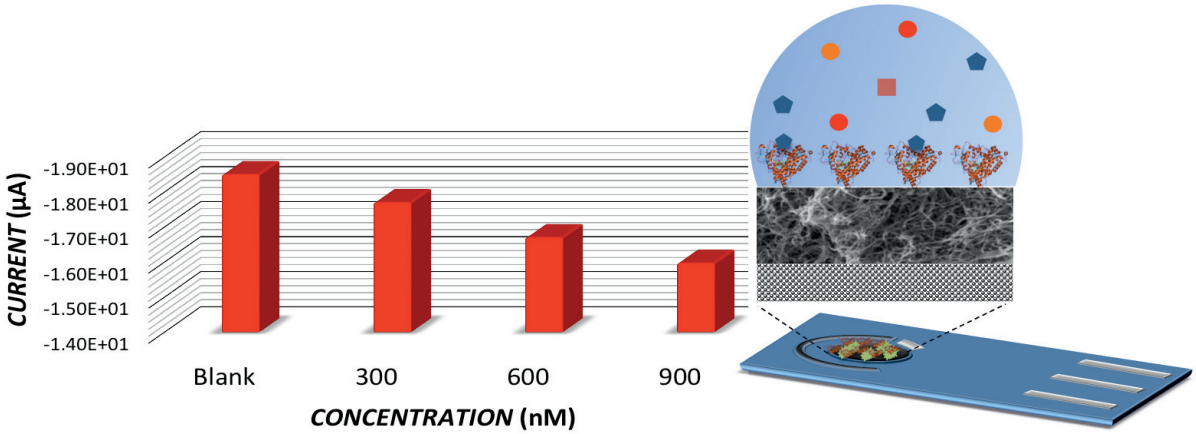

Figure 39. Left: response of nano-biosensor to different concentrations of target. Right: A schematic representation of developed enzymatic biosensors for studying electrochemistry of abiraterone, and its detection in buffer and human serum. Adapted with permission from [184]

msCYP3A4 reduction peaks identification

Four reduction peaks were clearly observed in the response of abiraterone and CYP3A4 interaction: they are located at -430 mV, -270 mV, -140 mV and 61 mV. In order to identify these peaks, electrochemical responses of different biosensors working on 900 nM drug solutions were compared (Figure 40). These peaks were identified by comparing the response of these different biosensors with each other and with independent observations published in the current literature by other authors. [207] A comparison of behavior in the presence and absence of abiraterone is presented in Figure 41.

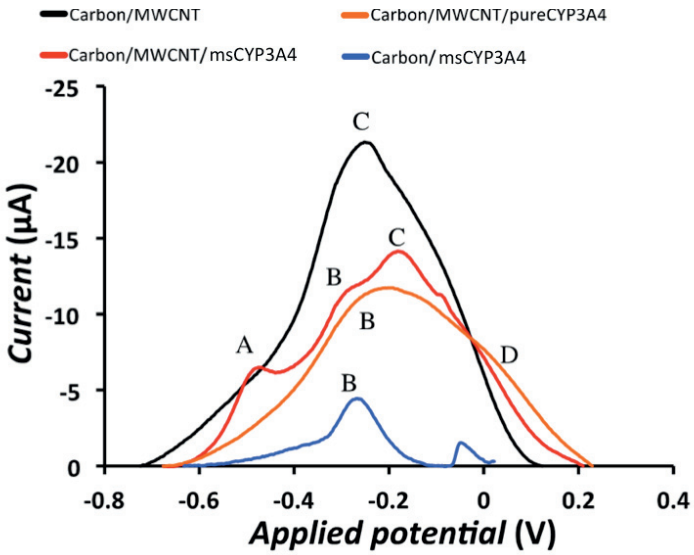

Figure 40. Identification of electrochemical peaks related to the interaction of abiraterone with CYP3A4 and MWCNTs. Adapted with permission from [184].

The analysis of those peaks shows that:

A. The first peak (-430 mV) was recorded only for biosensors with msCYP3A4. It did not exist on voltammograms of Carbon/MWCNT, so it is related to biomolecules. Moreover, it does not appear on voltammograms related to pure CYP3A4-based biosensors, so it belongs to CYP-reductase molecules that coexist with CYP3A4 protein in the microsome.

B. The Second peak (-270 mV) belongs to CYP3A4 protein, which is confirmed by the fact that it was observed in the response of all CYP3A4 based biosensors.

C. The third peak (-140 mV) appears only for the nanostructured biosensors, but not in the response of Carbon/msCYP3A4 biosensors. Therefore, it is identified as a MWCNTs peak.

D. The fourth peak (61 mV) was increasing over time, and was stabilized with increasing the number of cycles, so it was identified as a background peak, as confirmed by our group in other similar electrochemical systems. [207]

Abiraterone – CYP3A4 enzyme interaction

Voltammetric responses for each cytochrome-drug pair were first acquired in the absence of drugs (the blank signal), and then in presence of the drug, at increasing concentration within the pharmacological range. The inhibition of CYP3A4 by increasing the concentration of abiraterone was observed in voltammograms acquired by the Carbon/MWCNT/msCYP3A4 biosensor. The CYP3A4 Faradaic peak (-270 mV) is related to the reduction of the active site of the enzyme (heme group). This peak would increase/decrease in the presence of a substrate/inhibitor of the enzyme. The acquired response of the biosensor to 300 nM, 600 nM and 900 nM abiraterone showed a gradual inhibition and suppression of catalytic activity of CYP3A4. Background-subtracted reduction peaks are shown in Figure 41 (left), and their measured amplitudes are presented in Figure 41 (right) for

comparison. This inhibition reaction can be explained by the chemical structure of the drug and its interaction with enzyme molecules on the surface.

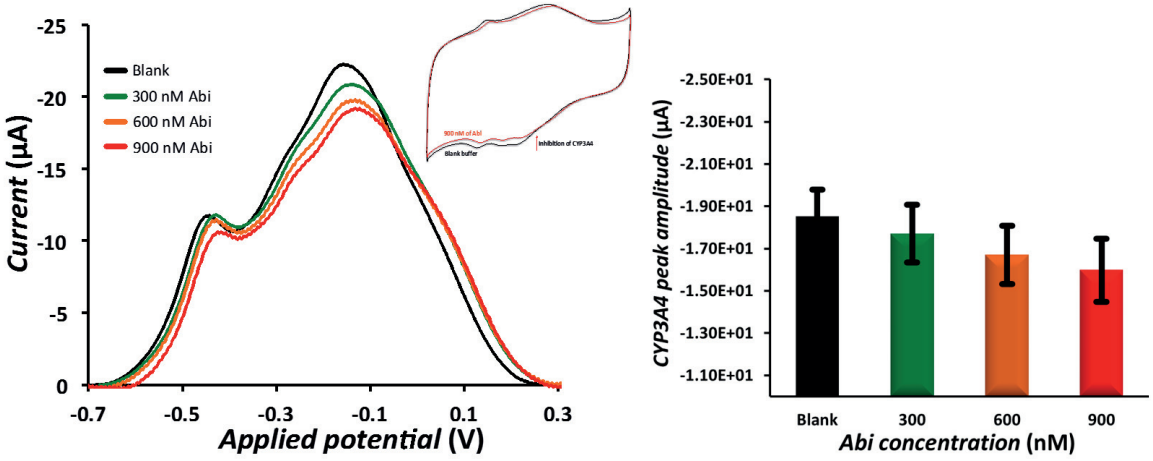

Figure 41. Left: the gradual inhibition of CYP3A4 catalytic activity by increasing abiraterone concentration; inset shows a complete voltammogram in buffer and after interaction with 900 nM abiraterone. Right: averaged reduction peak of CYP3A4 at different drug concentrations; Error bars are standard error of triplicate measurements. Reprint with permission [184].

The abiraterone structure harbors three main features, including the aromatic nitrogen-containing heterocycle (pyridine moiety), the hydrophobic steroidal core, and the hydroxyl group that all contribute to the high affinity of the drug for irreversible binding to cytochrome P450 enzymes. [218–221] This inhibition, which is mainly due to the complexation of the Fe^{+2} of the heme group of CYP3A4 and the sp2-hybridized nitrogen that exists in the pyridyl group, is described already in the literature. [220, 222] However, this is the first time that this phenomenon is presented utilizing electrochemical techniques. The redox reaction of CYP3A4 follows the Randles-Sevcik equation (Equation 20) that explains how the current depends directly on the scan rate. The scan rate used in this work was 70 mV per second, optimized for MWCNTs-based biosensors, as explained above.

3.4 Abiraterone detection in buffer and human serum

The dose-response curve of Carbon/MWCNT/msCYP3A4 in interaction with a wide range of abiraterone concentrations in buffer and in human serum was obtained to investigate further the effect of drugs on the catalytic activity of CYP3A4, and, above all, to calibrate the nanobiosensor for the detection of abiraterone in biosamples (Figure 42 and Figure 44).

Abiraterone screening in buffer

The interaction of abiraterone with CYP3A4 is investigated by experimenting Carbon/MWCNTs/msCYP3A4 biosensors to detect abiraterone in PBS solutions as a proof of concept. In-buffer abiraterone concentration monitoring mainly aims to study the catalytic behavior of CY3A4 and the possibility to exploit this behavior in a biosensor for drug monitoring in biological samples. The diminishing of the catalytic activity of CYP3A4, observed before, was considered as

the response of the nano-biosensor. Different concentrations of abiraterone (250 nM up to 1000 nM with steps of 250 nM, then up to 3000 nM with steps of 500 nM) were detected to form a dose-response curve representing the msCYP450 catalytic reaction in contact with abiraterone. This curve is presented Figure 42.

A clear inhibition of CYP3A4 was observed in the response, in the diminishing of its reduction peak as the drug concentration was increased. The dose-response curve also presented two significant properties of this reaction. First, an exponential decay of the CYP3A4 peak was observed for drug concentrations between zero and 1 µM. This range completely covers the therapeutic range of the targeted drug (therapeutic range is up to 1 µM), proving the capability of Carbon/MWCNT/msCYP3A4 for abiraterone concentration monitoring after proper optimization of the sensing system. Furthermore, by increasing the concentration from 1 µM to 3 µM, suppression of the reduction peak was saturated by an irreversible inhibition of majority of CYP3A4 proteins, after a reaction with abiraterone concentrations beyond 1 µM.

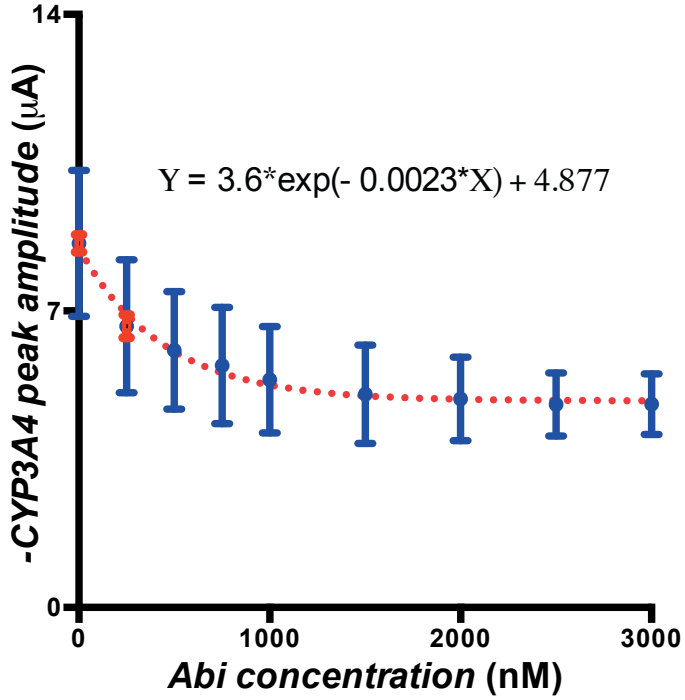

Figure 42. Dose-response curve of abiraterone in interaction with CYP3A4. The relevant equation is shown. Error bars in the figure indicate the inter-sensors variations, as each data point is an average of triplicate measurements carried out on three biosensors. Red error bars indicate intra-biosensor deviation used in the LOD calculation. Reprint with permission from [184]

The principle source of the response variations observed as error bars is the biosensor development procedure, including nanostructuring and enzyme immobilization by Van der Waals attachment and hydrophobic forces. This procedure is very effective in avoiding complexity and, more importantly, the denaturation of the enzyme that both are essential factors in POC biosensing. However, controlling the amount of immobilized enzymes on the surface is difficult, and this leads to inter-biosensor variations due to different amounts of probe proteins on the sensing surface.

The data points on Figure 42 follow an exponential decay equation (Equation 27). Where Y_0 = 8.482 µA is the start point, Plateau = 4.877 µA is the saturation region, and K = 0.002263 is the decay rate, and has the reciprocal of X-axis unit (1/nM).

$$Y = (Y_0 - Plateau)e^{-KX} + Plateau \tag{27}$$

Analysing these data leads to an LOD of 36.09 nM for in-buffer detection.

Abiraterone screening in human serum

Interaction of abiraterone with CYP3A4 in a PBS solution that caused an inhibition of catalytic activity of the enzyme was presented and discussed above. This diminishing of the catalytic activity of CYP3A4 was also observed as a response of the Carbon/MWCNTs/msCYP3A4 biosensor to abiraterone in human serum samples (Figure 43, left).

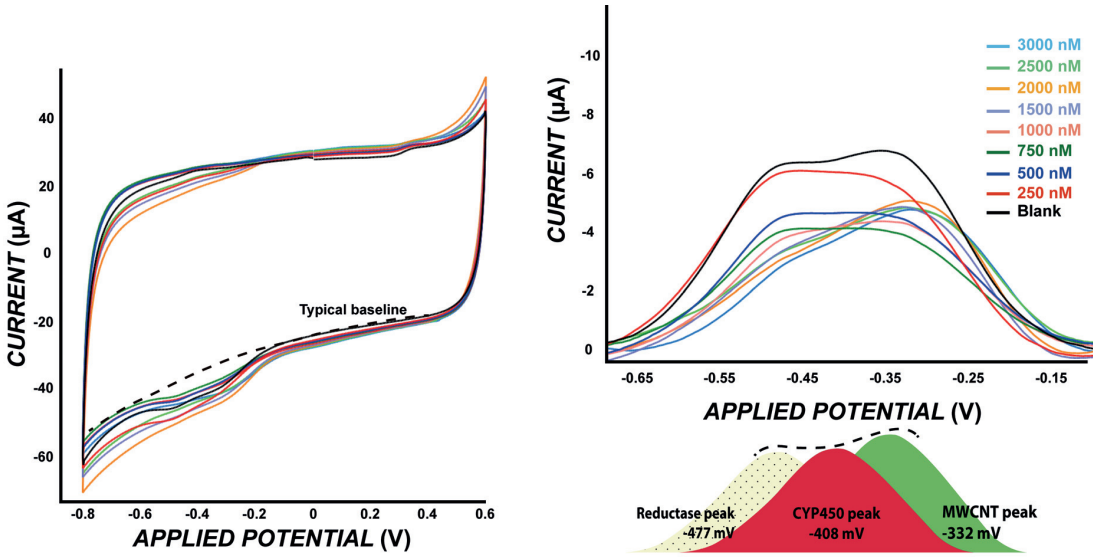

Figure 43. Left: voltammograms recorded for the detection of abiraterone in spiked human serum samples. The typical baseline used for analysis of Faradaic peaks are indicate in the figure. Right: Faradaic peaks after baseline correction using Nova software. The patterned yellow, red and violet peaks (not to scale) indicate the different peaks observed in this figure and the peak positions.

Different concentrations of abiraterone (250 nM up to 1000 nM with steps of 250 nM, then up to 3000 nM with steps of 500 nM) were observed, by the proposed biosensor, to obtain the dose-response behavior of the biosensor in human serum as explained earlier. Figure 43 presents the recorded responses of the biosensor after baseline correction. The reduction peak of CYP3A4 protein has been suppressed until the 1000 nM sample (pink curve), where further increments of drug concentration did not show further inhibitory effects. At this drug concentration most of the CYP4503A4 proteins are inhibited by the binding of abiraterone to their heme group. By increasing the concentration beyond 100 nM, and up to 3000 nM, the electroactive nature of abiraterone became dominant, as can be observed in the increase of the MWCNTs peak in Figure 43.

Reduction peak amplitudes of CYP3A4 in Figure 43 (right) corresponding to different abiraterone concentrations were measured in Nova software and were demonstrated on a graph (Figure 44) to obtain the dose-response curve of the enzymatic biosensor for in-serum abiraterone detection.

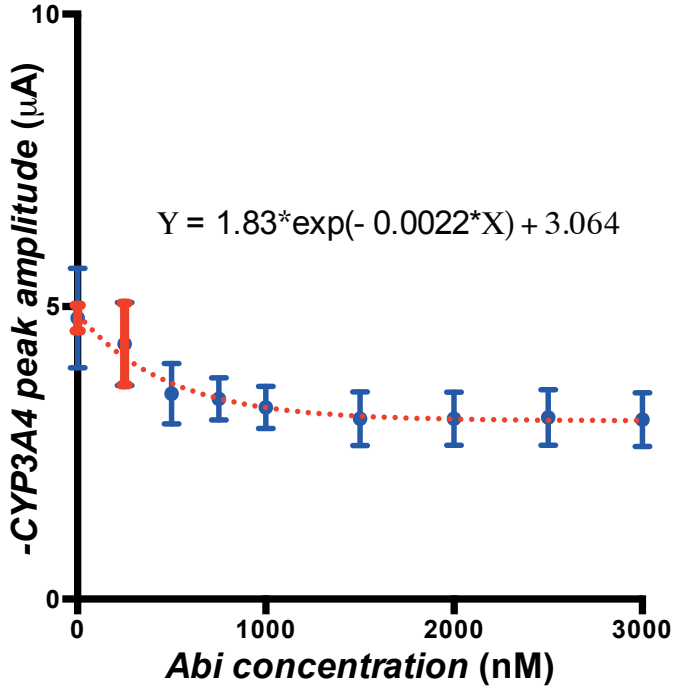

Figure 44. The dose-response curve of the nano-biosensor in interaction with abiraterone in human serum. The relevant equation is displayed. Error bars in the figure indicate the inter-sensor variations (on average RSD=26%), as each data point is an average of triplicate measurements carried out on three biosensors. Red error bars indicate the intra-biosensor deviation used in the LOD calculation.

The data points show an exponential decay following Equation 27 with an increase in the abiraterone concentration in human serum. Where Y_0 = 4.8 µA is the start point, Plateau = 3.064 µA is the saturation region, and K = 0.002233 is the decay rate, and is the reciprocal of the X-axis unit (nM^{-1}).

A limit of detection (LOD) of 230.26 nM has been calculated for the cSPE/MWCNTs/CYP3A4 biosensor as described in following section (section 3.4.1), according to the method described by Armbruster et al. [155] The dose-response curve shows a dynamic range up to 1 µM, while increasing the concentration beyond 1 µM demonstrated a plateau in the curve that means biosensor is saturated as a result of the irreversible inhibition of the majority of CYP3A4 proteins. The LOD and dynamic range are within the desired therapeutic range of abiraterone in the circulatory system of patients taking this drug, demonstrating the feasibility of developing CYP3A4-based biosensors for abiraterone detection in oncological treatments.

The suppression of the biosensor response by increasing the concentration of abiraterone has been observed in all the biosensors used for both in-buffer and in-serum detection. However, the observed standard deviation can be related to the different levels of catalytic activity of immobilized CYP3A4. It can also be the result of the different amount of immobilized enzymes on the sur-

face. The inter-electrode response variations are further improved for in-serum experiments thanks to changing the setup to cover just the active area of the electrode with a spiked sample for detection, rather than immersing the electrode in a beaker with a stirrer.

3.4.1 Statistical analysis

The method of Armbruster et al. [155] has been employed to analyze the dose-response curves fitted to nonlinear functions, and to calculate the corresponding LOD:

The first $LOD_{\Delta V}$ deviation of response was calculated using Equation 28 and 29, [155] and then it was converted to concentration, using the relevant equation (Equation 27).

$$LOB = mean_{blank} \pm 1.645(SD_{blank}) \quad (28)$$

$$LOD_{\Delta V} = LOB \pm 1.645(SD_{lowest-concentration}) \quad (29)$$

In analysis of the abiraterone monitoring dose-response curves the standard deviation between triplicate blank measurements carried out by one electrode were used (intra-electrode), rather than the standard deviation of 3 different biosensors (inter-electrode; demonstrated on Figure 42 and Figure 44 as error bars). Intra-electrode standard deviation was used in these calculations, because of the unique nature of developed enzymatic biosensors due to electrode-electrodes variations happening in production steps like nanostructuring and enzyme immobilization. These variations caused a big difference between the amplitude of different biosensors' response, while all of them followed a similar trend (exponential decay), and showed high sensitivity respect to blank signal. Therefore, they were considered to be more appropriate in demonstrating the real sensitivity of biosensors to the lowest detectable concentration of drug.

In order to calculate the LOD for in-buffer detection, the average of intra-electrode blank measurements, $mean_{blank}$ = 8.99 µA, the standard deviation between intra-electrode blank measurements, SD_{blank} = 0.21 µA, and the standard deviation of intra-electrode measurements on the lowest concentration of abiraterone tested (250 nM abiraterone), $SD_{lowest\text{-}concentration}$ = 0.27 µA, were used. Then, a limit of blank (highest blank measurement response), LOB = 8.63 µA, and consequently a $LOD_{\Delta V}$ = 8.19 µA were obtained using equations 28 and 29. Finally, by substituting the $LOD_{\Delta V}$ in the appropriate equation of dose-response curve for in-buffer detection (Figure 42 - inset) the LOD = 36.1 nM was calculated.

To calculate the LOD for in-serum detection, the corresponding intra-electrode parameters: $mean_{blank}$ = 4.8 µA, SD_{blank} = 0.22 µA, and $SD_{lowest\text{-}concentration}$ = 0.7 µA (for 250 nM abiraterone detection) were used. Then, a LOB = 4.438 µA, and consequently a $LOD_{\Delta V}$ = 4.158 µA were obtained exploiting equation 28 and 29. Finally, by substituting the $LOD_{\Delta V}$ in the fitting equation of dose-response curve for in-serum detection (Figure 44-inset) the LOD = 230.26 nM was calculated.

The reproducibility of the biosensor is indicated as the relative standard deviation percentage (RSD%), calculated by dividing the inter-electrode standard deviation by the mean value, multiply-

ing by 100 for each specific concentration, and then averaging them. Therefore, a reproducibility of 26% was calculated for this enzymatic biosensor.

3.4.2 Comparison of performance with current literature

Table 6 summarizes some recent advances in drug monitoring, utilizing enzymatic nano-biosensors suitable for POC applications. An amperometric biosensor based on CYP450 2B4 (isoforms named as CYP2B4 for simplicity) has been developed and successfully applied for cocaine determination. [223] The enzyme has been directly screen-printed onto the surface of SPEs. The ink was prepared by thoroughly mixing carbon ink with CYP2B4 (7% v/w) and immediately screen-printing it to form W.E. of redox cells. Their procedure has shown a good reproducibility, and a capability of detection down to 0.2 mM of cocaine. Carrara et al. [50] have reported a multi-panel drug detection system based on MWCNTs nanostructuring and CYP2C9 and CYP3A4 for naproxen and cyclophosphamide detection, respectively. In a more recent work by Baj-Rossi *et al.* a continuous and real-time monitoring of naproxen was reported that took advantage of a MWCNTs-nanostructured CYP1A2 based nano-biosensor for detection with a stable response for 16 hours. [208] An amperometric SPE-based biosensor with CYP2C9 in polyacrylamide hydrogel films as the sensing surface has been developed for bisphenol A determination. [224] The direct electrochemistry of CYP1A1 in a nano-Na-montmorillonite (nano-SWy-2) and dihexadecylphosphate (DHP) composite film on an edge-plane pyrolytic graphite electrode (EPG) has been obtained and the catalytic activity of the enzyme to benzo[a]pyrene has been investigated by the cyclic voltammetry. [225] In another publication, a CYP3A4-containing biosensor has been demonstrated for voltammetric caffeine detection, [226] constructed by adsorption of alternating layers of sub-nanometer gold particle-modified PAMAM (poly-amido-amine) dendrimers of generation 4.0, along with the enzyme in a layer-by-layer assembly technique. An amperometric method has been described and characterized by [227] for the determination of cocaine using SPE-based enzymatic biosensors. The enzyme CYP2B4 was covalently attached to screen-printed carbon electrodes. Experimental design methodology has been performed to optimize the pH and the applied potential, both variables that have an influence on the chronoamperometric determination of the drug. This method showed a reproducibility of 3.56% (n = 4), and good stability of the biosensor response.

Table 6 compares our results obtained in PBS and in serum. As expected, due to the presence of several proteins in the serum, the system exhibits better performance in PBS than in serum, although the limits of detection are within the pharmacological ranges for all the tested drugs, proving the feasibility of CYP450-based biosensors for measurements in a complex biological fluid. The decrease in sensitivity obtained in serum can be reasonably attributed to plasma proteins, such as albumin, bilirubin or hemoglobin, which can bind and interact with drug molecules, reducing the free drug concentration at the electrode surface. Plasma proteins can also be non-specifically adsorbed on the electrode surface, partially blocking the binding site of the enzyme, thus further reducing the signal.

Table 6. List of recently reported enzymatic drug detection, up to the current date

Target drug	Enzyme	LOD* (µM)		Linear Range (µM)	Ref.
		Buffer	Serum		
Cocaine	CYP2B4	200	-	200 – 1200	[223]
Naproxen	CYP2C9	82	-	21 – 515	[50]
Naproxen	CYP1A2	16	33	9 – 300	[208]
Cyclophosphamide	CYP3A4	12	33	10 – 75	[50]
Cyclophosphamide	CYP3A4	4.9	10.8	10 – 70	[66]
Ifosfamide	CYP3A4	2	7.1	20 – 140	[66]
Ftorafur	CYP1A2	0.7	0.8	1 – 8	[66]
Bisphenol A	CYP2C9	0.58	-	1.25 – 10	[224]
Benzo[a]pyrene	CYP1A1	0.58	-	3.3 – 16.56	[225]
Caffeine	CYP3A4	0.5	-	0.5 – 100	[226]
Cocaine	CYP2B4	0.023	-	0.019 – 0.166	[227]
Abiraterone	**CYP3A4**	**0.036**	**0.23**	**Up to 1**	**Present work**

* LOD: limit of detection

The optimized biosensor presented and characterized in this thesis is the very first electrochemical detection of abiraterone, and shows a superior performance in terms of limit of detection compared to other cytochrome-based biosensors for a wide set of molecules reported in the literature, based on our knowledge. A list of state-of-the-art enzymatic biosensors is presented in Table 6 as an example. The only work that has shown better performance is reported by Asturias-Arribas et al. [227] for detection of cocaine in a buffer. Nevertheless, their experiments have been performed in a buffer solution while this thesis has reported LOD for detection of the target drug in human serum that would suppress the performance due to the interference of many biomolecules also present in the sample.

3.5 Original contribution

An enzymatic electrochemical screen-print based biosensor (SPE/MWCNTs/msCYP3A4) suitable for POC detection of abiraterone in buffer and human serum is presented and successfully demonstrated in this thesis, to the best of our knowledge, for the first time.

The electrochemical characterization of abiraterone in interaction with the CYP3A4 enzyme was characterized in this thesis. Electrochemical responses of enzymatic biosensors exhibited the inhibitory effect of abiraterone on CYP3A4 proteins that is observed for the first time by an electrochemical method (CV). In addition, a comparison of the responses of various biosensors functionalized with different nanostructures and biomolecules identified the electrochemical peaks ap-

pearing in the responses of abiraterone: -430 mV for CYP-reductase, -270 mV for CYP3A4, -140 mV for MWCNTs and 61 mV as background peak (Figure 40).

Enzymatic electrochemical responses in buffer (Figure 41 and Figure 42) presented an exponential decay till 1 μM that is consistent with the abiraterone therapeutic range in the human body. This inhibition behavior saturates at concentrations beyond 1 μM.

Furthermore, the same system was exploited to detect abiraterone in human serum at therapeutic concentration. The observed dynamic range of response (Figure 44) for concentrations below 1 μM alongside the LOD of 249 nM proves the capability of the proposed biosensor for in-serum abiraterone detection, since they are consistent with the desired circulatory concentration range of drugs up to 1 μM in a patient's body. The comparison of the LOD of a biosensor in this study with the current literature confirms the superior performance of cSPE/MWCNTs/msCYP3A4 for drug detection in human serum (Table 6).

Chapter 4 Aptamer-based biosensors

For the continuous monitoring of therapeutic compounds, enzymatic biosensors that utilize CYP450 as specific bio-probes and amperometric detection as the analytical method have been developed as drug detection systems thanks to their simplicity and their compliance with POC TDM requirements. [208] CYP450-based electrochemical sensors present an optimal sensitivity and detection limit that addresses therapeutic ranges for many drugs, especially once coupled with multi-walled carbon nanotubes. [66, 196, 228] However, they enable lower selectivity compared to affinity-based biosensors considering that each CYP450 enzyme can have a wide range of substrates or inhibitors. The lifetime of this type of biosensors is also still fairly short, thus limiting their application to continuous monitoring. [208] The need for more robust electrochemical biosensors for continuous drug monitoring, with one specific target, is still not yet fully addressed. To overcome the above-mentioned issues, an n-channel metal-oxide semiconductor field-effect transistor device (n-MOSFET) with an extended gate functionalized with a drug-specific DNA aptamer, as well as a nanowire-based nano-biosensor with memristive behaviour are investigated in this section.

TFV is an antiretroviral drug that was approved by the FDA in 2001 for medical prevention and the treatment of patients with Human Immunodeficiency Virus (HIV) infections and treatments for Hepatitis-B. It is administered orally at a once-daily dose of 300 mg and in the form of Tenofovir disoproxil (prodrug of tenofovir) to increase the bioavailability. [44, 45] Based on the pharmacokinetics data after oral administration of TFV, the circulatory plasma concentration is in the range of from a few nano-molar up to 860 nM. Tenofovir does not involve any CYP450 enzyme in its metabolic pathway, and is metabolized by mitochondrial adenylate kinases. [44, 46, 47] Therefore, the proposed enzymatic biosensors biofunctionalized with CYP450 cannot be used for TFV monitoring. In addition, reaching such a low LOD that it would be possible to detect TFV is still a challenge for enzymatic biosensors. Therefore, to address this issue, affinity-based biosensors were proposed, developed and characterized in this thesis as a solution.

In the next section a brief background about different elements of the proposed affinity-based biosensors is presented, using DNA-aptamers as a recognition probe, as well as a review of the state-of-the-art.

4.1 Background and state-of-the-art of aptamer-based biosensors

Label-free TDM by means of electrochemical [229] and field-effect [230–232] biosensors has gathered significant interest in the last decade, since it can lead to personalized POC therapy applications. [63, 233–235] At the same time new detection methodology is emerging, to take advantage of memristive devices. [171] The affinity-based biosensor used in this thesis for TFV

detection relies on DNA-aptamers as a recognition element, and Field-effect and memristive Si-nanowires as a transducer. It is therefore worthwhile explaining more of these different approaches, while describing at the same time the most recent related advances in biosensing.

Aptamers are short oligonucleotide sequences that can strongly bind to their targets with high affinity and specificity thanks to specific conformational changes. Aptamers have several advantages compared to antibodies. For instance, a selection of aptamers is performed through an in vitro process. Once the aptamers are selected, they can be further synthesized in a controlled fashion with high purity and reproducibility. Additionally, aptamers are chemically more stable and retain most of their functionality even after multiple regeneration steps. [236, 237] Such a regeneration step is advantageous for continuous monitoring studies. For example, Ferguson et al. [233] have proposed a novel selective and sensitive real-time small molecule monitoring method that uses aptamers as recognition elements, and prevents the interaction of blood molecules with the sensing surface by a continuous flow diffusion filter in order to suppress sensor fouling. As oligonucleotides can be easily modified with different reactive chemical groups, their immobilization on surfaces can be easily controlled. Thanks to such flexibility, aptamers are very popular for the design and optimization of novel biosensors. [238] Such probes, e.g. DNA aptamers, are gaining significant attention for the detection of several small molecules. [239] One cutting-edge approach to mitigate the biofouling of sensing surface and decrease the non-specific response is protein imprinting [240, 241] and protein epitope imprinting. [242] Molecular imprinting is one of the few general, nonbiological methods for creating molecular receptors. In this technique functional and cross-linking monomers are co-polymerized in the presence of the target analyte (the imprint molecule), which acts as a molecular template. The functional groups of monomer-imprint molecule are held in position by polymerization, and following the removal of imprint molecule the complementary binding sites are maintained that is capable of rebinding the analyte with high selectivity (like a molecular memory). Epitope imprinting is an alternative to protein imprinting that uses just the reactive part of probe protein (epitope) in imprinting process rather than the whole protein and, thus, reduces the complexity due to large size of whole protein. Vibha et al. have used epitope imprinting approach to detect prostate specific antigen (PSA) in human plasma with high specificity and sensitivity (LOD = 0.1 pg mL^{-1}). [243] A highly specific aptasensor with strong antifouling properties is reported by Jolly et al. taking advantage of sulfo-betain as a zwiterionic[16] brush in recognition of its ability to repel interfering substances that are attracted due by electrostatic force. Using the novel sensing surface, they have achieved a remarkable LOD for PSA of 1 ng ml^{-1}. [244] Field-effect nanowires have also been recently developed and employed for POC detection of biomarkers as ultimately-scaled long-channel ISFETs. [231, 232, 245, 246] Ingebrandta et al. have reported an array of silicon nanowires, which were fabricated in a top-down process from silicon-on-insulator (SOI) substrates with a high yield for the label-free detection of proteins and DNA. [245] In other recent work of the group, [247] they have presented a scalable array consisting of 32 high-aspect ratio Si-nanowires such as nanoISFET. NanoISFET arrays deployed as pH sensors, which demonstrated exemplary sensor characteristics with pH sensitivity as

[16] Zwitterions (or dipolar ions) are neutral molecules containing both positive and negative electrical charge.

high as 43 ± 3 mV pH^{-1} and a device-to-device variation of 7% on the wafer scale. They have also exhibited POC application of the sensor by coupling it with a hand-held readout system for real-time pH measurement in liquids.

The field-effect aptamer-based biosensors proposed in this section rely on the well established and industry-friendly technology that is Metal-Oxide-Semiconductor Field-Effect Transistor (MOSFET). To produce the biosensor a typical MOSFET is manipulated by physically connecting the gate of the transistor to an external gold electrode, which is used for functionalization with an aptamer specific to a drug and exposed to the measurement sample. When the potential applied across the gate and the source (V_{gs}) is larger than the threshold voltage (V_{th}) of the device ($V_{gs}>V_{th}$), a conducting channel is formed between the source and the drain. Additionally, if a voltage is applied between the drain and the source ($V_{ds}>0$), then a current (I_d) begins to flow through the induced channel under the gate dielectric. This condition of the device is known as turn-on state, where the electron (I_d) enters the drain and exits the source. Any changes across V_{gs} can modulate the conductivity of the channel and alter I_d. If molecular interactions take place at the gate of the transistor, such as when negatively charged small molecules (for instance drugs) are captured by recognition probes (aptamers in this work), the minimum V_{gs} required to bring the n-MOSFET in the turn-on state is increased (gating effect). This is used to quantify the binding event by monitoring the shift of the transfer characteristic (I_d vs. V_{gs} curve) of the transistor after the target molecule binding. [248–251] The schematic of the AptaFET proposed and characterized for TFV detection is presented in Figure 45.

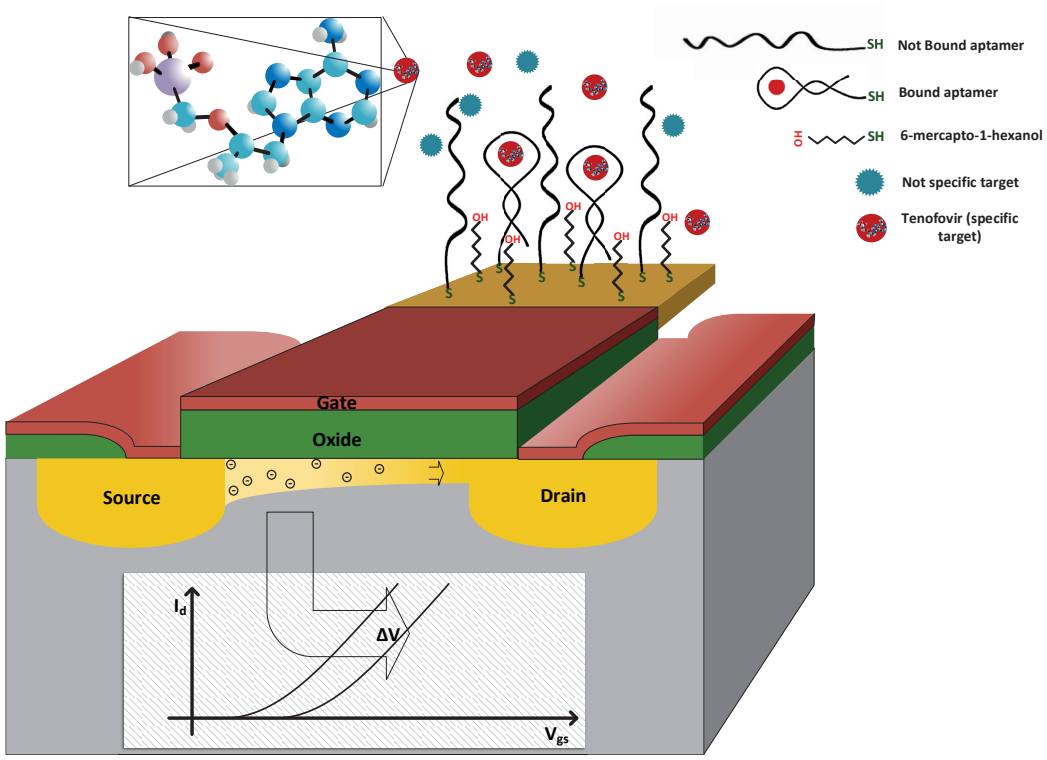

Figure 45. Schematic of AptaFET. The binding reaction is transformed to an electric signal through FET and observed as I_d-V_{gs} shift. TFV is indicated by red circle.

A recent work has reported a MOSFET-based biosensor for the label-free detection of pathogens with a limit of quantification equal to 1.9×10^5 colony forming unit per ml. They have taken advantage of the electric charge of bacteria binding to the glycosylated gates of a MOSFET for quantification in a straightforward manner. [252] Some applications where MOSFETs are employed for biosensing include: cancer therapy, [253] drug screening, [254, 255] POC disease detection [256] and diabetes management. [257]

In a very recent work, Pawan Jolly *et al.* [258] have reported a highly sensitive dual-mode biosensor for electrochemical detection of miRNAs. They have used uncharged peptide nucleic acid (PNA) bioprobes to increase the stability of the biosensing surface and to reduce the interferences of DNA-probes at the interface. Electrodes were washed after the incubation in a solution of targeted miRNA, and incubated in positively charged GNPs, and subsequently a ferrocene based redox maker. This approach facilitated a dual mode detection, as electrochemical impedance spectroscopy (EIS) was used to monitor the binding reaction, while square wave voltammetry (SWV) was exploited to detect the binding of GNPs that were electrostatically bound to just PNA-miRNA duplex and the redox marker of GNPs. This dual-mode detection provided a limit of detection of 0.37 fM and a wide dynamic range from 1 fM to 100 nM, along with clear distinction from mismatched target miRNA sequences. [258]

In addition, structures like semiconductor nanowires demonstrate great potential in bioassays miniaturization. [171, 245, 259–262] Thanks to their tuneable electron transport properties and their electrical response , strongly influenced even by minor perturbations. Nanowires offer the possibility for a direct and highly sensitive electrical readout thanks to their high surface-to-volume ratio obtained when designed at the nanoscale. [263] Memory effects, which already exist in nature, [264–266] are also observed in electronic-based devices as pronounced hysteresis with special features in their electrical characteristics. [267, 268] Nanoscale devices exhibiting memristive behavior have been theoretically conceived and presented for the first time by L. Chua in 1971 [269–271] and physically implemented in 2008 by HP laboratory. [272] They can be fabricated by various materials nowadays, and show immense potential in a plethora of applications. [273, 274] Such applications for nonlinear dynamical memory devices include computation and logic operations, [275–277] as well as storage applications. [278] Further use of these devices in biophysics and temporal dynamics has been observed. Nevertheless, so far the main focus is in the field of bio-inspired computation and neuronal systems. [279–283] The very first application of memristive nanowires for cancer diagnostics is reported by Tzouvadaki et al., [171] where they have exploited the hysteretic voltage gap for PSA detection. Memristive properties of silicon nanowires are used to develop an ultrasensitive PSA biosensor based on DNA aptamers. They have studied the impact of charged macromolecules binding on the surface on the electrical-conductivity hysteresis of nanowires. The nanofabricated memristive devices were then used to obtain an ultrasensitive electrochemical biosensor for the label-free detection of PSA with LOD of 23 aM, well below the clinically relevant range of detection for PSA in patient samples.

As a summary of the first section, two affinity-based biosensors have been introduced with potential applications in highly sensitive and selective therapeutic monitoring of anti-HIV drugs. The first

one is an aptamer based biosensor for continuous monitoring of drugs in buffer and plasma (named AptaFET), based on the combination of aptamers for target recognition and field-effect transistors for the transduction of the drug-probe interaction to an electric signal. The second biosensor takes advantage of DNA-aptamer regeneration, coupled with the memory-effect caused by the DNA-aptamer anchoring to the surface of silicon nanowires (Si-nanowires) for drug detection applications in human serum. An application of memristive Si-nanowires in drug monitoring is demonstrated here for the first time. Therefore, the second part of this section actually bridges the memristive effect and the hysteretic electrical properties expressed by nanoscale devices, and also with the DNA-aptamer natural and physical functions.

This ultrasensitive and selective label-free screening of TFV is initially shown in buffer and then efficaciously demonstrated in human serum in the following sections. The proposed field-effect and memristive approaches, based on such unique and definitively innovative nanoscale devices, holds great promise for the continuous monitoring of drugs in real time, paving the way for new integrations and multiplexing aspects in diagnostics and personalized medicine.

4.2 Aptamer-based field-effect biosensors for TFV detection

FETs and MOSFET have attracted much attention as they offer rapid, label-free, and cost effective detection of the analyte. In digital electronics MOSFET acts as a switch where, two electrodes (source and drain) are used to connect a semiconductor material (channel) and current flowing through the channel is electrostatically controlled by the gate. [248] In the case of an extended-gate MOSFET the external electrode of biosensor is functionalized with specific receptors for selectively capturing of desired biomolecules. In this work a n-MOS device has been used as the signal transducer that in combination with the gold extended gates, biofunctionalized with TFV specific aptamer (named TFV-aptamer), formed the AptaFET biosensor specific for TFV detection. A schematic of the biosensor is illustrated in Figure 45. The detail of the structure and MOSFET production is mentioned in the work of Formisano *et al.* [252] As explained earlier, the charged biomolecules when captured by probe molecules produce a gating effect, which is transduced into a readable signal in the form of change in electrical characteristics of the MOSFET such as drain-to-source current or channel conductance. [248, 249]

In this work the quality of specific and non-specific drug–aptamer interactions, at different buffer conditions, was measured by surface plasmon resonance (SPR). EIS was used to optimize the biosensing interface, by finding the best ratio between aptamer to 6-mercapto-1-hexanol (MCH) concentrations. To obtain the dose-response behavior of the system, the AptaFET biosensor was measured upon interaction with different concentrations of TFV in PBS buffer. Control experiments were carried out using abiraterone and enzalutamide[17] (non-specific drugs) and PSA-aptamer (non-specific aptamer). AptaFET application for drug monitoring in human plasma was investigated by detecting 500 nM of TFV in human plasma.

[17] A widely used anti-prostate cancer drug.

Real time drug monitoring is of great importance in POC TDM to pave the path towards vital applications in drug monitoring that enhance the efficacy of treatment and the patient's quality of life. For instance, many chemical treatments for cancer therapy are administered by the continuous intravenous infusion of a prescribed dose of medicine over a long period of time that lasts up to several hours. This is a time that the patient can be observed with real-time monitoring of the drug concentration, to stop the chemotherapy whenever the concentration has reached the required therapeutic range. This improves the efficacy and the time consumption for chemotherapy. Another important application is to develop implantable biosensors that are inserted in the body of the patient to monitor the concentration over time, and continuously to prevent the concentration passing beyond the minimum toxic concentration or decreasing to lower than the minimum effective concentration. This increases the efficacy of chemotherapy as the maintained concentration is assured to be in the proper range.

In this study, real-time impedance was used to investigate the performance of the sensing interface under flow conditions, enabling the application of the biosensor to real time drug monitoring.

4.2.1 Material and Method

Materials

Thiolated TFV-aptamers (5'-Aptamer-C6 Thiol-3') were commercially provided by BasePair Biotechnologies (Pearland, Houston, USA). Thiolated PSA-aptamer (5'-HS-(CH2)6-TTT TTA ATT AAA GCT CGC CAT CAA ATA GCT TT-3'), Human serum, MCH, potassium phosphate monobasic solution (KH_2PO_4), potassium phosphate dibasic solution (K_2HPO_4), potassium sulphate (K_2SO_4), potassium hexacyanoferrate (III), potassium hexacyanoferrate (II) trihydrate, magnesium chloride ($MgCl_2$), DMSO and phosphate buffer saline (PBS; 10 mM; pH-7.4) were all purchased from Sigma-Aldrich (UK). Aptamers were unfolded by heating them at 90 °C for 5 minutes and leaving them to cool down to room temperature. TFV, abiraterone and enzalutamide powders were purchased from Medchemtronica (Stockholm, Sweden) and were dissolved in dimethyl sulfoxide (DMSO) to the concentration of 5 mM as stock solution. Phosphate buffer (PB; 0.1 M pH-7.0) was prepared by adding 17 mM of KH_2PO_4, 33 mM of K_2HPO_4 and 500 nM of K_2SO_4 to distilled water. Polyamidoamine (PAMAM) dendrimers (4^{th} generation) were purchased from Dendritech, Inc. (Midland, Michigan, USA). All other reagents were of analytical grade. All aqueous solutions were prepared using 18.2 MΩ cm ultrapure water with a Pyrogard filter (Millipore, Feltham, UK).

Biosensors development

The sensing surface was developed for specific interaction with TFV, while MCH was used as a surface blocking agent and a spacer between aptamers (Figure 2). Gold disk working electrodes (radius 1.0 mm, CH Instruments, Austin, TX, USA) were cleaned based on the procedure published by Keighley *et al.* to provide a properly flat and contaminant-free surface for biomolecule immobilization. [284] Then they were biofunctionalized with sensing surfaces and were exploited in EIS experiments for sensing surface optimization (section 4.2.2).

Our innovative AptaFET biosensor consists of a home-designed n-MOSFET structure combined with an extended gate (Figure 45). Detailed information on the specifications of the n-MOS chip have been reported elsewhere. [248] Single-crystalline Si MOSFETs were fabricated using a CMOS 0.7 µm process at IMEC. The devices have no electrostatic discharge (ESD) protection elements in order to minimize their gate leakage current. Each chip contains five n-type MOSFETs with a common source contact. Different sized transistors have been used with widths (W) and lengths (L) ranging from 1340 to 3860 µm and from 2.0 to 0.7 µm, respectively, while keeping the W × L product at approximately 2700 μm^2. The chip was glued on a glass substrate containing evaporated gold electrodes (100 nm Au with 10 nm of Cr as an adhesion layer) consisting of a bonding pad connected to a 500 µm × 500 µm pad. The on-chip gate contact pads and the source, drain, and substrate contact pads were wire-bonded to a printed circuit board (PCB). The gates were then connected to the external Au electrodes as shown in Figure 46, The chip was first passivated with Glob-Top (Amicon) epoxy encapsulant.

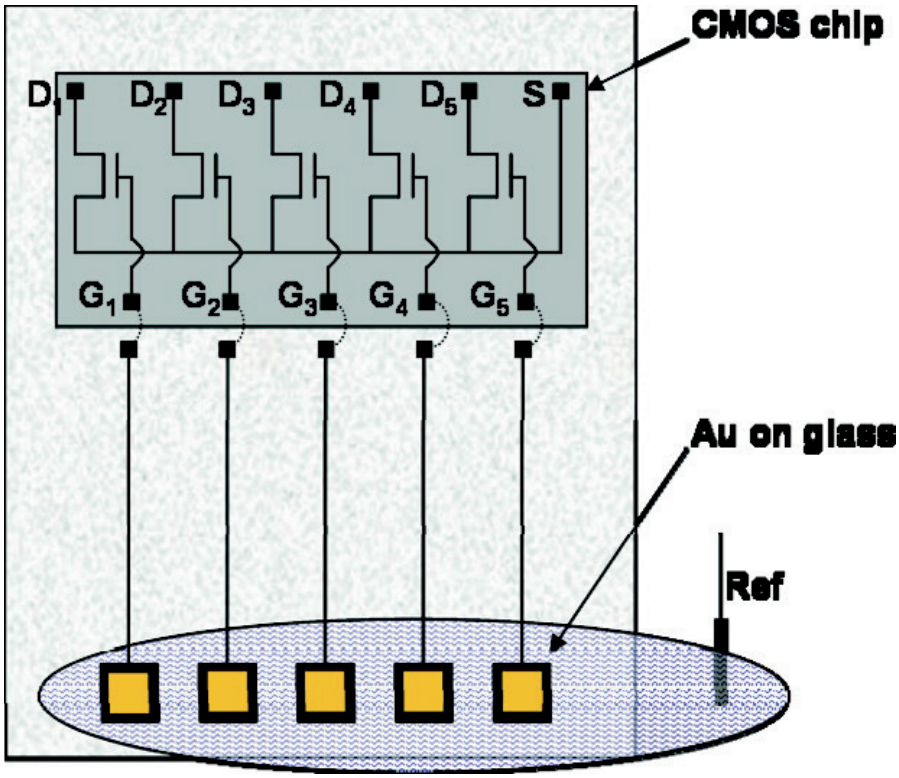

Figure 46. Schematic structure of a linear array of five MOSFETs connected to external gold electrodes as extended gold gates. Extended gates are exposed to the electrolytes for biosensor protection. S, D1−5, and G1−5 are the on-chip contact pads for source, drains, and gates, respectively. Reprinted with permission from [248].

To produce the extended gates, arrays of gold electrodes (180 nm Au thickness on 20 nm Cr) were deposited on a glass substrate, using thermal evaporation. Electrodes were cleaned by acetone, ethanol and ultrapure water, sequentially and repeatedly, and then they were functionalized with the sensing surface described earlier. The extended gate was, then, fabricated by connecting the biofunctionalized Au electrodes, fixed in a reaction cell, to the gate of the n-MOSFET via a metal wire. When the glass chip is immersed in an electrolyte, only these exposed Au areas are in contact with the solution.

Apparatus and setup

Surface plasmon resonance (SPR) measurements were performed using a Reichert SPR 7000DC (USA) dual channel flow spectrometer at 25 °C. 50 nm gold coated SPR gold chips, supplied by Reichert Technologies were used for studying the reaction on SPR. Prior to their modification, the chips were cleaned using piranha solution (3:1 H_2SO_4:H_2O_2) for 20 seconds and rinsed thoroughly with MilliQ water and dried using nitrogen gas. Modification of the SPR chips with DNA aptamers was performed in the same way as described earlier (Biosensor development). All buffers were filtered through 0.2 µm filters and degassed for 2 h by sonication prior to the experiment. To perform the experiment, 500 nM solutions of TFV and abiraterone were channelled over the biofunctionalized chips for 20 minutes with a flow rate of 25 µL min^{-1}, and followed by 5 minutes of a dissociation step to remove all the unbound residues.

For EIS experiments a µAUTOLAB III/FRA2 potentiostat (Metrohm, Netherlands), and a three-electrode cell setup consisting of biofunctionalized gold working electrode, Ag/AgCl reference electrode (via a salt bridge filled with 0.1 M PBS pH 7.4) and platinum counter electrode (ALS, Tokyo, Japan). The measurements were carried out in a PBS buffer solution containing 10 mM ferro/ferricyanide $[Fe(CN)_6]^{3-/4-}$ redox couples (hexacyanoferrate II/III), applying a 10 mV a.c. voltage superimposed on a +0.2 mV of d.c. potential (formal potential of the redox couple), in the frequency range 100 kHz to 0.1 Hz (61 frequency steps). After a stable signal was observed with blank solutions, the biofunctionalized electrodes were incubated in a 500 nM solution of TFV for 30 minutes and washed in buffer before the EIS spectra was measured.

For real time impedance monitoring, a three-electrode flow cell was connected to a CompactStat potentiostat (Ivium Technologies, The Netherlands), and immersed in flow of ferro/ferricyanide solution for measurement. The impedance was monitored every 0.2 s at a single frequency of 10 Hz with a 10 mV amplitude superimposed on a 0.2 V d.c. bias potential. Solutions of TFV and abiraterone were injected once a stable baseline was reached, to obtain the total concentration of 400 nM in the flow.

To operate the field-effect measurements using the AptaFET, a V_{ds} of 50 mV was applied across the drain to source and V_{gs} was swept from 0 to 4 V. These settings limited the I_d to less than 75 µA to avoid any false measurement due to device heating effects. Biofunctionalized electrodes were stabilized in PBS buffer, and then incubated for 30 minutes in 100 pM, 1 nM, 2 nM, 5 nM, 10 nM, 30 nM, 100 nM, 500 nM, 1 µM and 10 µM solutions of TFV in PBS-$MgCl_2$. They were then washed and measured in PBS to obtain the dose-response curve. The AptaFET was further measured with 500 nM of abiraterone and enzalutamide as negative controls using the same procedure. Finally, a PSA-aptamer with length (32 nucleotides) and two-dimensional structure similar to the TFV-aptamer was used in order to investigate the interaction of TFV with a non-specific sensing surface of the same length and structure. For the experiments on plasma samples, blank human plasma was injected with solutions of drugs to the final required drug concentrations.

4.2.2 Biosensing surface optimization

The procedure to find out the best sensing surface in terms of the sensitivity, selectivity, and level of complexity will now be explored. The focus of the optimization was to improve the performance of the TFV-aptamer interaction to enhance the specificity of the response. In addition, stability and reliability of the biosensor was tested using different chemistries for building the biorecognition surface. Several different sensing surfaces were practiced until, finally, a binary self-assembled layer of TFV-aptamer and MCH was chosen to be fabricated on the interface as sensing surfaces (Figure 47-50). To do so, different sensing surfaces were formed on the surface and tested by EIS.

The following sensing surfaces were examined in this optimization step:

1. Sensing surface: Ternary SAM of Aptamer, MCH and 1,6-Hexandithiol (HDT)

To form the sensing surface, first, a homogeneous SAM of Thiolated Aptamer and HDT with a ratio of 1:3000 was formed by incubating the completely-cleaned gold electrodes in the solution of the mixture overnight. Electrodes were then completely washed with ethanol and distilled water to remove any residues and unbound molecules. Electrodes were then incubated in an MCH solution to backfill any empty areas. Figure 47-Left demonstrates the schematic of the final ternary-SAM formed on the surface. Produced electrodes were washed with ethanol and water for the last time and kept in blank experimenting buffer (PBS) for 1 hour to reach stability.

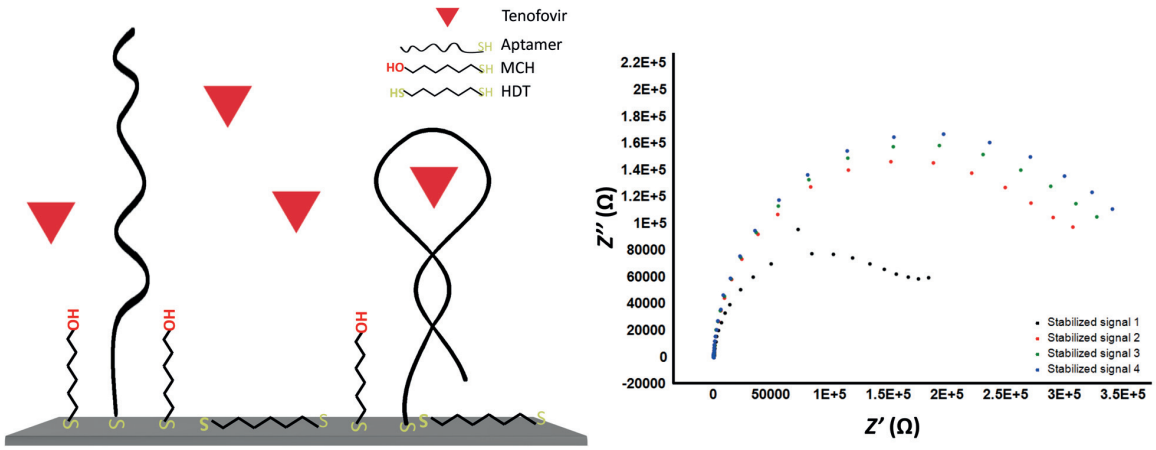

Figure 47. Left: schematic of the sensing surface including ternary SAM of aptamer, HDT and MCH. Right: an example of the EIS response of the sensing surface in blank solution.

Finally, the biosensors were tested by EIS, as described in the Apparatus and setup section. However, the recorded responses of biosensors showed some instability at the sensing surface.

2. The sensing surface: Aptamer over SAM of Mercaptopropainic acid (MPA)-Mercaptopropanol (MP)

The second tested sensing surface included a SAM of MPA and MP with tested ratios of 1:50 and 1:200, respectively. Again, a solution of mixture with the mentioned ratios was produced, in which cleaned gold electrodes were incubated overnight to form a homogeneous SAM. The surface was then incubated in PAMAM dendrimer solution (30 minutes)[18], glutaraldehyde (10 minutes) and 1 µM amine-terminated aptamer solution (30 minutes), subsequently. Finally, ethanolamine was used for backfilling (30 minutes) to block any unbound carboxyl group on the SAM. The surface of electrodes was washed with ethanol and distilled water between each incubation step and dried, gently. Therefore, the final sensing surface included aptamers that were immobilized over the SAM layer through dendrimes, as is illustrated in Figure 48 (left). The EIS responses of the biosensor showed a same level of sensitivity to the specific target and the negative control. This showed a low specificity of the sensing surface towards the specific target (Figure 48 right).

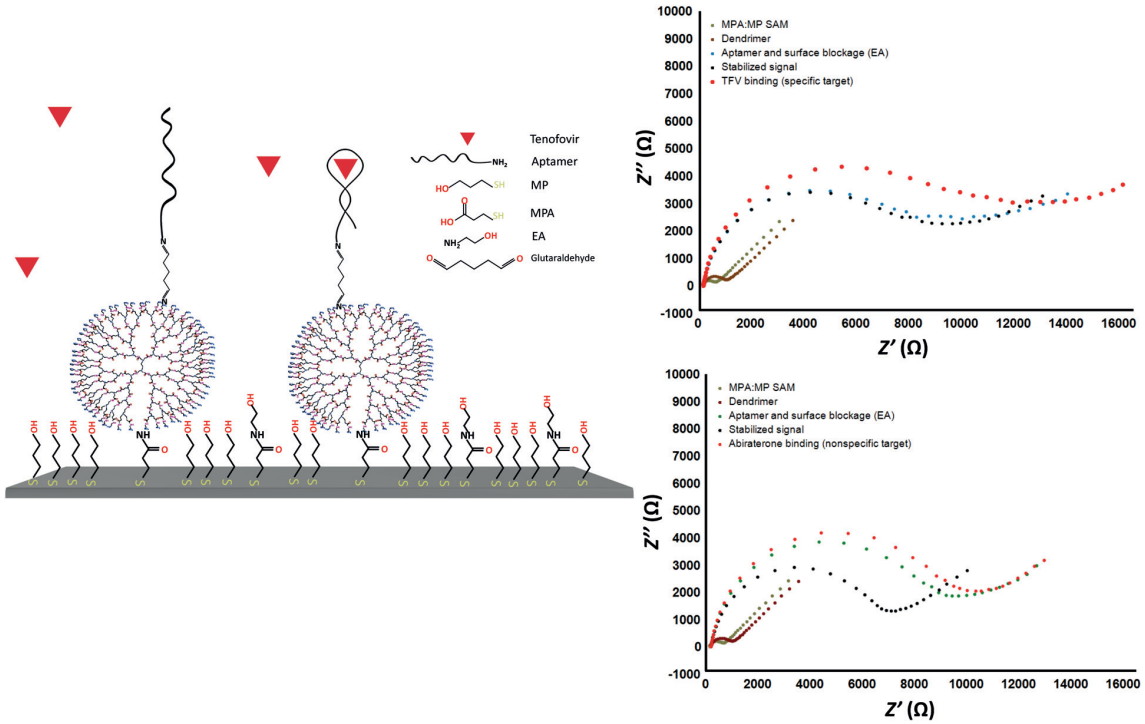

Figure 48. Left: a schematic of the sensing surface including aptamers over a layer of dendrimers that were immobilized over a SAM of MPA and MP. Top right: an example of EIS response of the sensing surface to 500 nM, with TFV as the specific target. Bottom right: the EIS response of the sensing surface to 500 nM abiraterone as negative control.

[18] Polyamidoamine (PAMAM) dendrimers are hyperbranched polymers with unparalleled molecular uniformity, narrow molecular weight distribution, defined size and shape characteristics, and a multifunctional terminal surface. These nanoscale polymers consist of an ethylenediamine core, a repetitive branching amidoamine internal structure, and a primary amine terminal surface. Dendrimers are "grown" off a central core in an iterative manufacturing process, with each subsequent step representing a new "generation" of dendrimer. Increasing generations (molecular weight) produce larger molecular diameters, twice the number of reactive surface sites, and approximately double the molecular weight of the preceding generation. PAMAM dendrimers also assume a spheroidal, globular shape at Generation 4 and above. Their functionality is readily tailored, and their uniformity, size, and highly reactive "molecular Velcro" surfaces are the functional keys to their use.

3. The sensing surface: Aptamer over SAM of Mercaptooctanoic acid (MOA)-MCH

The third tested sensing surface was a SAM of MOA and MCH with tested ratios of 1:50 and 1:200, respectively (Figure 49 left). The sensing surface was formed following the same procedure used for surface number 2, the only difference being the SAM layer. Then produced electrodes were tested by EIS again to detect 500 nM TFV and 500 nM abiraterone in PBS buffer containing 10 mM ferro/ferricyanide solution. As is presented in Figure 49-Right, measured EIS signal related to TFV measurement showed a 10% shift compared to baseline recorded in blank solution, and the negative control experiment had almost null shift after incubation with abiraterone.

Although these results showed a promising stability and specificity for the recognition element prepared by the mentioned procedure, the complexity and the long time required to form the layer were drawbacks that suppressed the potential of this surface to be chosen as the final sensing surface.

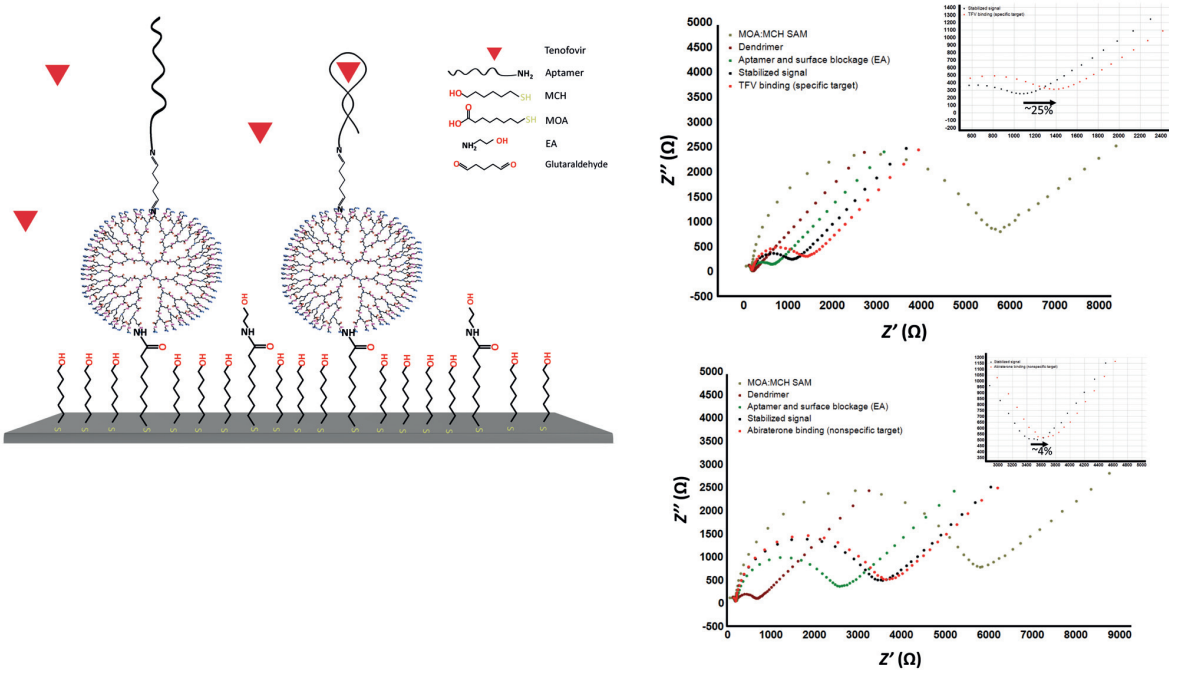

Figure 49. Left: a schematic of the sensing surface including aptamers over a layer of dendrimers that were immobilized over a SAM of MOA and MCH. Top right: an example of the EIS response of the sensing surface to 500 nM, with TFV as the specific target. Bottom right: the response to 500 nM abiraterone, as negative control.

4. Sensing surface: binary SAM of Aptamer-MCH

The gold electrodes were cleaned and then incubated in a solution of tenofovir-aptamer and MCH in PB buffer for 16 hours to form the biosensing surface. This step was followed by 50 minutes of 1 mM MCH backfilling to complete the surface blockage and lifting of the aptamers lying down on the surface. [285] These bioelectrodes were tested by EIS to detect 500 nM TFV for sensing surface optimization. The immobilization solution consisted of 1 µM of aptamer and 10, 50, 100 and

150 µM of MCH, in order to obtain different aptamer surface coverages (1:10, 1:50, 1:100 and 1:150 ratios of Aptamer:MCH, respectively).

EIS responses to negative control (Figure 50) were null, while specific response to targeted molecules (TFV) were approximately 15% of signal shift on average (Figure 50). Finally it was concluded that this biosensing surface exhibits higher sensitivity, higher specificity, and also makes a saving of time and effort, based on these measurements, compared with the response of other biosensors. Therefore, the binary SAM of aptamer:MCH was chosen as the proper sensing surface for highly selective TFV detection.

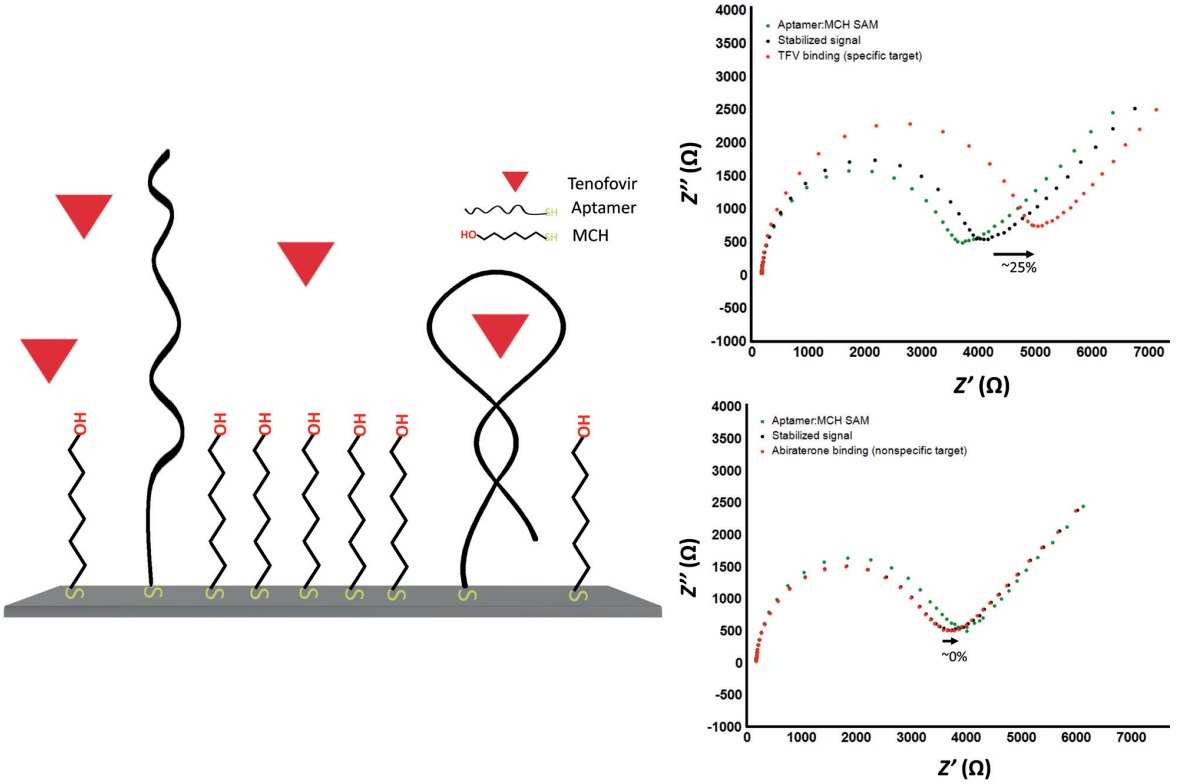

Figure 50. Left: schematic of the sensing surface including binary SAM of aptamer and MCH. Top right: the response of the sensing surface to 500 nM, with TFV as the specific target. Bottom right: the EIS response of the sensing surface to 500 nM, with abiraterone as negative control.

In order to achieve good sensitivity and specificity in our TFV aptasensor, an optimization of the sensor surface is fundamental. Changing the ratio of aptamer to MCH in the immobilization solution gives the possibility to modify the surface coverage of the aptamer and alter the interaction between the molecules on the surface. A balance is required between the amount of aptamers available on the surface and avoiding steric hindrance effects, due to the conformational changes of the aptamer required for the binding. This helps to increase the sensitivity and selectivity of the biosensor toward the TFV, which provides sufficiently low LOD and minimum non-specific interactions.

A schematic diagram of the fully formed sensing interface, containing the chemical structure of TFV, is presented in Figure 50-A. Upon binding of the aptamer to the drug, the aptamer undergoes a conformational change, increasing the charge density closer to the electrode, hence increasing the electrostatic potential barrier to the negatively charged redox marker – in other words, an increase in R_{ct} is observed.

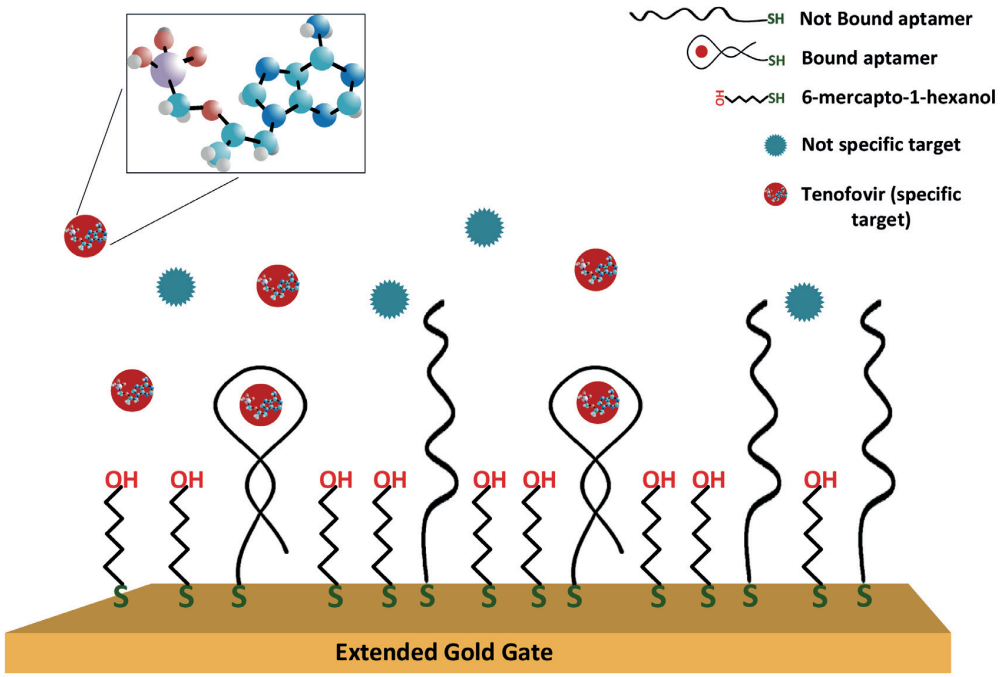

Figure 51. Binary SAM of TFV-aptamer and MCH as sensing surface of the biosensor. Inset: chemical structure of TFV with red for Oxygen, purple for phosphorus, light blue for carbon, white for hydrogen and dark blue for nitrogen.

The average of R_{ct} shifts for each aptamer:MCH ratio is presented in Figure 52. It is observed that the optimized ratio in terms of specific response is 1:100, showing 15.0 ± 5.5 % of R_{ct} shift with respect to the baseline (blank measurement). This value is ~2.4 times higher than 6.3 ± 0.9 % of shift corresponding to 1:50 ratio. Although in this experiment a large deviation was observed in the measured response, the trend of the recorded responses was the same for all samples and following the averaged signal.

The optimized ratio of 1:100, achieved in this work, was consistent with results reported by Formisano *et al.* [285] for a prostate specific antigen aptamer (PSA-aptamer):MCH binary layer. This PSA-aptamer had similar length (32 nucleotides) and two-dimensional structure as the TFV-aptamer used in this work. They also reported a surface density of aptamers equal to 1×10^{12} molecules cm^{-2} in their work for the similar sensing surface formed on a gold electrode of the same size and shape as in this work.

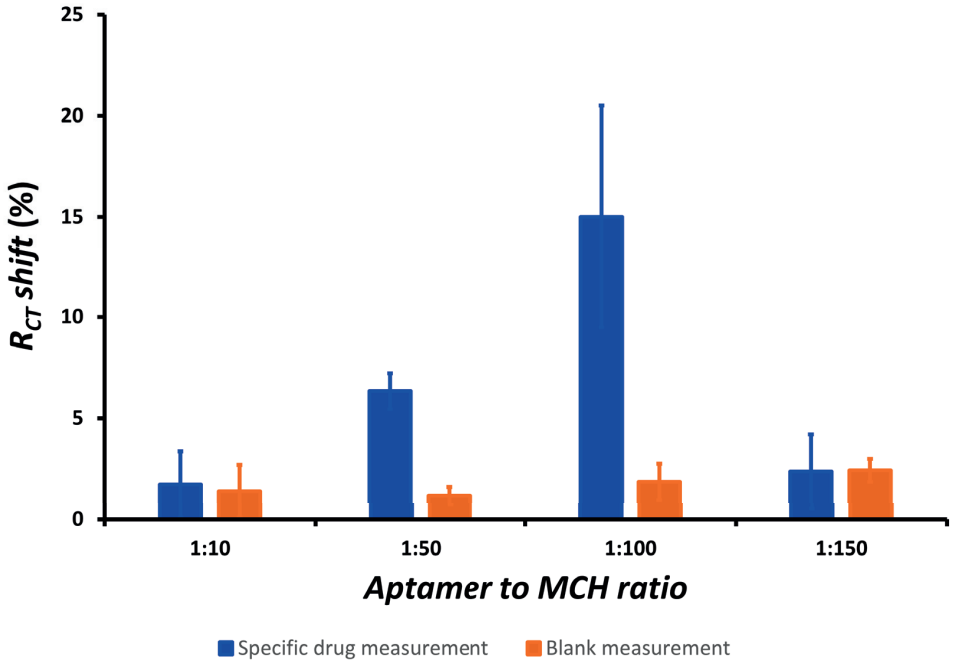

Figure 52. Sensing surface optimization. Blue bars indicate EIS responses of AptaFET to 500 nM of TFV exploiting various aptamer to MCH ratios. Highest R_{CT} shift for 1:100 ratio. Error bars in this and the following figures represent the standard error of triplicate measurements carried out on three electrodes.

The EIS response presented in Figure 52 shows a signal loss with either high and low aptamer to MCH ratio. This proves that too high a quantity of aptamers immobilised on the surface will prevent the binding and folding due to steric hindrance, as well as strong electrostatic repulsion between the aptamers. This will reduce the response amplitude of the system in terms of R_{ct} variation or lower I_d-V_{gs} characteristic shift for field-effect measurements. On the other hand, too high a ratio of aptamer to MCH leads to too few aptamers on the surface and, consequently, fewer recognition elements and reduction of the response. The latter also increases the possibility of a non-specific response of the system due to possible interactions of proteins with MCH.

4.2.3 Binding reaction investigation

SPR experiments were carried out as a primary study utilizing two parallel channels on each biofunctionalized chip, simultaneously, in order to verify the functionalization of the sensing surface. Consequently, binding targets to the sensing surface at different buffer conditions was studied using an SPR experiment, while one channel was used for a drug infused sample and the other one for blank buffer of the same type. The sensing surface was modified with MCH and TFV-aptamer, as is described in the bioelectrode development section (4.2.1 and 4.2.2). TFV and abiraterone solutions with a concentration of 500 nM were injected, and the variation of reflectivity angle was measured during the incubation cycle. This was followed by washing steps to remove all non-bonded residues. Abiraterone was used as a negative control to study specificity of detection. Experiments were carried out in PB (pH 7.0), PBS (10 mM; pH 7.4), and PBS containing 1 mM $MgCl_2$ (named PBS-$MgCl_2$). A washing step was carried out using the blank buffer as the same as the one infused with the drug. The recorded signals exhibited a much lower target binding effect for exper-

iments performed in PB and PBS with respect to PBS-$MgCl_2$, (Figure 53) in which binding reactions were clearly observed for both TFV (as target molecule) and abiraterone. Results of SPR experiments showed positive binding interaction for both experimented drugs that was observed as an increment of refractive index unit (RIU) in the SPR signal. Nevertheless, abiraterone molecules were removed from the surface during the dissociation cycle, while TFV molecules kept the binding to aptamers. After 20 minutes of incubation, specific interaction of aptamer/TFV resulted in a variation of the reflectivity angle of ΔRIU = 15 μRIU with respect to non-specific interaction and ΔRIU = 22 μRIU with respect to buffer.

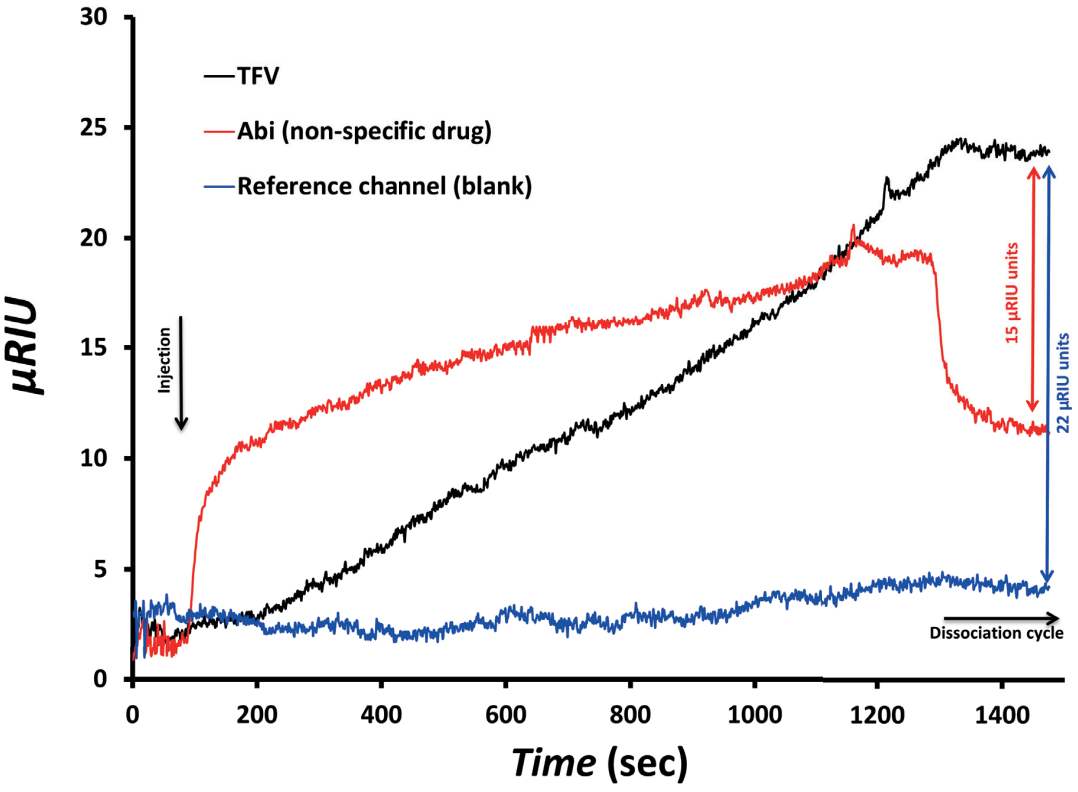

Figure 53. The specific interaction of TFV and TFV-aptamer (black line), and non-specific interaction of abiraterone with TFV-aptamer (red line). The blank response is illustrated in blue. 15 μRIU difference was recorded between specific and non-specific interactions.

While examining the issue of the selectivity of the presented sensor, we also observed with SPR some non-specific binding when passing a flow of abiraterone over the sensing surface (Figure 53 - red line). However, at the dissociation cycle, when the surface was washed with blank buffer, the majority of abiraterone molecules were washed away, while the TFV molecules maintained their uptake. This caused the abiraterone signal to be 15 μRIU lower than for TFV at the dissociation cycle. This non-specific interaction was expected, considering the chemical structure of abiraterone and the molecules on the surface. The abiraterone structure harbours three main features, including the aromatic nitrogen-containing heterocycle (pyridine moiety), the hydrophobic steroidal core, and the hydroxyl group that together make a high affinity of abiraterone for cytochrome P450 enzymes. On the other hand, they increase the non-specific binding of abiraterone

through unintended hydrophobic forces, or hydrogen binding to electronegative species that exist in the aptamer structure and on MCH. [219–221]

4.2.4 Dose-response behavior

In order to study the sensing performance of the system, the AptaFET biosensor was used to detect various concentrations of TFV. A typical response of AptaFET to 10 nM TFV solution respect to the blank baseline, and the $V_{threshold}$ (I-V characteristic) shift is demonstrated in Figure 54.

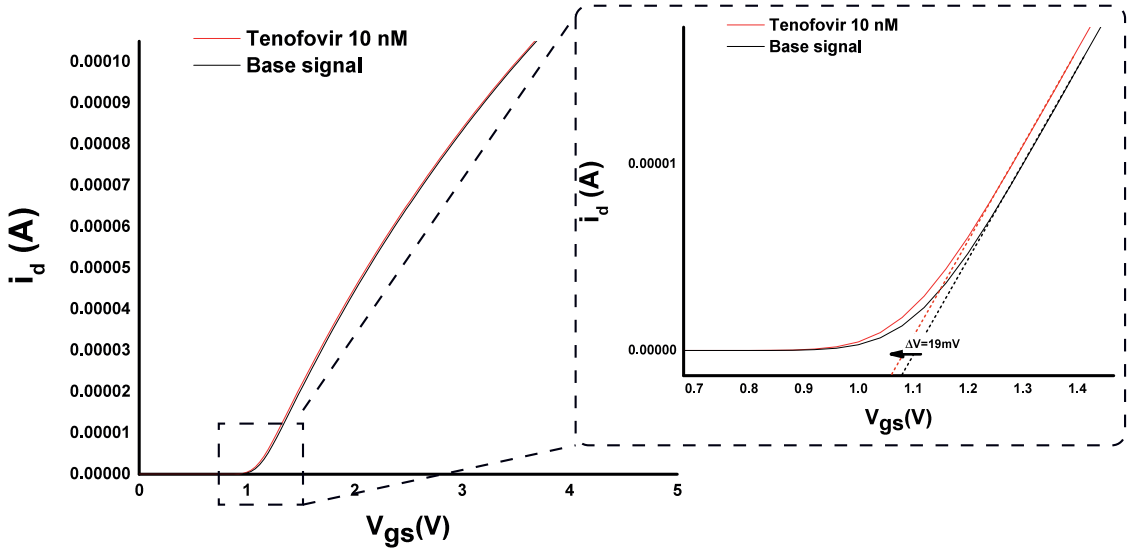

Figure 54. The current-Voltage characteristic of FET device before and after the binding reaction. Inset illustrates the threshold voltage shift after the interaction of the biosensor to 10 nM TFV solution.

The incubation procedure and other detailed information are described in section 4.2.1. In addition, the same experiment was carried out using 500 nM abiraterone and enzalutamide solutions as negative controls, on separate electrodes, without having preceeding reactions with TFV, to examine the selectivity of the AptaFET for TFV. To study the interaction of TFV with a non-specific sensing surface, electrodes were functionalized with a binary layer of PSA-aptamer and MCH (1:100 ratio), and tested by 500 nM TFV solution. The average voltage shift responses versus the logarithm of concentrations was illustrated on a graph to form the dose-response curve of AptaFET (Figure 55). Controls were also presented on the graph for comparison. The curve followed a sigmoidal behavior with a linear range between 1 nM and 100 nM, and showed saturation after 100 nM. A limit of detection of 1.2 nM was calculated for the biosensor as described in 4.3.6. Abiraterone, enzalutamie and PSA-aptamer experiments exhibited 1.3 ± 4.7 mV, 3.3 ± 0.9 mV and 2.7 ± 0.3 mV of I_d-V_{gs} shift (current-voltage characteristic of MOSFET device), respectively. These are negligible when compared to the 22.3 ± 1.8 mV shift obtained for TFV at the same concentration (500 nM).

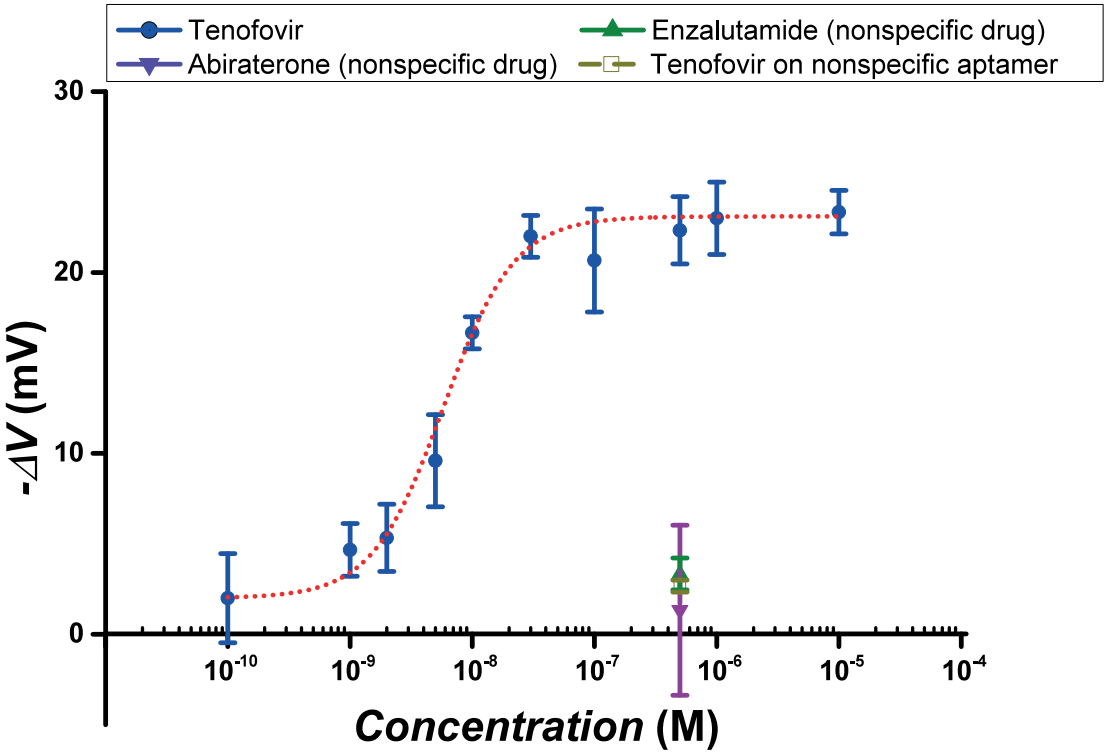

Figure 55. Dose-response curve of AptaFET biosensor. The specific response (blue points) fitted to the hill function with linear range between 1 nM and 100 nM, and EC50 of 5.8 ± 0.5 nM. Responses related to non-specific drugs and non-specific aptamers as negative controls in purple, green, and yellow.

The calculated LOD of the AptaFET is 1.2 nM (statistical analysis in 4.2.6), which is lower than what has been reported with usual electrochemical sensors, for example, on cytochromes P450. [66] As mentioned before, pushing the LOD to some nM range by means of the enzymatic biosensors proposed in a previous chapter is a challenge that is addressed at this part of the study, taking advantage of the sensitivity of field effect devices. This shows an extremely good performance for this innovative AptaFET in applications such as a TFV monitoring system. The LOD of the AptaFET falls well within the therapeutic range of TFV. In addition, the dose-response curve (Figure 55) exhibits a highly sensitive linear range between 1 nM and 100 nM. The linear range of the AptaFET is lower than the therapeutic target range, and the system saturates before the maximum range (~ 1 µM). This difference is an advantage for drug detection in human fluids, as it gives the possibility of sample dilution that will decrease the non-specific interactions and interferences related to the various metabolites that coexist in human plasma. To compare non-specific and specific responses, a high concentration of a non-specific drugs was used to show that, even at such high concentrations, the response of the biosensor is negligible. The aptamer used in this work has been characterized by Kammer et al. [286] using backscattering interferometry with a K_d value of 9 ± 1.4 nM. They have presented the specificity of the aptamer to its target by using penicillin as a negative control. The response of the AptaFET presented in this work is consistent with the data published by Kammer et al. The EC50 = 5.8 ± 0.5 nM, (section 4.3.6) which is calculated based on the dose-response curve for the biosensing surface, alongside the K_d value of 9 ± 1.4 nM [286] demonstrates a high affinity of the aptamer towards TFV and, thus, strong drug-aptamer bonding. The

possibility of setting loose bonded drugs without extensive efforts is very low. Nevertheless, we expect a small amount of drug dissociation and association on the surface that reaches equilibrium, and does not produce significant interference in biosensor response.

4.2.5 Applications: in-plasma detection and real-time drug monitoring

In-plasma TFV detection

The performance of the TFV AptaFET was also assessed using human serum. To start off with, the interference of non-specific coexisting proteins of human serum on the biosensor was measured. To perform the experiment, biofunctionalized electrodes were incubated in blank plasma (after stabilizing and taking the baseline in buffer) for half an hour and tested in PBS to obtain the response of plasma proteins and biolayer interactions. This interaction caused either small positive or small negative shifts as output, depending on the electrode, with an average response of -1.9 ± 4.6 mV. Secondly, AptaFET response in human plasma spiked with 500 nM of TFV was recorded, and compared with the baseline recorded for blank plasma. TFV binding reaction in human plasma produced a response of 16.3 ± 4.8 mV compared to a baseline in blank plasma – see Figure 56.

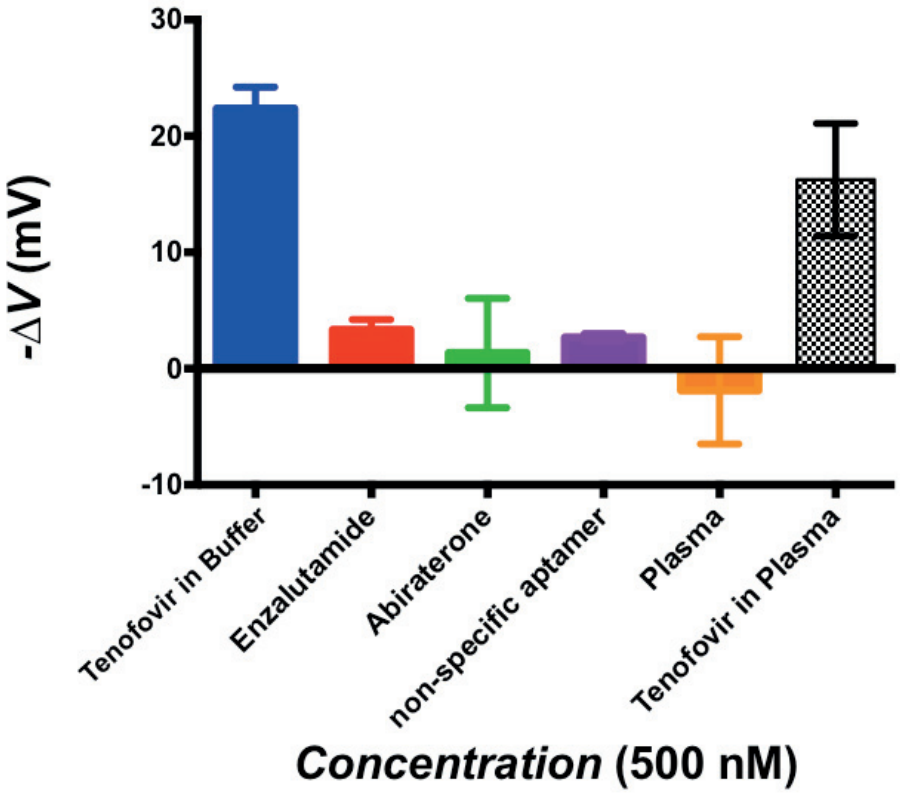

Figure 56. AptaFET response comparison. The response of the biosensor to TFV in PBS (blue), in human plasma (black pattern). Non-specific response to negative controls: enzalutamide (red), abiraterone (green) and blank blood plasma (orange). Non-specific response of TFV and PSA-aptamer interaction (purple bar). All target concentrations are 500 nM.

Figure 56 shows high selectivity achieved for the AptaFETs, both in PBS buffer and in blood plasma. Negligible non-specific binding responses are observed for controls such as enzalutamide and abiraterone, as well for the interaction of the target with non-specific sensing surfaces (anti-PSA aptamer). The data shows an AptaFET response for TFV detection in blood plasma comparable to the one obtained in buffer.

Exposure of the sensing surface to blank human plasma shows high resistance to fouling by plasma proteins, since the response of biosensors to non-specific plasma proteins was negligible compared to the specific response to drugs (orange bar in Figure 56). In addition, there is the possibility of exploiting the same detection system for a wide range of targets just by exchanging the TFV-aptamer with an aptamer specific to the new target, thanks to the low non-specific binding reactions between the biomolecules in the sample and the sensing surface. The possibility of extending the application to a wide range of targets has been reported before for other types of aptamer-based biosensors. [233]

The small positive and negative shifts of the FET output in response to plasma interaction was expected, since blood plasma contains various proteins with different charges that can bind to the surface and modulate the channel in different and contradictory ways. Moreover, abiraterone has also presented opposite signal shifts, which is due to the nature of its chemical structure; different interactions with the SAM layer causes different channel modulation and, therefore, opposite signal shift in the output.

Real-time TFV monitoring

The possibility of real-time monitoring with the proposed AptaFET was investigated as a proof of concept by using EIS to verify the binding reaction between TFV and the sensing surface at flow conditions. Real-time impedance measurements were used to investigate the TFV and aptamer interaction. Cleaned gold disc electrodes were functionalized with the optimized ratio of aptamer:MCH.

The real-part (Z') of the impedance at 10 Hz was then monitored in a flow of 10 mM ferro/ferricyanide solution. Once a stable signal was observed, TFV (in 10 mM ferro/ferricyanide) was injected to the flow to a final concentration of 400 nM. Z' started to increase after some seconds, and it stabilized at 123 ± 16 Ω after 2 minutes. The same experiment was performed using abiraterone as a non-specific target, which yielded null resistance increment in flow conditions. The results are shown in Figure 57 after baseline correction.

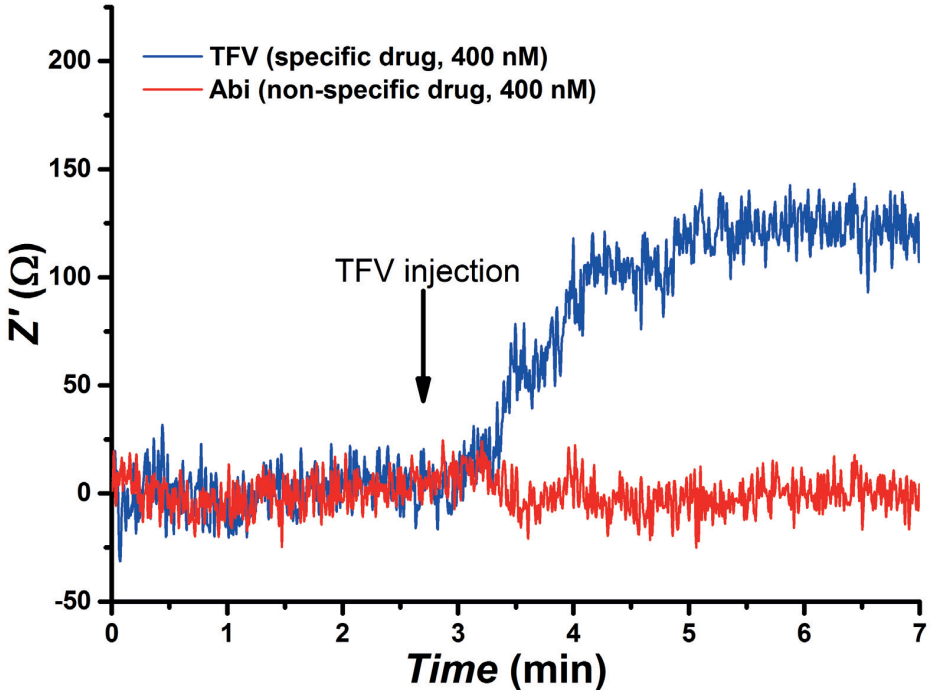

Figure 57. Real-time monitoring of the real part of the impedance at 10 Hz for an electrode modified with the TFV aptamer, upon injection of TFV as the specific target (blue) and abiraterone as the non-specific target (Abi; red). Baselines were subtracted for better comparison.

Comparison of the Real-time impedance responses of AptaFET to specific and nonspecific targets (Figure 57) in flow conditions shows the quality of TFV binding to the specific aptamer, and minimum non-specific interference at flow conditions. The recognition surface is the interface between the biosensor and the sample and, thus, has the main role in such an application. Therefore, successful drug detection in real time and at flow conditions using the same sensing surface of AptaFET can be considered as a proof of concept for the capability of AptaFET for this application.

The non-specific interactions of negative controls recorded by SPR, FET transducer and real-time EIS shows discrepancy that has been expected. This is mainly because SPR response is an indication of a binding reaction (or non-specific electrostatic interaction) between the target and the sensing surface (direct binding effect), while field effect and electrochemical impedance responses are due to the induced effect of binding reaction on the transducer (indirect binding effect). Therefore, they are related to the same bioevent, but the response of the biosensors has a different meaning. Secondly, the response of SPR is affected by all the molecules attached on the surface after the dissociation cycle by specific or nonspecific interaction, but in indirect response of FET and EIS the effect of specific interaction (combination of the binding of charged molecules and the resulting conformational change) induces more significant effect compared with the electrostatic attachment of small non-specific molecules on the surface. Considering the real-time experiment, performing the detection under flow format decreased the capability of non-specific target interaction with the surface, while the specific target bound on to its specific aptamer with high efficiency.

4.2.6 Statistical analysis

Nonlinear regression was used to fit a modified version of the Hill function (Equation 30) as an empirical model to the dose-response data obtained for the AptaFET presented in Figure 55. This model was prefered to the normal Hill function, because it correlates the recorded effect (response of biosensor) to the binding reaction (analyte concentration), while the conventional Hill function describes the relation between the binding reaction and the concentration of the occupied binding sites. [287, 288] The nonlinear regression analysis was performed using the requisite tools of Origin 8.5 (OriginLab, USA).

$$Y = E_{\min} + \frac{E_{\max} - E_{\min}}{1 + (\frac{10^{LogEC_{50}}}{10^{X}})^{n}} \quad (30)$$

To obtain the LOD of the biosensor, the $LOD_{\Delta V}$ was calculated using Equations 28 and 29, and then it was converted to concentration using the appropriate equation (Equation 30).

The parameters used in Equations 28 and 29 (section 3.4.1) for this analysis include $mean_{blank}$ = 1.8 mV, SD_{blank} = 1.2 mV, $SD_{lowest\text{-}concentration}$ = 4.3 mV (100 pM in this work). LOB = 3.8 mV, $LOD_{\Delta V}$ = 10.8 mV, and EC_{50} = 5.8 ± 0.5 nM as the calculated concentration that produces half the maximum binding response. The calculations result in a LOD of 1.2 nM for the AptaFET, an extremely good performance for an electrochemical sensor. The average reproducibility measured for the dose-response curve beyond the limit of detection is equal to 36.5%.

Although the dissociation constant (K_d) can be considered to be roughly equal to EC_{50}, it is not possible to calculate its exact value directly, using the appropriate model of this work. [288]

4.2.7 Comparison of performance with the current literature

A list of recent publications (after 2013) on small molecule monitoring is summarized in Table 7. The performance of the AptaFET in terms of the LOD and the linear range is better or comparable to other biosensors that are suitable for POC analytical applications (Table 7), or even the ones utilizing very complex and time consuming sample preparation or complex analytical processes. [289–294] These techniques are less suitable or not suitable at all for POC drug monitoring. For instance, fluorescent-based analytical methods need laboratory-labelling processes, which are complex and can interfere with the functionality of the biomolecule. Some label-free optical and mass spectrometry methods require professionals for their operation, in other cases their application is limited to a specific class of biomolecules (not all the molecules are ionizable).

Although low LODs have been obtained for some small molecules using different techniques, the LOD of this work is the lowest one in the literature for TFV detection, fully suitable for clinical applications. Comparing the data presented in this work with the literature shows the main advantage of our novel AptaFET with respect to many of the reported small molecule analytical

methods suitable for POC applications. This work compared well with other works in the literature [233, 239, 295, 296] in terms of sensitivity and selectivity. It works very well in human plasma with an extremely good detection and the capability to provide real-time monitoring.

Table 7. Examples of recently published works on small molecule detection.

Target	Analytical†	LOD	Linear range	References
POC-compliant detection methods				
Acetaminophen	Amperometry	2.1 nM	5 nM to 800 µM	[297]
Adenosine	EIS	20 fM	0.05 pM to 17 pM	[298]
Bisphenol A	FET	56 pM	1 to 10^4 fM	[299]
Chloramphenicol	SWV	5 nM	40 to 1000 nM	[300]
Cocaine	DPV	0.13 nM	0.1 to 10 nM	[301]
17β-estradiol	FET	50 nM	50 nM to 1.6 µM	[295]
Etoposide	DPV	5.4 nM	20 nM to 2 µM	[185]
Etoposide	SWV	1.29 µM	10 to 60 µM	[302]
Glucose	SWV	4 mM	4 to 20 mM	[97]
Glucose	FET	2 mM	2 to 8 mM	[303]
Kanamycin	SWV	14 pM	10 nM to 2 µM	[304]
Naproxen	CV	16 µM	Up to 300 µM	[208]
Oxytetracycline	SWV	0.22 nM	1.1 pM to 110 nM	[305]
Rifampicin	Amperometry	50 nM	2 to 14 µM	[306]
Streptomycin	SWV	10 nM	50 to 1000 nM	[300]
Tenofovir	**FET**	**1.2 nM**	**1 nM to 100 nM**	**This work**
Tenofovir	SWCAdSV	1.3 µM	1.7 to 17.4 µM	[307]
Theophylline	CV	50 nM	Up to 120 µM	[308]

†CV = Cyclic Voltammetry; SWV = square wave voltammetry; FET = field effect transistor; EIS = electrochemical impedance spectroscopy; DPV = differential pulse voltammetry; EMAT = electromagnetic acoustic transducer; LSV = linear sweep voltammetry; SWCAdSV = square-wave cathodic adsorptive stripping voltammetry; UV = ultraviolet; Vis = visible; BSI = backscattering interferometry.

At the end of this section of thesis, there were still a need to push the LOD to even lower values in order to cover the entire therapeutic range of TFV, even after the promising performance of this field effect biosensor. This also helped to offer a holistic methodology for monitoring a wide range of drugs, thanks to the possibility of extending the application of the proposed methodology to other targets just with small modifications. To achieve this aim, an innovative affinity-based biosensor was developed based on a miniaturized memristive Si-nanowire signal transducer with very high sensitivity, and aptamers as recognition molecules with high selectivity. The detailed information about this nano-biosensor, and the drug monitoring results it achieved are explained in the next section.

4.3 An aptamer-based memristive biosensor for TFV monitoring

DNA-aptamers are ideal candidates for absolutely new, ultrasensitive, highly specific and selective biosensors design. They also pave the way for real-time monitoring applications, thanks to their restorative properties. In this thesis we present the world's first reported DNA-aptamer regeneration achieved through a memristive technique, for drug detection in human serum. Silicon nanowires (Si-nanowires) anchored between Nickel Silicide (NiSi) pads, exhibiting memristive electrical characteristics, have been used in this part of thesis as an innovative approach for label-free, ultrasensitive drug monitoring. The SEM image in Figure 58 represents the structure and verifies the quality of the Si-nanowires used in this thesis with a length of 1 µm and a width of ~ 80 nm. The particular electrical response of these very special memristive nanodevices, modified by surface treatments, leverages the hysteretic properties exhibited by the memristive effect. The hysteretic loop in the electrical characteristic (I_d-V_{ds}) in the proposed memristive biosensor is observed, when it is subjected to a double voltage sweep (V_{ds} sweep), and also along the complete cycle consisting of DNA-aptamers immobilization, target binding and DNA-aptamers regeneration. It is then applied for the effective, ultrasensitive, label-free detection of tenofovir. After reporting the biosensor development (4.3.2), and casting more light on the binding mechanism as a proof of biomodifications methodology by SEM (4.3.3), the biosensor was tested with recognition surface regeneration (4.3.4) and, finally, TFV monitoring in buffer and human-serum (4.3.5).

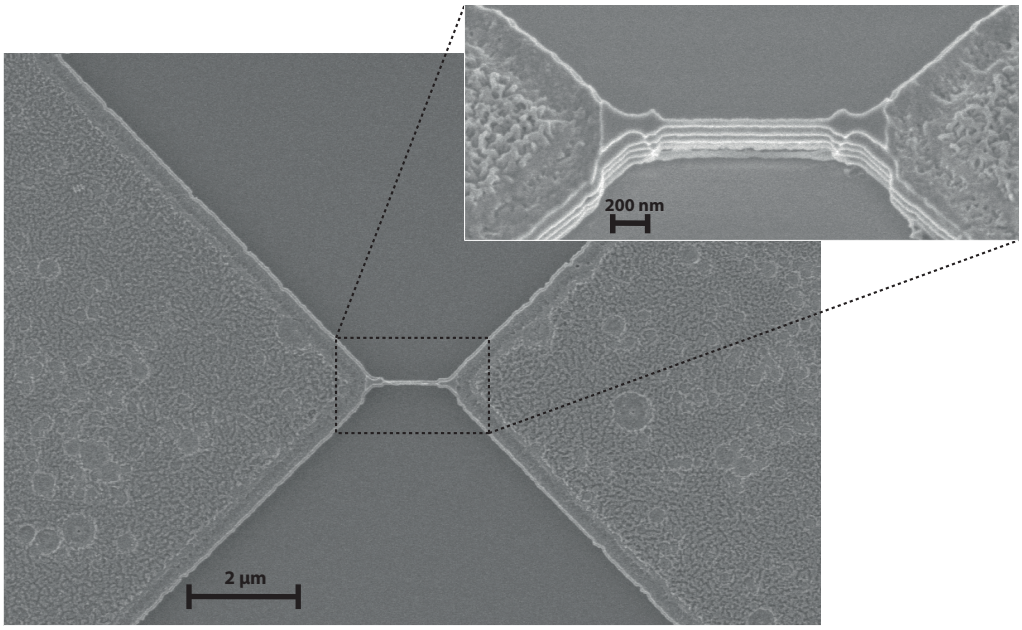

Figure 58. Schematic representation illustrating the memristive biosensor, and SEM micrograph depicting the Si-NW arrays anchored between the NiSi pads, which serve as electrical contacts of the freestanding memristive nano-device. Schottky-barrier junctions are formed between the Si and NiSi terminals. The position of the current minima for the forward and the backward regimes changes after the surface treatment, introducing a voltage difference in the semi-logarithmic current to voltage characteristics.

4.3.1 Memristive effect

In circuit theory, the three well-known basic elements are the resistor, the inductor and the capacitor (Figure 59). Those elements are defined as relationships between the four fundamental circuit

variables, which are the current *i*, the voltage *v*, the charge *q* and the flux ϕ. The forth fundamental element, the memristor, was introduced in 1971 by Leon Chua [309] linking charge and flux, by introducing a new parameter « *M* - memristance ». Memristor nomenclature, or resistor with memory effect, comes after the main property of these devices that is changing their resistance according to the charge flowing through them: [309]

$$d\varphi = Mdq \tag{31}$$

In the case of the constant M in linear elements, memristance is identical to resistance, but in memristive devices M is itself a function of *q*, yielding a nonlinear circuit element. [272]

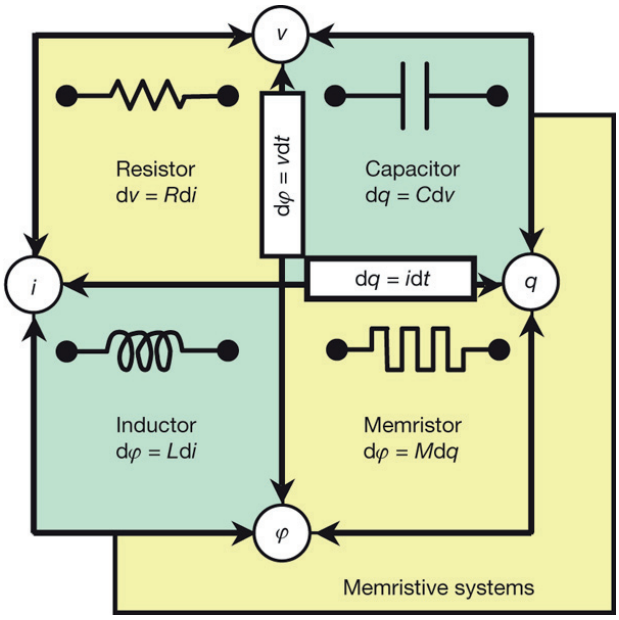

Figure 59. The four fundamental circuit elements: resistor, inductor, capacitor, and memristor. Reprinted with permission from [272].

The electrical model of the memristor element and its relationship with 3 other common elements of electrical circuits is illustrated in Figure 59.

In 1976 Chua and Kang [269] generalized the memristor concept to a much broader class of nonlinear dynamical systems they called memristive systems, which look like a nonlinear time-dependent version of Ohm's law.:

$$v = R(w,t)i \tag{32}$$

$$\frac{dw}{dt} = f(w,t) \tag{33}$$

Where *v* and *i* denote the port voltage and current, *w* is the variable state of the device - the state of the system - and *R* is a generalized resistance that depends upon the internal state of the device. Both *R* and function *f* are explicit functions of time. Equation 32 describes the memristor relation with time-dependent state variable « *w* ». The state of the device varies with time (Equation

33), and this means the system has a memory. In other words, the resistance will vary with the amount of charge passed through the element and is not a constant. [269, 272]

Voltage gap

Memristive nanowires are obtained via top-down techniques based on chemically-assisted etching processes, such as reactive ion etching, which are very aggressive and often result in surface roughness and silicon surface defects. Surface defects are usually associated with dangling bonds created by loose Si crystal atoms at the surface that leave unsaturated bonds behind them. These unsaturated bonds at the surface allow energy states within the forbidden energy gap, that are referred to as surface states. These energetically active surface states are continuously distributed in energy within the silicon band-gap with a charge state that is Fermi-level dependent. This means the surface states are associated with either acceptor-like or donor-like energy levels, and act as electron acceptors or electron donors, respectively.

Puppo et al. [310] have characterized a physics-based compact model that describes the occurrence of voltage-gaps on memristive nanowires. Their observations suggest that voltage gap based sensing is mostly based on the phenomenon of charge imbalance at the surface of the device, where charge traps continuously change their state if perturbed by an external bias, modified through exposure of the surface dangling bonds to different concentrations of biomarkers.

They have introduced three main contributors in the current-voltage characteristic of nanowires, including the surface current, bulk current and current component from Schottky contacts :

The dominant contributor is the surface current that includes two drift and diffusion components. Drift surface current is created by the hopping of charges, driven by an external voltage bias, from one surface trap to another, as well as a diffusive surface current caused by the concentration gradient of charged surface states. The bulk component of current is described by drift and diffusion components. Drift bulk current can be expressed as a function of the wire resistance and the voltage drop across it, while the diffusion component depends on the concentration gradient of the net charge into the nanowire. Nevertheless, the current in bulk nanowire is mostly diffusive, as drift current in the nanowire core seems to be negligible due to the full depletion of the channel, as a consequence of the NiSi Schottky barriers at both ends. The last factor affecting the electrical behavior of the device is the metal–semiconductor interface introducing a Schottky barrier. Positive and negative carriers see this barrier in their path, and with a proper forward bias, thermally-excited carriers can flow through the barrier and form the current (thermoionic emission). Under reverse bias the current is stopped as just a small fraction of carriers have enough energy to pass the barrier (leakage current).

The environmental modifications and surface functionalization alter these three components differently, leading to the modification of the current-voltage characteristic of the device. In other words, they finally change the pinch-off of the hysteresis loop, and form the so-called voltage gap (Figure 60). Thanks to its high dependence on external charges coming from the surrounding environment, the voltage gap can be used as a biosensing parameter.

As the surface currents are the main element of current voltage characteristics, the major alteration comes from the dynamic occupations of the nanowire surface state energy bands, enabled by the incoming external charges from the bio-species. Moreover, the surface charges induce a lowering of the Schottky barrier on the junctions of the device, that further modifies the voltage gap. This effect is similar to the impact of dopant atoms introduced in semiconductors at metal-semiconductor effective barrier height.

In the case of this thesis, the appearance of the voltage gap is mainly defined by charging phenomena at the surface of the nanowire, where the donor states (positively charged) trap the negative charge of the aptamer. Therefore, immobilization of a surface layer of aptamers carrying a negative net charge on the memristive device implies the loss of the pinched loop, and the appearance of the voltage gap at the electrical response of the nanowire. This leads to an accumulation of negative charge and thus a surface charge imbalance that is reflected by the different zero crossing points of the current in its forward and backward path, and finally an increment of the voltage gap. The further increment of net negative charge, from the uptake of a negatively charged target, for instance a drug, will increase the voltage gap more.

Practical realization and applications

In addition, to the theoretical definition, Chua also suggested a practical realization of a memristor using complex combinations of FET (field effect transistor), BJT (bipolar junction transistor) and operational amplifiers to obtain a circuit that behaves like a memristor. However, the first physical implementation of the memristor was proposed in 2008 by HP lab. [272] Using a simple analytical model called the Drift model, this work showed that memristance arises naturally in nanoscale systems where ionic transport and solid-state electronics are coupled under external bias. In 2011, Chua published a further work arguing that all two-terminal non-volatile memory devices based on resistance switching are memristors, regardless of the device's material and physical operating mechanisms [270] opening new perspectives in the study of memristive behaviour and in new applications involving memristive systems.

Memristive devices are two-terminal devices that present this kind of memory effect, and have been implemented in many applications, particularity in the field of memories and logic design. Furthermore, implementations of memristive devices include dense logic programmable circuits, [311] artificial synapses, [312] cellular nanoscale networks [313] and two-terminal Resistive RAMS (ReRAM) for standalone memories, Field Programmable Gate Arrays (FPGA) and Generic Memristive Structure (GMS) for 3D-FPGA. [314] Moreover, freestanding, two-terminal, Schottky-barrier, silicon nanowires anchored between NiSi pads, exhibiting memristive electrical characteristics, have been reported as a novel approach for label-free, ultrasensitive bio-sensing applications. [171, 315–318] As mentioned before, a hysteretic loop in the I_d-V_{ds} characteristic of the nanowire, when subjected to a double V_{ds} sweeps, is reported for those particular nanowire structures. Nevertheless, upon bio-functionalization of the nanowire surface with a probe molecule (e.g. antibodies or DNA-aptamers), a difference in zero current crossing according to the sweep direction appears (forward and backward sweeps), giving rise to the voltage sweeps split, the voltage gap, in the semi-logarithmic electrical characteristic of the device (Figure 60). The target molecule uptake

(e.g. specific antigen) changes the value of the voltage gap by masking or enhancing the effect of the probe molecule, depending on the type and the concentration of the reagent introduced.

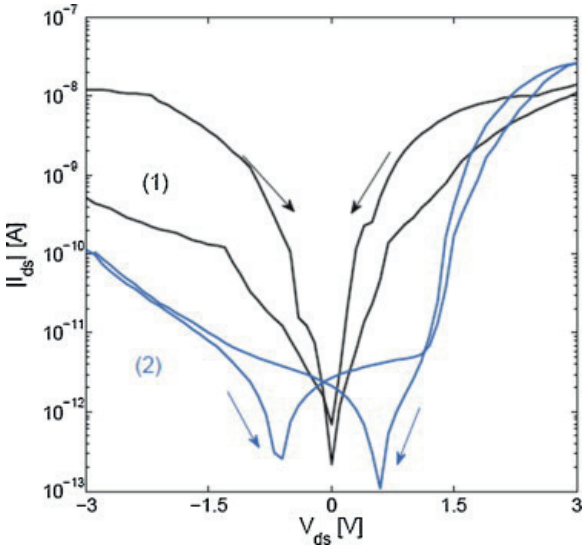

Figure 60. Electrical characteristics of memristive biosensors before (1) and after (2) bio-functionalization with antibodies. A double voltage sweep of the terminal voltage V_{ds} is performed, resulting in hysteretic behaviour of the device. Reprinted with permission from [315].

As described above, the appearance of the voltage gap is attributed to the effect of the extra charges surrounding the channel of the device, leading to simultaneous occurrence of molecule gating effects and the lowering of the Schottky-barrier at the junctions, as a consequence of the surface modification first with the bio-functionalization molecules, and, thereafter with the increasing uptake of target molecules. Thus, the voltage gap value gives rise to a label-free detection method. However, there are some interfering factors, such as temperature, humidity, and charges from dissolved ions in the solution, that can alter the *I-V* characteristic of a memristor and result in a fouling effect. [315] This happens mainly as a result of disturbance of the surface charge states by exposure of the surface dangling bonds to environmental factors. Thus, it is important to keep them constant between different experiments, to minimize the effect and the resulting false responses.

A detailed explanation and discussion on the processes required and results obtained for the fabrication, experimenting and response analysis of the proposed memristive nano-biosensor for HIV personalized medicine is reported below.

4.3.2 Material and Method

Materials

Amino group terminated TFV-aptamers (5'-Aptamer-C6 Amino-3') were commercially provided by BasePair Biotechnologies (Pearland, Houston, USA). Human serum, magnesium chloride ($MgCl_2$), DMSO and PBS (10 mM; pH-7.4) were all purchased from Sigma-Aldrich (Switzerland). PBS buffer

were always filtered through 0.2 µm filters before use. Sodium hydroxide solution (NaOH) were purchased from Sigma Aldrich (Switzerland) and diluted to the concentration of 1 M. Silane (3-Glycidyloxypropyl)trimethoxysilane (GPTES) were purchased from Sigma-Aldrich (Switzerland) and used as received. TFV, enzalutamide powders were purchased from Medchemtronica (Stockholm, Sweden) and were dissolved in dimethyl sulfoxide (DMSO) to the concentration of 5 mM. All other reagents were of analytical grade. All aqueous solutions were prepared using 18.2 MΩ cm ultrapure water with a Pyrogard filter (Millipore, Feltham, UK).

Electrical and Morphological Analysis

The electrical characteristics of the nanofabricated memristive structures are acquired using a probe station and a configuration of contact probes in the semi-logarithmic scale, using a Keithley 6430 semiconductor characterization system in a two terminal configuration by double sweeping the source to drain voltage between −2.4 V and +2.4 V. These measurements allow the observation of the changing hysteresis properties of the memristive biosensors as a function of the surface treatment that leads to a charge variation. Electrical characterization performed on wires after the nanofabrication process indicates a hysteretic loop at zero voltage for the forward and the backward scans of the current. The memory effect observed depends on the charge carrier rearrangement at the nano-scale, according to external disturbances, such as an applied voltage bias. The hysteresis modification after the surface treatment is studied in terms of voltage difference calculated between the forward and backward current minima of the electrical characteristic curves. All of the measurements were carried out at room temperature, in a stable environment of humidity and temperature. This helped to prevent interferences due to environmental effects, as nanowires had shown sensitivity to these environmental changes. The electrical experiments were performed in dry condition to increase the sensitivity of the biosensor. Therefore, after the incubation of nanowires in target samples they were washed by distilled water and dried gently by nitrogen gas flow. In addition to the electrical validation, morphological analysis of the memristive biosensors is carried out using a Scanning Electron Microscopic MERLIN, from Zeiss. The imaging is performed at 1.7 kV (Figure 58), 15 kV and staged at 34.9° (inset Figure 58) and 1.2 kV (Figure 62 and Figure 65). Due to the top-down nanofabrication process used, the width along the structures is not perfectly homogeneous. However, this can be considered as an asset, since it increases the freely available area for DNA aptamer binding, which increases DNA aptamer loading and hence better performance of the biosensors.

Memristive Nano-Biosensors Fabrication

Development of the proposed nano-biosensor combines a top-down nanofabrication approach for the realization of the memristive nanowires, as well as bottom-up strategies for the acquisition of the finalised memristive nano-biosensors.

Silicon nanowire devices are fabricated through a top-down fabrication process performed on (100) oriented Silicon-On-Insulator (SOI) wafers with low boron concentration (NA ≈ 10^{15} atoms

cm^{-3}). SOI substrates are used in semiconductor manufacturing, for example in microelectronics, to isolate the active part of devices. The complete process flow for the fabrication of the device, as represented in Figure 61, has 8 steps:

a) The first step consists of the patterning of the S/D regions by E-beam lithography (EBL system; Vistec BPG5000+, running at 100keV) on a positive photoresist for subsequent metal deposition and lift-off. After 5 min of dehydration on the hotplate (180°C), the wafer is spin coated with 120nm thick polymeric PR, the Poly(MethylMethAcrylate) (PMMA). First, low molecular weight PMMA-495K is spin coated (4000 rpm) on the wafer; then, after 10 min of PR baking on the hotplate, the substrate is spin coated (4000 rpm) with a second layer of high molecular weight PMMA-950K, and subsequently baked at 180°C for 10 min for resist polymerization.

b) The PR is then exposed on the electron beam (dose of around 220 $\mu C/cm^2$), developed in MiBK(Methyl isobutyl ketone):IPA(isopropanol) 1:3, and used for Ni deposition.

c) Before Ni deposition, the coated wafer is processed in an Oxford PRS900 oxygen plasma tool for PMMA descum (≈ 15 sec). This step is typically used for removing final portions of exposed resist, and minimizing the surface roughness features for metallization. In addition, in order to guarantee a good adhesion of the deposited metal to the substrate, the exposed Si surfaces are thoroughly cleansed of native oxide in a BHF bath for 15 sec, and immediately transferred to an Alliance-Concept DP650 sputtering tool. The sputtering tool provides the possibility of performing short non-aggressive Ar ion plasma cleansing steps to the substrate to remove any native oxide before the actual metal sputtering without breaking the chamber vacuum. Then, a 45 nmNi blanket deposition step is performed by sputtering.

d) Lift-off consists of the dissolution of the sacrificial layer (PR) together with the parts on the substrate that are covering it. In other words, after this process, only the Ni parts deposited in the exposed surfaces of the wafer, where the resist has been removed by EBL, will remain. Lift-off is performed by leaving the coated wafer immersed in acetone overnight, for dissolution of the sacrificial layer.

e) The substrate is processed with a three-step annealing procedure in forming gas (H_2–N_2) atmosphere, with a 25°C/min ramp-up from room temperature. In three steps, the temperature is maintained at 200°C for 20 min, 300°C for 20 min, and at 400°C for 20 min, respectively. In this process, the Ni is allowed to consume fully while diffusing in the Si, and the final NiSi layer thickness is determined via the initial metallic Ni layer thickness.

f) A negative tone photoresist, namely Hydrogen SilsesQuioxane (HSQ) at 2% concentration, was chosen for the high resolution and pattern requirements. This PR has good dry etching selectivity to Si and allows for a thin, ≈50 nm layer by spin coating. Moreover, HSQ allows for a fast exposure (negative tone) and high resolution.

g) After spin-coating, the photoresist is exposed to an electron beam (dose of ≈1800 μC/cm^2), and subsequently developed for 30 sec in MF-CD26.

h) Finally, vertically stacked and suspended silicon nanowire (Si-NW) arrays, anchored between two NiSi pillars, are assembled. EBL is used to pattern the nanowire mask on a high performance resist. After the patterning of the HSQ mask, the nanowires are defined through a single etching step comprising multiple DRIE cycles. DRIE is performed in the Alcatel AMS 200 SE plasma Si etcher, with a 22 sec long etching.

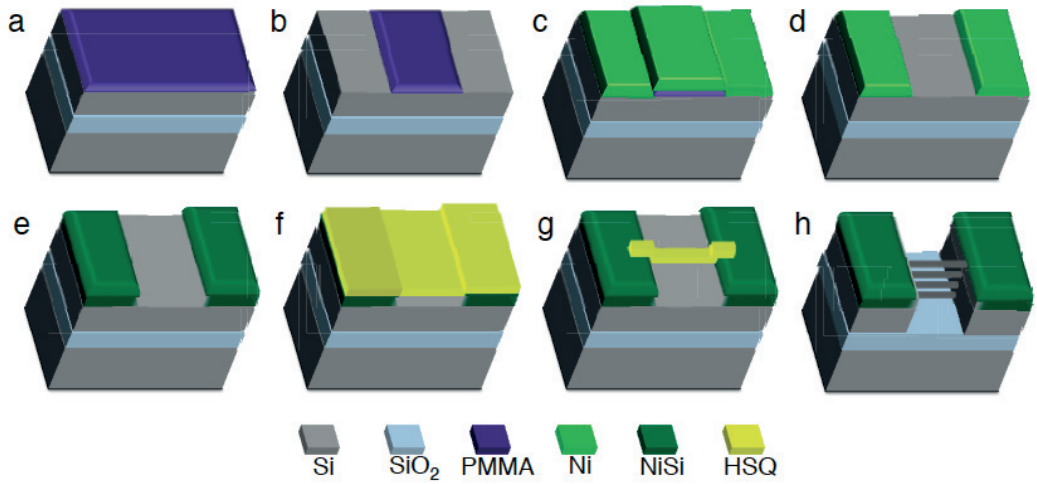

Figure 61. Process flow of Si-nanowires fabrication. Reprinted with permission from [316].

Morphological analysis by SEM (Figure 58 and Figure 62) verified the successful fabrication of Si-nanowires with length of ~ 1 um and width of ~ 80 nm.

Biofunctionalization

Biofunctionalization started with forming an absolutely homogeneous layer of GPTES molecules on the surface of silicon nanowires in a clean room, through a gas phase Salinization (CVD). To this aim, bare silicon nanowires were first activated by oxygen-plasma treatment for 15 minutes (Harrick Oxygen-Plasma, 200 mTorr, 29 W). This bombardment of the surface with high-energy oxygen ions formed a layer of hydroxyl groups on the surface (hydroxylation). Then, activated nanowires were placed in a desiccator in normal vacuum conditions along with 500 μL of the silane-solution, for 2 hours. Chemical reactions between hydroxyl groups and methoxy groups on silane molecules in gas phase formed durable and homogeneous binding (covalent bonds) of GPTES across the nanowire surfaces. [319, 320]

TFV-aptamers were functionalized with the amino group at their 3' terminal to be used as a handle for immobilization. For folding the aptamers to their active form, first, they were diluted to the final concentration of 2 μM in 10 mM PBS solution and 1 mM $MgCl_2$; then they were unfolded by heating them at 90 °C for 5 minutes and let them to cool down to room temperature (approximately 30 minutes). To finish the process, a sensing surface was formed over the silane-coated nanowires (described above) by incubating them in this solution of 2 μM TFV-aptamer, for 30

minutes. This interval assures the complete forming of the sensing surface by covalent binding between amino groups of aptamers and glycidyl groups of GPTES. After that, nanowire chips were washed with PBS and distilled water to remove any unbound aptamers and salts. Finally, the chips were dried by nitrogen gas, and stored at room temperature.

Regeneration procedure

A series of denaturation, pH shocking and refolding was used for surface regeneration (unbinding the target from the aptamer and restoring the aptamers to the unfolded and functional form they had before the conformational change): Nanowires were thoroughly washed with deionized water to remove any drugs or salts; they were then incubated in NaCl 2M solution at 85°C for 10 minutes in order to denature the aptamers and, thus, unbind the target from the aptamer; we then immersed them in NaOH 1M solution to give a pH shock to eliminate any remaining drug-aptamer binding, followed by deionized-water rinsing; finally they were inserted in a PBS-$MgCl_2$ 1mM solution at 85°C for 2 minutes and left to cool down for 15 minutes. This last step caused any denatured or collapsed aptamer to be refolded, and thus the sensing surface was functional for a new detection.

4.3.3 Surface characterization

The alterations of the surface morphology of the device during the consecutive treatment steps is a further proof of the efficiency bio-modification methodology that was applied. It is worth mentioning that surface analysis is performed immediately after each modification step, and no other intermediate step or treatment is applied to the devices than the treatment with the molecules of interest. This means that the morphology of the surface is clearly changed due to the reagents under experiment.

For morphology analysis, SEM images were taken after each functionalization step and the averaged width were measured at several parts of nanowires along the structure and on different devices to obtain good statistics. When analysed, the data depicted a mean-width increase equal to 3.25 ± 1.22 nm upon the immobilization of DNA-aptamers on the silanized surface compared to the mean-width of 82.78 ± 1.08 nm that was registered just after silanization. This value represents the binding of one layer of DNA-aptamers over GPTES molecules, since this increase is compatible with the length of DNA-aptamers that are reported in the current literature. For instance, Zhao et al. [321] have reported sizes in the range of 2.6 - 4.5 nm or 4.8 - 4.9 nm for DNA molecules immobilized over Au surfaces in salt and in aqueous solutions, respectively. In the literature, the aptamer height is also indicated with a value of 4-5 nm for aptamer hairpin loops immobilized on DNA crossover tiles [322] and of 4.15 nm for DNA-aptamers bound on the surface of Si-nanowires. [323]

It worth mentioning that, according to the literature, the binding of large molecules such as proteins on recognition probes increases the height of the biological assay that is a well-expected consequence of the presence of the large bio-molecules (e.g. proteases or proteins). [322–325]

Nevertheless, an opposite effect has been reported when up-taken molecules are small molecules such as adenosine. [321] This decrement can be explained by the conformational change in aptamer structure after the binding reaction. This phenomenon is observed in this study in the case of TFV binding, as the performed analysis on the SEM images of nanowires (Figure 62) after incubation in TFV solutions exhibited an average reduction of 1.95 ± 2.42 nm in the width of nanowires to only 84.08 ± 2.36 nm. The average difference after the drug binding, compared to the width just after aptamer immobilization (86.03 ± 0.57 nm), corresponds to the aptamer bending. This is mainly due to the folding effect that follows the drug up-take. Similar values have been reported in the literature for the DNA-aptamer conformational changes after the drug binding. [325] A good example is the work of Zhao et al. [321] that have presented a comparison between the initial heights for the unfolded DNA-aptamers of 4.8 nm, height of folded aptamer of 3.8 nm in the presence of adenosine (a small molecule at the size range of drugs) and, even, the case of unbounded, unfolded but largely collapsed aptamers due to the present of a salt solution. Their findings, consequently, resulted an average aptamer height of 2.6 nm. According to their work, aptamer heights differ between 1 nm to 2.2 nm based on different scenarios happening after the exposure to the small molecules in solution containing salt.

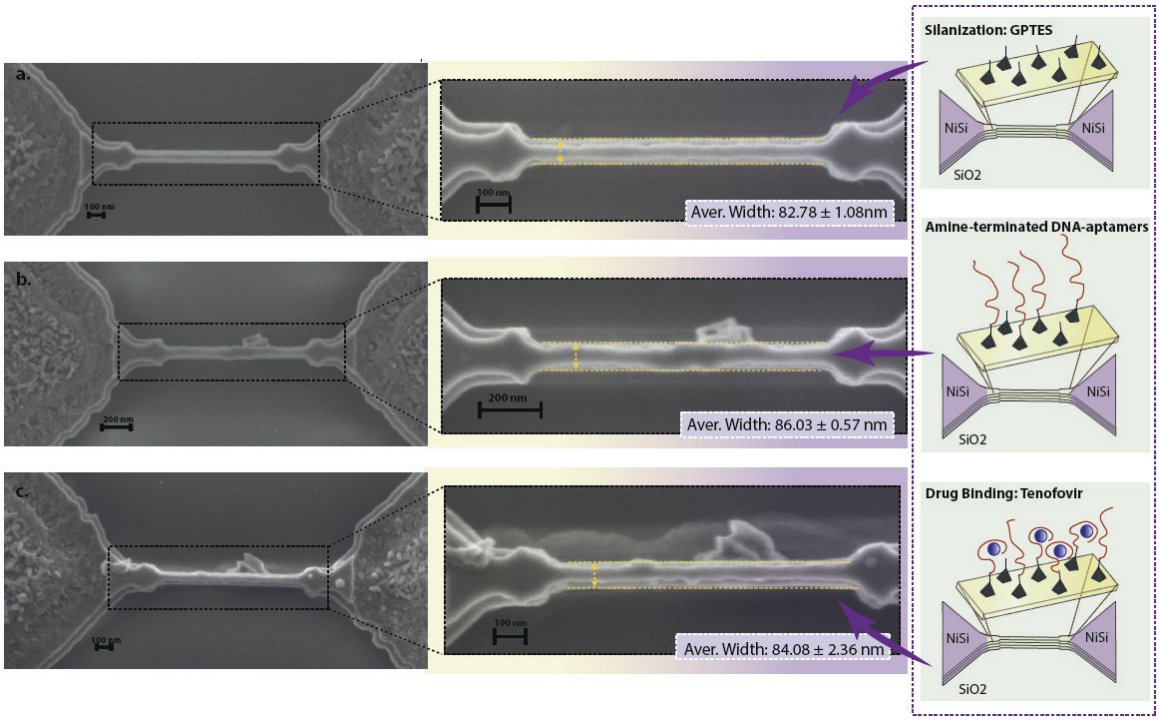

Figure 62. SEM micrograph depicting the nanodevices anchored between the NiSi pads, which serve as electrical contacts of the freestanding nanostructures. The nanodevices are imaged directly after the silanization process (a). After the DNA-aptamer immobilization on the surface (b). After exposure to TFV solution of 10 μM (c). The mean width of the nanodevices changes accordingly, following the conditions introduced by each surface treatment.

In the present study a combination of these phenomena occur as well, a fact that is also demonstrated by the average mean width difference value upon the exposure of the device to the drug solution, that indeed arises within the above-mentioned range. Upon the device exposure to the drug solution, part of the DNA-aptamers is folded after successfully binding with the target drug. However, not all DNA-aptamers finally bind efficiently with the TFV, and, as a consequence, those

aptamers remain unfolded or collapsed due to the presence of salts and positive substances that are included in the buffer or the serum solution. This phenomenon is well reflected through the standard error hereby presented. Namely, the value of the average difference varies from the height of a full standing aptamer on the silanized surface, to the height of folded aptamers. This is due to the drug binding that is desired for the system, and in some cases to a completely collapsed system on the surface.

4.3.4 TFV monitoring and TFV-aptamer regeneration

The whole sensing cycle, consisting of aptamer immobilization, TFV binding reaction, sensing-surface regeneration, and TFV re-binding, is efficiently recorded by monitoring the variations of the electrical hysteresis of the memristive nanostructures.

The voltage gaps are illustrated in Figure 63, after analysis of the hysteretic responses[19]. Figure 63 shows that, after treatment with DNA-aptamers, the electrical response of the nanodevices indicates a voltage difference of 116 ± 34 mV. Furthermore, as hypothesized, following the exposure of the nanodevices to the target drug solution of 100 nM, an increase of the voltage difference occurs as an aftereffect of the drug binding, reaching the value of 156 ± 24 mV - indicating an increase of 34.5 %. This change is caused by the charge-density modification at the surface of the device, due to the introduction of negatively charged drug molecules on the sensing surface. However, the most promising outcome was in the electrical response after the regeneration of the sensing surface, after the drug binding. Interestingly, it is demonstrated that the voltage difference decreases after the regeneration process to a value of 120 ± 15 mV, that coincides with a value corresponding to the voltage gap after aptamer immobilization on the surface.

The very same nano-devices are exposed to the drug solution once again, after regeneration, to verify the nano-biosensor reliability further, in repeated measurements, as well as the capability for further capture and detection of the target molecule. This time, a higher concentration, equal to 1 μM, is introduced. Higher concentration of reagent implies higher charge density and, as expected, their uptake results in a more pronounced modification of the voltage-gap. The recorded voltage difference indicates a value of 240 ± 23 mV - twice (100 % increment) the signal exhibited by DNA-aptamers, and 53.8 % more than the hysteretic response related to 100 nM TFV.

Finally, a further regeneration step is carried out to illustrate the nano-biosensor's repeated-regeneration character. It is indeed demonstrated that the voltage difference of 121 ± 39 mV registered after this further regeneration process coincides with the value achieved initially for the aptamer immobilization on the surface. It also replicates the one obtained after the first regeneration.

---

[19] Differences between the hysteresis of recorded signals observed as a voltage gap between the signals of nanowires recorded during forward and backward voltage scans.

That means that the biosensor is reproducible after any regeneration process, down at the original value of the voltage-gap, and, therefore, ready for a new measure of the target molecule concentration. The reproducibility of the hysteretic response after the two regeneration steps (compared to a blank response) were calculated to around 3.4 % and 4.3 %, respectively. The difference between percentages are negligible, even in comparison with measurement errors usually obtained in the detection of drug binding.

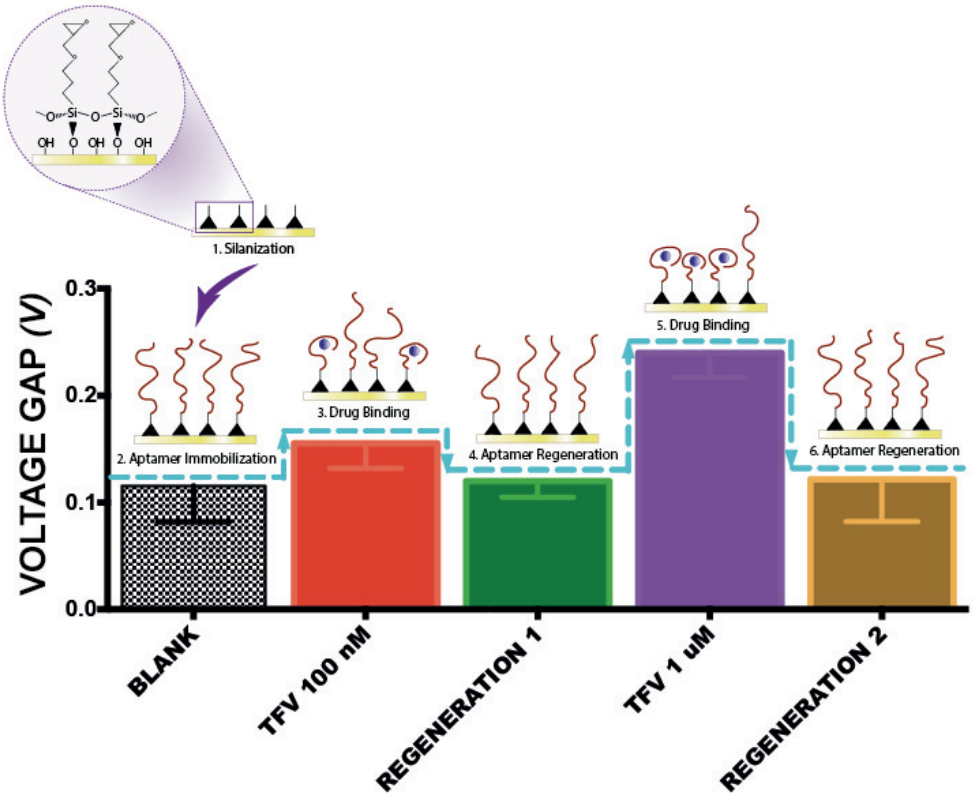

Figure 63. DNA-aptamer immobilization, target molecule binding and DNA-aptamer regeneration cycle, illustrated through the electrical hysteresis variations.

4.3.5 Label-free, effective drug screening

Having demonstrated the direct and highly efficient response of the nano-biosensor to various steps of drug detection and regeneration, we make further use of this holistic approach for label-free, ultrasensitive TFV monitoring in buffer and in human serum. A typical I-V characteristic of a single memristive Si-nanowire array, such as the hysteretic response of a memristive nano-biosensor, is presented in Figure 64. The voltage gap increased from 80 mV for blank measurement to 24 mV for detection of 1 μM of TFV.

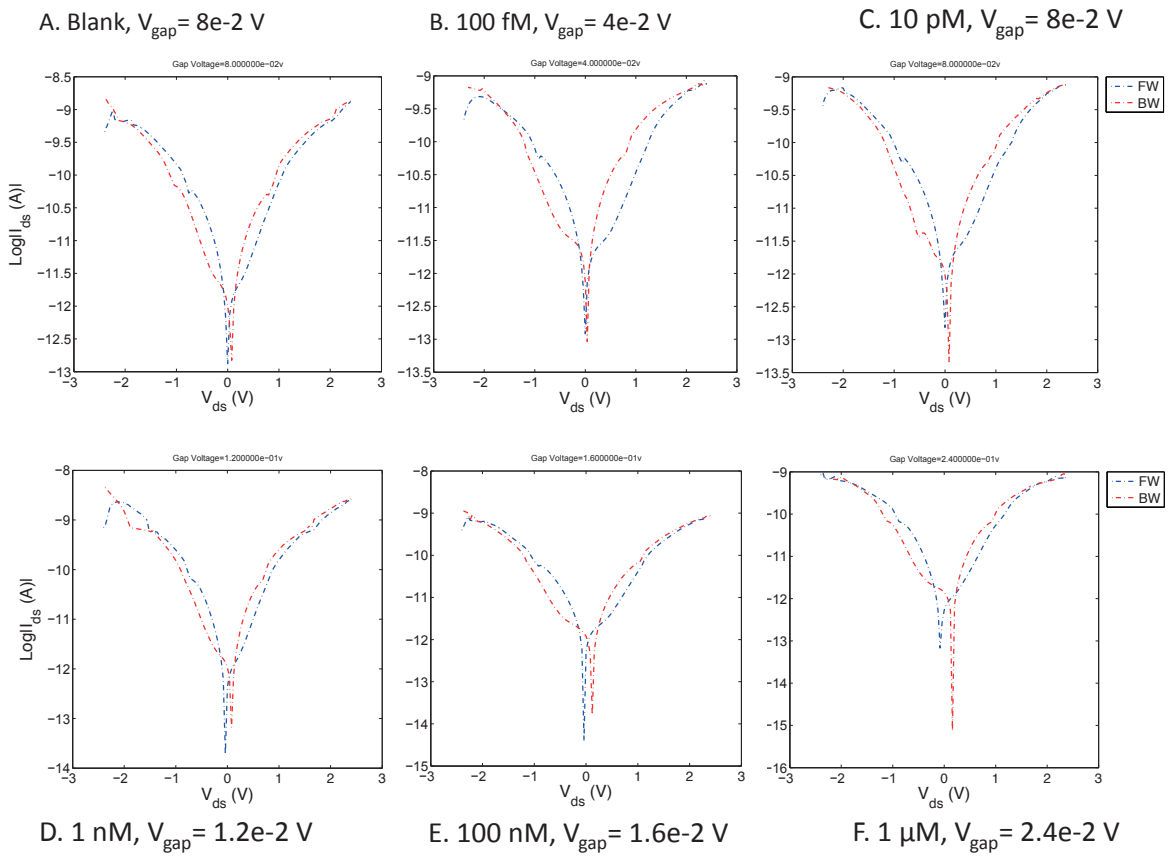

Figure 64. Typical hysteretic response of a memristive biosensor to increasing concentrations of TFV from blank (A.) up to 1 µM (F.)

The average voltage differences while increasing the concentration of TFV in buffer and human serum samples are recorded and presented in Figure 65. Solutions of TFV are prepared with concentrations in a range from 100 aM to 1 µM. This range is within, and slightly below, the clinical range of TFV, opening up the possibility for other future applications with diluted serum, as well as assuring an economy of reagents, thus requiring a minimum amount of clinical samples.

To show the performance of the proposed new biosensors more clearly, firstly TFV detection is attempted in PBS solutions, as a proof of concept. Secondly, effective drug detection in human serum is attempted and carefully characterized. In both cases, the successive uptakes of negative charge at the nano-device surface leads to an increasing trend in the voltage gap that follows the increasing concentration of the detection target drug - see Figure 65.

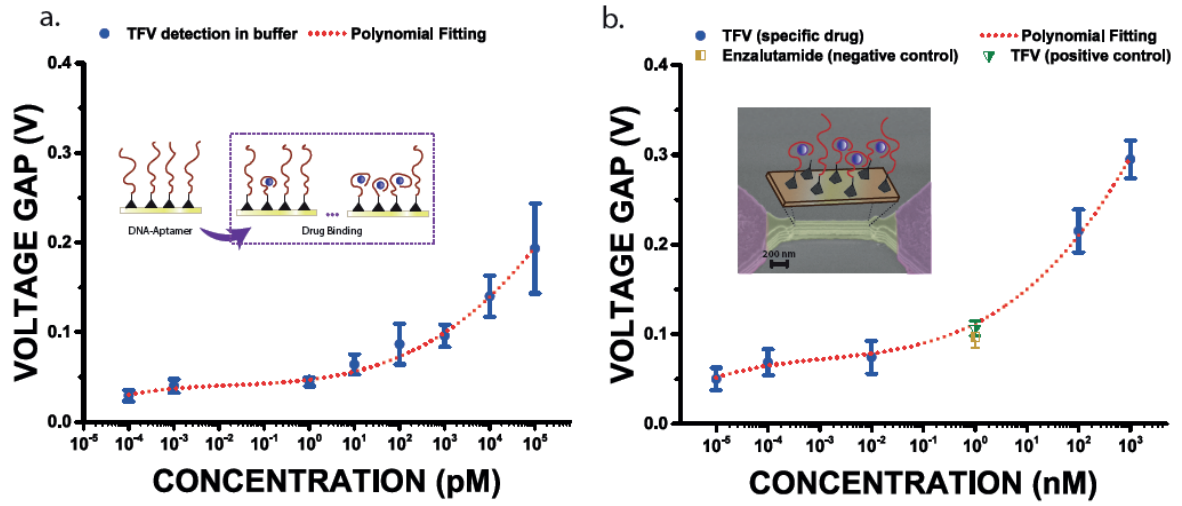

Figure 65. Analytical performance and effective drug detection through the electrical hysteresis variations in buffer solution (a) and in human serum solution (b).

In case of in-buffer detection, an average voltage gap of 29 ± 6 mV was obtained for 100 aM TFV.An increasing trend of this parameter of the hysteresis is depicted, after the dose increase, in Figure 65(a), up to a value of 193 ± 51 mV for 100 nM TFV solution, the maximum concentration implemented. In case of in-serum detection, a hysteretic response of 49 ± 35 mV is initially indicated for a concentration of 10 fM, that reached a final value of 295 ± 61 mV for 1 μM (see Figure 65 (b)). Both curves in Figure 65 are obtained by applying the data to third-order polynomial curves (Equation 34; 4.3.6). Further analysis of the data showed a promising LOD of 3.3 pM and 3.4 nM for in-buffer and in-serum detection, respectively.

As a positive control, in-serum detection of an intermediate TFV concentration (1 nM) was performed at the end of in-serum detection cycles, after the regeneration of the sensing surface. The hysteretic signal of the biosensor that was observed, as is depicted in Figure 65 with green markings, was 97 ± 31 mV. This was applied to the value predicted by the trend of the dose-response curve. This is quite an important result, demonstrating clearly the reliability of the proposed nanobiosensor, as well as the efficiency of the proposed method for continuous monitoring of therapeutic compounds. Furthermore, the implementation of a negative control drug, enzalutamide, is performed as an additional step, following the positive control. Importantly, the 89 ± 35 mV voltage gap obtained for the negative control detection brought no significant hysteresis modification (<9 % difference) for the very same drug concentration of 1 nM, therefore no drug binding occurred for the negative control case, exhibiting the specificity of the methodology applied.

4.3.6 Statistical analysis

The dose-response data obtained for the range of TFV concentrations in buffer and in human serum were analysed with Origin software, and were applied to a typical polynomial curve with equation of third-order, as is shown in Figure 65. The appropriate equation is:

$$y = \text{Intercept} + \alpha x^3 + \beta x^2 + \gamma x \quad (34)$$

With a root-mean-square value (**R**-Square) of 0.96 and a Residual Sum of Squares (RSS) of 1.33. The parameters in the appropriate equation of in-buffer detection mean that the Intercept = 47 ± 3 mV, and other coefficients are equal to:

$$\alpha = 4.59 \times 10^{-4} \pm 1.85 \times 10^{-4}, \beta = 0.0024 \pm 3.4024 \times 10^{-4}, \gamma = 0.0063 \pm 0.0026$$

While for in-serum detection **R**-Square = 0.99, RSS = 0.19, Intercept = 112 ± 12 mV and other coefficients are equal to:

$$\alpha = 9.39 \times 10^{-4} \pm 3.42 \times 10^{-4}, \beta = 0.0081 \pm 0.0016, \gamma = 0.0291 \pm 0.0034$$

A very low LOD = 3.3 pM for PBS buffer and LOD = 3.4 nM for human serum are calculated from 9 independent samples, as described in section 3.4.1, following the work of Armbruster et al. [155], whereas for in-buffer experiments $mean_{blank}$ = 0.048 mV, SD_{blank} = 0.0179 mV, $SD_{lowest\text{-}concentration}$ = 0.02 mV is the standard deviation of hysteretic responses related to the lowest concentration drug. The calculated LOB and $LOD_{\Delta V}$ (Equations 28 and 29) are equal to 0.077 mV and 0.11 mV, respectively. For in-serum experiments $mean_{blank}$ = 0.12 mV, SD_{blank} = 0.1 mV, $SD_{lowest\text{-}concentration}$ = 0.35 mV, LOB = 0.28 mV and $LOD_{\Delta V}$ = 0.34 mV. Finally, the appropriate equations were used to obtain the corresponding LOD.

4.3.7 Comparison with the current literature

A list of cutting-edge drug monitoring systems, recently reported in literature, is summarized in Table 8. The LODs demonstrated in this study for a memristive nano-biosensor are compared in the table, and they are highlighted as the best ever obtained, to the best of our knowledge, as reported in the literature for drug detection in general, and for TFV in particular (Table 8).

The LOD presented here demonstrates a sensitivity 10 times higher for in-buffer drug detection with respect to the literature, and shows a performance twice better for drug sensing in human serum than the best ever obtained. The best case reported so far in human serum is mentioned in the work of Radhapyari et al. [326], which reached 0.035 nM, but in 10 times-diluted human serum, while we reached 3.4 nM in undiluted serum – a far better performance. It is worth repeating the point that we worked with undiluted human serum, further indicating the higher sensitivity and efficiency of our suggested methodology, with respect to the best ever presented in the literature.

Table 8. State-of-the-art list of reported drug detection to date as example.

Target drug	Method*	Surface	LOD (nM)		Linear Range (nM)	Ref.	Comments
			Buffer	Bio-matrix			
6-mercaptopurine	Voltam	Graphite/Polypyrrole/MWCNT	-	80	200 - 100000	[327]	Diluted human urine sample
Gleevec	Conduc	Si-nanowire	-	-	Up to 100	[328]	-
Paracetamol	Voltam	MWCNT*	2.9	-	5 – 1000	[329]	-
Penicillin	Voltam	Boron-dopped diamond	-	320	400 - 100000	[330]	Human urine sample
Tamoxifen	Voltam	Enzyme/Polyaniline/Pt	0.2	-	27 - 297	[331]	-
Clenbuteral	Voltam	Benzedithiol-GNPs*	-	43.96	100 - 800	[332]	Diluted rat urine sample
Chloramphenicol	Ampero	Cds NPs/GNPs	0.14	-	0.15 – 2.94	[333]	-
Artesunate	Ampero	Gr-Polyaniline Nanocomposite	0.031	0.035	0.13 - 1	[326]	Highly diluted human serum
TFV	BSI	Glass chip	2.5	-	Up to 20	[286]	-
TFV	LC-MS	-	-	680	1360 to 350000	[334]	Human urine
TFV	Voltam	HMDE*	450	870	Up to 17000	[307]	Diluted and precipitated human plasma
TFV	LC-UV	-	-	10.4	35 to 3480	[335]	-
TFV	LC-MS	-	-	7	35 to 3480	[335]	-
TFV	**Field effect**	**MOSFET**	**1.2**	**-**	**1 to 100**	**Present work**	**PBS buffer**
TFV	**Memristive**	**Si-nanowire arrays**	**0.0033**	**3.4**	**0.001 to 1000**	**Present work**	**Human serum**

Voltam: voltammetry; Conduc: conductance; Ampero: amperometry; BSI: back scattering interferometry; LC: liquid chromatography; MS: mass spectroscopy; UV: ultra violet; MWCNT: multiwalled carbon nanotubes; GNP: gold nanoparticle; HMDE: hanging mercury drop electrode

The final performances of two proposed affinity based biosensors are presented in Table 8. The comparison between the LOD and the linear range shows that changing the transducer from field effect to memristive effect has drastically changed the biosensing performance. Taking advantage of the memristive nano-biosensor, the LOD for in-buffer detection of TFV was improved by 3 orders of magnitude, while a leading LOD for in-serum detection of TFV was also obtained. In addition, the dynamic range of the affinity based biosensor has been increased from 1-100 nM to 0.001-1000 nM. The superior performance of the memristive affinity-based biosensor provided the ultra-sensitivity and ultra-selectivity (presented by negative and positive controls) that was

expected in this study. This superior performance completely covers the therapeutic range of TFV and can be considered as the proper solution for POC TDM of AIDS, as well as most of the drugs that fall within the third class of drugs introduced in this thesis.

4.4 Original contribution

This chapter proposed and characterized a POC drug monitoring system (Figure 45) suitable for drug detection in human plasma (Figure 55) and real-time monitoring (Figure 56). In this section the possibility of human diagnostics by an aptamer-based field effect biosensor was successfully demonstrated. Biorecognition surface was optimized to maximize the specific and suppress the nonspecific interaction on the recognition surface, by testing many different chemistries and surfaces, as well as optimizing the aptamer to spacer agent ratio by EIS. The LOD and linear range of the biosensor (1.2 nM and 1 to 100 nM, respectively) fell inside the physiological ranges of the target (from a few nM up to 1 μM). The sensitivity and selectivity of the biosensor for the specific target was successfully tested (Figure 55). In addition, this method can be used for monitoring new biomolecules by exchanging the TFV-aptamer with another aptamer that is specifically produced for the new target. This proves the capability of the detection method being proposed, for use in the continuous monitoring of a wide range of small molecules in human plasma.

In order to improve the performance further, and to be able to cover the entire therapeutic range of TFV, a novel affinity-based biosensor is developed, based on miniaturized memristive Si-nanowire signal transducers with very high sensitivity. The binding reaction at the recognition surface of the biosensors induces a change in the voltage gap that is observed on the hysteretic I-V characteristic of memristive Si-nanowires. this modification can be used as the response of the biosensor.

An innovative application of the memristive effect is presented for the first time, in this thesis, as suitable for POC drug monitoring. The potential applications, such as continuous and real time monitoring, were investigated by portraying the regeneration capabilities and reusability of the nano-biosensor without degradation of its DNA-aptamer recognition properties.

The hysteretic electrical properties displayed by biofunctionalized nanofabricated silicon nanowire arrays are put to use successfully for drug monitoring. Moreover, a complete set of experiments, essential in the demonstration of the biosensor's capabilities, were successfully performed - including DNA-aptamer immobilization, target binding and DNA-aptamer regeneration.

The increment of the voltage gap - as registered in the hysteretic curves - occurs during the drug binding, after exposure of the nano-bio-devices to the target drug solutions. This change is as a consequence of the change in the charge density at the devices' surface. This increase is found to be strongly related to the concentration of the target detection molecules.

This also demonstrated that, after the regeneration step, the values achieved for the hysteresis voltage gap coincide with the value achieved initially just after the aptamer immobilization on the surface. This proves the general capability of this new memristive biosensor for continuous monitoring and reusability. Therefore, the successful label-free screening of TFV is demonstrated here

by achieving a superior LOD of 3.4 nM - a leading performance in state-of-the-art POC drug monitoring systems for in-human serum detection (Table 8).

This innovative approach holds great promise for the real time continuous monitoring of therapeutic drugs. Moreover, the application of this paradigm can be expanded to detect a wide range of different molecules by choosing the specific aptamer probes accordingly. This offers a potential for integration in more complex platforms for many different applications.

Chapter 5 Conclusion

5.1 Results achieved

The main objective of this thesis has been biosensor development for therapeutic drugs monitoring, with special focus on chemotherapy of prostate cancer and AIDS. To this aim, biosensors were classified into three different categories based on the electrochemical and biological properties of targeted drugs: A) SPE-based biosensors for electroactive drug monitoring. B) Enzymatic biosensors for the monitoring of drugs involving cytochrome p450 in their biological metabolic pathways. C) Affinity-based biosensors to target non-electroactive and non-enzymatic drugs. The latter also offers a reliable solution for highly selective POC drug monitoring. Three model drugs have been targeted and successfully detected in this study: etoposide, abiraterone, and tenofovir. The main achievements of this thesis can be classified in the following nine points:

First: Proposing a new methodology for the theoretical calculation of the electroactive surface area, and proving the concept in experimental conditions. The effective characterization of nanomaterial properties and their impact on electrochemical performance, making use of this methodology.

Second: Demonstrating the high performance of GNP-based nano-biosensors in contrast to the ones functionalized with MWCNTs and Bi_2O_3 nanoparticles, with three times the sensitivity of biosensors that are not nanostructured.

Third: Optimization of nano-biosensors in terms of nanostructuring and the detection method, and detection of etoposide in the therapeutic range.

Fourth: Demonstrating a quantum phenomenon, the Coulomb blockade, and its impact on boosting the electrochemical performance of nano-biosensors, for the first time.

Fifth: Characterizing the electrochemistry of the anti-prostate cancer drug, abiraterone, in direct interaction with MWCNTs, and in interaction with cytochrome P450 3A4, for the first time. Showing the electroactive and electrode-fouling characteristics of drug, as well as, its inhibitory effect on cytochrome P450 3A4.

Sixth: Development of an optimized enzymatic nano-biosensor for prostate cancer in personalized medicine, with superior performance between enzymatic biosensors for abiraterone detection.

Seventh: Extensive optimization of the recognition surface to maximize the binding reaction between tenofovir and its specific aptamer, and minimizing the biofouling effects. The study clearly demonstrates the importance of aptamer surface density on the drug-monitoring performance.

Furthermore, simple but effective chemistry suggests that a translational strategy can be easily applied to extend the application to other drugs by using their specific probe.

Eight: Development of an aptamer-based field-effect biosensor suitable for point-of-care personalized medicine for HIV, with a promising performance in detection of tenofovir, an anti-HIV drug. Demonstrating its applications for in-plasma detection and real time monitoring.

Ninth: Development of a novel memristive nano-biosensor for HIV personalized medicine and TDM. Demonstrating its outstanding performance as a reusable nano-biosensor by characterizing the superior regeneration capabilities of this memristive nano-biosensor. In-buffer and in-plasma detection of tenofovir with the best ever reported performance for drug monitoring.

5.2 Conclusion

The results of this study, and its implications for the POC TDM of malignant diseases, can be divided into 3 categories:

A direct-electrochemical biosensor was developed for the detection of Etoposide. The transducer element of the biosensor was optimized to reach sub-micromolar detection limits. The optimized nano-biosensor was then successfully used to detect etoposide in its therapeutic range.

An enzymatic biosensor was developed for the detection of abiraterone based on the optimized transducer. It was used to detect abiraterone in its therapeutic range in human serum with record performance levels.

An affinity-based biosensor was developed using memristive Si-nanowires as transducers for TFV detection. It was used to detect TFV in human serum successfully, with extremely high sensitivity and selectivity.

5.3 Future development

Many of the promising methodologies reported in this thesis were proposed for the first time, and they can benefit from further optimization and modification before reaching their final potential, and being made ready for industrialization. This is mainly because: firstly, offering solutions for all classes of drugs for a specific disease, as is done in this thesis, is very intensive and requires a lot of time and effort, while at the same time it provides broader advances and deeper insights into biosensing. Secondly, a deep investigation has been done in this work to study in detail the physics behind many phenomena that have been used for many years in electrochemical detection, such as the Coulomb blockage. Thirdly, very few data or no data have been available about the drugs targeted in this thesis and, thus, basic study on the electrochemistry of the targeted drugs was performed on them in this thesis, often for the first time. Therefore, some possible future studies to push forward the solutions proposed here are as follows:

- The integration of nanostructured sensors with miniaturised custom-made microelectronics on a single chip. Miniaturised medical devices require the combination of microfabri-

cated electrochemical platforms with ad hoc low-noise electronics on a printed circuit board.

- The integration of different solutions proposed here on a single multiplexed platform for multisensing. Simultaneous measurements of more than one analyte, for instance a cocktail of drugs used for prostate cancer treatment, is possible. Taking into account the information reported in this work about nanostructuring a proper multiple detection can be achieved within adequate concentration ranges. The chemical crosstalk between different platforms on a device, or resulting from multiple measurements within one platform, and the influence of interfering species can be suppressed by the appropriate nanostructuring of each electrode.

- The integration of the system with proper microfluidics for real-time and in-human plasma detection, taking advantage of the proposed methodologies in this work for real time and under-flow monitoring applications. This can help to suppress the chemical crosstalk, and also provides the possibility for developing Lab-On-Chip biosensing systems.

- Many different nanomaterials can be deposited simply, using a drop-coating technique, keeping the additional electroactive area the same, and investigating the boosted impact on the biosensing performance and, more importantly, the physical and chemical reasons behind it.

- The results achieved are promising for realizing a fully operational implantable device in human subjects. To this final aim, recognition surfaces should be formed in such a way that they provide stable catalytic or binding activity for several months, at least. Further experiments are needed to understand for how long the proposed biosensors retain their activity when they are immobilized in a substrate, or when they are in prolonged contact with a biological fluid. In this respect, some strategies to improve an enzyme's immobilization and protection, such as entrapment in a matrix, or confinement behind a protective membrane should be investigated and optimized. However, a loss of activity in the recognition surface is inevitable in the long term, due to the denaturation of biomolecules. Therefore, an additional back-up methodology for refreshing the sensing surface, such as the implementation of an "enzyme reservoir" in the implantable sensor, can be considered. Moreover, other techniques can be employed to assure a long-lasting implantable biosensor including testing the long-term endurance of the device with corrosion tests before implantation, or the development and implementation of long-lasting protective membranes to prevent the electrodes from biofouling. Providing adequate vascularization around the implant by proper packaging, to prevent the blockage of analyte diffusion by the formation of fibrotic tissue around the implant. Nanoscaling to help the host to tolerate the implant with less body response. A very deep and sophisticated investigation into the long term biocompatibility of the implant.

References

1. About PCAST. In: White House. https://www.whitehouse.gov/node/8421. Accessed 19 Dec 2016

2. President's Council of Advisors on Science and Technology Priorities for personalized medicine [online].

3. Nebert DW, Vesell ES (2006) Can personalized drug therapy be achieved? A closer look at pharmaco-metabonomics. Trends Pharmacol Sci 27:580–586. doi: 10.1016/j.tips.2006.09.008

4. Fackler JL, McGuire AL (2009) Paving the Way to Personalized Genomic Medicine: Steps to Successful Implementation. Curr Pharmacogenomics Pers Med 7:125–132. doi: 10.2174/187569209788653998

5. Corona G, Rizzolio F, Giordano A, Toffoli G (2012) Pharmaco-metabolomics: An emerging "omics" tool for the personalization of anticancer treatments and identification of new valuable therapeutic targets. J Cell Physiol 227:2827–2831. doi: 10.1002/jcp.24003

6. Goodacre R Metabolomics – the way forward. Metabolomics 1:1–2. doi: 10.1007/s11306-005-1111-7

7. Lee J–., Kohn EC (2010) Proteomics as a guiding tool for more effective personalized therapy. Ann Oncol 21:vii205-vii210. doi: 10.1093/annonc/mdq375

8. Jiang Z, Dragin N, Jorge-Nebert LF, Martin MV, Peter Guengerich F, Aklillu E, Ingelman-Sundberg M, Hammons GJ, Lyn-Cook BD, Kadlubar FF, Saldana SN, Sorter M, Vinks AA, Nassr N, von Richter O, Jin L, Nebert DW (2006) Search for an association between the human CYP1A2 genotype and CYP1A2 metabolic phenotype: Pharmacogenet Genomics 16:359–367. doi: 10.1097/01.fpc.0000204994.99429.46

9. Clayton TA, Baker D, Lindon JC, Everett JR, Nicholson JK (2009) Pharmacometabonomic identification of a significant host-microbiome metabolic interaction affecting human drug metabolism. Proc Natl Acad Sci 106:14728–14733. doi: 10.1073/pnas.0904489106

10. Zanger UM, Schwab M (2013) Cytochrome P450 enzymes in drug metabolism: Regulation of gene expression, enzyme activities, and impact of genetic variation. Pharmacol Ther 138:103–141. doi: 10.1016/j.pharmthera.2012.12.007

11. Ingelman-Sundberg M (2003) Human drug metabolising cytochrome P450 enzymes: properties and polymorphisms. Naunyn Schmiedebergs Arch Pharmacol 369:89–104. doi: 10.1007/s00210-003-0819-z

12. Rang HP, Ritter JM, Flower RJ, Henderson G (2014) Rang & Dale's Pharmacology: with STUDENT CONSULT Online Access. Elsevier Health Sciences

13. Mehrotra N, Gupta M, Kovar A, Meibohm B (2006) The role of pharmacokinetics and pharmacodynamics in phosphodiesterase-5 inhibitor therapy. Int J Impot Res 19:253–264. doi: 10.1038/sj.ijir.3901522

14. Sultana J, Cutroneo P, Trifirò G (2013) Clinical and economic burden of adverse drug reactions. J Pharmacol Pharmacother 4:73. doi: 10.4103/0976-500X.120957

15. Institute of Medicine (US) Committee on Quality of Health Care in America (2000) To Err is Human: Building a Safer Health System. National Academies Press (US), Washington (DC)

16. Carleton BC, Smith MA (2006) Drug safety: Side effects and mistakes or adverse reactions and deadly errors? Br Columbia Med J 48:329.

17. Rottenkolber D, Schmiedl S, Rottenkolber M, Farker K, Saljé K, Mueller S, Hippius M, Thuermann PA, Hasford J, for the Net of Regional Pharmacovigilance Centers (2011) Adverse drug reactions in Germany: direct costs of internal medicine hospitalizations. Pharmacoepidemiol Drug Saf 20:626–634. doi: 10.1002/pds.2118

18. Paving the way for personalized medicine. Technical report, U.S. Department of Health and Human Services, U.S. Food and Drug Administration, October, 2013. - Google Search. https://www.google.ch/webhp?sourceid=chrome-instant&ion=1&espv=2&ie=UTF-8#q=Paving+the+way+for+personalized+medicine.+Technical+report%2C+U.S.+Department+of+Health+and+Human+Services%2C+U.S.+Food+and+Drug+Administration%2C+October%2C+2013. Accessed 7 Nov 2016

19. Hug BL, Keohane C, Seger DL, Yoon C, Bates DW (2012) The costs of adverse drug events in community hospitals. Jt Comm J Qual Patient Saf 38:120–126.

20. Montellano PRO de, Voss JJD (2005) Substrate Oxidation by Cytochrome P450 Enzymes. In: Montellano PRO de (ed) Cytochrome P450. Springer US, pp 183–245

21. Wulfkuhle JD, Edmiston KH, Liotta LA, Petricoin EF (2006) Technology Insight: pharmacoproteomics for cancer—promises of patient-tailored medicine using protein microarrays. Nat Rev Clin Oncol 3:256–268. doi: 10.1038/ncponc0485

22. Guengerich FP (2005) Human Cytochrome P450 Enzymes. In: Montellano PRO de (ed) Cytochrome P450. Springer US, pp 377–530

23. Guengerich FP (2008) Cytochrome P450 and Chemical Toxicology. Chem Res Toxicol 21:70–83. doi: 10.1021/tx700079z

24. Ingelman-Sundberg M (2004) Pharmacogenetics of cytochrome P450 and its applications in drug therapy: the past, present and future. Trends Pharmacol Sci 25:193–200. doi: 10.1016/j.tips.2004.02.007

25. Kang J-S, Lee M-H (2009) Overview of Therapeutic Drug Monitoring. Korean J Intern Med 24:1–10. doi: 10.3904/kjim.2009.24.1.1

26. Nicoll D, Lu CM, Pignone M, McPhee SJ (2012) Pocket Guide to Diagnostic Tests, Sixth Edition, 6 edition. McGraw-Hill Education / Medical, New York

27. Gross AS (2001) Best practice in therapeutic drug monitoring. Br J Clin Pharmacol 52:5–9. doi: 10.1111/j.1365-2125.2001.00770.x

28. Momper JD, Wagner JA (2014) Therapeutic Drug Monitoring as a Component of Personalized Medicine: Applications in Pediatric Drug Development. Clin Pharmacol Ther 95:138–140. doi: 10.1038/clpt.2013.227

29. Haouala A, Zanolari B, Rochat B, Montemurro M, Zaman K, Duchosal MA, Ris HB, Leyvraz S, Widmer N, Decosterd LA (2009) Therapeutic Drug Monitoring of the new targeted anticancer agents imatinib, nilotinib, dasatinib, sunitinib, sorafenib and lapatinib by LC tandem mass spectrometry. J Chromatogr B 877:1982–1996. doi: 10.1016/j.jchromb.2009.04.045

30. Saint-Marcoux F, Sauvage F-L, Marquet P (2007) Current role of LC-MS in therapeutic drug monitoring. Anal Bioanal Chem 388:1327–1349. doi: 10.1007/s00216-007-1320-1

31. Hiemke C (2008) Clinical utility of drug measurement and pharmacokinetics – therapeutic drug monitoring in psychiatry. Eur J Clin Pharmacol 64:159–166. doi: 10.1007/s00228-007-0430-1

32. Malvezzi M, Carioli G, Bertuccio P, Rosso T, Boffetta P, Levi F, Vecchia CL, Negri E (2016) European cancer mortality predictions for the year 2016 with focus on leukemias. Ann Oncol mdw022. doi: 10.1093/annonc/mdw022

33. Denmeade SR, Isaacs JT (2002) A history of prostate cancer treatment. Nat Rev Cancer 2:389–396. doi: 10.1038/nrc801

34. Gomella LG (2009) Effective Testosterone Suppression for Prostate Cancer: Is There a Best Castration Therapy? Rev Urol 11:52–60.

35. Hakki T, Bernhardt R (2006) CYP17- and CYP11B-dependent steroid hydroxylases as drug development targets. Pharmacol Ther 111:27–52. doi: 10.1016/j.pharmthera.2005.07.006

36. FDA Approval for Abiraterone Acetate. In: Natl. Cancer Inst. https://www.cancer.gov/about-cancer/treatment/drugs/fda-abirateroneacetate. Accessed 2 Nov 2016

37. European Medicines Agency - Human medicines - CHMP summary of positive opinion for Zytiga. http://www.ema.europa.eu/ema/index.jsp?curl=pages/medicines/human/medicines/002321/smops/Positive/human_smop_000245.jsp&mid=WC0b01ac058001d127. Accessed 2 Nov 2016

38. Government of Canada HC (2012) Summary Basis of Decision (SBD): Zytiga - 2012 - Health Canada. http://www.hc-sc.gc.ca/dhp-mps/prodpharma/sbd-smd/drug-med/sbd_smd_2012_zytiga_138343-eng.php#a2. Accessed 2 Nov 2016

39. Acharya M, Bernard A, Gonzalez M, Jiao J, Vries RD, Tran N (2012) Open-label, phase I, pharmacokinetic studies of abiraterone acetate in healthy men. Cancer Chemother Pharmacol 69:1583–1590. doi: 10.1007/s00280-012-1865-3

40. Organization WH, UNAIDS (2009) AIDS Epidemic Update: December 2009. WHO Regional Office Europe

41. Lopez AD, Mathers CD (2006) Measuring the global burden of disease and epidemiological transitions: 2002–2030. Ann Trop Med Parasitol 100:481–499. doi: 10.1179/136485906X97417

42. O'Keefe EP (2013) Nucleic Acid Delivery: Lentiviral and Retroviral Vectors. Mater Methods. doi: 10.13070/mm.en.3.174

43. Cullen BR (1991) Human immunodeficiency virus as a prototypic complex retrovirus. J Virol 65:1053–1056.

44. De Clercq E (2009) Anti-HIV drugs: 25 compounds approved within 25 years after the discovery of HIV. Int J Antimicrob Agents 33:307–320. doi: 10.1016/j.ijantimicag.2008.10.010

45. De Clercq E (2001) Antiviral drugs: current state of the art. J Clin Virol 22:73–89. doi: 10.1016/S1386-6532(01)00167-6

46. Fung HB, Stone EA, Piacenti FJ (2002) Tenofovir disoproxil fumarate: A nucleotide reverse transcriptase inhibitor for the treatment of HIV infection. Clin Ther 24:1515–1548. doi: 10.1016/S0149-2918(02)80058-3

47. Anton PA, Cranston RD, Kashuba A, Hendrix CW, Bumpus NN, Richardson-Harman N, Elliott J, Janocko L, Khanukhova E, Dennis R, Cumberland WG, Ju C, Carballo-Diéguez A, Mauck C, McGowan I (2012) RMP-02/MTN-006: A Phase 1 Rectal Safety, Acceptability, Pharmacokinetic, and Pharmacodynamic Study of Tenofovir 1% Gel Compared with Oral Tenofovir Disoproxil Fumarate. AIDS Res Hum Retroviruses 28:1412–1421. doi: 10.1089/aid.2012.0262

48. Touw DJ, Neef C, Thomson AH, Vinks AA, others (2005) Cost-effectiveness of therapeutic drug monitoring: a systematic review. Ther Drug Monit 27:10–17.

49. Gross AS (1998) Best practice in therapeutic drug monitoring. Br J Clin Pharmacol 46:95–99.

50. Carrara S, Cavallini A, Erokhin V, De Micheli G (2011) Multi-panel drugs detection in human serum for personalized therapy. Biosens Bioelectron 26:3914–3919. doi: 10.1016/j.bios.2011.03.009

51. Dzyadevych SV, Arkhypova VN, Soldatkin AP, El'skaya AV, Martelet C, Jaffrezic-Renault N (2008) Amperometric enzyme biosensors: Past, present and future. IRBM 29:171–180. doi: 10.1016/j.rbmret.2007.11.007

52. Weinshilboum R, Wang L (2004) Pharmacogenomics: bench to bedside. Nat Rev Drug Discov 3:739–748. doi: 10.1038/nrd1497

53. Evans WE, Relling MV (2004) Moving towards individualized medicine with pharmacogenomics. Nature 429:464–468. doi: 10.1038/nature02626

54. Benet LZ, Kroetz D, Sheiner L, Hardman J, Limbird L (1996) Pharmacokinetics: the dynamics of drug absorption, distribution, metabolism, and elimination. Goodman Gilmans Pharmacol Basis Ther 3–27.

55. Spear BB, Heath-Chiozzi M, Huff J (2001) Clinical application of pharmacogenetics. Trends Mol Med 7:201–204. doi: 10.1016/S1471-4914(01)01986-4

56. Phillips JE, Bogema S, Fu P, Furmaga W, Wu AH, Zic V, Hammett-Stabler C (2003) Signify® ER Drug Screen Test evaluation: comparison to Triage® drug of abuse panel plus tricyclic antidepressants. Clin Chim Acta 328:31–38.

57. Peace MR, Tarnai LD, Poklis A (2000) Performance evaluation of four on-site drug-testing devices for detection of drugs of abuse in urine. J Anal Toxicol 24:589–594.

58. Toxicology Products & Services - Alere. http://www.alere.com/en/home/products-services/toxicology.html. Accessed 7 Nov 2016

59. Point-of-Care Therapeutic Drug Monitoring System | Omnica.

60. Vrouwe EX, Luttge R, van den Berg A (2004) Direct measurement of lithium in whole blood using microchip capillary electrophoresis with integrated conductivity detection. Electrophoresis 25:1660–1667.

61. Vrouwe EX, Luttge R, Vermes I, Van Den Berg A (2007) Microchip capillary electrophoresis for point-of-care analysis of lithium. Clin Chem 53:117–123.

62. Het Medimate MiniLab | medimate.com. https://www.medimate.com/nl/het-medimate-minilab. Accessed 8 Nov 2016

63. Wang J (1999) Amperometric biosensors for clinical and therapeutic drug monitoring: a review. J Pharm Biomed Anal 19:47–53.

64. Wang J (2006) Electrochemical biosensors: towards point-of-care cancer diagnostics. Biosens Bioelectron 21:1887–1892.

65. Baj-Rossi C, Kilinc EG, Ghoreishizadeh SS, Casarino D, Jost TR, Dehollain C, Grassi F, Pastorino L, De Micheli G, Carrara S (2014) Full fabrication and packaging of an implantable multi-panel device for monitoring of metabolites in small animals. IEEE Trans Biomed Circuits Syst 8:636–647.

66. Baj-Rossi C, Micheli GD, Carrara S (2012) Electrochemical Detection of Anti-Breast-Cancer Agents in Human Serum by Cytochrome P450-Coated Carbon Nanotubes. Sensors 12:6520–6537. doi: 10.3390/s120506520

67. Xiao F, Zhao F, Li J, Yan R, Yu J, Zeng B (2007) Sensitive voltammetric determination of chloramphenicol by using single-wall carbon nanotube–gold nanoparticle–ionic liquid composite film modified glassy carbon electrodes. Anal Chim Acta 596:79–85.

68. Ploegmakers H, Moritz PA, Toll P, Van Oort WJ (1989) Computerized cyclic voltammetric detection after HPLC of the antineoplastic agents etoposide, teniposide, adriamycin and its metabolite adriamycinol in urine samples. J Anal Methods Chem 11:106–112.

69. Bharathi S (1998) Sol–gel-derived nanocrystalline gold–silicate composite biosensor. Anal Commun 35:29–31.

70. Authier L, Grossiord C, Brossier P, Limoges B (2001) Gold nanoparticle-based quantitative electrochemical detection of amplified human cytomegalovirus DNA using disposable microband electrodes. Anal Chem 73:4450–4456.

71. Tang H, Chen J, Yao S, Nie L, Deng G, Kuang Y (2004) Amperometric glucose biosensor based on adsorption of glucose oxidase at platinum nanoparticle-modified carbon nanotube electrode. Anal Biochem 331:89–97.

72. Murzin DY, Salmi T (2016) Catalytic Kinetics: Chemistry and Engineering. Elsevier

73. Bio/CMOS Interfaces and Co-Design | Sandro Carrara | Springer.

74. Trouillon R, M. Gijs MA (2016) Dynamic electrochemical quantitation of dopamine release from a cells-on-paper system. RSC Adv 6:31069–31073. doi: 10.1039/C6RA02487D

75. Hart JP, Crew A, Crouch E, Honeychurch KC, Pemberton RM (2004) Some Recent Designs and Developments of Screen-Printed Carbon Electrochemical Sensors/Biosensors for Biomedical, Environmental, and Industrial Analyses. Anal Lett 37:789–830. doi: 10.1081/AL-120030682

76. Wang J (1994) Decentralized electrochemical monitoring of trace metals: from disposable strips to remote electrodes. Plenary lecture. Analyst 119:763–766. doi: 10.1039/AN9941900763

77. Renedo OD, Alonso-Lomillo MA, Martínez MJA (2007) Recent developments in the field of screen-printed electrodes and their related applications. Talanta 73:202–219. doi: 10.1016/j.talanta.2007.03.050

78. Ju H, Xueji Z, Wang J (2011) NanoBiosensing: Principles, Development and Application. Springer Science & Business Media

79. Merkoci A (2009) Biosensing Using Nanomaterials. John Wiley & Sons

80. Rosi NL, Mirkin CA (2005) Nanostructures in Biodiagnostics. Chem Rev 105:1547–1562. doi: 10.1021/cr030067f

81. Qi WH, Wang MP (2004) Size and shape dependent melting temperature of metallic nanoparticles. Mater Chem Phys 88:280–284. doi: 10.1016/j.matchemphys.2004.04.026

82. Daniel M-C, Astruc D (2004) Gold Nanoparticles: Assembly, Supramolecular Chemistry, Quantum-Size-Related Properties, and Applications toward Biology, Catalysis, and Nanotechnology. Chem Rev 104:293–346. doi: 10.1021/cr030698+

83. Robel I, Kuno M, Kamat PV (2007) Size-Dependent Electron Injection from Excited CdSe Quantum Dots into TiO2 Nanoparticles. J Am Chem Soc 129:4136–4137. doi: 10.1021/ja070099a

84. Tvrdy K, Frantsuzov PA, Kamat PV, Schatz GC (2011) Photoinduced electron transfer from semiconductor quantum dots to metal oxide nanoparticles. Proc Natl Acad Sci U S A 108:29–34.

85. Tekin HC, Gijs MAM (2013) Ultrasensitive protein detection: a case for microfluidic magnetic bead-based assays. Lab Chip 13:4711. doi: 10.1039/c3lc50477h

86. Ruffert C, Ramadan Q, Gijs MAM (2014) Fabrication of a high aspect ratio (har) micropillar filter for a magnetic bead-based immunoassay. Microsyst Technol 20:1869–1873.

87. Santamarina JC, Klein KA, Wang YH, Prencke E (2002) Specific surface: determination and relevance. Can Geotech J 39:233–241.

88. M. Tiggelaar R, Verdoold V, Eghbali H, Desmet G, E. Gardeniers JG (2009) Characterization of porous silicon integrated in liquid chromatography chips. Lab Chip 9:456–463. doi: 10.1039/B812301B

89. Lowell S, Shields JE (2013) Powder Surface Area and Porosity. Springer Science & Business Media

90. Paykov O, Hawley H (2013) A Protein-Retention Method for Specific Surface Area Determination in Swelling Clays. Geotech Test J 36:20120197. doi: 10.1520/GTJ20120197

91. Cerato AB, Lutenegger AJ (2002) Determination of surface area of fine-grained soils by the ethylene glycol monoethyl ether (EGME) method.

92. (2012) Colloidal Gold: Principles, Methods, and Applications. Elsevier

93. Sun Y, Xia Y (2002) Shape-controlled synthesis of gold and silver nanoparticles. Science 298:2176–2179.

94. Sau TK, Murphy CJ (2004) Room temperature, high-yield synthesis of multiple shapes of gold nanoparticles in aqueous solution. J Am Chem Soc 126:8648–8649.

95. Murray CB, Kagan and CR, Bawendi MG (2000) Synthesis and Characterization of Monodisperse Nanocrystals and Close-Packed Nanocrystal Assemblies. Annu Rev Mater Sci 30:545–610. doi: 10.1146/annurev.matsci.30.1.545

96. Li L, Hu J, Yang W, Alivisatos AP (2001) Band Gap Variation of Size- and Shape-Controlled Colloidal CdSe Quantum Rods. Nano Lett 1:349–351. doi: 10.1021/nl015559r

97. Taurino I, Sanzó G, Mazzei F, Favero G, De Micheli G, Carrara S (2015) Fast synthesis of platinum nanopetals and nanospheres for highly-sensitive non-enzymatic detection of glucose and selective sensing of ions. Sci Rep. doi: 10.1038/srep15277

98. Bollella P, Fusco G, Tortolini C, Sanzò G, Favero G, Gorton L, Antiochia R (2016) Beyond graphene: Electrochemical sensors and biosensors for biomarkers detection. Biosens Bioelectron. doi: 10.1016/j.bios.2016.03.068

99. Favero G, Fusco G, Mazzei F, Tasca F, Antiochia R (2015) Electrochemical Characterization of Graphene and MWCNT Screen-Printed Electrodes Modified with AuNPs for Laccase Biosensor Development. Nanomaterials 5:1995–2006. doi: 10.3390/nano5041995

100. Xue K, Zhou S, Shi H, Feng X, Xin H, Song W (2014) A novel amperometric glucose biosensor based on ternary gold nanoparticles/polypyrrole/reduced graphene oxide nanocomposite. Sens Actuators B Chem 203:412–416. doi: 10.1016/j.snb.2014.07.018

101. Zhao K, Pan Z, Mora-Seró I, Cánovas E, Wang H, Song Y, Gong X, Wang J, Bonn M, Bisquert J, Zhong X (2015) Boosting Power Conversion Efficiencies of Quantum-Dot-Sensitized Solar Cells Beyond 8% by Recombination Control. J Am Chem Soc 137:5602–5609. doi: 10.1021/jacs.5b01946

102. Labelle AJ, Thon SM, Masala S, Adachi MM, Dong H, Farahani M, Ip AH, Fratalocchi A, Sargent EH (2015) Colloidal Quantum Dot Solar Cells Exploiting Hierarchical Structuring. Nano Lett 15:1101–1108. doi: 10.1021/nl504086v

103. Ning Z, Gong X, Comin R, Walters G, Fan F, Voznyy O, Yassitepe E, Buin A, Hoogland S, Sargent EH (2015) Quantum-dot-in-perovskite solids. Nature 523:324–328. doi: 10.1038/nature14563

104. Zhou F, Feng H, Fang Y, Sun Q, Qian Z (2016) Phenylsulfonic acid functionalized carbon quantum dots based biosensor for acetylcholinesterase activity monitoring and inhibitor screening. RSC Adv 6:105454–105460. doi: 10.1039/C6RA18978D

105. Weng X, Chen L, Neethirajan S, Duffield T (2015) Development of quantum dots-based biosensor towards on-farm detection of subclinical ketosis. Biosens Bioelectron 72:140–147. doi: 10.1016/j.bios.2015.05.008

106. Yang C, Hu L, Zhu H-Y, Ling Y, Tao J-H, Xu C-X (2015) rGO quantum dots/ZnO hybrid nanofibers fabricated using electrospun polymer templates and applications in drug screening involving an intracellular H 2 O 2 sensor. J Mater Chem B 3:2651–2659. doi: 10.1039/C4TB02134G

107. Nguyen NH, Duong TG, Hoang VN, Pham NT, Dao TC, Pham TN (2015) Synthesis and application of quantum dots-based biosensor. Adv Nat Sci Nanosci Nanotechnol 6:15015. doi: 10.1088/2043-6262/6/1/015015

108. Comini E, Baratto C, Concina I, Faglia G, Falasconi M, Ferroni M, Galstyan V, Gobbi E, Ponzoni A, Vomiero A, Zappa D, Sberveglieri V, Sberveglieri G (2013) Metal oxide nanoscience and nanotechnology for chemical sensors. Sens Actuators B Chem 179:3–20. doi: 10.1016/j.snb.2012.10.027

109. Trindade T, O'Brien P, Pickett NL (2001) Nanocrystalline semiconductors: synthesis, properties, and perspectives. Chem Mater 13:3843–3858.

110. Alivisatos AP (1996) Perspectives on the physical chemistry of semiconductor nanocrystals. J Phys Chem 100:13226–13239.

111. Ding Y, Dong Y, Bapat A, Nowak JD, Carter CB, Kortshagen UR, Campbell SA (2006) Single nanoparticle semiconductor devices. IEEE Trans Electron Devices 53:2525–2531.

112. Liu B, Wang Z, Dong Y, Zhu Y, Gong Y, Ran S, Liu Z, Xu J, Xie Z, Chen D, others (2012) ZnO-nanoparticle-assembled cloth for flexible photodetectors and recyclable photocatalysts. J Mater Chem 22:9379–9384.

113. Bredol M, Kaczmarek M (2009) Potential of Nano-ZnS as Electrocatalyst†. J Phys Chem A 114:3950–3955.

114. Willner I, Baron R, Willner B (2007) Integrated nanoparticle–biomolecule systems for biosensing and bioelectronics. Biosens Bioelectron 22:1841–1852.

115. Jiang L, You T, Deng W-Q (2013) Enhanced photovoltaic performance of a quantum dot-sensitized solar cell using a Nb-doped TiO2 electrode. Nanotechnology 24:415401.

116. Guo F, He J, Li J, Wu W, Hang Y, Hua J (2013) Photovoltaic performance of bithiazole-bridged dyes-sensitized solar cells employing semiconducting quantum dot CuInS 2 as barrier layer material. J Colloid Interface Sci 408:59–65.

117. Zeng H, Duan G, Li Y, Yang S, Xu X, Cai W (2010) Blue luminescence of ZnO nanoparticles based on non-equilibrium processes: defect origins and emission controls. Adv Funct Mater 20:561–572.

118. Kairdolf BA, Smith AM, Stokes TH, Wang MD, Young AN, Nie S (2013) Semiconductor quantum dots for bioimaging and biodiagnostic applications. Annu Rev Anal Chem Palo Alto Calif 6:143.

119. Zhang H, Wu P, Li Y, Liao L, Fang Z, Zhong X (2010) Preparation of bismuth oxide quantum dots and their photocatalytic activity in a homogeneous system. ChemCatChem 2:1115–1121.

120. Ge M, Li Y, Liu L, Zhou Z, Chen W (2011) Bi2O3- Bi2WO6 composite microspheres: hydrothermal synthesis and photocatalytic performances. J Phys Chem C 115:5220–5225.

121. Shipway AN, Willner I (2001) Nanoparticles as structural and functional units in surface-confined architectures. Chem Commun 2035–2045.

122. Banks CE, Davies TJ, Wildgoose GG, Compton RG (2005) Electrocatalysis at graphite and carbon nanotube modified electrodes: edge-plane sites and tube ends are the reactive sites. Chem Commun 829–841.

123. Zhang JZ (1997) Ultrafast studies of electron dynamics in semiconductor and metal colloidal nanoparticles: Effects of size and surface. Acc Chem Res 30:423–429.

124. Periasamy AP, Yang S, Chen S-M (2011) Preparation and characterization of bismuth oxide nanoparticles-multiwalled carbon nanotube composite for the development of horseradish peroxidase based H 2 O 2 biosensor. Talanta 87:15–23.

125. Shumyantseva VV, Carrara S, Bavastrello V, Riley DJ, Bulko TV, Skryabin KG, Archakov AI, Nicolini C (2005) Direct electron transfer between cytochrome P450scc and gold nanoparticles on screen-printed rhodium–graphite electrodes. Biosens Bioelectron 21:217–222.

126. Pingarrón JM, Yañez-Sedeño P, González-Cortés A (2008) Gold nanoparticle-based electrochemical biosensors. Electrochimica Acta 53:5848–5866.

127. Wang Q, Zheng J (2010) Electrodeposition of silver nanoparticles on a zinc oxide film: improvement of amperometric sensing sensitivity and stability for hydrogen peroxide determination. Microchim Acta 169:361–365.

128. Nie Z, Petukhova A, Kumacheva E (2010) Properties and emerging applications of self-assembled structures made from inorganic nanoparticles. Nat Nanotechnol 5:15–25.

129. Sun S (2006) Recent advances in chemical synthesis, self-assembly, and applications of FePt nanoparticles. Adv Mater 18:393–403.

130. Guascito MR, Chirizzi D, Picca RA, Mazzotta E, Malitesta C (2011) Ag nanoparticles capped by a nontoxic polymer: Electrochemical and spectroscopic characterization of a novel nanomaterial for glucose detection. Mater Sci Eng C 31:606–611.

131. Ghosh SK, Pal T (2007) Interparticle coupling effect on the surface plasmon resonance of gold nanoparticles: from theory to applications. Chem Rev 107:4797–4862.

132. Hernández-Santos D, González-García MB, García AC (2002) Metal-nanoparticles based electroanalysis. Electroanalysis 14:1225–1235.

133. Liu G, Lin Y (2005) A renewable electrochemical magnetic immunosensor based on gold nanoparticle labels. J Nanosci Nanotechnol 5:1060–1065.

134. German N, Ramanavicius A, Voronovic J, Ramanaviciene A (2012) Glucose biosensor based on glucose oxidase and gold nanoparticles of different sizes covered by polypyrrole layer. Colloids Surf Physicochem Eng Asp 413:224–230.

135. Volder MFLD, Tawfick SH, Baughman RH, Hart AJ (2013) Carbon Nanotubes: Present and Future Commercial Applications. Science 339:535–539. doi: 10.1126/science.1222453

136. Kurkina T, Vlandas A, Ahmad A, Kern K, Balasubramanian K (2011) Label-Free Detection of Few Copies of DNA with Carbon Nanotube Impedance Biosensors. Angew Chem Int Ed 50:3710–3714. doi: 10.1002/anie.201006806

137. Snow ES, Perkins FK, Houser EJ, Badescu SC, Reinecke TL (2005) Chemical Detection with a Single-Walled Carbon Nanotube Capacitor. Science 307:1942–1945. doi: 10.1126/science.1109128

138. Chen Z, Tabakman SM, Goodwin AP, Kattah MG, Daranciang D, Wang X, Zhang G, Li X, Liu Z, Utz PJ, Jiang K, Fan S, Dai H (2008) Protein microarrays with carbon nanotubes as multicolor Raman labels. Nat Biotechnol 26:1285–1292. doi: 10.1038/nbt.1501

139. Taurino I, Carrara S, Giorcelli M, Tagliaferro A, De Micheli G (2012) Carbon nanotubes with different orientations for electrochemical biodevices. IEEE Sens J 12:3356–3362.

140. Carrara S, Boero C, De Micheli G (2009) Quantum dots and wires to improve enzymes-based electrochemical bio-sensing. In: Int. Conf. Nano-Netw. Springer, pp 189–199

141. Boero C, Carrara S, Vecchio G, Calzà L, Micheli G (2011) Highly sensitive carbon nanotube-based sensing for lactate and glucose monitoring in cell culture. IEEE Trans Nanobioscience 10:59–67.

142. Taurino I, Magrez A, Matteini F, Forró L, De Micheli G, Carrara S (2013) Direct growth of nanotubes and graphene nanoflowers on electrochemical platinum electrodes. Nanoscale 5:12448–12455.

143. Singh C, Shaffer MS, Windle AH (2003) Production of controlled architectures of aligned carbon nanotubes by an injection chemical vapour deposition method. Carbon 41:359–368.

144. Boccaccini AR, Cho J, Roether JA, Thomas BJ, Minay EJ, Shaffer MS (2006) Electrophoretic deposition of carbon nanotubes. Carbon 44:3149–3160.

145. Cadek M, Murphy R, McCarthy B, Drury A, Lahr B, Barklie RC, In het Panhuis M, Coleman JN, Blau WJ (2002) Optimisation of the arc-discharge production of multi-walled carbon nanotubes. Carbon 40:923–928.

146. Journet C, Bernier P (1998) Production of carbon nanotubes. Appl Phys Mater Sci Process 67:1–9.

147. Paradise M, Goswami T (2007) Carbon nanotubes–production and industrial applications. Mater Des 28:1477–1489.

148. Shokoohi S, Naderi G, Davoodi A (2016) Mechanical Properties of Nanomaterials. In: Nanocomposite Mater. CRC Press, pp 129–145

149. Falvo MR, Clary GJ, Taylor RM, Chi V, Brooks FP, Washburn S, Superfine R (1997) Bending and buckling of carbon nanotubes under large strain. Nature 389:582–584. doi: 10.1038/39282

150. Walters DA, Ericson LM, Casavant MJ, Liu J, Colbert DT, Smith KA, Smalley RE (1999) Elastic strain of freely suspended single-wall carbon nanotube ropes. Appl Phys Lett 74:3803–3805. doi: 10.1063/1.124185

151. Demczyk BG, Wang YM, Cumings J, Hetman M, Han W, Zettl A, Ritchie RO (2002) Direct mechanical measurement of the tensile strength and elastic modulus of multiwalled carbon nanotubes. Mater Sci Eng A 334:173–178. doi: 10.1016/S0921-5093(01)01807-X

152. Tombler TW, Zhou C, Alexseyev L, Kong J, Dai H, Liu L, Jayanthi CS, Tang M, Wu S-Y (2000) Reversible electromechanical characteristics of carbon nanotubes under local-probe manipulation. Nature 405:769–772. doi: 10.1038/35015519

153. Sadezky A, Muckenhuber H, Grothe H, Niessner R, Pöschl U (2005) Raman microspectroscopy of soot and related carbonaceous materials: spectral analysis and structural information. Carbon 43:1731–1742.

154. Mocak J, Bond AM, Mitchell S, Scollary G (2009) A statistical overview of standard (IUPAC and ACS) and new procedures for determining the limits of detection and quantification: Application to voltammetric and stripping techniques (Technical Report). Pure Appl Chem 69:297–328. doi: 10.1351/pac199769020297

155. Armbruster DA, Pry T (2008) Limit of blank, limit of detection and limit of quantitation. Clin Biochem Rev 29:S49–52.

156. Schneider CA, Rasband WS, Eliceiri KW, others (2012) NIH Image to ImageJ: 25 years of image analysis. Nat Methods 9:671–675.

157. Peigney A, Laurent C, Flahaut E, Bacsa RR, Rousset A (2001) Specific surface area of carbon nanotubes and bundles of carbon nanotubes. Carbon 39:507–514. doi: 10.1016/S0008-6223(00)00155-X

158. Haruehanroengra S, Wang W (2007) Analyzing Conductance of Mixed Carbon-Nanotube Bundles for Interconnect Applications. IEEE Electron Device Lett 28:756–759. doi: 10.1109/LED.2007.901584

159. Fotouhi L, Fatollahzadeh M, Heravi MM (2012) Electrochemical behavior and voltammetric determination of sulfaguanidine at a glassy carbon electrode modified with a multi-walled carbon nanotube. Int J Electrochem Sci 7:3919–3928.

160. Carrara S, Baj-Rossi C, Boero C, De Micheli G (2014) Do Carbon Nanotubes contribute to Electrochemical Biosensing? Electrochimica Acta 128:102–112. doi: 10.1016/j.electacta.2013.12.123

161. Hubbard AT (1969) Study of the kinetics of electrochemical reactions by thin-layer voltammetry: I. theory. J Electroanal Chem Interfacial Electrochem 22:165–174.

162. Streeter I, Wildgoose GG, Shao L, Compton RG (2008) Cyclic voltammetry on electrode surfaces covered with porous layers: an analysis of electron transfer kinetics at single-walled carbon nanotube modified electrodes. Sens Actuators B Chem 133:462–466.

163. Yin H, Ai S, Shi W, Zhu L (2009) A novel hydrogen peroxide biosensor based on horseradish peroxidase immobilized on gold nanoparticles–silk fibroin modified glassy carbon electrode and direct electrochemistry of horseradish peroxidase. Sens Actuators B Chem 137:747–753.

164. Yang G, Yuan R, Chai Y-Q (2008) A high-sensitive amperometric hydrogen peroxide biosensor based on the immobilization of hemoglobin on gold colloid/l-cysteine/gold colloid/nanoparticles Pt–chitosan composite film-modified platinum disk electrode. Colloids Surf B Biointerfaces 61:93–100.

165. Hu G, Ma Y, Guo Y, Shao S (2008) Electrocatalytic oxidation and simultaneous determination of uric acid and ascorbic acid on the gold nanoparticles-modified glassy carbon electrode. Electrochimica Acta 53:6610–6615.

166. Woo S, Kim Y-R, Chung TD, Piao Y, Kim H (2012) Synthesis of a graphene–carbon nanotube composite and its electrochemical sensing of hydrogen peroxide. Electrochimica Acta 59:509–514.

167. Habibi B, Pournaghi-Azar MH (2010) Simultaneous determination of ascorbic acid, dopamine and uric acid by use of a MWCNT modified carbon-ceramic electrode and differential pulse voltammetry. Electrochimica Acta 55:5492–5498.

168. Taufik S, Yusof NA, Tee TW, Ramli I (2011) Bismuth oxide nanoparticles/chitosan/modified electrode as biosensor for DNA hybridization. Int J Electrochem Sci 6:1880–1891.

169. Li NB, Park JH, Park K, Kwon SJ, Shin H, Kwak J (2008) Characterization and electrocatalytic properties of Prussian blue electrochemically deposited on nano-Au/PAMAM dendrimer-modified gold electrode. Biosens Bioelectron 23:1519–1526.

170. Yu A, Liang Z, Cho J, Caruso F (2003) Nanostructured electrochemical sensor based on dense gold nanoparticle films. Nano Lett 3:1203–1207.

171. Tzouvadaki I, Jolly P, Lu X, Ingebrandt S, De Micheli G, Estrela P, Carrara S (2016) Label-Free Ultrasensitive Memristive Aptasensor. Nano Lett 16:4472–4476.

172. Averin DV, Likharev KK (1986) Coulomb blockade of single-electron tunneling, and coherent oscillations in small tunnel junctions. J Low Temp Phys 62:345–373.

173. Van Bentum PJM, Van Kempen H, Van de Leemput LEC, Teunissen PAA (1988) Single-electron tunneling observed with point-contact tunnel junctions. Phys Rev Lett 60:369.

174. Devoret MH, Esteve D, Urbina C (1992) Single-electron transfer in metallic nanostructures. Nature 360:547–553.

175. Schönenberger C, Van Houten H, Donkersloot HC (1992) Single-electron tunnelling observed at room temperature by scanning-tunnelling microscopy. EPL Europhys Lett 20:249.

176. Erokhin V, Facci P, Carrara S, Nicolini C (1995) Observation of room temperature mono-electron phenomena on nanometre-sized CdS particles. J Phys Appl Phys 28:2534.

177. Facci P, Erokhin V, Carrara S, Nicolini C (1996) Room-temperature single-electron junction. Proc Natl Acad Sci 93:10556–10559.

178. Slowey AJ, Marvin-DiPasquale M (2012) How to overcome inter-electrode variability and instability to quantify dissolved oxygen, Fe (II), Mn (II), and S (- II) in undisturbed soils and sediments using voltammetry. Geochem Trans 13:1–20.

179. Holthuis JJM, Van Oort WJ, Römkens F, Renema J, Zuman P (1985) Electrochemistry of podophyllotoxin derivatives: Part i. Oxidation mechanism of etoposide (vp 16–213). J Electroanal Chem Interfacial Electrochem 184:317–329.

180. Fan F-RF, Bard AJ (1997) An electrochemical coulomb staircase: detection of single electron-transfer events at nanometer electrodes. Science 277:1791–1793.

181. Chen S, Murray RW, Feldberg SW (1998) Quantized capacitance charging of monolayer-protected Au clusters. J Phys Chem B 102:9898–9907.

182. Arbuck SG, Douglass HO, Crom WR, Goodwin P, Silk Y, Cooper C, Evans WE (1986) Etoposide pharmacokinetics in patients with normal and abnormal organ function. J Clin Oncol 4:1690–1695.

183. Hande KR, Wedlund PJ, Noone RM, Wilkinson GR, Greco FA, Wolff SN (1984) Pharmacokinetics of High-Dose Etoposide (VP-16-213) Administered to Cancer Patients. Cancer Res 44:379–382.

184. Aliakbarinodehi N, De Micheli G, Carrara S (2016) Enzymatic and Nonenzymatic Electrochemical Interaction of Abiraterone (Antiprostate Cancer Drug) with Multiwalled Carbon Nanotube Bioelectrodes. Anal Chem 88:9347–9350. doi: 10.1021/acs.analchem.6b02747

185. Bozal-Palabiyik B, Dogan-Topal B, Uslu B, Can A, Ozkan SA (2013) Sensitive voltammetric assay of etoposide using modified glassy carbon electrode with a dispersion of multi-walled carbon nanotube. J Solid State Electrochem 17:2815–2822. doi: 10.1007/s10008-013-2184-2

186. Coleman MD (2010) Human Drug Metabolism: An Introduction. John Wiley & Sons

187. Ingelman-Sundberg M (2004) Human drug metabolising cytochrome P450 enzymes: properties and polymorphisms. Naunyn Schmiedebergs Arch Pharmacol 369:89–104.

188. Denisov IG, Makris TM, Sligar SG, Schlichting I (2005) Structure and Chemistry of Cytochrome P450. Chem Rev 105:2253–2278. doi: 10.1021/cr0307143

189. Sono M, Roach MP, Coulter ED, Dawson JH (1996) Heme-containing oxygenases. Chem Rev 96:2841–2888.

190. Atkins WM (2005) Non-Michaelis-Menten kinetics in cytochrome P450-catalyzed reactions. Annu Rev Pharmacol Toxicol 45:291–310.

191. Houston JB, Galetin A (2005) Modelling atypical CYP3A4 kinetics: principles and pragmatism. Arch Biochem Biophys 433:351–360.

192. Makris TM, Denisov I, Schlichting I, Sligar SG (2005) Cytochrome P450: Structure, Mechanism, and Biochemistry. Springer US

193. Huang N, Agrawal V, Giacomini KM, Miller WL (2008) Genetics of P450 oxidoreductase: sequence variation in 842 individuals of four ethnicities and activities of 15 missense mutations. Proc Natl Acad Sci 105:1733–1738.

194. Bistolas N, Wollenberger U, Jung C, Scheller FW (2005) Cytochrome P450 biosensors—a review. Biosens Bioelectron 20:2408–2423.

195. Johnson DL, Lewis BC, Elliot DJ, Miners JO, Martin LL (2005) Electrochemical characterisation of the human cytochrome P450 CYP2C9. Biochem Pharmacol 69:1533–1541.

196. Schneider E, Clark DS (2013) Cytochrome P450 (CYP) enzymes and the development of CYP biosensors. Biosens Bioelectron 39:1–13.

197. Sadeghi SJ, Fantuzzi A, Gilardi G (2011) Breakthrough in P450 bioelectrochemistry and future perspectives. Biochim Biophys Acta BBA-Proteins Proteomics 1814:237–248.

198. Estabrook RW, Faulkner KM, Shet MS, Fisher CW (1996) [5] Application of electrochemistry for P450-catalyzed reactions. Methods Enzymol 272:44–51.

199. Shumyantseva VV, Bulko TV, Bachmann TT, Bilitewski U, Schmid RD, Archakov AI (2000) Electrochemical reduction of flavocytochromes 2B4 and 1A2 and their catalytic activity. Arch Biochem Biophys 377:43–48.

200. Shumyantseva VV, Bulko TV, Usanov SA, Schmid RD, Nicolini C, Archakov AI (2001) Construction and characterization of bioelectrocatalytic sensors based on cytochromes P450. J Inorg Biochem 87:185–190.

201. Baj-Rossi C, De Micheli G, Carrara S (2011) P450-based nano-bio-sensors for personalized medicine. Intech

202. Mie Y, Suzuki M, Komatsu Y (2009) Electrochemically driven drug metabolism by membranes containing human cytochrome P450. J Am Chem Soc 131:6646–6647.

203. Dodhia VR, Sassone C, Fantuzzi A, Di Nardo G, Sadeghi SJ, Gilardi G (2008) Modulating the coupling efficiency of human cytochrome P450 CYP3A4 at electrode surfaces through protein engineering. Electrochem Commun 10:1744–1747.

204. Sultana N, Schenkman JB, Rusling JF (2005) Protein film electrochemistry of microsomes genetically enriched in human cytochrome P450 monooxygenases. J Am Chem Soc 127:13460–13461.

205. Rivas L, Murgida DH, Hildebrandt P (2002) Conformational and redox equilibria and dynamics of cytochrome c immobilized on electrodes via hydrophobic interactions. J Phys Chem B 106:4823–4830.

206. Williams PA, Cosme J, Sridhar V, Johnson EF, McRee DE (2000) Microsomal cytochrome P450 2C5: comparison to microbial P450s and unique features. J Inorg Biochem 81:183–190.

207. Baj-Rossi C, Müller C, von Mandach U, De Micheli G, Carrara S (2015) Faradic Peaks Enhanced by Carbon Nanotubes in Microsomal Cytochrome P450 Electrodes. Electroanalysis 27:1507–1515.

208. Baj-Rossi C, Rezzonico Jost T, Cavallini A, Grassi F, De Micheli G, Carrara S (2014) Continuous monitoring of Naproxen by a cytochrome P450-based electrochemical sensor. Biosens Bioelectron 53:283–287. doi: 10.1016/j.bios.2013.09.058

209. Sakai-Kato K, Kato M, Homma H, Toyo'oka T, Utsunomiya-Tate N (2005) Creation of a P450 Array toward High-throughput Analysis. Anal Chem 77:7080–7083. doi: 10.1021/ac050714y

210. Chang G, Morigaki K, Tatsu Y, Hikawa T, Goto T, Imaishi H (2011) Vertically Integrated Human P450 and Oxygen Sensing Film for the Assays of P450 Metabolic Activities. Anal Chem 83:2956–2963. doi: 10.1021/ac103059k

211. Habermüller K, Mosbach M, Schuhmann W (2000) Electron-transfer mechanisms in amperometric biosensors. Fresenius J Anal Chem 366:560–568.

212. Fantuzzi A, Fairhead M, Gilardi G (2004) Direct electrochemistry of immobilized human cytochrome P450 2E1. J Am Chem Soc 126:5040–5041.

213. Sotiropoulou S, Vamvakaki V, Chaniotakis NA (2005) Stabilization of enzymes in nanoporous materials for biosensor applications. Biosens Bioelectron 20:1674–1679. doi: 10.1016/j.bios.2004.07.019

214. Huang H, Bai W, Dong C, Guo R, Liu Z (2015) An ultrasensitive electrochemical DNA biosensor based on graphene/Au nanorod/polythionine for human papillomavirus DNA detection. Biosens Bioelectron 68:442–446. doi: 10.1016/j.bios.2015.01.039

215. Batra B, Lata S, Pundir CS (2013) Construction of an improved amperometric acrylamide biosensor based on hemoglobin immobilized onto carboxylated multi-walled carbon nanotubes/iron oxide nanoparticles/chitosan composite film. Bioprocess Biosyst Eng 36:1591–1599. doi: 10.1007/s00449-013-0931-5

216. Yang P, Li X, Wang L, Wu Q, Chen Z, Lin X (2014) Sandwich-type amperometric immunosensor for cancer biomarker based on signal amplification strategy of multiple enzyme-linked antibodies as probes modified with carbon nanotubes and concanavalin A. J Electroanal Chem 732:38–45. doi: 10.1016/j.jelechem.2014.08.030

217. Kim JH, Jun S-A, Kwon Y, Ha S, Sang B-I, Kim J (2015) Enhanced electrochemical sensitivity of enzyme precipitate coating (EPC)-based glucose oxidase biosensors with increased free CNT loadings. Bioelectrochemistry 101:114–119. doi: 10.1016/j.bioelechem.2014.08.017

218. Yin L, Hu Q (2014) CYP17 inhibitors—abiraterone, C17,20-lyase inhibitors and multi-targeting agents. Nat Rev Urol 11:32–42. doi: 10.1038/nrurol.2013.274

219. Hu Q, Yin L, Jagusch C, Hille UE, Hartmann RW (2010) Isopropylidene substitution increases activity and selectivity of biphenylmethylene 4-pyridine type CYP17 inhibitors. J Med Chem 53:5049–5053.

220. Pinto-Bazurco Mendieta MA, Negri M, Jagusch C, Müller-Vieira U, Lauterbach T, Hartmann RW (2008) Synthesis, biological evaluation, and molecular modeling of abiraterone analogues: novel CYP17 inhibitors for the treatment of prostate cancer. J Med Chem 51:5009–5018.

221. DeVore NM, Scott EE (2012) Structures of cytochrome P450 17A1 with prostate cancer drugs abiraterone and TOK-001. Nature 482:116–119.

222. Deb S, Chin MY, Adomat H, Guns EST (2014) Abiraterone inhibits 1α, 25-dihydroxyvitamin D 3 metabolism by CYP3A4 in human liver and intestine in vitro. J Steroid Biochem Mol Biol 144:50–58.

223. Asturias-Arribas L, Alonso-Lomillo MA, Domínguez-Renedo O, Arcos-Martínez MJ (2013) Electrochemical determination of cocaine using screen-printed cytochrome P450 2B4 based biosensors. Talanta 105:131–134. doi: 10.1016/j.talanta.2012.11.078

224. Sun P, Wu Y (2013) An amperometric biosensor based on human cytochrome P450 2C9 in polyacrylamide hydrogel films for bisphenol A determination. Sens Actuators B Chem 178:113–118. doi: 10.1016/j.snb.2012.12.055

225. Wu Y, Liu X, Zhang L, Wang C (2011) An amperometric biosensor based on rat cytochrome p450 1A1 for benzo[a]pyrene determination. Biosens Bioelectron 26:2177–2182. doi: 10.1016/j.bios.2010.09.027

226. Müller M, Agarwal N, Kim J (2016) A Cytochrome P450 3A4 Biosensor Based on Generation 4.0 PAMAM Dendrimers for the Detection of Caffeine. Biosensors 6:44. doi: 10.3390/bios6030044

227. Asturias-Arribas L, Alonso-Lomillo MA, Domínguez-Renedo O, Arcos-Martínez MJ (2011) CYP450 biosensors based on screen-printed carbon electrodes for the determination of cocaine. Anal Chim Acta 685:15–20. doi: 10.1016/j.aca.2010.11.006

228. Harwood GJ, Pouton CW (1996) Amperometric enzyme biosensors for the analysis of drugs and metabolites. Adv Drug Deliv Rev 18:163–191.

229. Salvati E, Stellacci F, Krol S (2015) Nanosensors for early cancer detection and for therapeutic drug monitoring. Nanomed 10:3495–3512.

230. Poghossian A, Schöning MJ (2014) Label-Free Sensing of Biomolecules with Field-Effect Devices for Clinical Applications. Electroanalysis 26:1197–1213.

231. Pachauri V, Ingebrandt S (2016) Biologically sensitive field-effect transistors: from ISFETs to NanoFETs. Essays Biochem 60:81–90. doi: 10.1042/EBC20150009

232. Ingebrandt S (2015) Bioelectronics: Sensing beyond the limit. Nat Nanotechnol 10:734–735. doi: 10.1038/nnano.2015.199

233. Ferguson BS, Hoggarth DA, Maliniak D, Ploense K, White RJ, Woodward N, Hsieh K, Bonham AJ, Eisenstein M, Kippin TE, others (2013) Real-time, aptamer-based tracking of circulating therapeutic agents in living animals. Sci Transl Med 5:213ra165–213ra165.

234. Lillie G, Payne P, Vadgama P (2001) Electrochemical impedance spectroscopy as a platform for reagentless bioaffinity sensing. Sens Actuators B Chem 78:249–256.

235. Yu J, Liu Z, Yang M, Mak A (2009) Nanoporous membrane-based cell chip for the study of anti-cancer drug effect of retinoic acid with impedance spectroscopy. Talanta 80:189–194.

236. Bunka DHJ, Stockley PG (2006) Aptamers come of age – at last. Nat Rev Microbiol 4:588–596. doi: 10.1038/nrmicro1458

237. Jolly P, Formisano N, Estrela P (2015) DNA aptamer-based detection of prostate cancer. Chem Pap 69:77–89.

238. Toh SY, Citartan M, Gopinath SC, Tang T-H (2015) Aptamers as a replacement for antibodies in enzyme-linked immunosorbent assay. Biosens Bioelectron 64:392–403.

239. Walter J-G, Heilkenbrinker A, Austerjost J, Timur S, Stahl F, Schepe T (2012) Aptasensors for small molecule detection. Z Für Naturforschung B 67:976–986.

240. Haupt K, Mosbach K (2000) Molecularly Imprinted Polymers and Their Use in Biomimetic Sensors. Chem Rev 100:2495–2504. doi: 10.1021/cr990099w

241. Iskierko Z, Sosnowska M, Sharma PS, Benincori T, D'Souza F, Kaminska I, Fronc K, Noworyta K (2015) Extended-gate field-effect transistor (EG-FET) with molecularly imprinted polymer (MIP) film for selective inosine determination. Biosens Bioelectron 74:526–533. doi: 10.1016/j.bios.2015.06.073

242. Nishino H, Huang C-S, Shea KJ (2006) Selective Protein Capture by Epitope Imprinting. Angew Chem Int Ed 45:2392–2396. doi: 10.1002/anie.200503760

243. Tamboli VK, Bhalla N, Jolly P, Bowen CR, Taylor JT, Bowen JL, Allender CJ, Estrela P (2016) Hybrid Synthetic Receptors on MOSFET Devices for Detection of Prostate Specific Antigen in Human Plasma. Anal Chem. doi: 10.1021/acs.analchem.6b02619

244. Jolly P, Formisano N, Tkáč J, Kasák P, Frost CG, Estrela P (2015) Label-free impedimetric aptasensor with antifouling surface chemistry: A prostate specific antigen case study. Sens Actuators B Chem 209:306–312. doi: 10.1016/j.snb.2014.11.083

245. Ingebrandt S, Vu X-T, Eschermann JF, Stockmann R, Offenhausser A (2011) Top-Down Processed SOI Nanowire Devices for Biomedical Applications. ECS Trans 35:3–15. doi: 10.1149/1.3571972

246. Nguyen TC, Vu XT, Freyler M, Ingebrandt S (2013) PSPICE model for silicon nanowire field-effect transistor biosensors in impedimetric measurement mode. Phys Status Solidi A 210:870–876. doi: 10.1002/pssa.201200919

247. Rani D, Pachauri V, Mueller A, Vu XT, Nguyen TC, Ingebrandt S (2016) On the Use of Scalable NanoISFET Arrays of Silicon with Highly Reproducible Sensor Performance for Biosensor Applications. ACS Omega 1:84–92. doi: 10.1021/acsomega.6b00014

248. Estrela P, Paul D, Song Q, Stadler LK, Wang L, Huq E, Davis JJ, Ferrigno PK, Migliorato P (2010) Label-free sub-picomolar protein detection with field-effect transistors. Anal Chem 82:3531–3536.

249. Chi L-L, Chou J-C, Chung W-Y, Sun T-P, Hsiung S-K (2000) Study on extended gate field effect transistor with tin oxide sensing membrane. Mater Chem Phys 63:19–23.

250. Estrela P, Stewart AG, Yan F, Migliorato P (2005) Field effect detection of biomolecular interactions. Electrochimica Acta 50:4995–5000. doi: 10.1016/j.electacta.2005.02.075

251. Nguyen TC, Schwartz M, Vu XT, Blinn J, Ingebrandt S (2015) Handheld readout system for field-effect transistor biosensor arrays for label-free detection of biomolecules. Phys Status Solidi A 212:1313–1319. doi: 10.1002/pssa.201431862

252. Formisano N, Bhalla N, Heeran M, Martinez JR, Sarkar A, Laabei M, Jolly P, Bowen CR, Taylor JT, Flitsch S, others (2016) Inexpensive and fast pathogenic bacteria screening using field-effect transistors. Biosens Bioelectron 85:103–109.

253. Beyer GP, Mann GG, Pursley JA, Espenhahn ET, Fraisse C, Godfrey DJ, Oldham M, Carrea TB, Bolick N, Scarantino CW (2008) An implantable MOSFET dosimeter for the measurement of radiation dose in tissue during cancer therapy. IEEE Sens J 8:38–51.

254. Freeman R, Gill R, Willner I (2007) Following a protein kinase activity using a field-effect transistor device. Chem Commun 3450–3452.

255. Bhalla N, Di Lorenzo M, Pula G, Estrela P (2015) Protein phosphorylation detection using dual-mode field-effect devices and nanoplasmonic sensors. Sci. Rep. 5:

256. Tarasov A, Gray DW, Tsai M-Y, Shields N, Montrose A, Creedon N, Lovera P, O'Riordan A, Mooney MH, Vogel EM (2016) A potentiometric biosensor for rapid on-site disease diagnostics. Biosens Bioelectron 79:669–678.

257. Ali SMU, Nur O, Willander M, Danielsson B (2009) Glucose detection with a commercial MOSFET using a ZnO nanowires extended gate. IEEE Trans Nanotechnol 8:678–683.

258. Jolly P, Batistuti MR, Miodek A, Zhurauski P, Mulato M, Lindsay MA, Estrela P (2016) Highly sensitive dual mode electrochemical platform for microRNA detection. Sci Rep. doi: 10.1038/srep36719

259. Patolsky F, Lieber CM (2005) Nanowire nanosensors. Mater Today 8:20–28. doi: 10.1016/S1369-7021(05)00791-1

260. Zheng G, Patolsky F, Cui Y, Wang WU, Lieber CM (2005) Multiplexed electrical detection of cancer markers with nanowire sensor arrays. Nat Biotechnol 23:1294–1301. doi: 10.1038/nbt1138

261. Stern E, Klemic JF, Routenberg DA, Wyrembak PN, Turner-Evans DB, Hamilton AD, LaVan DA, Fahmy TM, Reed MA (2007) Label-free immunodetection with CMOS-compatible semiconducting nanowires. Nature 445:519–522. doi: 10.1038/nature05498

262. Duan X, Li Y, Rajan NK, Routenberg DA, Modis Y, Reed MA (2012) Quantification of the affinities and kinetics of protein interactions using silicon nanowire biosensors. Nat Nanotechnol 7:401–407. doi: 10.1038/nnano.2012.82

263. Patolsky F, Zheng G, Lieber CM (2006) Fabrication of silicon nanowire devices for ultrasensitive, label-free, real-time detection of biological and chemical species. Nat Protoc 1:1711–1724. doi: 10.1038/nprot.2006.227

264. Frost WN, Castellucci VF, Hawkins RD, Kandel ER (1985) Monosynaptic connections made by the sensory neurons of the gill- and siphon-withdrawal reflex in Aplysia participate in the storage of long-term memory for sensitization. Proc Natl Acad Sci 82:8266–8269.

265. Lendlein A, Kelch S (2002) Shape-Memory Polymers. Angew Chem Int Ed 41:2034–2057. doi: 10.1002/1521-3773(20020617)41:12<2034::AID-ANIE2034>3.0.CO;2-M

266. Lehn J-M (2007) From supramolecular chemistry towards constitutional dynamic chemistry and adaptive chemistry. Chem Soc Rev 36:151–160. doi: 10.1039/B616752G

267. Wu J, McCreery RL (2009) Solid-State Electrochemistry in Molecule/ TiO2 Molecular Heterojunctions as the Basis of the TiO2 “Memristor.” J Electrochem Soc 156:P29–P37. doi: 10.1149/1.3021033

268. Pershin YV, Ventra MD (2011) Memory effects in complex materials and nanoscale systems. Adv Phys 60:145–227. doi: 10.1080/00018732.2010.544961

269. Chua LO, Kang SM (1976) Memristive devices and systems. Proc IEEE 64:209–223. doi: 10.1109/PROC.1976.10092

270. Chua L (2011) Resistance switching memories are memristors. Appl Phys A 102:765–783. doi: 10.1007/s00339-011-6264-9

271. Chua LO, Kang SM (1977) Section-wise piecewise-linear functions: Canonical representation, properties, and applications. Proc IEEE 65:915–929. doi: 10.1109/PROC.1977.10589

272. Strukov DB, Snider GS, Stewart DR, Williams RS (2008) The missing memristor found. Nature 453:80–83. doi: 10.1038/nature06932

273. Berzina T, Smerieri A, Bernabò M, Pucci A, Ruggeri G, Erokhin V, Fontana MP (2009) Optimization of an organic memristor as an adaptive memory element. J Appl Phys 105:124515. doi: 10.1063/1.3153944

274. Son DI, Kim TW, Shim JH, Jung JH, Lee DU, Lee JM, Park WI, Choi WK (2010) Flexible Organic Bistable Devices Based on Graphene Embedded in an Insulating Poly(methyl methacrylate) Polymer Layer. Nano Lett 10:2441–2447. doi: 10.1021/nl1006036

275. Yang JJ, Strukov DB, Stewart DR (2013) Memristive devices for computing. Nat Nanotechnol 8:13–24. doi: 10.1038/nnano.2012.240

276. Yang JJ, Pickett MD, Li X, Ohlberg DAA, Stewart DR, Williams RS (2008) Memristive switching mechanism for metal/oxide/metal nanodevices. Nat Nanotechnol 3:429–433. doi: 10.1038/nnano.2008.160

277. Borghetti J, Snider GS, Kuekes PJ, Yang JJ, Stewart DR, Williams RS (2010) “Memristive” switches enable “stateful” logic operations via material implication. Nature 464:873–876. doi: 10.1038/nature08940

278. Kuekes PJ, Stewart DR, Williams RS (2005) The crossbar latch: Logic value storage, restoration, and inversion in crossbar circuits. J Appl Phys 97:34301. doi: 10.1063/1.1823026

279. Tuma T, Pantazi A, Le Gallo M, Sebastian A, Eleftheriou E (2016) Stochastic phase-change neurons. Nat Nanotechnol 11:693–699. doi: 10.1038/nnano.2016.70

280. Pickett MD, Medeiros-Ribeiro G, Williams RS (2013) A scalable neuristor built with Mott memristors. Nat Mater 12:114–117. doi: 10.1038/nmat3510

281. Ohno T, Hasegawa T, Tsuruoka T, Terabe K, Gimzewski JK, Aono M (2011) Short-term plasticity and long-term potentiation mimicked in single inorganic synapses. Nat Mater 10:591–595. doi: 10.1038/nmat3054

282. Kuzum D, Jeyasingh RGD, Lee B, Wong H-SP (2012) Nanoelectronic Programmable Synapses Based on Phase Change Materials for Brain-Inspired Computing. Nano Lett 12:2179–2186. doi: 10.1021/nl201040y

283. Jo SH, Chang T, Ebong I, Bhadviya BB, Mazumder P, Lu W (2010) Nanoscale Memristor Device as Synapse in Neuromorphic Systems. Nano Lett 10:1297–1301. doi: 10.1021/nl904092h

284. Keighley SD, Li P, Estrela P, Migliorato P (2008) Optimization of DNA immobilization on gold electrodes for label-free detection by electrochemical impedance spectroscopy. Biosens Bioelectron 23:1291–1297.

285. Formisano N, Jolly P, Bhalla N, Cromhout M, Flanagan SP, Fogel R, Limson JL, Estrela P (2015) Optimisation of an electrochemical impedance spectroscopy aptasensor by exploiting quartz crystal microbalance with dissipation signals. Sens Actuators B Chem 220:369–375.

286. Kammer MN, Olmsted IR, Kussrow AK, Morris MJ, Jackson GW, Bornhop DJ (2014) Characterizing aptamer small molecule interactions with backscattering interferometry. The Analyst 139:5879–5884. doi: 10.1039/C4AN01227E

287. Gesztelyi R, Zsuga J, Kemeny-Beke A, Varga B, Juhasz B, Tosaki A (2012) The Hill equation and the origin of quantitative pharmacology. Arch Hist Exact Sci 66:427–438.

288. Motulsky H, Christopoulos A (2004) Fitting models to biological data using linear and nonlinear regression: a practical guide to curve fitting. OUP USA

289. Bahram M, Hoseinzadeh F, Farhadi K, Saadat M, Najafi-Moghaddam P, Afkhami A (2014) Synthesis of gold nanoparticles using pH-sensitive hydrogel and its application for colorimetric determination of acetaminophen, ascorbic acid and folic acid. Colloids Surf Physicochem Eng Asp 441:517–524.

290. Goux E, Lespinasse Q, Guieu V, Perrier S, Ravelet C, Fiore E, Peyrin E (2016) Fluorescence anisotropy-based structure-switching aptamer assay using a peptide nucleic acid (PNA) probe. Methods 97:69–74.

291. Li Y, Xu J, Wang L, Huang Y, Guo J, Cao X, Shen F, Luo Y, Sun C (2016) Aptamer-based fluorescent detection of bisphenol A using nonconjugated gold nanoparticles and CdTe quantum dots. Sens Actuators B Chem 222:815–822.

292. Rau S, Hilbig U, Gauglitz G (2014) Label-free optical biosensor for detection and quantification of the non-steroidal anti-inflammatory drug diclofenac in milk without any sample pretreatment. Anal Bioanal Chem 406:3377–3386.

293. Kukec RR, Grabnar I, Mrhar A, Lipovec NČ, Čufer T, Vovk T (2016) A simple dried blood spot method for clinical pharmacological analyses of etoposide in cancer patients using liquid chromatography and fluorescence detection. Clin Chim Acta 452:99–105.

294. Wang Q, Yang L, Yang X, Wang K, Liu J (2013) Use of mercaptophenylboronic acid functionalized gold nanoparticles in a sensitive and selective dynamic light scattering assay for glucose detection in serum. Analyst 138:5146–5150.

295. Zheng HY, Alsager OA, Wood CS, Hodgkiss JM, Plank NO (2015) Carbon nanotube field effect transistor aptasensors for estrogen detection in liquids. J Vac Sci Technol B 33:06F904.

296. Taurino I, Magrez A, Matteini F, Cavallini A, Forró L, De Micheli G, Carrara S (2014) High-performance multipanel biosensors based on a selective integration of nanographite petals. Nano Lett 14:3180–3184.

297. Adhikari B-R, Govindhan M, Chen A (2015) Sensitive detection of acetaminophen with graphene-based electrochemical sensor. Electrochimica Acta 162:198–204.

298. Wang Y, Feng J, Tan Z, Wang H (2014) Electrochemical impedance spectroscopy aptasensor for ultrasensitive detection of adenosine with dual backfillers. Biosens Bioelectron 60:218–223.

299. Zhu Y, Zhou C, Yan X, Yan Y, Wang Q (2015) Aptamer-functionalized nanoporous gold film for high-performance direct electrochemical detection of bisphenol A in human serum. Anal Chim Acta 883:81–89.

300. Xue J, Liu J, Wang C, Tian Y, Zhou N (2016) Simultaneous electrochemical detection of multiple antibiotic residues in milk based on aptamers and quantum dots. Anal Methods 8:1981–1988.

301. Taghdisi SM, Danesh NM, Emrani AS, Ramezani M, Abnous K (2015) A novel electrochemical aptasensor based on single-walled carbon nanotubes, gold electrode and complimentary strand of aptamer for ultrasensitive detection of cocaine. Biosens Bioelectron 73:245–250.

302. Aliakbarinodehi N, Micheli GD, Carrara S (2015) Optimized electrochemical detection of anticancer drug by carbon nanotubes or gold nanoparticles. In: Res. Microelectron. Electron. PRIME 2015 11th Conf. PhD. pp 25–28

303. Lin Y-H, Chu C-P, Lin C-F, Liao H-H, Tsai H-H, Juang Y-Z (2015) Extended-gate field-effect transistor packed in micro channel for glucose, urea and protein biomarker detection. Biomed Microdevices 17:1–9.

304. Zhou N, Luo J, Zhang J, You Y, Tian Y (2015) A label-free electrochemical aptasensor for the detection of kanamycin in milk. Anal Methods 7:1991–1996.

305. Yan Z, Gan N, Li T, Cao Y, Chen Y (2016) A sensitive electrochemical aptasensor for multiplex antibiotics detection based on high-capacity magnetic hollow porous nanotracers coupling exonuclease-assisted cascade target recycling. Biosens Bioelectron 78:51–57.

306. Ajayi RF, Sidwaba U, Feleni U, Douman SF, Tovide O, Botha S, Baker P, Fuku XG, Hamid S, Waryo TT, others (2014) Chemically amplified cytochrome P450-2E1 drug metabolism nanobiosensor for rifampicin anti-tuberculosis drug. Electrochimica Acta 128:149–155.

307. Jain R, Sharma R (2013) Cathodic Adsorptive Stripping Voltammetric Detection and Quantification of the Antiretroviral Drug Tenofovir in Human Plasma and a Tablet Formulation. J Electrochem Soc 160:H489–H493. doi: 10.1149/2.105308jes

308. MansouriMajd S, Teymourian H, Salimi A, Hallaj R (2013) Fabrication of electrochemical theophylline sensor based on manganese oxide nanoparticles/ionic liquid/chitosan nanocomposite modified glassy carbon electrode. Electrochimica Acta 108:707–716.

309. Chua L (1971) Memristor-the missing circuit element. IEEE Trans Circuit Theory 18:507–519.

310. Puppo F, Traversa FL, Ventra MD, Micheli GD, Carrara S (2016) Surface trap mediated electronic transport in biofunctionalized silicon nanowires. Nanotechnology 27:345503. doi: 10.1088/0957-4484/27/34/345503

311. Rose GS, Rajendran J, Manem H, Karri R, Pino RE (2012) Leveraging memristive systems in the construction of digital logic circuits. Proc IEEE 100:2033–2049.

312. Pershin YV, Di Ventra M (2010) Experimental demonstration of associative memory with memristive neural networks. Neural Netw 23:881–886. doi: 10.1016/j.neunet.2010.05.001

313. Laiho M, Lehtonen E (2010) Arithmetic operations within memristor-based analog memory. In: 2010 12th Int. Workshop Cell. Nanoscale Netw. Their Appl. CNNA 2010. IEEE, pp 1–4

314. Sacchetto D, Gaillardon P-E, Zervas M, Carrara S, De Micheli G, Leblebici Y (2013) Applications of multi-terminal memristive devices: a review. IEEE Circuits Syst Mag 13:23–41.

315. Carrara S, Sacchetto D, Doucey M-A, Baj-Rossi C, De Micheli G, Leblebici Y (2012) Memristive-biosensors: A new detection method by using nanofabricated memristors. Sens Actuators B Chem 171:449–457.

316. Puppo F, Doucey M-A, Di Ventra M, De Micheli G, Carrara S (2014) Memristor-based devices for sensing. In: 2014 IEEE Int. Symp. Circuits Syst. ISCAS. IEEE, pp 2257–2260

317. Tzouvadaki I, Madaboosi N, Soares RRG, Chu V, Conde JP, De Micheli G, Carrara S (2015) Biofunctionalization study of Memristive-Biosensors for early detection of prostate cancer. In: Ph Res. Microelectron. Electron. PRIME 2015 11th Conf. On. IEEE, pp 17–20

318. Tzouvadaki I, Puppo F, Doucey M-A, De Micheli G, Carrara S (2015) Computational Study on the Electrical Behavior of Silicon Nanowire Memristive Biosensors. IEEE Sens J 15:6208–6217.

319. Witucki GL (1993) A silane primer: chemistry and applications of alkoxy silanes. J Coat Technol 65:57–57.

320. Berdat D, Marin A, Herrera F, Gijs MAM (2006) DNA biosensor using fluorescence microscopy and impedance spectroscopy. Sens Actuators B Chem 118:53–59. doi: 10.1016/j.snb.2006.04.064

321. Zhao W, Chiuman W, Lam JCF, McManus SA, Chen W, Cui Y, Pelton R, Brook MA, Li Y (2008) DNA Aptamer Folding on Gold Nanoparticles: From Colloid Chemistry to Biosensors. J Am Chem Soc 130:3610–3618. doi: 10.1021/ja710241b

322. Liu Y, Lin C, Li H, Yan H (2005) Aptamer-Directed Self-Assembly of Protein Arrays on a DNA Nanostructure. Angew Chem 117:4407–4412. doi: 10.1002/ange.200501089

323. Kim KS, Lee H-S, Yang J-A, Jo M-H, Hahn SK (2009) The fabrication, characterization and application of aptamer-functionalized Si-nanowire FET biosensors. Nanotechnology 20:235501. doi: 10.1088/0957-4484/20/23/235501

324. Godonoga M, Lin T-Y, Oshima A, Sumitomo K, Tang MSL, Cheung Y-W, Kinghorn AB, Dirkzwager RM, Zhou C, Kuzuya A, Tanner JA, Heddle JG (2016) A DNA aptamer recognising a malaria protein biomarker can function as part of a DNA origami assembly. Sci Rep. doi: 10.1038/srep21266

325. Song S, Wang L, Li J, Fan C, Zhao J (2008) Aptamer-based biosensors. TrAC Trends Anal Chem 27:108–117. doi: 10.1016/j.trac.2007.12.004

326. Radhapyari K, Kotoky P, Das MR, Khan R (2013) Graphene–polyaniline nanocomposite based biosensor for detection of antimalarial drug artesunate in pharmaceutical formulation and biological fluids. Talanta 111:47–53. doi: 10.1016/j.talanta.2013.03.020

327. Karimi-Maleh H, Tahernejad-Javazmi F, Atar N, Yola ML, Gupta VK, Ensafi AA (2015) A Novel DNA Biosensor Based on a Pencil Graphite Electrode Modified with Polypyrrole/Functionalized Multiwalled Carbon Nanotubes for Determination of 6-Mercaptopurine Anticancer Drug. Ind Eng Chem Res 54:3634–3639. doi: 10.1021/ie504438z

328. Wang WU, Chen C, Lin K, Fang Y, Lieber CM (2005) Label-free detection of small-molecule–protein interactions by using nanowire nanosensors. Proc Natl Acad Sci U S A 102:3208–3212. doi: 10.1073/pnas.0406368102

329. Goyal RN, Gupta VK, Chatterjee S (2010) Voltammetric biosensors for the determination of paracetamol at carbon nanotube modified pyrolytic graphite electrode. Sens Actuators B Chem 149:252–258. doi: 10.1016/j.snb.2010.05.019

330. Švorc Ľ, Sochr J, Tomčík P, Rievaj M, Bustin D (2012) Simultaneous determination of paracetamol and penicillin V by square-wave voltammetry at a bare boron-doped diamond electrode. Electrochimica Acta 68:227–234. doi: 10.1016/j.electacta.2012.02.071

331. Radhapyari K, Kotoky P, Khan R (2013) Detection of anticancer drug tamoxifen using biosensor based on polyaniline probe modified with horseradish peroxidase. Mater Sci Eng C 33:583–587. doi: 10.1016/j.msec.2012.09.021

332. Bo B, Zhu X, Miao P, Pei D, Jiang B, Lou Y, Shu Y, Li G (2013) An electrochemical biosensor for clenbuterol detection and pharmacokinetics investigation. Talanta 113:36–40. doi: 10.1016/j.talanta.2013.03.056

333. Kim D-M, Rahman MA, Do MH, Ban C, Shim Y-B (2010) An amperometric chloramphenicol immunosensor based on cadmium sulfide nanoparticles modified-dendrimer bonded conducting polymer. Biosens Bioelectron 25:1781–1788. doi: 10.1016/j.bios.2009.12.024

334. Simiele M, Carcieri C, De Nicolò A, Ariaudo A, Sciandra M, Calcagno A, Bonora S, Di Perri G, D'Avolio A (2015) A LC–MS method to quantify tenofovir urinary concentrations in treated patients. J Pharm Biomed Anal 114:8–11. doi: 10.1016/j.jpba.2015.05.001

335. Barkil ME, Gagnieu M-C, Guitton J (2007) Relevance of a combined UV and single mass spectrometry detection for the determination of tenofovir in human plasma by HPLC in therapeutic drug monitoring. J Chromatogr B 854:192–197. doi: 10.1016/j.jchromb.2007.04.015

Nima Aliakbarinodehi

CORE COMPETENCIES

A. **Electrochemical bioassays for pathogens/metabolites/drugs monitoring**

B. **Modeling and simulation of MEMS sensors/actuators**

C. **Nanofabrication and functionalization of microelectrodes in cleanroom**

D. **Surface functionalization by nanostructures**

E. **Digital electronics engineering**

F. **Fostering teamwork and collaboration**

EDUCATION

Oct 2013-Present

PhD in Biotechnology with focus on Biosensing and research fellow of Marie Curie European Program (PROSENSE-ITN)
Integrated Systems Laboratory (LSI), École polytechnique fédérale de Lausanne (EPFL), Switzerland

Thesis: Ultra Selective and Sensitive Electrochemical Detection of Anti-Cancer and Anti-Viral Drugs by Optimized Nano-Bio-Sensors

- Electrochemical, field effect, memristive etc. analyte detection
- Surface nanostructuring by carbon nanotubes and nanoparticles
- Surface biofunctionalization with enzymes, DNA, antibody
- Topography and metrology
- Nanofabrication of microelectrodes in clean room
- 3 papers published, 1 submitted, 2 under preparation

Sep 2010-Mar 2013

MSc in Electronic Micro and Nanosystems (MEMS), (GPA: 27.73/30),
Politecnico di Torino, Italy

Thesis (at EPFL): Electrochemical Properties of Nanostructures for Biosensing: Bismuth Nanoparticles versus Carbon Nanotubes & Au Nanoparticles

- Piezoelectric accelerometer design and simulation by CoventorWare
- Microfluidic channel simulation in COMSOL multiphysics

Sep 2004-Feb 2010

BSc in Electrical Engineering, Major: Electronics, (GPA: 14.52/20), Mazandaran University, Iran

Thesis: Design and implementation of mixed-signal electronic circuit of an answering machine

Contact Information

Av. De Valmont 12, 1010 Lausanne, Switzerland

+41791942624

nima.aliakbari@gmail.com

https://ch.linkedin.com/in/nima-aliakbari-0a3779b2

SKYPE: nima.aliakbari

Languages

ENGLISH	C1
ITALIAN	A1
FRENCH	A1
PERSIAN	Native

Personal Details

16/09/1986

MARRIED

IRANIAN

DRIVING LICENCE

HOLDING SWISS PERMIT B SINCE 2013

PROFESSIONAL EXPERIENCE

2008 – 2009 **Electronics and Automation Engineering**
Eshtad Company (Eshtad Co.), Tehran, Iran

Working as an electronics engineer to design circuits, draw PCB layout and implement circuits.

2008 **Electronics and Automation Engineering**
Faraz Danesh Asia Corporation (FDA Co.), Tehran, Iran

1-month internship to design micro controllers & VHDL-FPGA based circuits, and PCB design.

TECHNICAL EXPERTISE

Analytical methods

Cyclic/Square Wave Voltammetry, Chronoamperometry, Electrochemical Impedance Spectroscopy, Field Effect and Memristive effect, Quartz Chrystal Microbalance

MEMS design and simulation

COMSOL, CoventorWare, Matlab

Surface nanostructuring and functionalization

Templated-Nanoporous Film Electrodeposition, Drop-coating, Inkjet Printing, Chemical Vapor Deposition, oxygen plasma

Surface topography & metrology

AFM, SEM, FTIR & ATR spectrometry, UV spectrometry

Digital-electronic circuits development

AVR micro-controllers

Nanofabrication

Photolithography, wet etching, chemical vapor deposition, oxygen plasma

SCIENTIFIC ACTIVITIES

Related PhD Courses

June 2015 **Electrochemical nano-bio-sensing and bio/CMOS interfaces,** Lecturer(s): Carrara Sandro. Oral presentation
http://edu.epfl.ch/coursebook/en/electrochemical-nano-bio-sensing-and-bio-cmos-interfaces-MICRO-614

March 2015 **Theoretical Microfluidics,** Lecturer(s): Gijs Martinus, Lehnert Thomas. Oral exam
http://edu.epfl.ch/coursebook/en/theoretical-microfluidics-MICRO-718

Other skills

Data analysis
Nova software, Igor Pro, ImageJ, Excel, OriginLab, Prism

Electronic circuits design and analysis
Orcad, Multisim

Programming
C, C++

Computer
Microsoft Office (Word, Excel, Power point, Visio), Windows (XP, W7, W10), Macintosh (OS X Yosemite, El Capitan)

Leisure activities

Outdoor activities
hiking and nature walking, cinema

Sport activities
Squash

Watching movies
drama, mystery, thriller

March 2014 **Pharmacology and pharmacokinetics,** Lecturer(s): Firsov Dmitri, Kellenberger Stephan. Written exam and oral presentation
http://edu.epfl.ch/coursebook/en/pharmacology-and-pharmacokinetics-BIO-478

Jan 2014 **Reliability of MEMS,** Lecturer(s): Herbert Shea. Oral exam
http://edu.epfl.ch/coursebook/en/reliability-of-mems-edoc-MICRO-615

November 2013 **Scanning Electron Microscopy Techniques,** Lecturer(s): Cantoni Marco, La Grange Thomas. Written exam
http://edu.epfl.ch/coursebook/en/scanning-electron-microscopy-techniques-a-MSE-636-A

Conferences & Summer/Winter Schools

Feb 2014 **CCMX Winter School Surface Science and Coatings, Lecturer(s):** Brune Harald, Various lecturers. Oral presentation
http://edu.epfl.ch/coursebook/en/ccmx-winter-school-surface-science-and-coatings-MSE-634

June 2015 **11th Conference on PhD Research in Microelectronics and electronics, Lecturers: Various lecturers.** Oral presentation
http://web.eng.gla.ac.uk/prime2015/index.php

2013 – 2016 **PROSENSE Initial training network events, Lecturers: various lecturers**, Poster and Oral presentation
http://www.prosense-itn.eu/page-91788-en.html

- Conference: Prostate Cancer Diagnosis, September 2016, Bath, UK
- Spring school: Lable-free techniques for electronic sensing of biomolecules, April 2016, Zwebrucken, Germany
- Winter School: New nano-bio-sensing tools for theragnostics, February 2016, Lausanne, Switzerland
- Workshop: Integration of biosensing in multiplex lab-on-a-chip devices, July 2015, Lisbon, Portugal
- Workshop: Biosensor construction, January 2015, Cardiff/Pontypool, UK
- Workshop: Clinical perspectives and commercial forces on biosensor devices, September 2014, Bath, United Kingdom
- Workshop: Application of lectins in various format of analysis for glycoprofiling, January 2014, Bratislava, Slovakia

Secondment and Visits

April 2015 **Royal United Hospital, Bath, UK, 3 days visit:** discussion on most modern anticancer drug compounds to be considered

2015 – 2016 **University of Bath, Bath, UK, 4 months secondment:** development of aptamer based biosensors for tenofovir (HIV drug) detection

PUBLICATIONS

Conferences

Aliakbarinodehi, N., De Micheli, G., & Carrara, S. (2015, June). Optimized electrochemical detection of anti-cancer drug by carbon nanotubes or gold nanoparticles. In Ph. D. Research in Microelectronics and Electronics (PRIME), 2015 11th Conference on (pp. 25-28). IEEE.

Journals

Aliakbarinodehi, N., Taurino, I., Pravin, J., Tagliaferro, A., Piccinini, G., De Micheli, G., & Carrara, S. (2015). Electrochemical nanostructured biosensors: carbon nanotubes versus conductive and semi-conductive nanoparticles. Chemical Papers, 69(1), 134-142.

Aliakbarinodehi, N., De Micheli, G., & Carrara, S. (2016). Enzymatic and Nonenzymatic Electrochemical Interaction of Abiraterone (Antiprostate Cancer Drug) with Multiwalled Carbon Nanotube Bioelectrodes. Analytical Chemistry, 88(19), 9347-9350.

Aliakbarinodehi, N., Jolly, P., Bhalla, N., Miodek, A., De Micheli, G., Estrela, P. & Carrara, S. Highly Selective and Sensitive Drug Monitoring Suitable for Point-Of-Care Detection: Aptamer based Field-Effect Biosensor For Tenofovir Detection. Scientific Reports accepted

Aliakbarinodehi, N., De Micheli, G., & Carrara, S. (2016). Highly sensitive enzymatic MWCNTs-based biosensors for detection of abiraterone in human serum. NanoBioScience accepted.

Tzouvadaki, I. and Aliakbarinodehi, N., Giovanni De Micheli, Sandro Carrara. Coupling Aptamers Regeneration and Memristive effect for Ultrasensitive and Continuous Drug Monitoring. Submitted to RSC Nanoscale.

Stradolini, F. and Aliakbarinodehi, N., Tzouvadaki, I., Taurino, I., De Micheli, G., Bhalla, V., Carrara, S. Multi-Walled Carbon Nanotubes VS Fullerene: Comparison of Bio-sensing Properties in Direct Detection of Sedative Drugs. Under preparation

Aliakbarinodehi, N., De Micheli, G. & Carrara, S. Investigating the role of gold nanoparticles' size to raise Quantum Blockade and its effect on electron transfer between analyte and bioelectrode. Under preparation